The mid-Pleistocene climate transition in the Japan Sea: Insights of a combined palaeoceanographic and -monsoon, multi-proxy study using marine sediments of IODP Site U1427 from the shallow, southern Japan Sea

Thesis submitted for the degree of Doctor of Philosophy

Newcastle University, United Kingdom

Submitted by

Sonja Felder

School of Geography, Sociology and Politics

Newcastle University

July 2020

Abstract

In this thesis marine sediments from the Japan Sea (IODP Expedition 346, “Asian monsoon”, Site U1427) are used to investigate the expression of the mid-Pleistocene transition (MPT) in this marginal basin. The thesis establishes a revised geochronology (age model) for the sediments of Site U1427 across the MPT using benthic foraminifera-based trace element and oxygen stable isotope analyses. A multi-proxy approach was applied to decipher the marine versus terrestrial sources of particles in a shallow marine setting with close proximity to land. Combined, these approaches enabled to build a new conceptual model of the palaeoceanography of the Japan Sea across the MPT.

Establishing a geochronology for Site U1427 by comparing the benthic foraminiferal oxygen isotope record with a well-dated global reference stack of the same kind, is challenging because the Japan Sea, in contrast to the open ocean, is suggested to have been nearly isolated from the open ocean during glacial sea-level lowstands. This isolation restricted water mass exchange and led to widespread carbonate dissolution, which hampers the creation of continuous oxygen isotope records, and, counterintuitive, reduces glacial oxygen isotope ratios through the effect low saline (and low oxygen isotope ratio) waters accumulating in the basin. Instead, the geochronology is established by combining the benthic foraminiferal oxygen isotope record with trace element and shipboard colour reflectance data, and comparing those with age markers (biostratigraphic, palaeo-magnetic, tephra-chronological) and a well-dated, global reference stack (LR04-stack). This approach resulted in identification of marine isotope stages (MIS) 39-17 in the analysed sediments.

The Japan Sea sediments, including Site U1427, are influenced by the East Asian monsoons and glacio-eustatic sea-level variabilities, which both control marine productivity in the basin. The applied multi-proxy approach, combining bulk sediment organic matter parameters, i.e. total organic carbon (TOC), total nitrogen contents (TN) and carbon isotope ratios ($\delta^{13}C_{org}$), as well as carbonate content ($CaCO_3$) and Rock-Eval pyrolysis, proved indispensable to decipher the signals, as the close proximity to land (35 km to shore) brought some proxies to the limitations of interpretability. In short, $CaCO_3$ is used as a proxy for marine (carbonate) productivity, while TOC-TN (C/N) ratios, $\delta^{13}C_{org}$ and Rock-Eval pyrolysis parameters

indicate the origin of organic matter (OM), although this is a summary and other processes additionally influence these proxies. The interpretation of C/N ratios is difficult as the proxy is likely influenced by an inorganic component to nitrogen, leading to low C/N ratios and an overestimation of marine-derived organic matter. Combining individual analyses to the above multi-proxy approach enables estimating variations in contributions of marine- and terrigenous-derived organic matter, hence providing clues on changes in monsoon precipitation and sea-level stands across the MPT. The sediments of Site U1427 record monsoon variations on sub-orbital timescales and indicate enhanced precipitation/freshwater input at times during certain glacials, such as MIS 36.

A major outcome of this thesis is a revised palaeoceanographic model for the Japan Sea encompassing MPT. Previously, our understanding of the palaeoceanography of the Japan Sea was extrapolated from the most recent glacial-interglacial cycles. The palaeoceanographic model presented in this thesis proposes a better glacial connection between the open ocean and the shallow, southern Japan Sea during the early MPT, MIS 39-25, and a switch to the modern glacial near-isolation of the Japan Sea starting during the later stages of the MPT, MIS 24-17, caused by relatively higher glacial sea-levels, both globally and in the Japan Sea, during the early MPT compared to its later stage.

Acknowledgments

I would like to thank the NERC IAPETUS DTP and my CASE partner, the British Geological Survey (BGS), for funding this project and the Integrated Ocean Drilling Program (IODP), especially the IODP Expedition 346 participants, for generating numerous, very helpful data sets from Site U1427 and for making these data sets and the sediment samples available for use in this thesis. I would also like to thank the UK IODP division for providing financial support to attend the Urbino Summer School in Paleoclimatology (2015) and the 2nd post-cruise meeting in Melbourne (2016), which helped greatly in fostering connections with experts in the scientific field surrounding my PhD project. I would also like to thank the European Consortium for Ocean Research Drilling (ECORD) for funding that enabled being trained in and undertake foraminifera trace element training at the Godwin Laboratory for Palaeoclimate Research with pioneers of the method at the University of Cambridge. Mervyn Greaves, at the Godwin Laboratory, for his support, patience and positive feedback on my writing for the grant application, thesis, and subsequent publications.

I am also very grateful to my main supervisor, Andrew Henderson, for offering this project and to my other official advisors, Melanie Leng (BGS) and Kate Manzo (Newcastle University) for their support and feedback on written pieces, including successful funding applications to enable the isotope analyses. A special thanks to Thomas Wagner (Heriot-Watt University Edinburgh) who, although removed from the supervisory team early, continued to support this project by in-kind Rock-Eval analyses and who helped to shape the thesis through his input. This input made me feel able to move away from the initial project outline and to investigate peculiar data which subsequently led to the main finding.

I am incredibly grateful to Takuya Sagawa (Institute of Science and Engineering, Kanazawa University, Japan), who became an advisor in all foraminifera-related matters. After I initiated contact, he happily replied to this (then) unknown student from the other side of the world, and later organised the surface sample material, used as a modern reference values in foraminiferal isotopes and Mg/Ca ratios, and an unpublished data set for an Mg/Ca-temperature core-top calibration from the Japan Sea. At this point, I would also like to thank the participants of JAMSTEC Expedition KR-15-10, who collected the surface sample material.

I would also like to thank Tracy Ace (School of Earth and Environment, University of Leeds) for hassle-free use of her excellent micropalaeontological facilities at a time when personal circumstances prevented me from working at Newcastle. Thank you also to the technical staff at the School of Civil Engineering and Geosciences (CEGs, Newcastle University) and BGS NIGL (Keyworth) for their support through laboratory/analytical training and critical data quality control. Especially, Bernhard “Berni” Bowler (CEGs) for his continuous advice in the set-up, testing, supply of round robin material, assistance in mixing of in-house reference materials tweaked to the samples of Site U1427 and in the every-day running of the JENA TIC analyser, used for carbonate analyses. It was steep learning curve but an exciting experience, which I don’t want to miss, and the knowledge and skills gained resulted in critical thesis data analyses and will certainly be beneficial to an academic career.

I would also like to thank my viva examiners, Louise Callard and Sev Kender, for their time to discuss and their feedback on this thesis.

Finally, I would like to thank the students in the PGR cohorts I came into contact with, especially the Human Geography/Politics/Sociology cohort at Newcastle University, whom I shared an office with and who welcomed me, the only Physical Geography PGR at the time, into their circle. I would like to express my gratitude especially to Diana, Laura and Izzy who kept on helping me through difficult PhD phases with dinners, chats and laughter. I would also like to thank the IAPETUS DTP cohort, especially Lyndsey, and the Earth Surface Science Institute PGR cohort at the University of Leeds, and, of course Emily, Politics department of Newcastle University, for her motivational words and for offering her couch to sleep on.

Last but not least, I would like to thank my family, including my parents, Chris and Eva, for their continuous support, kind words and hugs and kisses whenever needed. I would also like to thank my newly found childcare-friends in Leeds, from nursery to more senior academics, who listened to my nags and made me see the funny side of the problematics a PhD can bring. I would like to thank especially Claire, Dave and Benji, Marlous and Robyn, Fay, Ben and Daisy, Helene and Yoann, Viktoria, Richard and Gabriel as well as Linda and Leo.

Thank you for all your support!

Table of contents

List of figures

List of tables

List of abbreviations and symbols

Al	Aluminium
AMOC	Atlantic meridonal overtruning circulation
b*	Colour reflectance index
Ba	Barium
C	Carbon
Ca	Calcium
$CaCO_3$	Calcium carbonate

CCD	Calcium carbonate compensation depth
CCSF-D, CSF-A	Depth scales in sediment cores
Cd	Cadmium
CLP	Chinese loess plateau
cm/ka	centimetres per thousand years
C/N ratio	Carbon to nitrogen ratio
CO_2	Carbon dioxide
δ	δ-notation for isotope records
$\delta^{13}C_{org}$	$\delta^{13}C$ of organic matter
$\delta^{13}C_{Uvigerina\ spp./Bull./Pach.}$	$\delta^{13}C$ of foraminifera
$\delta^{18}O_{Uvigerina\ spp./Bull./Pach.}$	$\delta^{18}O$ of foraminifera
$\delta^{18}O_{Planktonic}$	$\delta^{18}O$ of combined planktonic foraminifera species
DI	Deionised water
DOC	Dansgaard-Oeschger cycles
EA-IRMS	Element analyser coupled isotope ratio-mass spectrometer
EAM	East Asian monsoon
EASM	East Asian summer monsoon
EAWM	East Asian winter monsoon
ECS	East China Sa
ECSCW	East China Sea coastal water
EDX	Energy dispersive x-ray spectroscopy
Fe	Iron
G-IG	Glacial-interglacial (cycle)
g/cm^2ka	Gramms per cubic centimetre per thousand years
HC	Hydrocarbons
HCl	Hydrochloric acid
HI	Hydrogen index (Rock-Eval pyrolysis parameter)
IODP	Integrated Ocean Drilling Program
K	Potassium
ka	Thousand years, i.e. 41,000 years = 41 ka
KC	Kuroshio Current
LGM	Last glacial maximum
LR04	Open ocean $\delta^{18}O$ reference stack
Ma	Million years
MAR	Mass accummulation rate
m CCSF-D	Metres in sediment core, IODP depth scale

mg	Milligrams
Mg	Magnesium
$Mg/Ca_{Uvigerina\ spp.}$	Magnesium-calcium ratio of *Uvigerina* spp.
mg HC/g TOC	Amount of hydrocarbons per gram organic matter
mg CO_2/g TOC	Amount of carbon dioxide per gram organic matter
NH_4^+	Ammonium
µg	Micrograms
µm	Micrometres
MIS	Marine isotope stage
mm/a	Millimetres per year
mmol/mol	Milli-mol per mol
Mn	Manganese
MPT	Mid-Pleistocene transition
N	Nitrogen
Na	Natrium
NADW	North Atlantic deep water
ODP	Ocean Drilling Program
OI	Oxygen index (Rock-Eval pyrolisis parameter)
OM	Organic matter
‰	Permil
RE	Rock-Eval pyrolysis
rsd	Relative standard deviation
SEM	Scanning electron microscopy
Si	Silicon
SR	Sedimentation rate
SST	Sea surface temperature
S_1-, S_2-, S_3-peak	Parameters of Rock-Eval pyrolysis
TC	Total carbon
THC	Thermohaline circulation
THP	Tibet-Himalaya Plateau
Ti	Titanium
TIC	Total inorganic carbon
T_{max}	Parameter of Rock-Eval pyrolysis
TN	Total nitrogen
TOC	Total organic carbon
TSS	Tsushima Strait

TWC	Tsushima warm current
wt%	Weight percent
Zn	Zink

Chapter 1: Introduction

1.1 Introduction

During the most recent period of Earth's history, the Quaternary (2.58 million years (Ma) to present; Cohen and Gibbard, 2011), climate that was characterised by switches between glacials and interglacials (Ruddiman, 2001a). During glacials, global average temperatures were lower and some of the ocean water was contained in ice-sheets, lowering global average sea-levels. In contrast, during interglacials, temperatures were higher, leading to smaller ice-sheets and relatively higher global average sea-levels.

The switches between glacials and interglacials are thought to be controlled by so-called Milankovitch cycles in the Earth's orbital parameters, which determine the amount of solar radiation received on the Earth's surface and hence have a strong control on climate (see chapter 2; Milanković, 1949). The glacial-interglacial (G-IG) switches, or cycles, are recorded in, for example, the oxygen isotope composition of calcite shells from microscopic marine organisms, so-called foraminifera (see chapter 2; e.g. Shackleton and Opdyke, 1973, 1976; Hays et al., 1976; Berger and Loutre, 1991; Wilson et al., 2002; Laskar et al., 2004).

Across the early Quaternary period (2.58 to ~1.2 Ma), G-IG cycles varied at a frequency of 41 thousand years (ka) (e.g. Zachos et al., 2001; Lisiecki and Raymo, 2005), but approximately half-way through the Quaternary, during the Pleistocene epoch (2588 to 11 ka; Cohen and Gibbard, 2011), the G-IG cyclicity shifted to 100 ka. Between about 1200 and 600 ka, G-IG cycles became prolonged and glacials became more intense, producing greater sea-level falls and larger ice-sheets that started to decay more rapidly at glacial terminations (e.g. Shackleton and Opdyke, 1976; Pisias and Moore, 1981; Lisiecki and Raymo, 2005). This transitional period is referred to as the mid-Pleistocene transition, MPT.

Crucially, the change from the 41 ka to the 100 ka dominant orbital mode took place seemingly unprovoked by any major shifts in the orbital parameters. Therefore, the Milankovitch insolation cycles alone cannot explain the MPT, which led to numerous theories as to what might have caused this shift in climate change frequency, with several explanations involving feedback mechanisms internal to the Earth's climate system (see chapter 2). These feedback mechanisms include

changes in ice-sheet dynamics (e.g. Imbrie et al., 1993; Raymo, 1997; Clark et al., 2006; Chalk et al., 2017) and feedback mechanisms associated with the global carbon cycle (e.g. Shackleton, 2000; Ruddiman, 2003, 2004; Hönisch et al., 2009; Higgins et al., 2015), including changes in oceanic circulation patterns with increased CO_2 uptake and reduced outgassing into the atmosphere (e.g. de Menocal, 1995; Martínez-Garcia et al., 2011; Pena and Goldstein, 2014; Lear et al., 2016; Chalk et al., 2017; Kender et al., 2018; Sosdian et al., 2018; Farmer et al., 2019a; Hasenfratz et al., 2019). Large-scale atmospheric circulation patterns, such as the East Asian monsoon (EAM) have also been suggested as possible important influences, acting as fast conveyers of climate signals and triggers between ocean basins and across continents (Porter and An, 1995; Clark et al., 1999; Tada, 2004; Kubota et al., 2010; Tada et al., 2015a).

The modern EAM influences the water supply of nearly 1/3 of the world's population (Tada et al., 2013) in one of the world's most densely populated areas (East Asia), with many parts of socio-economic life being adapted to the monsoon and making the population vulnerable to unanticipated monsoon variations, such as draughts and flooding (IPCC members, 2013, 2014). The EAM gains heat and moisture from the Pacific and Indian Oceans and affects large parts of Asia (e.g. Wang et al., 2001), and is itself affected by climatic changes in regions as far away as Europe and the North Atlantic (Clark et al., 1999). Through its great extent, the EAM might have been relaying climate signals and triggers between the North Atlantic and North Pacific Oceans during the MPT, contributing to the almost simultaneous nature of this event.

An example for the suggested teleconnection are coexisting variations in the EAM and so-called Dansgaard-Oeschger cycles (DOC) rapid glacial warming events that are well-studied in North Atlantic sediments and reported for the last 1.4 Ma (e.g. Bond et al., 1992; Dansgaard et al., 1993; GRIP members, 1993; Raymo et al., 1998; Jansen et al., 2000; Tada, 2004; Kubota et al., 2010; Hernández-Almeida et al., 2012; Birner et al., 2016; Hodell and Channell, 2016). Fast-paced variations in the EAM, proposed to be associated with DOCs, have also been studied in cave speleothems across Asia (e.g. Wang et al., 2001; Cheng et al., 2016), but these records are often of too low resolution to record millennial-scale variability and their interpretation is not straightforward, as they may reflect seasonality, moisture sources or regional circulation patterns rather than variations in EAM precipitation intensity

(Clemens et al., 2010; Maher and Thompson, 2012; Zhang et al., 2018). Therefore, marine EAM records are more reliable recorders of precipitation intensity and, in addition, they extend far beyond the MPT, allowing to investigate potentially investigate the DOC-EAM link across the MPT. The Japan Sea, a marginal basin of the Northwest Pacific Ocean, comprises sediments with centimetre- to millimetre-scale dark/light sediment colour alternations, which are the result of variations in marine organic matter productivity/preservation and have been associated with monsoon and possibly DOC variations (e.g. Stein and Stax, 1992a,b; Tada et al., 1999; Tada, 2004; Ikehara and Itaki, 2007). More specifically, the productivity/preservation changes are linked to the East Asian summer monsoon (EASM) as it controls the amount and strength of nutrient-enriched water runoff and hence the nutrient-delivery to the Japan Sea via the Tsushima Strait, TSS (see chapter 2) (e.g. Tada et al., 1999; Oba et al., 1991).

The Japan Sea palaeoceanography is sensitive to glacio-eustatic sea-level variations, as the basin is connected to the open ocean (i.e. the Northwest Pacific and East China Sea, ECS) via shallow sills of less than 130 m water depth (e.g. Oba et al., 1991). The main inflow to the Japan Sea, and main nutrient source, is in the south via the Tsushima Strait, TSS. Nutrient-enriched, warm waters from the ECS are transported through the TSS via the so-called Tsushima Warm Current (TWC) which is linked to the amount of water runoff from the Asian landmass (i.e. EASM). The shallow Tsushima Strait (~130 m water depth) is suggested to have nearly dried up during the most recent glacial sea-level lowstands. During the late Pliocene/early Pleistocene (~2700 to 1200 ka) the average eustatic glacial sea-level drop was around ~–60 to –80 m, while across the most recent glacials (last ~900 ka) the development of the large Northern Hemisphere ice sheets led to average glacio-eustatic sea-level drops of about –120 m (*c.f.* Sosdian and Rosenthal, 2009). It is argued that the impact of glacial sea-level lowstands of similar extend as the Tsushima Strait sill water depth (~130 m) restricted or prevented the inflow via the TSS and hence reduced glacial marine productivity in the Japan Sea due to reduced nutrient input. This palaeoceanographic model of the Japan Sea has been developed based on sediment records covering the most recent G-IG cycles and it is assumed to be valid for at least the last ~1.7 Ma (e.g. Oba et al., 1991; Tada et al., 1999; Kitamura and Kimoto, 2006; Itaki, 2016; Gallagher et al., 2015; Saavedra-Pellitero et al., 2018). Whether this palaeoceanographic model applies to glacials across and,

more crucially, before the MPT, when glacio-eustatic sea-level variations were smaller (e.g. Sosdian and Rosenthal, 2009), is currently unknown.

The palaeoceanography of the Japan Sea leads to difficulties in generating high-resolution geochronologies that arise from wide-spread poor calcite preservation and an unusual behaviour of calcite oxygen isotopes in the Japan Sea. While in the open ocean oxygen isotopes are mainly controlled by global temperatures/ice-volume, in the Japan Sea they are additionally controlled by a local influence, i.e. reduced water salinity due to glacial isolation of the basin (see above). During glacials over the last 1.7 Ma it has been proposed that the combination of restricted water exchange with the open ocean and continued freshwater input through runoff and precipitation overrode the global oxygen isotope signal and led to unusually low glacial oxygen isotope values recorded in foraminiferal calcite (see chapter 2) (e.g. Oba et al., 1991; Tada et al., 1999). Even across this relatively short and well-studied time period there are deviations from the above-mentioned counterintuitive oxygen isotope interpretation. Oba et al. (1991) show a foraminiferal calcite-based oxygen isotope record which extends to 85 ka ago, encompassing two glacial cycles and, while eustatic sea-level fluctuations occurred during both, they are not consistently apparent as excursions to low glacial oxygen isotope values. This finding raises the question by how much the sea-level would need to drop to induce the salinity-related reverse oxygen isotope pattern in the Japan Sea records, and if this would change across the MPT given that glacio-eustatic sea-level variations were smaller.

Additionally, a detailed chemo-stratigraphy based on foraminiferal oxygen isotope values in the Japan Sea has so far been hindered by the poor preservation of carbonates, including foraminifera shells, especially during glacial periods (e.g. Oba et al., 1991; Dunbar et al., 1992; Tada, 1994). For a long time a reliable chemo-stratigraphy only reached back as far as 800 ka ago (Minami, 2003, Tada, 2004). Only recently a foraminifera-based chemo-stratigraphy was established from a shallow water site in the southern Japan Sea with much better carbonate preservation, IODP Expedition 346 Site U1427 (see chapter 3, sections 3.1, 3.2). This chemo-stratigraphy encompasses the last ~870 ka (Sagawa et al., 2018), but at Site U1427 a continuous succession of sediments was recovered, which encompasses approximately the last ~1.3 Ma (Tada et al., 2015a, b). Therefore, this site may lend itself to the extension of an isotope chemo-stratigraphy for the Japan Sea across the MPT.

1.2 Research Aims

This thesis addresses how the palaeoceanography of the Japan Sea and the monsoon precipitation intensity changed across the MPT. A focused program investigating the natural variations in, and history of, the EAM was undertaken by the Integrated Ocean Drilling Program (IODP; now International Ocean Discovery Program) with a number of monsoon-oriented ship expeditions during the mid-2010s in the northern Indian Ocean, the north-western Pacific and its adjacent marginal seas (IODP detailed planning group members, 2008), including the Japan Sea (see chapter 2, figure 2.7 and chapter 3, section 3.1). In this thesis, sediment samples of the shallow-water IODP Site U1427 are used to investigate these changes.

While the upper ~250 m of sediment interval at Site U1427 have been studied in some detail (Black et al., 2018; Gallagher et al., 2018; Sagawa et al., 2018; Tada et al., 2018; Saavedra-Pellitero et al., 2019; Peterson and Schimmenti, 2020), the sediments below ~260 m, which encompass the MPT, have received little attention. As an example, for Site U1427 a preliminary age model was produced on-board during Expedition 346 (Tada et al., 2015b) and recent studies have improved the age model for the upper ~350 m of sediment cores of the site (Sagawa et al., 2018; Gallagher et al., 2018). This improved age model is based on a close relationship between foraminiferal oxygen isotope values and a high resolution, shipboard colour reflectance record of b* (chapter 3, section 3.2.3), showing lower oxygen isotope values when b* is low. While the low b* values suggest reduced marine (biosilica) productivity, the low oxygen isotope values suggest a glacial interval (Sagawa et al., 2018). Sagawa et al. assume this relationship between b* and oxygen isotopes would continue across the MPT, but this hypothesis was never actually tested. This implies that, first, the chronological control on the sedimentary record of Site U1427 below 350 m, and especially the lowermost 100 m, is still limited and hence hinds a successful palaeoenvironmental study, which requires a solid geochronological model to enable comparison with other locations/sites to put the newly gathered information into a global context. Second, it is not clear if the smaller glacio-eustatic sea-level variations before the MPT (see section 1.1; e.g. Sosdian and Rosenthal, 2009) may have altered the relationship between b* and foraminiferal oxygen isotopes, making it vital to test this hypothesis.

Beside the potential of Site U1427 to enable generating a chemo-stratigraphy for the Japan Sea across the MPT due to its good carbonate preservation, it is also likely

that the sediments at this site record EASM variations. Located right underneath the path of the Tsushima warm current (TWC), the main control on nutrient-input to the Japan Sea, which is affected by ESAM variability, suggests the sediments of Site U1427 may record EAM variations expressed as variable marine productivity (chapter 2) (Tada et al., 2013, 2015a, b, c). In addition, the site's high and constant sedimentation rates may enable gathering high-resolution EASM records.

The specific research objectives of this PhD project are:

1) To establish a geo-chronology for the sediment interval ~250-525 m CCSF-D of Site U1427, which contain sediments deposited during the MPT, by
    - constructing a $\delta^{18}O$ record based on foraminiferal calcite, attempting continuity across glacials, and
    - assessing its comparability to a well-dated open ocean reference stack, LR04-stack, and relating them to each other where possible.
2) To investigate the potential of the sediments of Site U1427 to archive variations in the EASM across the MPT through analysis of marine productivity, TWC inflow/freshwater and terrigenous input across orbital and sub-orbital timescales.
3) To assess how glacio-eustatic sea-level variations across the MPT affected the glacial isolation of the shallow, southern Japan Sea (Site U1427) and test the hypothesis of continued anomalous low glacial $\delta^{18}O$ values across the MPT.

1.3 Thesis Structure

This chapter outlined the overarching motivation and research objectives of this thesis. Chapter 2 reviews our current understanding of Quaternary climate controls and theories behind the MPT before introducing marine sediment climate archives and the specifics surrounding the interpretation of proxy records from the Japan Sea. Chapter 3 outlines the laboratory protocols, sample selection and analyses limitations for the different methods that have been applied. In chapter 4 the preliminary age model for the investigated interval of Site U1427, i.e. ~260-525 m, is revised and recently published age indicators/markers added to develop a revised age-depth

relationship for this interval. Furthermore, chapter 4 a chemo-stratigraphy is developed for the interval, based on a newly created benthic foraminiferal $\delta^{18}O$ record. This revised age model is then put in global context by comparison with a well-dated, open ocean reference stack. Chapter 5 deciphers the varying contributions of terrigenous input and marine productivity to the sediments of this near-shore, shallow-water site, which are thought to be associated with changes in the EASM precipitation intensity (on orbital and sub-orbital timescales) and glacio-eustatic sea-level variations (orbital-scales). Chapter 6 focusses on the effects of changing glacio-eustatic sea-level variations on the palaeoceanography of the shallow, southern Japan Sea across the MPT. The findings are then summarised and concluded in chapter 7 before remaining and new research questions are discussed.

Chapter 2: Quaternary Climate, the Mid-Pleistocene Transition, Marine Proxy Records and the Palaeoceanography of the Japan Sea

2.1 Introduction

One of the main controls on the Earth's climate are external, orbital parameters (on timescales of ~20-400 ka, e.g. Ruddiman, 2001b) and their complex, not yet fully understood feedback mechanisms within the Earth's atmosphere, hydrosphere, lithosphere, cryosphere and biosphere, such as greenhouse gasses, ice albedo and vegetation cover. Even though the controls on climate mechanisms and their positive and negative feedbacks have received much attention recently (see below), there are still conundrums in the Earth's climate history that have not been fully explained. One of these is the mid-Pleistocene transition (MPT), centred between ~1200 and 600 ka, which forms the temporal focal point of this thesis. During the MPT the periodicity of glacial-interglacial (G-IG) cycles decreased in frequency but increased in amplitude, meaning that the difference in temperature, ice-volume and sea-level between glacials and interglacials increased, while switches between them occurred less frequent. The MPT has been described from a number of climate archives in the ocean and on land, and a number of hypothesis have been proposed as to what might have caused it (section 2.3 and appendix A). This chapter aims to provide the background to the MPT and justification for the selected study area, the shallow, southern Japan Sea (see section 2.4).

2.2 Global Climate and Milankovitch Cycles

The Earth's orbital path around the Sun and the amount of solar radiation it receives (insolation) are the main controls on Earth's climate. Over timescales of hundreds of thousands of years insolation changes predictably and in regularly recurring intervals controlled by a set of orbital parameters, collectively called Milankovitch cycles (Milanković, 1949). According to Milankovitch, the cycles control insolation and hence the Earth's surface heating and seasonality at higher latitudes and therefore the Earth's climate which shift between the ice-ages (glacials) and warm stages (interglacials). The Milankovitch cycles control insolation through (i) variations in the angle/tilt of the Earth's spin axis between polar north and celestial north (obliquity), which in turn controls the intensity of seasons, varying at 41 ka cycles (figure 2.1a), (ii) the shape of the Earth's orbit around the sun (eccentricity),

which exerts a strong control on seasons by modulating their amplitude (supressing/strengthening seasons in opposing hemispheres at high eccentricities through its effects on weather), varying over 100 and 400 ka (figure 2.1b), and (iii) the wobble of the Earth's spin axis (precession), varying at cycles that culminate in 19 and 23 ka cyclicity (figure 2.1c) (after Milanković, 1949; Hays et al., 1976; Zachos et al., 2001; Maslin and Ridgwell, 2005).

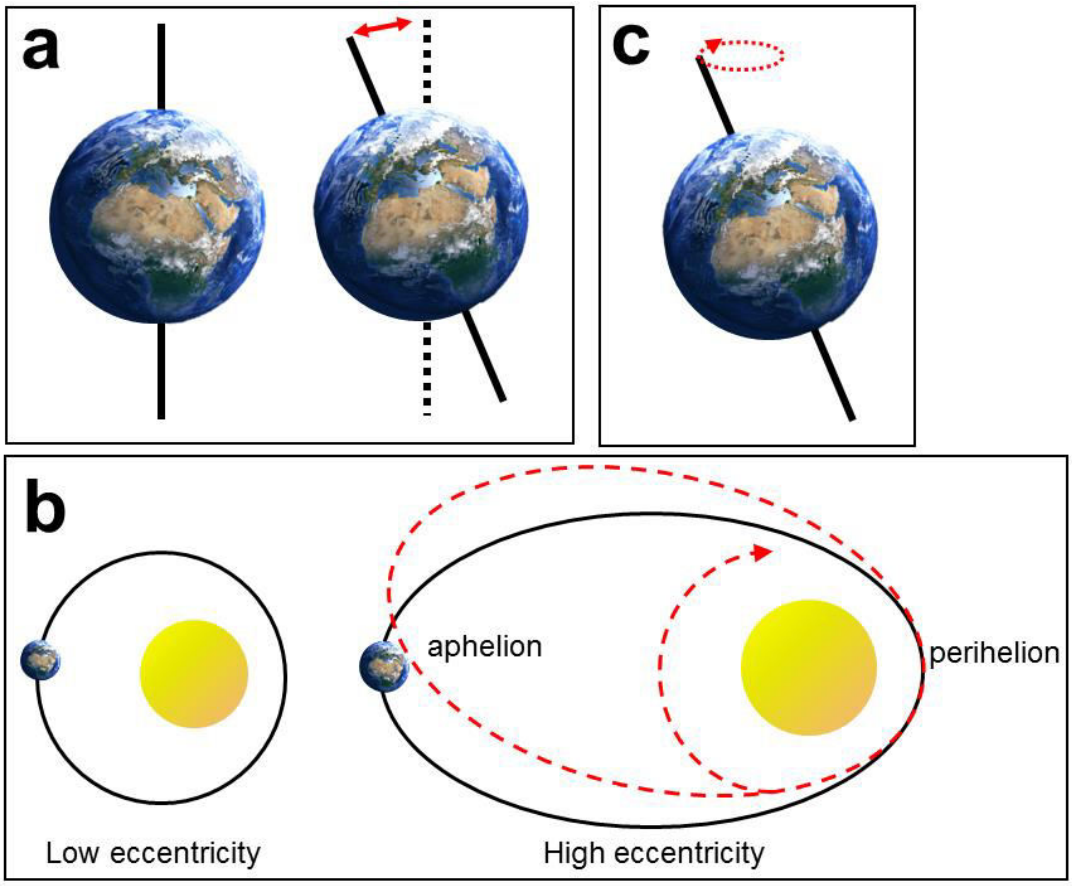

Figure 2.1. Milankovitch parameters showing low and high obliquity (fig. 2.1a), low and high eccentricity (fig. 2.1b) and the movements of precession, i.e. precession of the Earth's orbit (fig. 2.1b, red dashed line) and precession of the Earth's spin axis (fig. 2.1c).

To test Milankovitch's theory, climate records, long enough to document the full-scale of natural climate variability are needed. Instrumental temperature climate records only go back ~170 years (Brohan et al., 2006), therefore longer climate records are needed. These so-called proxy records are closely linked to past (palaeo) climate and include records of tree rings (figure 2.2a) (up to 1 ka; McCarroll and Loader, 2005;), lake sediments (pollen, lake levels, ~20 ka; National Paleoclimate Data Centre, Boulder, Colorado; figure 2.2b) ice cores (up to ~800 ka, Kitamura, 2016; figure 2.2a), Chinese loess deposits (up to ~3 Ma, Ruddiman,

2001c; figure 2.2a) and cave speleothems (Chinese speleothems up to 640 ka; Cheng et al., 2016), but the longest, and most widespread palaeo-archive are ocean sediments (up to ~200 Ma; e.g. Duxbury et al. 2005; Ruddiman, 2001c) (figure 2.2c).

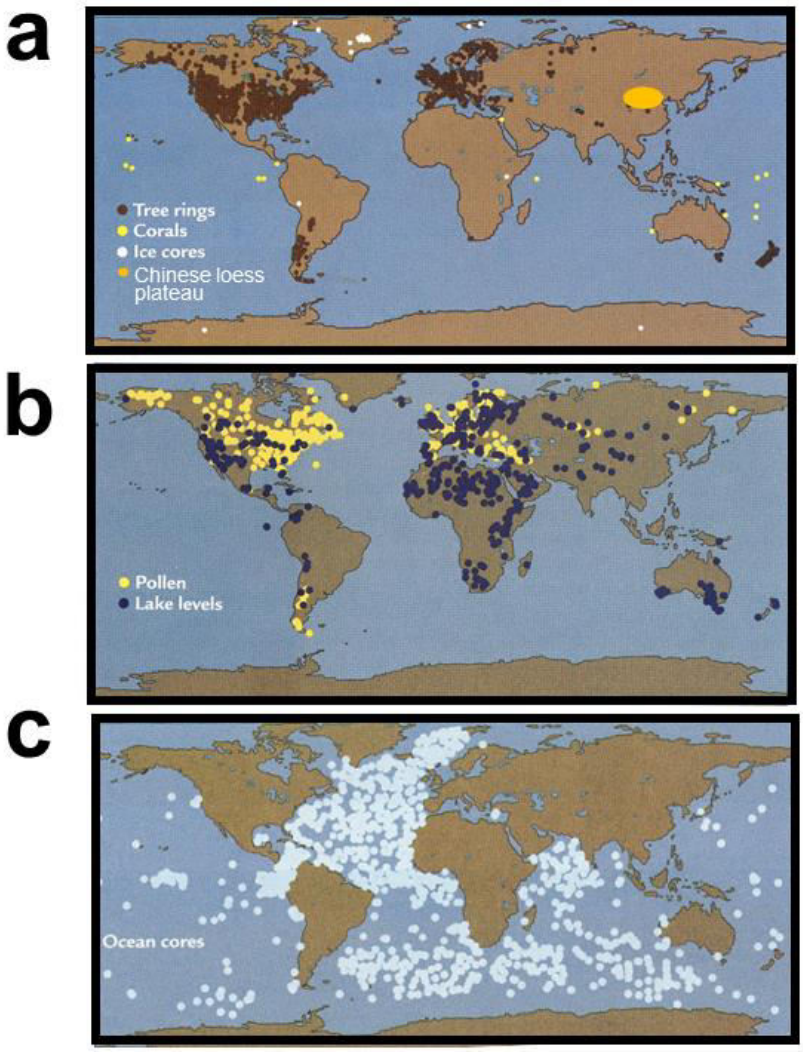

Figure 2.2. Global distribution of climate proxy record sites of tree rings, corals, ice cores and the Chinese loess plateau (fig. 2.2a), lake sediments (fig. 2.2b) and marine sediment sites (fig. 2.2c) (state 2001). From Ruddiman (2001c) with approximate location of the Chinese loess plateau after Ao et al, 2012 (fig. 2.2a).

Contained in ocean sediments are (amongst others) microscopic, single-celled marine organisms (foraminifera) that make up their shells from calcium carbonate ($CaCO_3$) (e.g. Bé et al., 1977). The oxygen in these shells, like elsewhere on the planet, consist of the three oxygen isotopes which occur in different abundances on Earth (^{16}O abundance of 99.76 % of total oxygen, ^{17}O abundance 0.04 %, ^{18}O abundance 0.20 %; Garlick, 1966). Switches in states (solid, fluid, gaseous) involves isotope fractionation which is a preferential selection process (figure 2.3). For example, when water evaporates and changes into the gaseous phase, fractionation

leads to the lighter oxygen isotope (^{16}O) preferentially being incorporated into the gaseous phase, leaving the remaining water relatively enriched in the heavier isotopes (^{18}O) (figure 2.3) (Ruddiman, 2001c, and Hoefs, 2004, for summaries). Fractionation also takes place in condensation leading to precipitation being enriched in ^{18}O compared to the remaining vapour. In the hydrological cycle these fractionation processes are affected by other parameters such as temperature, altitude and transport distance (illustrated in figure 2.3) (for further details see e.g. Muller and MacDonald, 2000; Ruddiman, 2001c; Hoefs, 2004; Leng, 2006). The isotope composition of ocean water is directly related to the hydrological cycle, with water evaporation from the oceans, transport in the atmosphere and its return to the oceans through precipitation, freshwater runoff and/or melting of ice sheets.

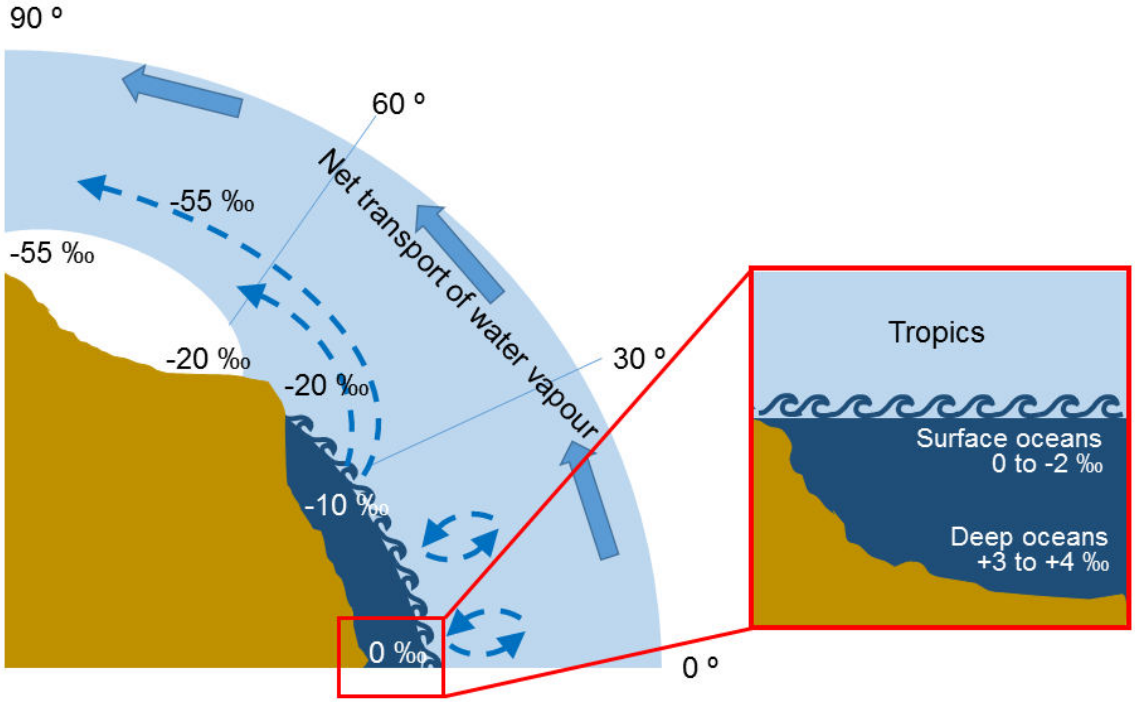

Figure 2.3. Oxygen isotope fractionation in the global ocean, atmosphere and cryosphere system, showing the modern global water vapour cycle from the tropics to the poles and associated $\delta^{18}O$ fractionation, leading to higher values in tropical waters compared to ice at the poles and typical modern $\delta^{18}O$ values. Modified after Ruddiman (2001d).

On a global scale there are measureable differences in the isotopic composition (ratio of heavier ^{18}O versus lighter ^{16}O isotopes, expressed as $\delta^{18}O$) of the mean ocean water over G-IG cycles. These $\delta^{18}O$ differences are recorded in foraminifera shells, which secrete their calcite shells in (near-) isotopic equilibrium with the surrounding seawater, and mainly respond to temperature and the $\delta^{18}O$ of the

surrounding seawater which is a function of global ice volume and water salinity (e.g. Emiliani, 1955; Haq et al., 1987; Ruddiman, 2001d; Lisiecki and Raymo, 2005; Maslin and Swann, 2006). Foraminiferal $\delta^{18}O$ records are therefore closely linked with the waxing and waning of the large continental ice sheets, showing higher $\delta^{18}O$ values during glacials and lower $\delta^{18}O$ values during interglacials (figure 2.4).

Pioneering work by Emiliani established a nomenclature for the G-IG cycles in $\delta^{18}O$ based on cycle counting, starting at the present (marine isotope stage, MIS, 1) and giving each glacial an even and each interglacial an odd number (Emiliani, 1955). The analysis of the foraminiferal calcite-based $\delta^{18}O$ records showed frequencies similar to those predicted by Milankovitch's theory of orbital parameters (e.g. Shackleton and Opdyke, 1973, 1976; Hays et al., 1976; Berger and Loutre, 1991; Laskar et al., 2004).

However, the Milankovitch cycles alone cannot fully explain all shifts in palaeo-climate. Controlled by insolation changes there are a number of feedback mechanisms within the Earth's climate system. Although a lot of research has investigated the complex interactions between astronomical forcing and feedback mechanisms within the Earth's climate system (e.g. Imbrie et al., 1993; de Menocal, 1995; Raymo, 1997; Shackleton, 2000; Ruddiman, 2003, 2004; Clark et al., 2006; Hönisch et al., 2009; Martínez-Garcia et al., 2011; Pena and Goldstein, 2014; Higgins et al., 2015; Lear et al., 2016; Chalk et al., 2017; Kender et al., 2018; Sosdian et al., 2018; Farmer et al., 2019a; Hasenfratz et al., 2019), these internal feedback mechanisms and their interactions are not yet fully understood. This leads to a number of shifts in the Earth's climate history that cannot yet be fully explained, one particularly being the mid-Pleistocene transition.

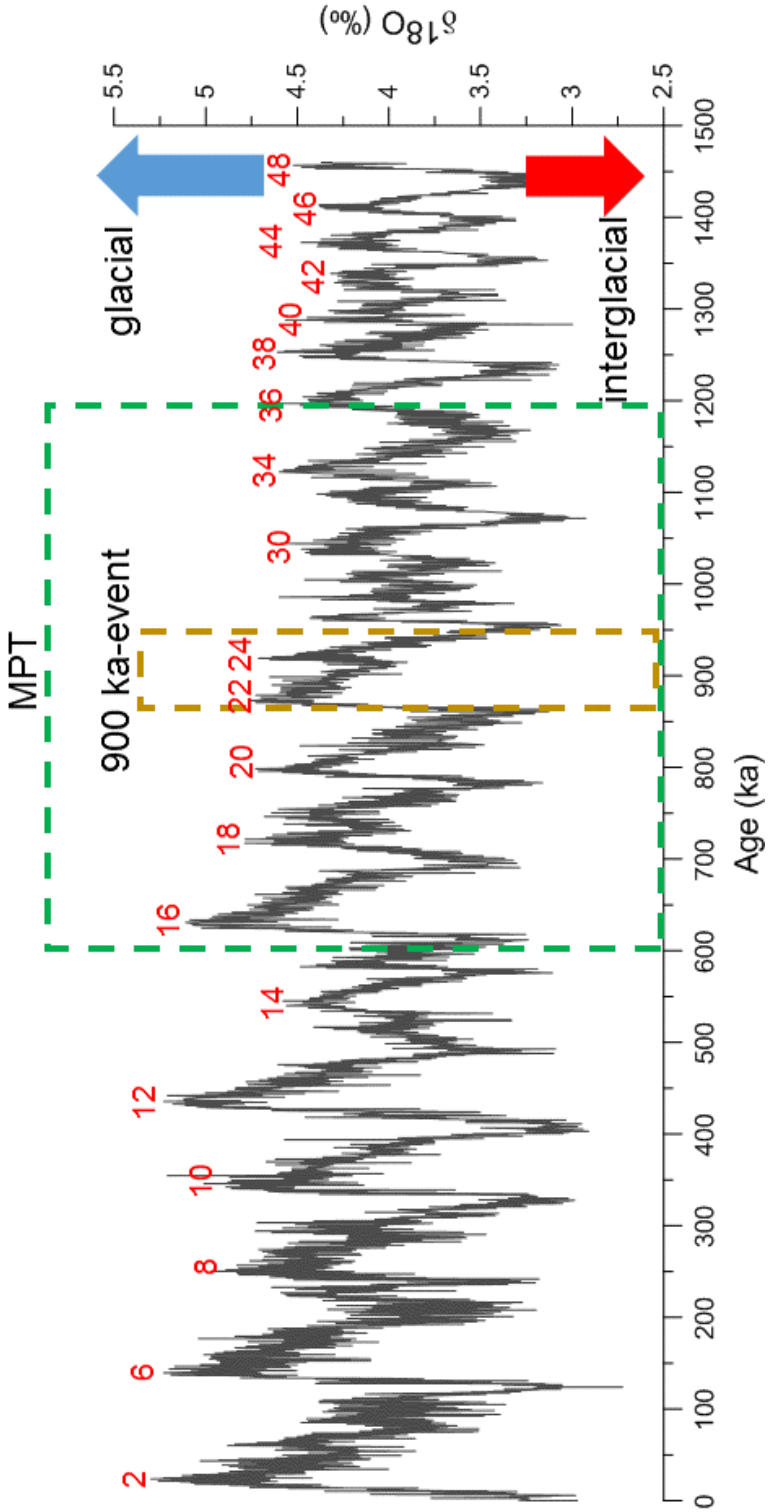

Figure 2.4. G-IG cycles (with marine isotope stages, red numbers) across the Pleistocene (last 1500 ka) as indicated by a collation (stack) of marine benthic foraminiferal $\delta^{18}O$ records (LR04-stack; from Lisiecki and Raymo, 2005). During the earlier Pleistocene (right side) the periodicity of G-IG cycles was higher (i.e. occurring more frequent, ever ~41 ka), while during the late Pleistocene (left) the frequency had become lower (~100 ka) and the signal amplitude had increased. The approximate timing of the transitional period (MPT) is indicated by the green box. The 900 ka-event (see section 2.3) is indicated by the golden box.

2.3 Quaternary Climate History and the Mid-Pleistocene Transition

2.3.1 Changes in glacial-interglacial cycles across the mid-Pleistocene transition

During the most recent period of Earth's history, the Quaternary (2.58 Ma to present; Cohen and Gibbard, 2011), the climate has been characterised by a gradual atmospheric CO_2 decline and cooling trend (e.g. Zachos et al., 2001; Ruddiman, 2003, 2004; Sosdian and Rosenthal, 2009). Although polar ice caps existed before, with the beginning of the Quaternary much larger polar (northern hemispheric) ice sheets started to appear, as inferred from sensitive marine geochemical palaeo-proxy records, such as marine calcite-based oxygen stable isotope ($\delta^{18}O$) records (figure 2.4) (e.g. Berger and Loutre, 1991; Maslin et al., 2001; Zachos et al., 2001; Mudelsee and Raymo, 2005; Rohling et al., 2014).

Approximately half-way through the Quaternary period, during the Pleistocene epoch (2588 to 11 ka; Cohen and Gibbard, 2011), the mid-Pleistocene transition (MPT) occurred. The MPT is characterised in marine benthic foraminiferal $\delta^{18}O$ records, such as the LR04-stack (figure 2.4), by a change in the periodicity of G-IG cycles from 41 to quasi 100 ka, by the onset of abrupt G terminations (saw-tooth structure) and an increase in signal amplitudes (e.g. Shackleton and Opdyke, 1976; Pisias and Moore, 1981; Lisiecki and Raymo, 2005). The early Pleistocene G-IG cycles were characterised by an obliquity-dominated ~41 ka periodicity, with relatively low signal amplitudes in $\delta^{18}O$ and being symmetrical, with gradual ice build-up and decay (figure 2.4). In contrast, the G-IG cycles of the last ~800 ka are characterised by a quasi-100 ka periodicity, higher $\delta^{18}O$ signal amplitudes, i.e. greater differences between glacial/interglacial ice-volume/sea-level/temperature, and abrupt glacial terminations with rapid ice-decay (figure 2.4). While there is ongoing debate on the structure of the MPT, whether it was abrupt or gradual, and the exact timing of the onset of the 100 ka cyclicity, there is consensus that the MPT is centred between 1200 and 600 ka (figure 2.4) (e.g. Ruddiman et al., 1989; Maslin and Ridgwell, 2005; Clark et al., 2006; McClymont et al., 2013; Ford and Raymo, 2020; Peng et al., 2020).

2.3.2 Potential mechanisms of change

Crucially, the MPT occurred in the absence of any changes in the orbital parameters, which sparked a debate about the dominant Milankovitch parameter driving climate before and after the MPT, and the mechanisms that have led to the

MPT. There is general consensus that the pre-MPT 41 ka cycles were controlled by obliquity, which influences on insolation through controlling in seasonality (see figure 2.1). There is ongoing debate as to what drives the modern quasi 100 ka G-IG cyclicity because the most obvious driver, eccentricity, which varies at 100 ka (section 2.2), is the orbital parameter with the weakest influence on insolation (e.g. Berger and Loutre, 1991; Imbrie et al., 1992; Imbrie et al., 1993; Park and Maasch, 1993; Berger and Jansen, 1994; Tiedemann et al., 1994; Maslin and Ridgwell, 2005; Clark et al., 2006; Elderfield et al., 2012; Farmer et al., 2019b; Bajo et al., 2020). Therefore, feedback mechanisms within the Earth's climate system must have started to amplify the eccentricity insolation signal or led to a non-linear response to insolation forcing, essentially allowing the skipping of obliquity/precession cycles and prolonging glacials and interglacials (Imbrie et al., 1993; Mudelsee and Schulz, 1997; Mudelsee and Stattegger, 1997; Raymo, 1997; Raymo et al., 1997; Paillard, 1998; Berger et al., 1999; Clark et al., 1999; Shackleton, 2000; Maslin et al., 2001; Head and Gibbard, 2005; Maslin and Ridgwell, 2005; Hönisch et al., 2009; Martínez-Garcia et al., 2011; Ganopolski and Calov, 2011; Abe-Ouchi et al, 2013; Pena and Goldstein, 2014; Higgins et al., 2015; Maslin and Brierley, 2015; Tzedakis et al., 2017; Chalk et al., 2017; Diester-Haas et al., 2018; Martin-Garcia et al., 2018; Bajo et al., 2020).

Proposed feedback mechanisms to explain the MPT include changes in ice-sheet dynamics and a decline in atmospheric CO_2, which changed the response of Earth's climate system to orbital/insolation forcing (Clark et al., 2006). Ice-sheet dynamics may have changed through the ablation of soft rocks, regolith, underneath the Laurentide ice-sheet (North America) throughout the Quaternary (Clark and Pollard, 1998; Clark et al., 2006; Chalk et al., 2017). The rougher surface of the bed rock underneath would have slowed down the ice-flow and given the ice-sheet greater stability, allowing it to grow larger and withstand insolation forcing/melting for longer, hence prolonging G-IG cycles (Imbrie et al., 1993; Raymo, 1997; Clark et al., 1998; Bintanja and van de Wal, 2008; Hodell et al., 2008; McClymont et al., 2013). A combination of ice-sheet dynamics/regolith-hypothesis with the atmospheric CO_2 decline has also been proposed (e.g. Willeit et al., 2019).

A number of feedback mechanisms have been proposed for the atmospheric CO_2 drawdown/temperature fall, which are related to changes in the global carbon cycle (e.g. Shackleton, 2000; Ruddiman, 2003, 2004; Hönisch et al., 2009; Higgins et al.,

2015). The proposed mechanisms include weathering of silicate-bearing rocks, volcanism and tectonics (Raymo et al., 1997; Denton, 2000; Kender et al., 2018; Viaggi et al., 2018), pyrite weathering (Kölling et al., 2019) and circulation changes between the ocean-atmosphere and within the ocean itself (e.g. Broeker and Denton, 1990; Imbrie et al., 1993; Diester-Haass et al., 2018; see also below).

Central to the debate is where the removed atmospheric CO_2 was stored during glacials, and the oceans may have played an important role as ocean circulation and ventilation can affect carbon burial and outgassing into the atmosphere (Broecker, 1991; Broecker, 1982a; Hoogakker et al., 2006; Sosdian and Rosenthal, 2009; Martínez-Garcia et al., 2011; Pena and Goldstein, 2014; Lear et al., 2016; Hasenfratz et al., 2019). There is ample evidence for ocean circulation changes in the oceans across the MPT that could contribute to an atmospheric CO_2 drawdown, such as weakening of deep-ocean circulation, reduced CO_2 exchange between deep and surface ocean waters, and an increase biological productivity through iron fertilisation, as summarised by Farmer et al. (2019a).

In detail, a slowdown in ocean circulation, more specifically reduced North Atlantic deep-water (NADW) formation, an integral part to the global thermohaline circulation (THC; Broecker, 1991), has been suggested for the MPT. For example, during MIS 24-22 (figure 2.4) and subsequent glacials of the 100 ka-world there is evidence for reduced NADW formation and its southward export to the southern Ocean, i.e. the Atlantic meridonal overturning circulation AMOC, which weakened THC and increased CO_2 storage in the deep-ocean (Broecker, 1982a; Elderfield et al., 2012; Pena and Goldstein, 2014; Farmer et al., 2019b). The weakened circulation may have led to greater amounts of CO_2 stored in the deep ocean, as inferred from more corrosive and nutrient-enriched Atlantic deep waters (Lear et al., 2016; Sosdian et al., 2018). Similarly, there is evidence for reduced Pacific Ocean circulation, as inferred from reduced oxygenation and more corrosive waters in the low latitude Pacific (Diz et al., 2020).

The oceans could have further reduced atmospheric CO_2 through a strengthening of the biological pump. Reconstructions of iron fluxes to the sub-Antarctic Southern Ocean find peaks in glacial iron input, i.e. dust, increased from ~1250 ka gradually across the MPT, and if this iron was bioavailable then it could have increased ocean CO_2 sequestration (Martínez-Garcia et al., 2011; Chalk et al., 2017). In addition, there is evidence for a stronger glacial density stratification of the ocean water

column, e.g. from the Southern Ocean (Hasenfratz et al., 2019) and the northern hemisphere (Bering Sea, Kender et al., 2018), which resulted in reduced CO_2 outgassing and increased CO_2 storage in the oceans (e.g. deMenocal, 1995; Martínez-Garcia et al., 2011; Lear et al., 2016; Chalk et al., 2017; Kender et al., 2018).

2.3.3 Sea-level changes

The reduced atmospheric CO_2 and associated temperature decline likely have contributed to a significant ice volume increase around 900 ka, and themed the “900 ka-event” (figures 2.4 and 2.5a) (e.g. Elderfield et al., 2012; Rohling et al., 2014). Associated with the ice volume increase is a sea-level drop of up to –120 m during MIS 22 (figure 2.5b) (e.g. Bintanja et al., 2005; Sosdian and Rosenthal, 2009; Elderfield et al., 2012; Rohling et al., 2014; Berends et al., 2019). Globally average glacio-eustatic sea-level variations were smaller before the MPT, dropping by on average ~–60 to –80 m between ~2700 and 1200 ka (*c.f.* Sosdian and Rosenthal, 2009), while during the most recent, late Pleistocene glacials, sea-level falls increased to up to –120m +/-32 m due to the development of large northern hemispheric ice sheets (figure 2.5b) (*c.f.* Sosdian and Rosenthal, 2009; Lambeck et al., 2014).

The sea-level estimates shown in figure 2.5 are global averages, modelled from $\delta^{18}O$ data of the LR04-stack (Bintanja et al., 2005; Elderfield et al., 2012; Rohling et al., 2014; Berends et al., 2019). Indicating global mean eustatic sea-level variations over the ~1100 ka is the model by Bintanja et al. (2005), with a more recent model based on the LR04-stack across the last 3.6 Ma presented in Berends et al. (2019). Another sea-level model encompassing the entire MPT can be found in Elderfield et al. (2012) but this model focusses on a marine site near New Zealand only. The Elderfield et al. (2012) model suggests relatively stable interglacial sea-levels and an abrupt ice-volume increase and sea-level fall around 900 ka (MIS 24/22), after which glacial sea-levels are lower than before. A northern hemispheric sea-level reconstruction is presented in Rohling et al. (2014) and is based on a $\delta^{18}O$ record from Gibraltar in the Mediterranean Sea, encompassing the last 5300 ka.

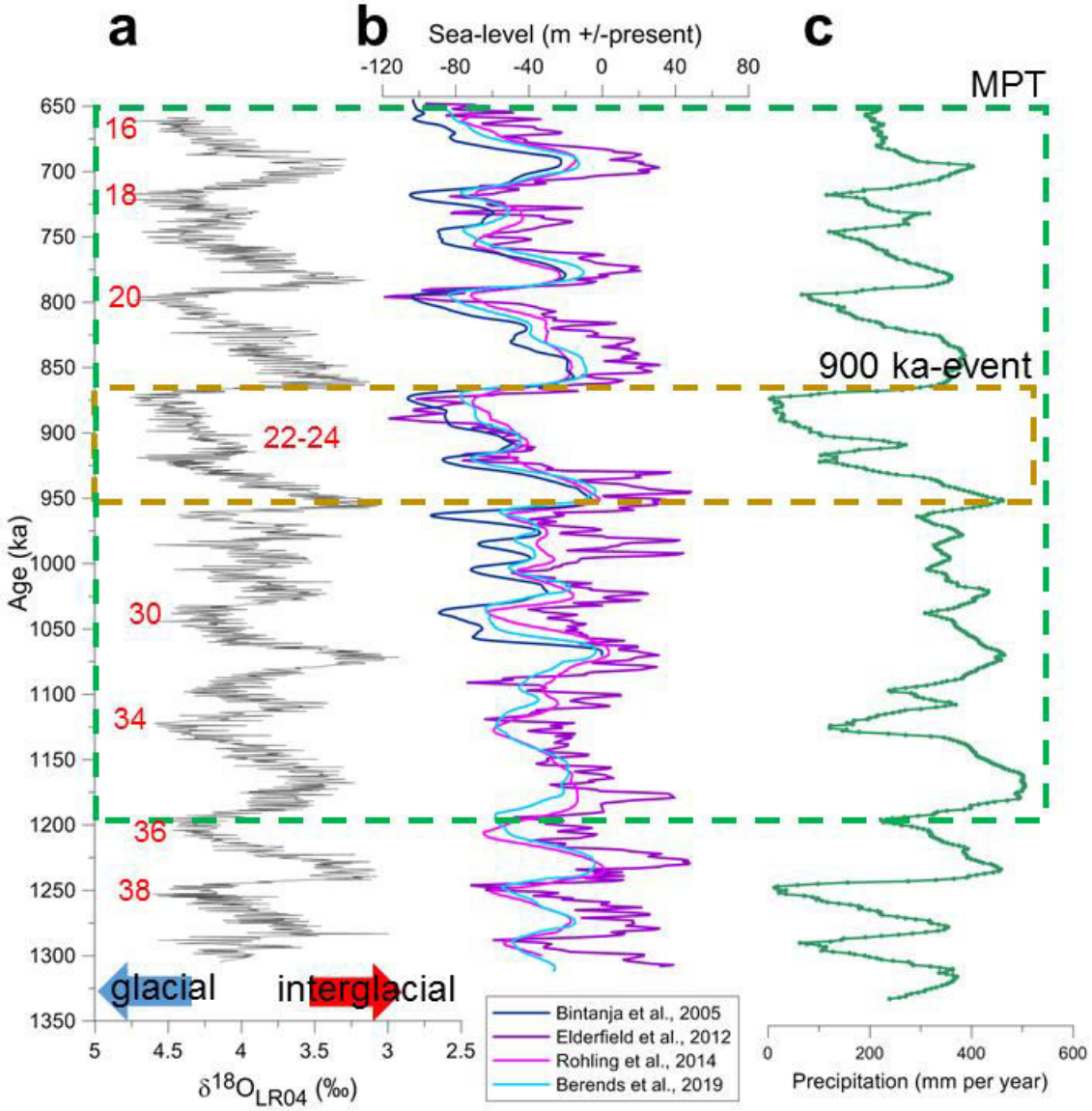

Figure 2.5. Comparison of the $\delta^{18}O$ LR04-stack by Lisiecki and Raymo (2005) with marine isotope stage (red numbers) (fig. 2.5a), global average glacio-eustatic sea-level reconstructions (Bintanja et al., 2005; Elderfield et al., 2012; Rohling et al., 2014; Berends et al., 2019) (fig. 2.5b) and precipitation intensity changes on the Chinese Loess Plateau (Peng et al., 2020) (fig. 2.5c) across the MPT (green box) and the 900 ka-event (golden box).

The pronounced 900 ka-event, at MIS 24-22, is suggested to be an time interval characterised by high ice volume accumulation during MIS 24 and reduced melting during MIS 23 due to an insolation minima in the southern hemisphere (Elderfield et al., 2012). Both of these processes supressed melting during MIS 23 and weakened its expression in the $\delta^{18}O$ records (figure 2.5a). Global climate culminated in the ice sheet expansion and associated sea-level drop of MIS 22, which has been suggested to be the onset of the full glaciations with prolonged glacial cycles caused by longer melting times and resulting in the emergence of the modern 100 ka frequency in G-IG cycles (Mudelsee and Stattegger, 1997; Clark et al., 2006;

Elderfield et al., 2012). The 900 ka-event is also evident in ocean carbon records, such as foraminiferal $\delta^{13}C$, as a major perturbation (e.g. Shackleton, 1977; Raymo et al., 1997), and it has been argued that the excursion in $\delta^{13}C$ was the result of a one-off input of ^{12}C-enriched material, eroded from the exposed shelves (Raymo et al., 1997). However, more recently, it has been suggested that the carbon cycle perturbation precedes the sea-level fall and hence the sea-level fall could not be the shelf erosion event and $\delta^{13}C$ perturbation (Elderfield et al., 2012). More likely, changes in ocean circulation and reduced AMOC led to the expression of the 900 ka-event in proxy records (*cit. op*.; Tachikawa et al., in press).

2.3.4 Changes in the East Asian monsoon

Besides the open ocean $\delta^{18}O$ records, the MPT is also manifested in $\delta^{18}O$ records from marginal seas, such as the Mediterranean Sea (Rohling et al., 2014), Bering Sea (Kender et al., 2018), as well as in records from the terrestrial realm. Continental ice-sheets were able to build up outside of high latitudes and high altitudes from ~1.2 Ma, with northern hemisphere glaciations becoming more extensive from 900 ka/MIS 22 onwards, documented in evidence for ice covering north America, the Alps, and the African mountains (Head and Gibbard, 2005). Records of the East Asian monsoon (EAM) system, a large-scale atmospheric circulation pattern that is divided into the winter monsoon (EAWM), characterised by dry north westerly winds, and the summer monsoon (EASM), characterised by warm and humid air, which controls precipitation across large parts of Asia (Wang et al., 2005), also record the MPT. In general, EAM precipitation intensity shows strong G-IG cyclicity (figure 2.5c) (e.g. Sun et al., 2006; Peng et al., 2020). Across the MPT, EASM proxy records (such as loess-paleosol sequences and facies as well as loess magnetic susceptibility records from the Chinese loess plateau (CLP), suggest lengthening of G-IG cycles (e.g. Kukla, 1987; Ding et al., 1991; Dodonov, 2005; Heslop et al., 2002; Han et al., 2012) and gradual strengthening of the EAM (e.g. An et al., 1990; Han et al., 2012; Meng et al., 2018). The 900 ka-event is characterised by reduced precipitation in the EASM, as inferred from CLP sediment sequences and susceptibility records (figure 2.5c) (Peng et al., 2020). Large-scale atmospheric circulation patterns, such as the EAM system, have been proposed as possible important influences during the MPT, acting as a fast conveyers of climate signals between ocean basins and across continents (Porter and An, 1995; Clark et al., 1999; Tada, 2004; Kubota et al., 2010; Tada et al., 2015a).

On tectonic timescales monsoon systems have a significant impact on the global carbon cycle as they control chemical weathering in large parts of the world and they can affect carbon burial in the oceans through their influence on sedimentation rates and nutrient input (Raymo et al., 1988; Raymo and Ruddiman, 1992). A strengthening in the EAM, for example, occurring at ~2500 ka together with uplift events in the Tibet-Himalaya plateau (THP**;** figure 2.6) (Li et al., 2014), coincides roughly with the onset of global cooling trend (see above; e.g. Zachos et al., 2001; Ruddiman, 2003, 2004; Sosdian and Rosenthal, 2009). In addition to its potential influence on atmospheric greenhouse gas concentrations (*op. cit.*) uplift of such vast areas as the THP have the potential to change atmospheric circulation patterns (e.g. Kutzbach and Guetter, 1989; Ruddiman and Kutzbach, 1990; Tada et al., 2016). It has been argued that the uplift of the THP around 2500 ka formed a barrier for atmospheric circulation patterns, which led to the path of the westerly jet stream to become less stable during its winter/glacial mode and it started to meander around the THP (Tada, 2004; figure 2.6). The meandering of the glacial westerlies lead to variations in the EAM on shorter, sub-orbital timescales (EAM millennial-scale variations reported in e.g. Tada et al., 1999; Ikehara and Itaki, 2007; Tada et al., 2015) and has been hypothesised to be connected with so-called Dansgaard-Oeschger cycles (DOCs) in other parts of the northern hemisphere (Tada, 2004).

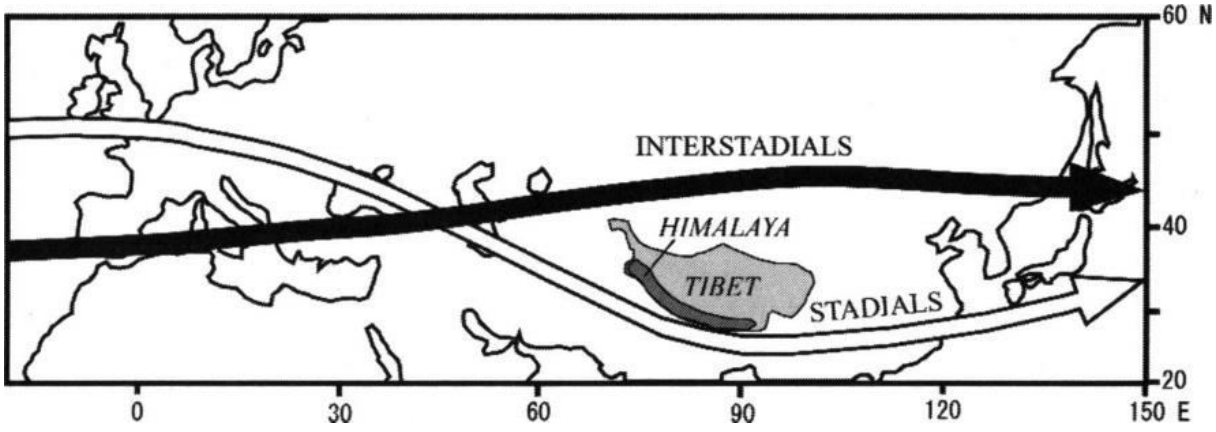

Figure 2.6. The two meandering modes of the glacial/winter westerly jet stream across Eurasia, meandering around the circulation barrier which the Tibet-Himalaya plateau represents. Figure taken from Tada (2004).

DOCs consist of rapid (decadal-scale in duration and repeating every several thousand years) glacial warming events during which temperatures almost reached interglacial values (Dansgaard et al., 1993) that have been reported from archives in the northern hemisphere, such as the North Atlantic and Pacific Oceans and their

marginal basins (e.g. Jansen and Sjøholm, 1991; Bond et al., 1992; Dansgaard et al., 1993; GRIP members, 1993; Tada et al., 1999; Wang et al., 2001; Jansen et al., 2000; Maslin et al., 2001; Moreno et al., 2002; Hernández-Almeida et al., 2012; Birner et al., 2016; Hodell and Channell, 2016; Müller et al., 2018), as well as from the southern hemisphere (Jouzel et al., 2007) for the last 1.4 Ma (Raymo et al., 1998; Janssen et al., 2000). This wide distribution of DOC records suggests a fast teleconnection across continents and between ocean basins, and the EAM has been proposed as such teleconnection mechanism (Tada, 2004; Kubota et al., 2010). In theory, the EASM penetrates further north during DOC interstadials (figure 2.6), increasing the relative amount of rainfall recorded (Moreno et al., 2002; Tada, 2004). Challenges remain in the relationship between DOC events and EASM variaitons, as few of the EASM recorders (e.g. speleothem carbonate $\delta^{18}O$ from the Chinese Hulu Cave, e.g. Clemens et al., 2010; Wang et al., 2008; Wang et al., 2001; loess-paleosol sequences of the CLP, e.g. An et al., 1990; Li et al., 2017; Sun et al., 2019; Peng et al., 2020) are long enough to cover the MPT and/or can resolve millennial-scale variability.

The sediments of the Japan Sea show showing dark/light sediment alternations, suggested to be associated with DOCs in the EASM (section 2.4). These sediment alternations become more frequent and more distinct with the beginning of the MPT at ~1200 ka/MIS 36 (Tada, 1994), which is concurrent with a strengthening in the EASM precipitation and in the EAWM wind intensity, described from northern China and the CLP (e.g. An et al., 1990; Heslop et al., 2002; Li et al., 2008; Han et al., 2012; Meng et al., 2018; Peng et al., 2020). A recently drilled shallow water site in the Japan Sea was hoped to hold continuous and high-resolution climate archives and might provide a Rosetta stone for the temporal linking of DOCs and EASM variability (see section 2.4).

2.4 The Japan Sea

2.4.1 The modern Japan Sea

The Japan Sea (also Sea of Japan or East Sea) is a semi-enclosed marginal basin in the northwest Pacific (figure 2.7). Its tectonic evolution as a back-arc basin began with its opening during the late Oligocene to mid-Miocene (ca. 28-13 Ma ago) when a deep-water marginal sea was formed, which began shoaling and experienced a phase of tectonic calm during the late Miocene (~10 to 7 Ma), followed

by another shoaling of the basin during the Pliocene (~7 to 2.5 Ma) and another lull in tectonic activity during the Quaternary (~2.5 Ma to present; see Tada et al., 1994, and Matsuzaki et al., 2018, for a review). Across the MPT, despite the area being located in a tectonically very active region with volcanic events having taken place in southern Japan and the Japanese Isles across the MPT, no local uplift events could be identified (Yoon, 1997; Kitamura and Kawagoe, 2006; Itaki, 2016). Today, the Japan Sea has an average water depth of 1350 m (maximum of 3700 m in the northern part, Oba et al., 1991) although ~26 % of it is shallower than 200 m (Wang, 2004; figure 2.7) and it exceeds 1,000,000 km^2 in size (Tada, 1994). The Japan Sea is connected to the Pacific Ocean via a number of shallow sills, all having water depths of less than 130 m at present (Oba et al., 1991; figure 2.7).

The main inflow of ocean water is through the shallow Tsushima Strait (TSS) in the south (sill depth ~130 m) and is a key driver of oceanographic circulation in the Japan Sea. Under the influence of the modern glacio-eustatic sea-level fluctuations (120 +/-32 m, *c.f.* Sosdian and Rosenthal, 2009; up to –134 m, *c.f.* Lambeck et al., 2014), the TSS can significantly restrict the connection between the Japan Sea and the open ocean, namely the northwest Pacific, East China and Yellow Seas, and limit water mass exchange during glacial sea-level lowstands (see section 2.4.2) (e.g. Ingle, 1975; Oba et al., 1991; Tada, 1994, Matsui et al., 1998; Tada et al., 1999; Watanabe et al., 2007).

Through the TSS the Tsushima warm current (TWC) enters the Japan Sea (figure 2.7). The TWC is a branch of the Kuroshio Current, which is redirected onto the East China Sea (ECS) shelf where it mixes with the lower-saline, nutrient-enriched (relative to TWC) water masses forming the East China Sea Coastal Water (ECSCW), before entering the Japan Sea through the TSS (Nitani, 1972; Oba et al., 1991; Qui, 2001; Gallagher et al., 2015). In the Japan Sea the TWC splits into three branches, with the majority of the TWC flowing northwards along the coast of the Honshu Island and exiting through the Tsugaru Strait, while a small amount continues along the western coast of Hokkaido, flowing into the Okhotsk Sea (figure 2.7) (for a review see Gallagher et al., 2015). On its path, the TWC creates eddies and upwelling, hence mixing the water column (Mann and Lazier, 2006; Das et al., 2018).

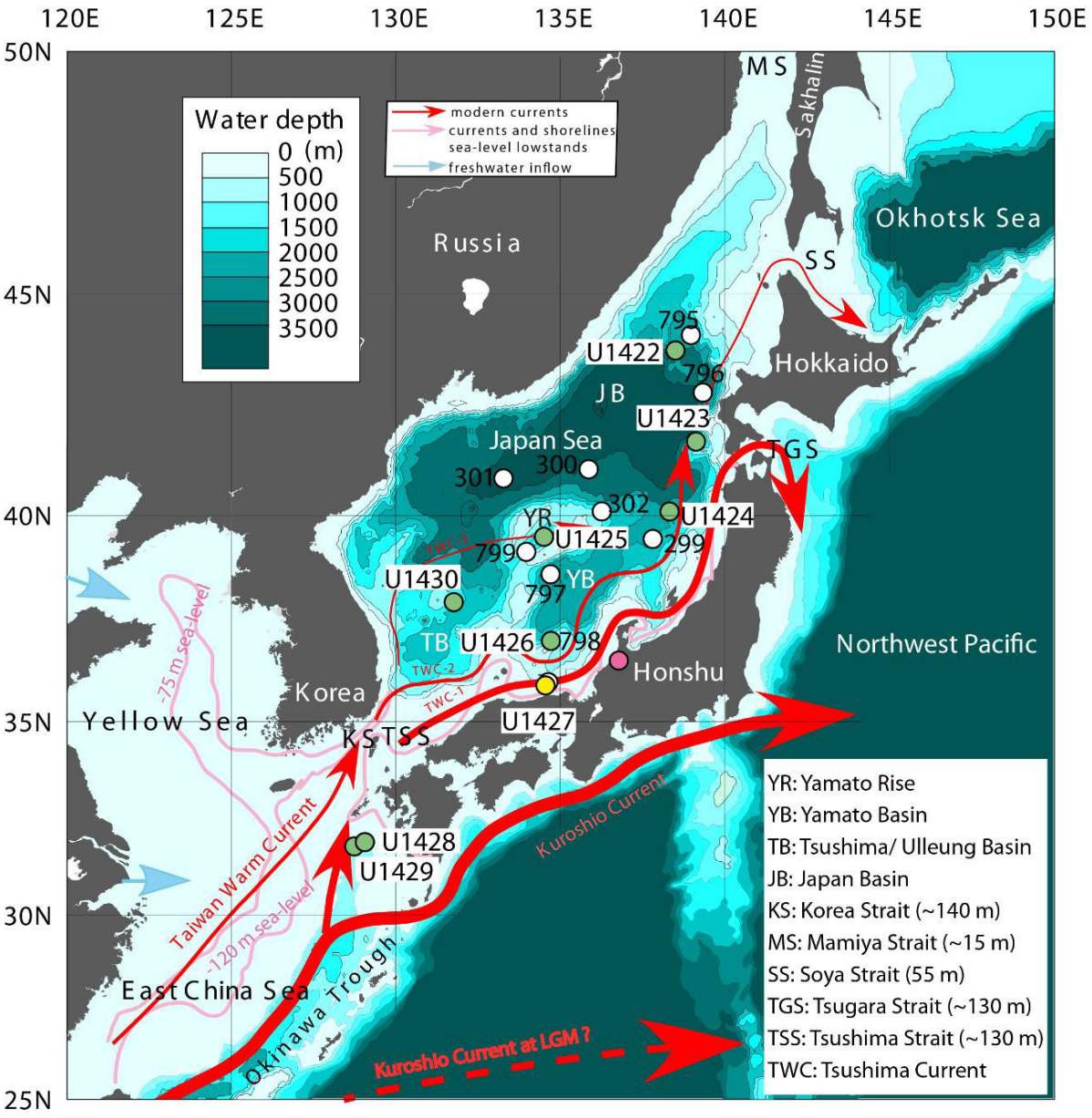

Figure 2.7. Bathymetric map of the Japan Sea (Tada et al., 2013) with major ocean current system at present (after Inoue, 1989, and Tomczak and Godfrey, 1994), approximate locations of major freshwater inflow, i.e. Yellow (northern) and Yangtze (southern) River mouths, and location of DSDP/ODP/IODP coring sites (Tada et al., 2015b; Sagawa et al., 2018). Present day sill depths are listed (legend, Oba et al., 1991; Tada et al., 1999; Lee and Choi, 2015) and the palaeo-shorelines at sea-level lowstands of –75 and –120 m (LGM-like) below present (after Kao et al., 2005, and Park and Chu, 2006, for the East China and Yellow Seas, and after Ujiié and Ujiié, 1999, for the Japan Sea) and the possibly shifted path of the Kuroshio current during LGM-like sea-level lowstands after Ujiié and Ujiié, 1999).

In winter the TWC cools on its northwards migration, sinking to greater water depths and forms the oxygen-rich Japan Sea proper water (Nishiyama et al., 1990; Kitamura and Kimoto, 2006), which is characterised by relatively high oxygen content

and relatively constant salinities of 34.06-34.08 ‰ and temperatures of 0.0-0.6 ºC, and at present represents water masses below 300 m water depth (Gamo and Horribe, 1983; Watanabe et al., 1991).

The TWC is considered the main supply of heat, oxygen and nutrients to the Japan Sea and is hence thought to be the key control on marine productivity in the basin (section 2.4.2, 2.4.3) (e.g. Tada, 1994; Tada et al., 1999). Its consistency (temperature, nutrients, salinity) depends on variations in relative contributions of the Kuroshio Current and ECSCW. The Kuroshio Current is characterised by salinities of >34.5 ‰ and temperatures of 20-25 ºC, while the ECSCW is relatively lower saline (<33.5 ‰) and cooler (10-20 ºC) (Tada, 2004). The ECSCW is enriched in nutrients in comparison with the Kuroshio Current (Tada et al., 1999) and hence relatively greater contributions of ECSCW to the TWC have the potential to boost primary productivity in the Japan Sea. At present the sea surface TWC composition at the TSS varies inter-annually, being cooler and higher saline during winter (13-15 ºC, 34.4-34.6 ‰ salinity) and warmer, lower saline during summer (24-26 ºC, 31-32 ‰) (Lee, 2007), reflecting the inter-annual variations in the EASM precipitation intensity (see section 2.4.3).

2.4.2 Palaeoceanography

The palaeoceanography of the Japan Sea is heavily influenced by glacio-eustatic sea-level fluctuations through the shallow sills that connect it with the open ocean (Oba et al., 1991; Tada et al., 1999), and by variations in the EASM precipitation intensity, which is a major control on the nutrient input and water salinity in the basin (see section 2.4.3). For a recent review on palaeoceanography and TWC inflow see Itaki (2016) and/or Gallagher et al. (2015). Most of our understanding of the palaeoceanography of the Japan Sea, including the inflow of the TWC, is based on studies of the most recent glacial cycles, between the present and MIS 7, and little is known of its palaeoceanography before (Gallagher et al., 2015; Itaki et al., 2018; Gallagher et al., 2018; Sagawa et al., 2018; Saavedra-Pellitero et al., 2019).

Glacio-eustatic sea-level variations are one control on the inflow of the TWC and it has been suggested that the TWC flowed into the Japan Sea during each interglacial sea-level highstand over the last 3.5 or 1.7 Ma, and was restricted during glacials (Tada, 1994; Kitamura and Kimoto, 2006). This has been inferred from numerous palaeontological studies in which warm water surface fauna (foraminifera,

diatoms, coccolithophores), originating from the ECS, were found in interglacial sediments of the Japan Sea (Oba et al., 1991; Kitamura et al., 2001; Kitamura and Kimoto, 2006; Hoiles et al., 2012; Gallagher et al., 2015; Itaki, 2016; Gallagher et al., 2018; Saavedra-Pellitero et al., 2019), and by an overall increase in numbers of primary producers (e.g. diatoms; Koizumi, 1992). The interglacial TWC inflow is also inferred from better bottom water oxygenation in comparison to glacials which implies water column mixing (Oba et al., 1991; Tada, 1994) and the presence of oxygen-rich Japan Sea proper water (section 2.4.1).

In contrast, during glacial sea-level lowstands the connection with the open ocean has been restricted and the TWC inflow may have been completely cut off through the shoaling of the southern sills (Oba et al., 1991; Tada, 1994; Kitamura et al., 1997; Tada et al., 1999; Kitamura et al., 2001; Kido et al., 2007; Hoiles et al., 2012; Oba and Irino, 2012; Gallagher et al., 2018; Saavedra-Pellitero et al, 2019). For sea-level lowstands as during the last glacial maximum (LGM, ~22-19 ka; around –120 m and up to –134 m below present; Yokoyama et al., 2000; Bintanja et al., 2005; Lambeck et al., 2014) the formation of an isthmus between Ryukyu and Taiwan has been hypothesised (Ujiié and Ujiié, 1999; Ujiié et al., 1991, 2003; Ahagon et al., 1993; Itaki, 2016). This isthmus would have prevented the TWC from entering the Japan Sea. The isthmus formation is however controversial and comparative faunal studies on-land contradict the existence of such a land-bridge as faunas seem to have developed independently (Ota, 1998). It is more likely that a shallow, narrow strait continued to exist in the south. Lee et al. (2008) suggested the Korea Strait between Korea and the Island of Tsushima could have persisted during the LGM as a 10 m deep and ~10 km wide passage, allowing some water mass exchange. In any case, LGM-like glacial sea-level lowstands would have exposed large parts of the shallow ECS shelf and redirected the Yangtze and Yellow River mouths to positions much closer to the TSS (Park and Chu, 2006). This closer proximity of a major freshwater source to the Japan Sea, could potentially have led to the glacial Japan Sea becoming more sensitive to changes in the freshwater input/TWC inflow during glacial sea-level lowstands.

Another factor contributing to reduced glacial TWC inflow is a possible shift in the path of the Kuroshio Current (KC). At present the path of the KC is through the Okinawa Trough and onto East China Sea shelf, before part of it enters the Japan Sea through the TSS, called Tsushima Warm Current (figure 2.7). During the LGM it

has been hypothesised that the KC path may have been diverted out of the Okinawa Trough and into the Pacific Ocean making it difficult for the TWC to enter the Japan Sea (figure 2.7) (Ujiié et al., 1991; Kao et al., 2005, 2006). More recent ocean models however suggest the KC path may not have changed (Gallagher et al., 2015, and references within).

2.4.3 Marine productivity and Asian monsoon precipitation

The East Asian monsoon system has a strong control on nutrient input, water salinity, water mass stratification and upwelling in the East Asian marginal seas (Tada et al., 1999; Tada, 2004; Itaki et al., 2004; Ikehara and Itaki, 2007; Kubota et al., 2010; Gallagher et al., 2018), including the East China and Japan Seas. In the Japan Sea, EASM precipitation influences primary productivity through controlling the inflow and composition of TWC, i.e. the relative contribution of nutrient-rich ECSCW to the TWC (figure 2.7).

Eustatic sea-level fluctuations also control productivity by limiting the inflow of nutrient-rich waters (Tada et al., 2015a). At times of enhanced EASM precipitation during interglacials a higher amount of freshwater runoff from the Asian continent is brought to the coast via the Asian river systems, predominantly the Yangtze and Yellow Rivers, which both discharge into the ECS (figure 2.8a). The strong river outflow causes the KC to upwell on the ECS shelf and, additionally, leads to a relative greater contribution of nutrient-rich ECSCW to the TWC (Oba et al., 1991). Consequently, at times of strong monsoonal precipitation the nutrient supply to the Japan Sea and its primary productivity are high but organic matter preservation may be low due to the improved deep water oxygenation (figure 2.8a).

During glacial sea-level lowstands of the late Pleistocene, when global average glacial sea-level may have dropped by –120 to –134 m (Sosdian and Rosenthal, 2009; Lambeck et al., 2014), the Japan Sea sills were strongly reduced and had nearly dried up (section 2.4.2). This restricted water mass exchange with the adjacent Pacific Ocean, Yellow and East China Seas, consequently lead to the TWC inflow being restricted or completely cut off (figure 2.8b). Under these conditions nutrient supply to the basin, needed to prime marine productivity, is limited. This relationship between sea-level and productivity is supported by evidence of almost no primary (silicate) productivity, inferred from biogenic silica accumulation, during late Pleistocene glacial sea-level lowstands (Tada, 1994).

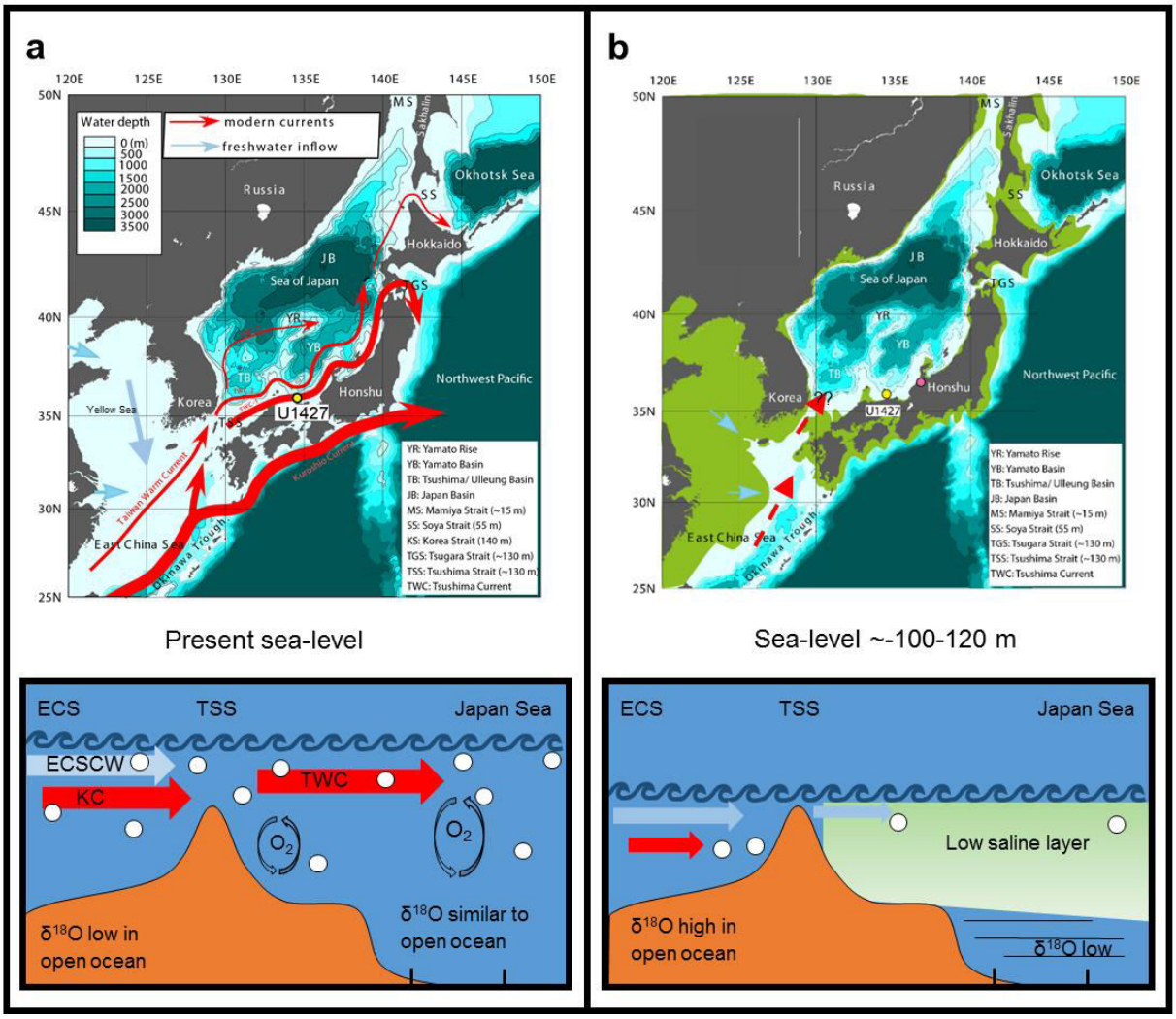

Figure 2.8. Palaeoceanographic modes of the Japan Sea with major ocean currents (red and blue arrows labelled KC, ECSCW and TWC), intensity of marine productivity (white dots), drill sites (black vertical lines) and stratification of the water column (horizontal lines in bottom water). At the present sea-level (fig. 2.8a) water mass exchange with the open ocean is possible, leading the inflow of warm, nutrient-rich waters through the Tsushima Strait, driving high productivity and oxygenated water column, and leading to foraminiferal $\delta^{18}O$ values similar to those of the open ocean. At late Pleistocene glacial sea-level lowstands (fig. 2.8b) the water mass exchange was restricted, which led to reduced productivity, a stratified water column and unusually low foraminiferal $\delta^{18}O$ values.

During glacials, when the Japan Sea was nearly isolated, the TWC inflow is restricted, leading to a less well mixed water column. In addition, the continued (but reduced) input of low-saline waters via the TSS (in the form of ECSCW and TWC; Oba et al., 1991; Lie et al., 2003; Kubota et al., 2010), possibly also precipitation over the Japan Sea itself, and local fluvial runoff from the surrounding landmasses (Keigwin and Gobarenko, 1992; Tada et al., 1992, 1994; Gallagher et al., 2018), leads to the formation of a low-saline surface layer on top of the water column. As a

result of the near isolation and low-saline surface layer the Japan Sea water column becomes stratified (figure 2.8b). This density stratification leads to the formation of dysoxic or anoxic bottom waters. As a result of anoxia organic matter is better preserved bioturbation is reduced, leading to the deposition of dark, organic matter-rich, metre-thick, laminated sediments (Oba et al, 1991). In contrast, during interglacials, increased water column mixing leads to improved oxygenation of deep waters and the deposition of lighter, organic matter-poorer sediments. These environmental processes hence lead to orbital-scale variability in sediment lithology and can be correlated across the basin (Oba et al., 1991; Tada et al., 1992; Watanabe et al., 2007; Sagawa et al., 2018; Irino et al., 2018; Gallagher et al., 2018).

On sub-orbital timescales, precipitation controls primary productivity through controlling the relative contribution of nutrient-rich ECSCW to the TWC, and hence exerting a similar effect on water column mixing and lithology as eustatic sea-level fluctuations do on orbital timescales. Although glacials are in general characterised by reduced EASM precipitation in the catchment areas of Yangtze and Yellow Rivers (Tada et al., 1999) the TWC inflow is weaker but Yellow and Yangtze River mouths shift to positions closer to the TSS, e.g. Yellow River mouth to ~45 km NW of Cheju Island (the large island just south of the TSS, south of Korea) at SL of –90 m (Oba et al., 2012), which may allow the weakened EASM precipitation to still affect the Japan Sea (figure 2.8b).

Glacial sediments of deep water sites in the Japan Sea show dark/light alternations/laminations on millimetre- to centimetre-scale. These thin sediment alternations are thought to be associated with millennial-scale variability in the EASM in association with DOCs and are thought to be traceable across the entire Japan Sea (e.g. Tada, 2004; Tada et al., 2013). It has been argued that the colour of the dark layers is the result of organic matter-enriched sediments, which are the product of enhanced palaeo-productivity by enhanced nutrient input and enhanced organic matter preservation through reduced bottom water oxygenation (Tada et al., 1999). Both enhanced nutrient input and reduced bottom water oxygenation are controlled by enhanced contributions of low-saline, nutrient-rich ECSCW to the TWC at times of higher EASM precipitation (Tada et al., 1999). Furthermore, it has been argued that the increase in low-saline waters lowers vertical mixing of the water column and increases density stratification, and ultimately leads to reduced oxygenation of deep waters, which results in better preservation of organic matter (Oba et al., 1991; Tada

et al., 1999). Enhanced contributions of ECSCW to the TWC are thought to be linked with increased fluvial discharge of the Yangtze and Yellow Rivers, as a response to increased EASM precipitation during interglacials and DOC interstadials (Tada et al., 1999). It has therefore been proposed that the think dark layers in the Japan Sea were deposited during DOC interstadials when the EASM precipitation is thought to have been enhanced, while the light layers are to be a result of decreased EASM precipitation in association with DOC stadials (Tada et al., 1999; Tada et al., 2013; see sections 2.3). However, the connection between DOCs and millennial-scale variability in the EASM could not yet be constrained due to issues in the establishment of detailed chemo-stratigraphies for the Japan Sea (see section 2.4.4). In order to investigate the suggested close relationship between DOCs and EASM millennial-scale variability across the MPT a climate archive covering the MPT that allows establishing a high-resolution chemo-stratigraphy is needed.

2.4.4 Calcite preservation and stable isotope records

Variations in eustatic sea-level and EASM precipitation also affect calcite preservation and stable isotope ($\delta^{18}O$) records in the Japan Sea, through their impact on sea water in salinity and water column stratification (deep water oxygenation) (sections 2.4.1-2.4.3). Under restricted conditions during glacials with near isolation of the Japan Sea bottom waters can become corrosive to carbonates in the post-depositional degradation of organic matter (e.g. Stein, 1991). In association with the fluctuations in water mass oxygenation/stratification, the calcium carbonate compensation depth (CCD), the water depth at which carbonate production equals carbonate dissolution and hence beyond which there is no carbonate deposition in the sediments, varies strongly over G-IG cycles. At present, the CCD is in ~2000 m water depth (Ichikura and Ujiie, 1976; Oba et al., 1991), but it varied greatly with G-IG cycles over the last 2500 ka (Tada, 1994), with reports of widespread carbonate dissolution at water depths >500 m during glacial sea-level lowstands, when the water column became stratified (Ikehara, 1991; Ikehara et al., 1994).

These widespread glacial carbonate dissolution events so far hampered the establishment of a continuous foraminiferal-based isotope chemo-stratigraphy for the Japan Sea (e.g. Oba et al., 1991; Dunbar et al., 1992; Tada, 1994), which could be used to improve age models across the basin by linking them with well-dated reference records, such as presented in figure 2.4 (Lisiecki and Raymo, 2005). Such a detailed isotope-stratigraphy would establish a better temporal framework for the

dark/light sediment alternations from the Japan Sea and enable testing the proposed relationship between the sediment alternations, DOC stadials/interstadials and EASM precipitation intensity (section 2.3, 2.4.3). However, for a long time a reliable chemo-stratigraphy only reached back as far as 800 ka (Tada, 2004), and, most recently, from sediments of a shallow water site in the Japan Sea (Site U1427; figure 2.7), established a foraminifera-based chemo-stratigraphy that reaches back as far as MIS 21 (~870 ka) (Sagawa et al., 2018). This new chemo-stratigraphy was used in correlations of dark/light sediment alternations across other sites from the Japan Sea (Irino et al., 2018; Sagawa et al., 2018; Tada et al., 2018). The timescale of the MPT however is not yet fully covered by this high-resolution stratigraphy.

In addition to creating issues in the establishment of age models, the strong salinity fluctuations in the Japan Sea superimpose on the global temperature/ ice-volume signal in $\delta^{18}O$ records. During glacials, when the near isolation of the Japan Sea coincides with continued freshwater input, a low-saline layer forms which affects water column mixing (figure 2.8) and $\delta^{18}O$ records. Since freshwaters tend to have lower $\delta^{18}O$ values compared to ocean water (see figure 2.3), this local input of low-$\delta^{18}O$ impacts on the $\delta^{18}O$ values of the glacial Japan Sea and the foraminiferal carbonates precipitated within it (e.g. Oba et al., 1991; Dunbar et al., 1992; Tada, 1994; Tada et al., 1999; Matzui et al., 1998; Kido et al., 2007; Yokoyama et al., 2007; Oba and Irino, 2012; Sagawa et al., 2018). Hence, $\delta^{18}O$ records of the Japan Sea are characterised by relatively lower glacial values compared to interglacials, which implies an unusual warming or freshening of the waters (Oba et al., 1991; Dunbar et al., 1992). As an example for the unusual behaviour of $\delta^{18}O$ records in the Japan Sea, planktonic foraminiferal $\delta^{18}O$ across the LGM (interval ~11-22 ka) show values dropping from +5 to +1 ‰ (Oba et al., 1991), while planktonic foraminiferal $\delta^{18}O$ in the northwest Pacific off Japan in the same interval show an increase from –1 to +3 ‰ (Sagawa et al., 2005). Oba et al. (1991) also calculated a surface salinity for the LGM of ~+28 ‰ (modern value ~+34 ‰; Oba et al., 2012). The impact of this was lower planktonic foraminiferal $\delta^{18}O$ values that would have led to the interpretation of the surface water during the LGM being up to 2 ºC warmer than at present (Oba et al., 1991, 2012), contradicting our general understanding of the LGM and the lower LGM temperatures inferred from association studies of local marine fauna (see Kido et al., 2007; Oba et al., 2012, and references within). So, while in the open ocean $\delta^{18}O$ records reflect global mean ice-volume/temperature (e.g. Lisiecki and Raymo,

2005), in the Japan Sea contributions of low-saline waters compensate during glacials for the increased ice-volume $\delta^{18}O$ values, in general showing opposing trends compared with the open ocean, of relatively lower (higher) $\delta^{18}O$ values during glacials (interglacials). The Japan Sea $\delta^{18}O$ behaviour is, in detail, more complex than this, with some glacials showing enhanced glacial values (e.g. Oba et al., 1991; Sagawa et al., 2018).

The above described phenomenon of low glacial $\delta^{18}O$ values is typical for the Japan Sea and is thought to have prevailed during at least the majority of glacials of the Quaternary, though its exact onset is still in debate, varying between 2500 ka (Tada, 1994), 1700 ka (Kitamura, 2007) and the last 1600 ka (Hoiles et al., 2012). The atypical low-$\delta^{18}O$ glacial values have previously been described from both planktonic (Kido et al., 2007; Yokoyama et al., 2007; Oba and Irino, 2012) and benthic foraminiferal isotope records (Oba et al., 1991; Dunbar et al., 1992), though the expression is weaker in the benthic records compared with the planktonics (e.g. *G. bulloides* offset between glacials and interglacials ~2 ‰, *Uvigerina akitaensis* ~1 ‰, Dunbar et al., 1992). This untraditional and complex interpretation of the Japan Sea $\delta^{18}O$ records means they are usually supported by salinity-independent temperature proxies, such as association counts of warm/cold water organisms (e.g. foraminifera, radiolarians, diatoms, ostracods, coccolithophores; e.g. Oba et al., 1991; Kido et al., 2007; Gallagher et al., 2018 for a review), or chemical proxies such as alkenones (Yokoyama et al., 2007) and foraminiferal Mg/Ca ratios (e.g. Oba et al., 1991; Tada et al., 1999; Kido et al., 2007).

2.5 Summary

In this chapter showed that the MPT is characterised by increased fluctuations in global ice-volume/temperature and hence increased amplitudes in sea-level fluctuations (section 2.3), and that the palaeoceanography of the Japan Sea, a marginal basin in the northwest Pacific (section 2.4), is sensitive to these sea-level fluctuations and, in addition, to variations in the EASM precipitation intensity (section 2.4). Variations in EASM and eustatic sea-level fluctuations can be recorded in marine sediments of the Japan Sea, though the Japan Sea palaeoceanographic settings can hinder or complicate their interpretation (see calcite preservation and $\delta^{18}O$ records, section 2.4.4).

Despite these issues, as outlined in chapter 1, this study aims to establish a foraminiferal $\delta^{18}O$-based chemo-stratigraphy for the Japan Sea. A first, near continuous, high-resolution foraminiferal-based $\delta^{18}O$ record of Japan Sea was recently presented in Sagawa et al. (2018) and Gallagher et al. (2018). Their records, created from the sediments of a very shallow-marine (~330 m water depth) in the southern Japan Sea (IODP Site U1427), extends from the present back to ~400 ka and continues to ~850 ka (MIS 21), although with some of the gaps during glacials, due to calcite dissolution (section 2.4.4). The sediments of Site U1427 were selected for this thesis as they promise to enable the creation of the first continuous and high-resolution $\delta^{18}O$ record for the Japan Sea encompassing the MPT in detail (see Chapter 3).

This site (U1427) may also enable high-resolution reconstruction of the EASM precipitation variabilities across the MPT, hence allowing to test the monsoon-hypothesis as an important actor during the MPT (Tada et al., 2015a,b) through examining the variations in the input of low-saline waters to the shallow, southern Japan Sea. Since the site is located underneath a branch of the TWC (figure 2.7 and chapter 3, section 3.2), variations in the EASM may be recorded in proxy records of surface productivity (section 2.4.3) and are likely to also be expressed in the anticipated $\delta^{18}O$ record (section 2.4). As sediments, although predominantly above the investigated interval, show millimetre- and centimetre-scale dark/light sediment alternations (hypothesised to be associated with DOCs, section 2.4.3) and have a good carbonate preservation throughout (Tada et al., 2015c), the site could act as a Rosetta stone providing key chronological control for the Japan Sea, enabling investigations into the relationship between the EASM and DOCs (Tada et al., 2013).

Chapter 3: Material and Methods

During the course of this PhD a number of different analytical methods were used. This chapter summarises the applied geochemical, micropalaeontological and sedimentological methods, laboratory procedures and their limitations. At the beginning a brief description is given on IODP Expedition 346 (section 3.1) and Site U1427 shipboard with the shipboard data used in this study (section 3.2), as well as Expedition KR-15-10 site WB10, used as a modern reference (section 3.3). This is followed by external data used throughout the analytical chapters (section 3.4), before the chapter finishes with methods and protocols applied within this study (section 3.5). Section 3.5 starts with an outline of the material split for analyses (section 3.5.1), followed by a description of bulk sediment methods (sections 3.5.2-3.5.6), before detailing the process of sample splitting and treatment for the generation of foraminifera proxy records (sections 3.5.7-3.5.13).

3.1 IODP Expedition 346

The first sediment cores from the Japan Sea were gathered during the Deep Sea Drilling Project (DSDP) Leg 31 (Karig et al., 1975; Ingle et al., 1975) and Ocean Drilling Program (ODP) Legs 127 and 128 in the 1970's (Ujii'e and Ichikura, 1973, Ichikura and Ujii'e, 1976; Oba et al., 1991, Tada 1994) which had a strong focus on the tectonic development of the basin. Over the last ~25 years little work was done until 2013, when the ODP successor program, the Integrated Ocean Drilling Program (IODP), returned to the region with Expedition 346. This expedition focussed on gathering sediment cores that promised to produce continuous sediment records allowing the reconstruction of the evolution of the East Asian monsoon system on orbital and millennial timescales (Tada et al., 2013; 2015a). Besides fundamental scientific advances it was recognising that the East Asian summer monsoon (EASM) at present affects the water supply of ~1/3 of the global population (Tada et al., 2015a). So to better assess future EAM variations due to climate change that will affect the population, the studies on the sediment cores of Expedition 346 aim to better understand the complex ocean-atmosphere interactions in the EAM-affected region over the recent geologic past (last ~5 Ma; Tada et al., 2015a). On longer timescales, Expedition 346 goals were to better understand the Miocene basin development and evolution of the EAM in response to the Tibet-Himalaya Plateau

(THP) uplift, which is still poorly understood, and to reconstruct variations in surface- and deep water circulation and surface primary productivity within the Japan Sea, which are thought to be related to variations in the EAM and glacio-eustatic sea-level (Tada et al., 2013, 2016; see chapter 2, section 2.4).

During Expedition 346 relatively continuous sediment sequences were collected from seven sites in the Japan Sea and two sites in the East China Sea, including the shallow water Site U1427 from the southern Japan Sea (figure 3.1 and section 3.2) (Tada et al., 2015a).

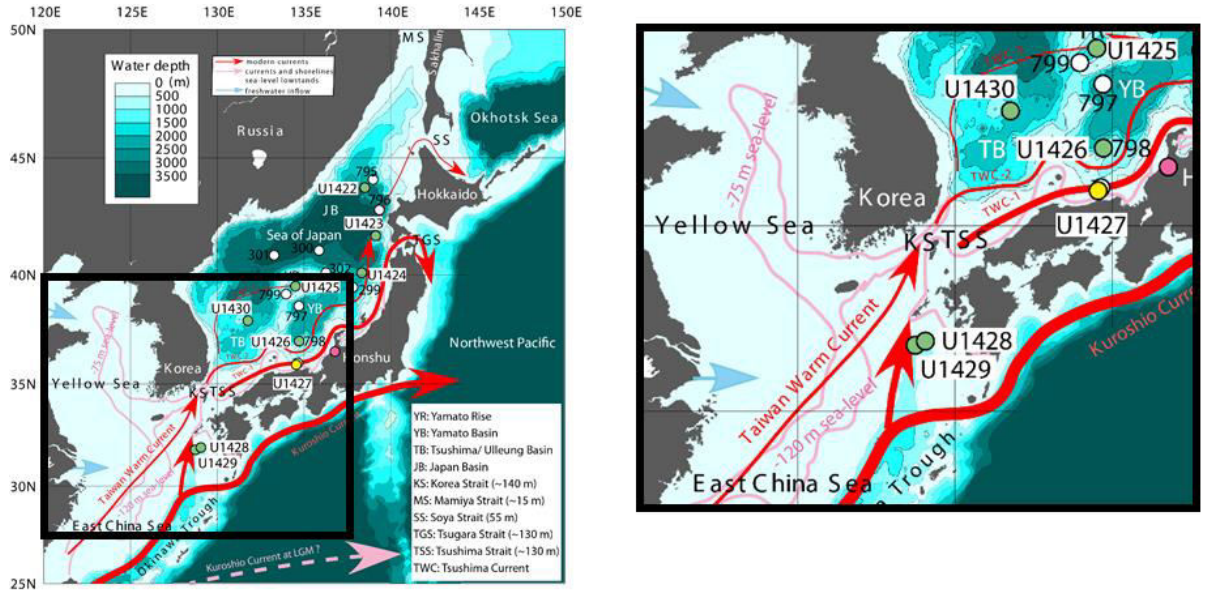

Figure 3.1. Bathymetric map of the Japan Sea and adjacent northwestern Pacific Ocean and East China Sea, with the Japan Sea's major ocean current systems (red arrows), DSDP/ODP/IODP coring sites (circles) and sill depths (see legend, bottom right). The investigated site, U1427 ~330 m water depth, sedimentation rates of ~35-40 cm/ka; Tada et al., 2015b), is highlighted with a yellow circle. The approximate position of the Omma formation outcrops near Kanazawa City are indicated by a pink circle (far right side of figure). Figure altered after Tada et al., 2015a.

3.2 IODP Expedition 346, Site U1427

IODP Site U1427 is located in the southern part of the Japan Sea (Yamato Basin, at 35º57.92'N, 134º26.06'E; figure 3.1) in a water depth of ~330 m and about 35 km offshore Japan's provinces Tajima/Tottori, on the outer margin of the Japanese continental shelf (Tada et al., 2015b). In order to estimate the palaeo-water depth development of the site since the MPT uplift/subsidence as well as sediment accumulation and compaction need to be considered. Tectonically the Japan Sea

was quiet since the MPT (last ~1250 ka) with tectonically induced uplift of about 100 m, which was counteracted by about 50 m thermal subsidence (Chough et al., 2000). Shipboard data estimates continuous and relatively constant sedimentation rates around 35-40 cm/ka (Tada et al., 2015b), which suggests about 500 m of sediment particles having been deposited over the last 1250 ka. To calculate the compaction of these loosely packed sediment particles, p-wave velocities can be used as an indicator since its travelling velocity changes with sediment density/compaction. While p-wave velocities are a commonly recorded parameter on-board IODP expeditions, at Site U1427 degassing of the sediments led to measuring disturbances and hence the p-wave log has been recorded for the uppermost six metres only (p-wave velocities: 1493-1564 m/s) (Tada et al., 2015b). This makes estimates of sediment compaction and palaeo-water depths for the sediments encompassing the MPT very challenging. The good carbonate preservation at Site U1427 (Tada et al., 2015b and this study) implies since deposition of the investigated sediments started, the palaeo-water depth has always been shallower than 500 m, which is the shallowest palaeo-depth of the calcium carbonate compensation depth (Ikehara, 1991; Ikehara et al., 1994). Additionally, being located on a marginal terrace (see figure 3.5), a result of extensional tectonics in a back-arc basin, the overall vertical tectonic movement of Site U1427 was therefore one of subsidence, not of uplift, i.e. the palaeo-water depth was more likely shallower than deeper than at present.

Site U1427 is situated underneath a branch of the Tsushima warm current (TWC) whose inflow is sensitive to glacio-eustatic sea-level fluctuations and EASM precipitation intensity (see chapter 2, section 2.4), both of which have a strong control on marine primary productivity in the Japan Sea (chapter 2, section 2.4) (e.g. Oba et al., 1991; Tada et al., 2015b). This particular setting potentially holds sediments that provide an opportunity to study the interrelationship between terrestrial climate and oceanography (Tada et al., 2015b). However, while sites in such close proximity to land have the potential for much higher sedimentation rates than further offshore, and hence may provide an opportunity for high resolution palaeo-studies, the close proximity to land is also likely to lead to complications in the interpretation of the proxy-records due to dynamic depositional conditions, i.e. varying sources and contributions of sediment particles as input from land or from marine productivity. Historically, the potentially more complicated to interpret near-shore settings were avoided, and scientific ocean drilling initially focussed on sites far

offshore, in deep open ocean waters (see figure 2.2), and where the majority of analytical tools for the investigation of past climatic and palaeoceanographic changes (proxies) were developed (see, for example, website of the IODP programme; https://www.iodp.org/about-iodp/history).

Shipboard analyses demonstrate Site U1427 is characterised by continuous and high sedimentation rates (average shipboard ~35-40 cm/ka), which should allow for high-resolution palaeo-studies, as well as an excellent carbonate preservation as the site is located above the carbonate compensation depth (CCD; see chapter 2, section 2.4.4 for details). So far, the preservation of carbonate microfossils in previously cored deeper-water sites from the Japan Sea was very poor (>500 m; e.g. Ingle et al., 1990). As a result, it has not been possible to establish an oxygen isotope stratigraphy (chapter 2, section 2.4.4; e.g. Dunbar et al., 1992). Site U1427 is considered to have been above the CCD throughout the cored interval (lower Pleistocene to Holocene) (Tada et al., 2015b), including the MPT, and the good preservation of foraminifera shells was confirmed by microscopic analyses of this study (see appendix B).

The focal point of this thesis is the MPT and therefore this study focuses on the lower interval of sediment cores recovered at Site U1427 (~260-525 m CCSF-D; see section 3.2.1 for details). According to the shipboard age model (Tada et al., 2015b; see also chapter 4, section 4.3) these sediments span the MPT and, while much work has recently been published on the upper ~250 m (Miller and Dickens, 2017; Black et al., 2018; Itaki et al., 2018; Gallagher et al., 2018; Sagawa et al., 2018; Saavedra-Pellitero et al., 2019), including establishing an isotope chemo-stratigraphy from the present to ~870 ka (MIS 21; Sagawa et al., 2018), little work has yet been done on the lower part. This thesis is the first study of the lower sediment interval of Site U1427.

3.2.1 Applied depth scale

At Site U1427 a total of three holes were cored and sediment samples from all three holes are used in this thesis. The shipboard report uses the depth scales CSF-A (depth in metres below sea floor, regardless of gaps or overlaps between cored holes), CCSF-A (a composite depth scale created to fill gaps by overlapping with another hole) and CCSF-D (continued splicing of sediment cores leading from a multi-hole to the creation of a single, continuous sediment sequence) for Site U1427

(see figure 3.2) (IODP, 2011; Tada et al., 2015b; Lu et al., 2018). On-shore, splicing continued until 2018, when a revised depth scale version was released, labelled “m U1427_Patched_CCSF-D_rev20170310” (Irino et al., 2018). This has subsequently been used in publications of the upper interval of Site U1427 (*op. cit.*) and is referred to in this thesis as “m” or “m CCSF-D”.

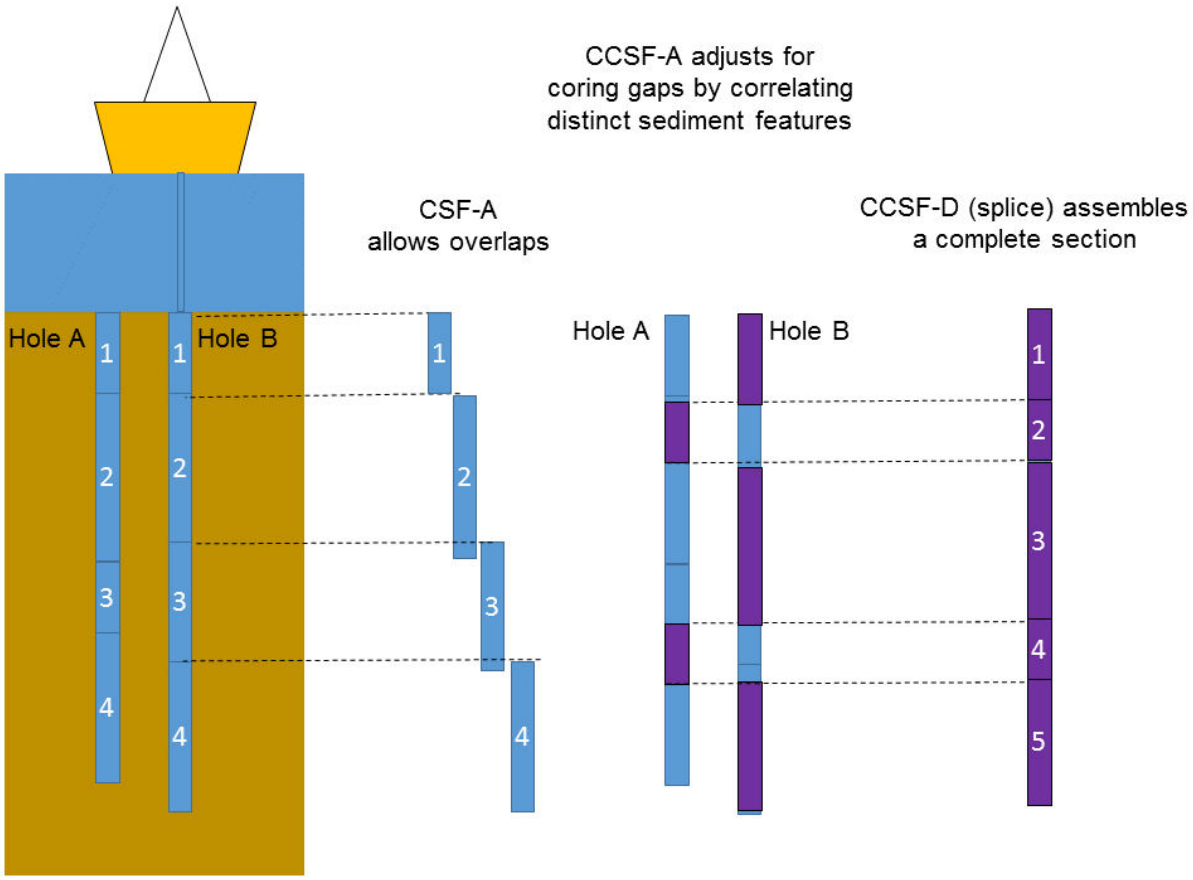

Figure 3.2. Illustration of the IODP depth scales CSF-A, CCSF-A and CCSF-D as used in the shipboard report (Tada et al., 2015a, b, c). Altered after IODP depth scale terminology document (IODP, 2011).

Sample selection was initially based on an even spread across the investigated interval, based on the most up-to-date depth scale available at the time, CSF-A. When a revised depth scale first became available in 2017 (CCSF-D), the sample selection for this thesis was finished. For comparability with other publications from Site U1427, all sample depths were transferred into the CCSF-D scale, which led to the records looking a little patchy in places.

The lowermost interval below 440 m is only covered by a single hole, so that samples in this interval fall below the depth at which a comparison between the holes was possible and are therefore out of splice. For these samples the CCSF-D depth

was calculated by adding the same amount of offset to the CCSF-A scale as was added to the last sample within the splice, in this case 11.755 m (Takuya Itaki, pers. comm., April 2017). The full list of samples with their depths on the different depth scales can be found in appendix A.

3.2.2 Shipboard lithological description

The shipboard report provides a detailed lithological description with core section photographs (figures 3.3a, 3.3b) (Tada et al., 2015c). The investigated interval belongs to subunit A2 (beginning at 125 m CSF-A) and consists of fine-grained (silt and clay with minor occurrences of sand) homogenous hemipelagic sediments. The unit is characterised by olive-grey to greyish green alternation between biogenic component/biosiliceous-rich (consisting of (mainly) nannofossils and (secondary) diatoms and sponge spiculae ooze), and biogenic-poor silty clay or clayey silt, rich in terrigenous material. The sediments show disperse intercalations of and shell fragments of shallow-water origin, most abundant between ~400 and ~475 m (~370-450 m CSF-A) with calcareous microfossils (including foraminifera) becoming rare below ~475 m (figure 3.3a). In contrast to subunit A1 (above the investigated interval) subunit A2 shows only minor amounts of dispersed pyrite and volcanic material (such as tephra layers, volcanic glass) and laminated sediments. Distinct dark/light sediment alternations (lamination) are a typical feature at deep water sites in the Japan Sea (e.g. Oba et al., 1991; Tada, 2004; Tada et al., 1999) but their expression is weaker (faint colour changes) at Site U1427 and across the investigated interval they are absent, apart from between 345-375 m (Tada et al., 2015b, c). This lithological feature makes it difficult to correlate the sediments of Site U1427 across the Japan Sea (Irino et al., 2018; Sagawa et al., 2018; Tada et al., 2018).

Based on the shipboard age model (section 3.2.4) and the relationship of b* values over glacial-interglacial cycles (section 3.2.3), sediments contain more biogenic components during interglacials, while glacials are characterised by enhanced abiogenic components in a finer-grained matrix (Tada et al., 2015c). Shipboard findings further suggest a negative correlation between grain-size and higher contributions of terrigenous material in the sediments, showing smaller grain-sizes together with higher terrigenous input. Six prolonged intervals of very fine-grained and siliciclastic-rich sediments were identified (Tada et al., 2015c), predominantly occurring above the only laminated interval, 345-375 m CCSF-D (figure 3.3c).

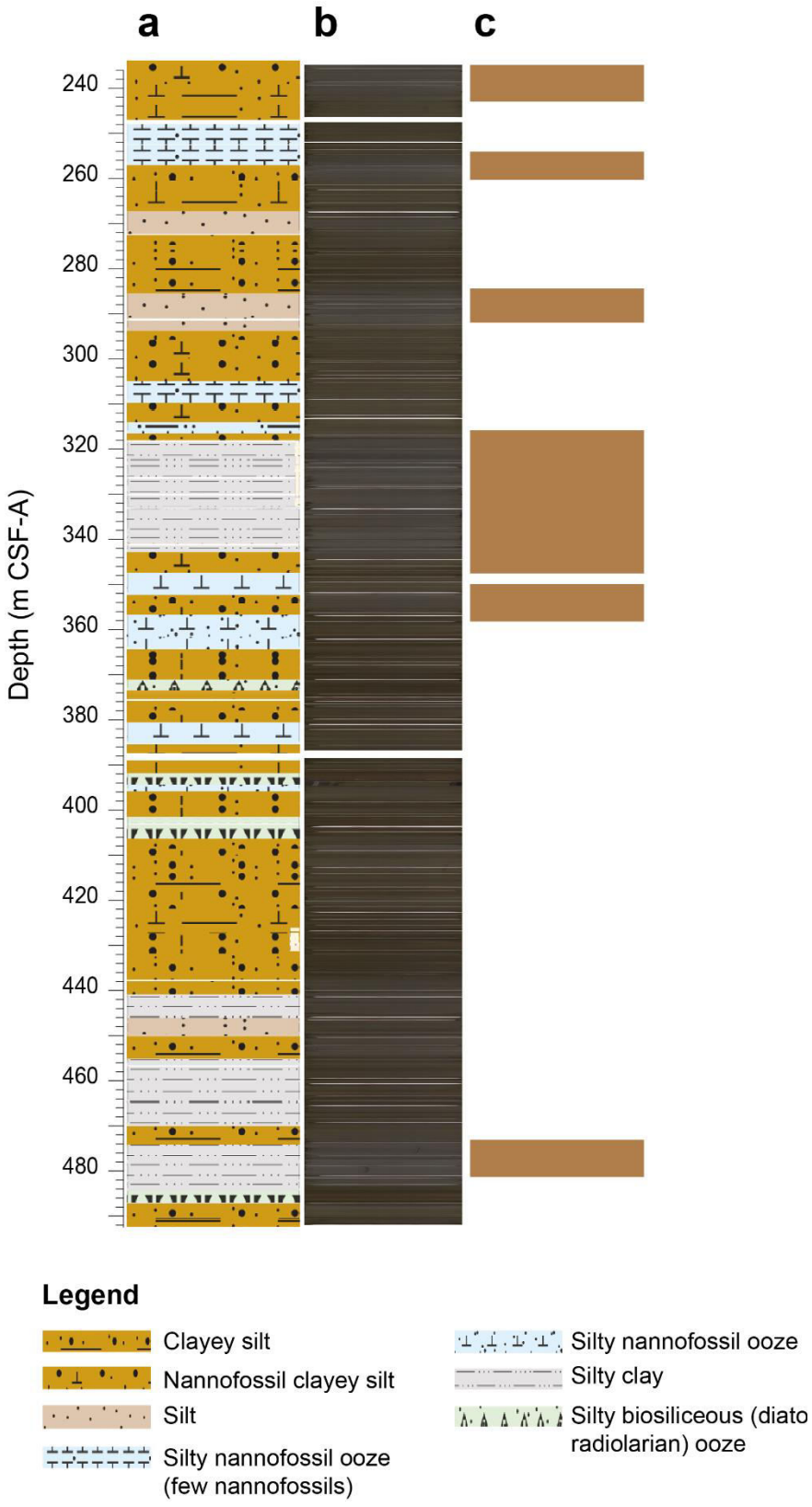

Figure 3.3. Lithological core description (Hole A, with legend beneath; fig. 3.3a), core section photographs (fig. 3.3b), microscopic smear-slide analysis indicting siliciclastic-rich intervals (from core catcher samples; fig. 3.3c) and indication of marine isotope stages (based on findings shown in chapter 4). Figures 3.3a-c are modified after Tada et al. (2015c) to cover the ~260-525 m CCSF-D only. Note, this figure is presented in CSF-A.

While the interval 260-525 m is otherwise heavily bioturbated, a single interval between 345-~375 m CCSF-D (318-342 m CSF-A) occurs where bioturbation was reduced (absent) and laminated sediments occur. This interval contains greyish-green, siliciclastic-rich (minor amounts of diatoms) silty-clays with laminated layers (millimetre-scale). Laminations are a common feature in the sediments of deeper-water sites in the Japan Sea. Here, laminations are preserved as a result of dis- or anoxic bottom water conditions during glacial sea-level lowstands, when the water mass stratification caused by the formation of a fresher (less dense) layer on top of the Japan Sea, reduces mixing of the water column and oxygenation of the deeper water masses (>500 m; Chapter 2, section 2.4). At Site U1427 the brief presence of lamination combined with low amount of dispersed pyrite suggests this lamination was not caused by disoxic/anoxic conditions, but instead this shallow-water site was well-oxygenated across the investigated interval (Tada et al., 2015b). The distinct yellow colour of the pore waters have previously been related to dissolved organic carbon (Briucaud et al., 1981; Tada et al., 2015,b) and it is speculated they originate from fermentation and methanogenesis that may occur within the sediments of Site U1427 (Tada et al., 2015b).

*3.2.3 Shipboard colour reflectance index, b**

During Expedition 346 a high-resolution colour reflectance record, b*, was established on core sections of the deepest hole, Hole A, at Site U1427 (figure 3.4a) (Tada et al., 2015b). This record shows high frequency variations throughout, suggesting the sediment record is sensitive to palaeoceanographic changes and that proxy records should record past climate variability. On-board a close relationship between lithology, grain-size and sediment colour (b*) was identified (Tada et al., 2015b). In lithologic subunit A2, which encompasses the entire section investigated, siliciclastic-rich intervals are finer grained and show lower b* values, i.e. darker/more blueish in colour, than biogenic-rich, coarser sediments, which have higher b* values. This relationship makes b* a useful indicator of the varying contributions of terrigenous input (siliciclastic-rich) and marine palaeo-productivity (biogenic silica-rich). Low (high) b* corresponds to biogenic silicate-poor (-rich) sediments, indicating intervals of low (high) palaeo-productivity (Tada et al., 2015b).

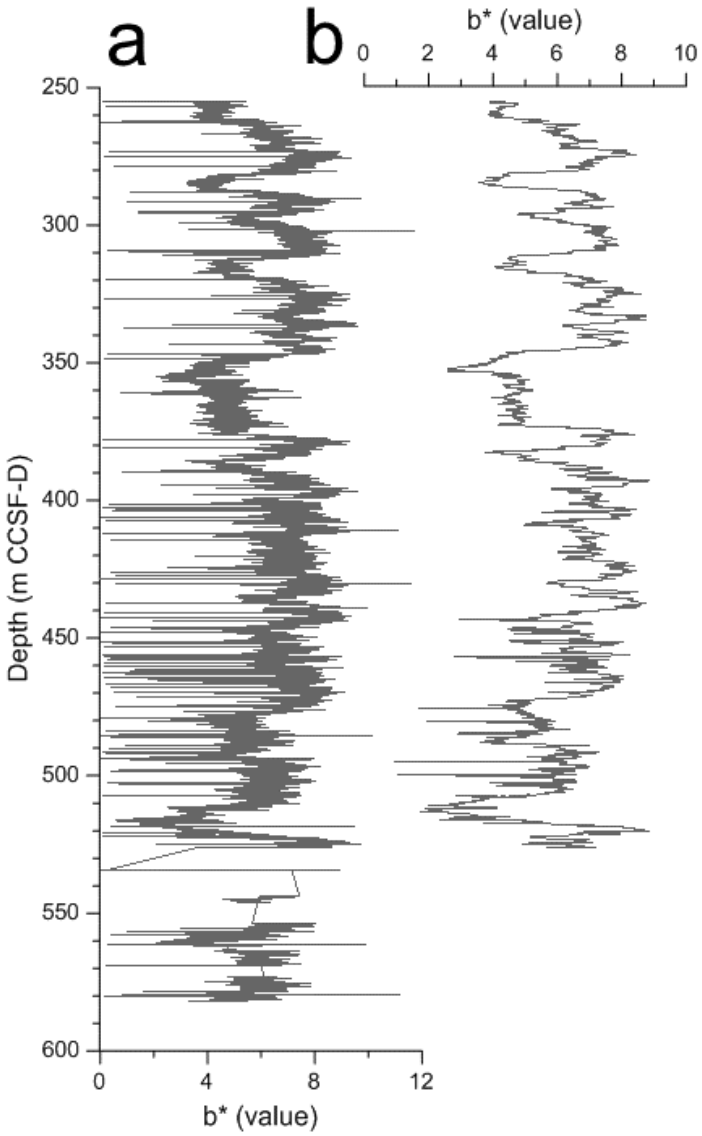

Figure 3.4. Shipboard b* index (Tada et al., 2015b) converted into the CCSF-D depth scale in (otherwise) unaltered condition (fig. 3.4a), and with smoothed data using a 60 point running mean, as used throughout this thesis (fig. 3.4b).

Through the relationship between b* and palaeo-productivity the index may be useful in the Japan Sea to indicate glacials (interglacials) in sediment cores with their relatively lower (higher) marine productivity (see chapter 2, section 2.4). Reduced productivity during glacials leads to reduced amount of biogenic silicate in the sediments, resulting in low b* values, while in contrast interglacials with enhanced marine productivity produce biogenic silica-rich sediments with high b* values (Tada et al., 2015b).

For use in this study, b* was reduced to cover only the MPT interval of 260-525 m interval only and compressed to a 60 point running mean average to enable data processing on the computer. The b* index was then converted to the CCSF-D depth

scale (figure 3.4b). While the original b* record continues below 525 m CCSF-D, sampling for proxy records was discontinued below this depth because coring difficulties (mainly gas expansion) meant that core recovery was very low and a large void of nearly 30 m between ~530 and 560 m made it impossible to continue high-resolution proxy records below this depth (figure 3.4a).

3.2.4 Shipboard age model

Fundamental to any palaeoenvironmental study is a good age model. In marine palaeo-studies different kinds of tools and age models are available. For example absolute chronological methods using the decay of radioactive isotopes and/or relative chronological methods, such as biostratigraphy and isotope-based chemo-stratigraphy. One widely applied approach in palaeoceanographic studies is developing a relative chronology based on the visual alignment of multiple records, possibly from one or more locations within a region, and their correlation with a well-dated, calibrated proxy record. The latter is used as a geochronological reference and can be linked to the same kind of proxy record from the new location. The most widely applied proxy record for these correlation-based age models are $\delta^{18}O$ records of marine carbonates. There is a close link between the waxing and waning of large continental ice sheets (i.e. glacials and interglacials) and the marine carbonate $\delta^{18}O$ values (Emiliani, 1955; chapter 2, section 2.2). These kind of age models have, however, proven challenging in the Japan Sea due to the counterintuitive interpretation and glacial dissolution of carbonates in deeper parts of the basin, which prohibit biostratigraphy and creation of continuous $\delta^{18}O$ records (see chapter 2, section 2.4).

A shipboard preliminary age model was produced using eight biostratigraphic datums (first and last occurrences of specific micro- and nanno-fossil species) and one geo-magnetic datum across 260-525 m (Tada et al., 2015b; see also chapter 4, section 4.3.1), which were tied to the geomagnetic polarity time scale (GPTS2012; Gradstein et al., 2012). From this they calculated sedimentation rates for the investigated interval of Site U1427 of ~42-63 centimetres per thousand years (cm/ka). A revision of shipboard age model and its age datums for the investigated interval are made in chapter 4, including a proposal for a higher-resolution age model for the investigated interval.

3.2.5 Shipboard geochemical, micropalaeontological and mineralogical data

Shipboard bulk sediment geochemical parameters were measured on ten samples. The resulting range of the calcium carbonate content ($CaCO_3$) is 4.0-16.4 wt% (average 10.0 wt%), the range of the total organic carbon content (TOC) is 0.7-1.6 wt% (average 1.1 wt%) and the range of the total nitrogen content (TN) is 0.2-0.3 wt% (average 0.3 wt%) (Tada et al., 2015b).

Shipboard foraminifera analyses found moderate to well preserved foraminifera shells present in most depths between 260-525 m. The planktonic foraminiferal assemblage reflects temperate to subarctic species, with sub-tropic species occurring at certain intervals (Tada et al., 2015b). The assemblage is dominated by *Globigerina bulloides* (d'Orbigny, 1826; hereafter *G. bulloides*), *Neogloboquadrina pachyderma* sinistral (hereafter *N. pachyderma* (s)) and dextral coiling (both Ehrenberg, 1861), indicating upwelling and cool water conditions (Bé, 1977; Domitsu and Oda, 2005). The tropical species *Globigerinoides ruber* is present in the sediments below ~507 m (at 473 m, 487 m and 492 m CSF-A) indicating warm water intrusions at these times, apparently related to interglacial sea-level highstands (Tada et al., 2015b).

The benthic foraminiferal assemblage reflects shelf to upper slope habitats typical for enhanced organic matter flux and/or dysoxic sea floor and pore water conditions (Tada et al., 2015b). The benthic genus *Uvigerina spp*. (d'Orbigny, 1826) is one of the most abundant foraminifera across the investigated interval (reduced numbers only occur at ~310 and ~390 m), and is associated with high marine productivity and is tolerant to slightly dysoxic conditions (Jorissen et al., 2007).

3.3 JAMSTEC KR-15-10, Site WB10 (surface sediment sample)

During IODP Expedition 346 no sea floor surface sediment was gathered and no bottom water temperature measurements were taken at Site U1427. In order to compare down-hole measurements to the present state and to enable a depth-temperature transect for benthic foraminifera-based Mg/Ca calibration of the southern Japan Sea (sections 3.5.10, 3.5.11), a set of surface samples from JAMSTEC KR15-10 expedition were selected. It became clear that only one sample contained sufficient numbers of benthic foraminifera to enable the analyses. The only surface sample (0-1 cm depth in sediment) used is site WB10 (core MC03; off Wakasa Bay, 36°00.25'N, 134°59.95'E), ~50 km east of Site U1427, located in a similar water depth (269 m) and with a similar lithology (bioturbated olive-black silty

clays) (Sagawa et al., 2015; figure 3.5). The in-situ sea floor temperature, measured during the expedition on 4th July 2015, was 1.74 +/-0.2 ºC and late Quaternary sedimentation rates are estimated to be 10-25 cm/ka (Sagawa et al., 2015).

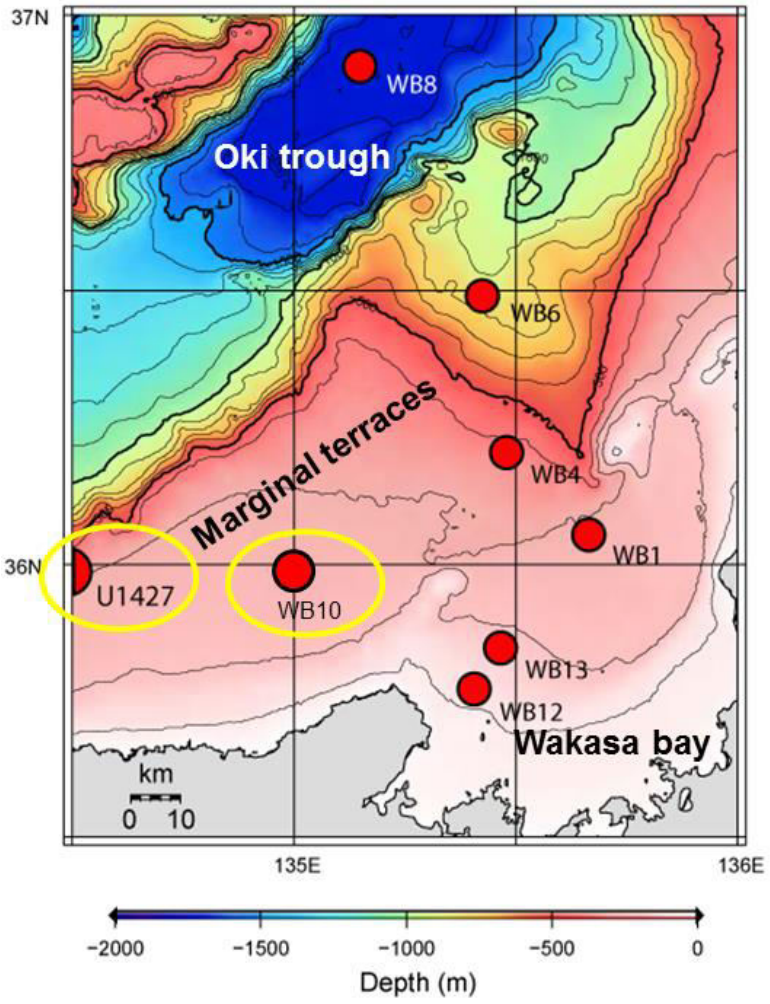

Figure 3.5. Bathymetric map with locations of Expediton KR15-10 coring sites (Sagawa et al., 2015), including Site WB10, which provided the surface sample amd measurements used in this study. Also shown IODP Site U1427 (Tada et al., 2015b). Figure modified after Ikehara (1991), Sagwa et al. (2015) and Tada et al. (2015a).

3.4 Oxygen Isotope Reference Stack

As described in chapter 2 (section 2.2) and above (section 3.2.4), the $\delta^{18}O$ of benthic foraminiferal calcite can be a proxy for glacial-interglacial cycles since its composition (in the open ocean) mainly responds to temperature and the $\delta^{18}O$ of the surrounding seawater which is a function of global ice volume and water salinity (e.g. Ruddiman, 2001d; Lisiecki and Raymo, 2005; Maslin and Swann, 2006). Owing to

the global nature of these parameters $\delta^{18}O$ records of several sites can be compared and lined up, creating $\delta^{18}O$ stacks.

A compilation of benthic foraminiferal $\delta^{18}O$ records covering the last 5.3 Ma (Pliocene-Pleistocene) from 57 globally distributed open-marine sites, called the LR04-stack (Lisiecki and Raymo, 2005), has become a widely applied stratigraphic reference record in palaeoceanographic studies (see also figure 2.4). Due to the nature of stacks, which uses an average of the $\delta^{18}O$ signals at each point in time, some MIS become better defined in the stack while others disappear because they are only small or do not appear in all $\delta^{18}O$ records (Lisiecki and Raymo, 2005). As a way of dating the LR04-stack has been orbitally tuned to obliquity, as calculated by Laskar et al., 2004), and individual records were shifted to fit, giving the impression of globally synchronous events and reducing original leads and lags between sites, which are acknowledge by the authors to have existed (Lisiecki and Raymo, 2005). The error of the age model is estimated to be ~4-6 ka across the MPT, with individual $\delta^{18}O$ records overall having a temporal resolution of >12 ka and containing 10-20 samples per G-IG cycle in the Pleistocene (Lisiecki and Raymo, 2005). The majority of $\delta^{18}O$ records included in the LR04-stack used *Cibicidoides wuellersdorfi* and *Uvigerina peregrina* shells for their $\delta^{18}O$ records and the genus *Uvigerina* dominates the benthic foraminifera assemblage at Site U1427 (section 3.2.5).

For the correlation between open ocean $\delta^{18}O$ records and the LR04-stack a graphic correlation software can be used, provided in Lisiecki and Lisiecki (2002). This is, however, not possible for the oxygen isotope records from the Japan Sea due to the salinity imprint that lead to an anti-correlation with $\delta^{18}O$ records from the open ocean during glacials, i.e. showing lower $\delta^{18}O$ values and higher values during interglacials (chapter 2, section 2.4.4). Therefore, the correlation between foraminiferal $\delta^{18}O$ records from the Japan Sea with the LR04-stack, or in fact any other open ocean stack, needs to be a visual correlation only. This is done by combining age-depth markers with shipboard b* index, and foraminiferal $\delta^{18}O$ and trace element data (chapter 4).

For use in this study (see chapter 4), the LR04-stack was cropped for the revision of the age model to reflect the relevant time-slice, 600-1300 ka, and the nomenclature by Lisiecki and Raymo (2005) is used, encompassing MIS 40-17 (table 3.1). In this nomenclature even numbers are allocated to high $\delta^{18}O$ glacials and odd

numbers to low $\delta^{18}O$ interglacials, as established by Emiliani (1955). Terminations are defined by the temporal midpoint between the end and start of rapid changes in the LR04-stack (Lisiecki and Raymo, 2005), and this approach has been applied in this thesis (chapter 4).

MIS	Start (ka)	End (ka)	MIS	Start (ka)	End (ka)
17	676	712	29	1014	1031
18	712	761	30	1031	1062
19	761	790	31	1062	1081
20	790	814	32	1081	1104
21	814	866	33	1104	1114
22	866	900	34	1114	1141
23	900	917	35	1141	1190
24	917	936	36	1190	1215
25	936	959	37	1215	1244
26	959	970	38	1244	1264
27	970	982	39	1264	1286
28	982	1014	40	1286	1304

Table 3.1. Marine isotope stages (MIS) with their respective start and end as presented in Lisiecki and Raymo (2005).

3.5 Methods Applied in this Thesis

A variety of geochemical, sedimentological and micropalaeontological analyses were carried out down-core Site U1427 and on the surface sediment sample (section 3.3), and in total 517 samples were analysed applying up to nine different methods to individual samples. The methods encompass determination of bulk sediment organic parameters (section 3.5.2), carbonate content (section 5.3.4), Rock-Eval pyrolysis (section 3.5.6), grain-size distribution (section 3.5.8) and (semi-quantitative) facies description (section 3.5.9). Foraminifera (section 3.5.7) were isolated from the sediments and analysed for their stable isotope composition ($\delta^{18}O$, $\delta^{13}C$, section 3.5.10), possible diagenetic alteration (section 3.5.11) and trace element composition (Mg/Ca, section 3.5.12), which allowed temperature estimates (section 3.5.13). This methods-section starts by introducing the sub-sampling of samples (section 3.5.1), then proceeds to summarise the applied methods, their functional principles and limitations.

3.5.1 Sampling and sample splitting at Site U1427

Sediment samples provided for use in this thesis are from all three Holes drilled at Site U1427 (Hole A, B, C; see appendix A), spaced 50 to 100 cm apart, and consist of 1 cm wide scoop sediment samples (volume of ~30 cm^3). The bulk sediment was freeze-dried and split, following the illustration of figure 3.5., prior to preparation for analyses. While not all methods could be applied to the whole sample collection due to sometimes lengthy laboratory protocols, careful sample selection enabled high-quantity, high-quality information gain.

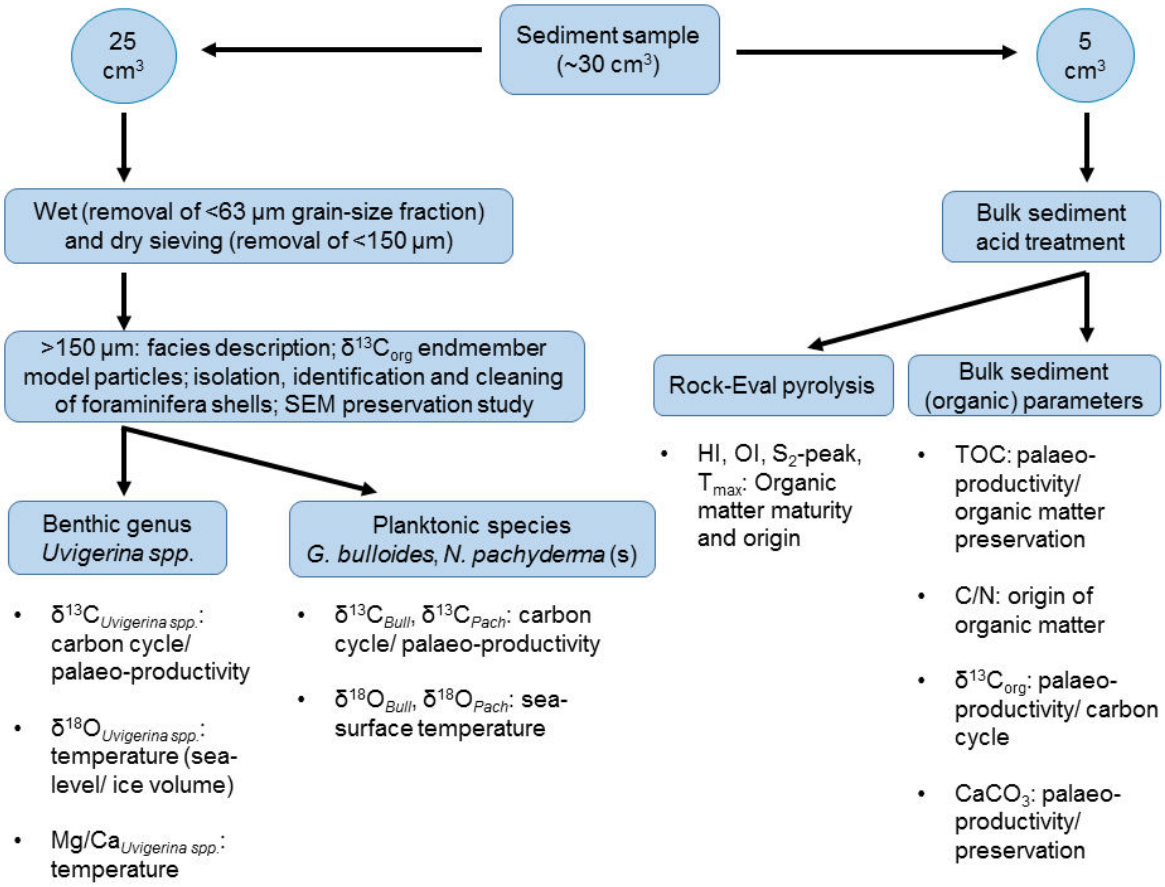

Figure 3.6. Schematic flow chart of sub-sampling for analyses, including methods applied and target proxy records (interpretations).

3.5.2 Bulk sediment organic parameters ($\delta^{13}C_{org}$, TOC, TN, C/N ratios)

Organic matter (OM) only makes up a small proportion of the sediment, but it provides a wide range of insights about past marine productivity, temperatures and source dynamics (terrigenous or marine origin) make the analysis of OM an important tool in palaeoceanographic and -environmental reconstructions. Most of marine-derived OM is produced by phytoplankton in the photic zone (<100 m; Stein, 1991), hence its information refers to surface water condition. After death the OM sinks

through the water column and settles on the sea floor, with some of it becoming archived in the sediments (Stein, 1991; Meyers, 1997).

Marine surface productivity is limited by nutrient availability. While carbon (C) is available in great amount in aquatic systems, nitrogen (N) and phosphorous concentrations are limited and not all of it may be bio-available (Brasier, 1995; Moore et al., 2013). In the Japan Sea, marine phosphorous is limited (Tada et al., 2018), showing lower phosphorus concentrations than the adjacent northwest Pacific Ocean (Moore et al., 2013), and phosphorous input is thought to be controlled by the inflow of nutrient-rich ECSCW via the TWC (Tada, et al., 1999; Yanagi, 2002; Tada, 2004; Fujine et al., 2009; see also chapter 2, section 2.4).

Bulk sediment organic parameters, namely the ratio of total organic carbon content (TOC) to total nitrogen content (TN), the ratio of C to N (C/N ratios) and the isotope ratio of bulk organic matter ($\delta^{13}C_{org}$), are used to reconstruct marine palaeo-productivity and sedimentary OM source variations. In the Japan Sea tracing palaeo-productivity can enable the reconstruction of the East Asian summer monsoon via their intrinsic link between monsoon intensity and the supply of productivity-limiting nutrients (Chapter 2, section 2.4), although this may be limited to interglacial sea-level highstands when the TWC could penetrate into the Japan Sea.

The TOC content in marine sediments from the Japan Sea is primarily linked to marine surface water palaeo-productivity (Wefer et al., 1999). However, the application of TOC as a productivity proxy is not straight forward because the TOC content may be influenced by a mixed signal of marine productivity and terrigenous input of OM, and by a preservation signal through OM decomposition by oxygenation and microbial activity within the sediments (Meyers and Terranes, 2001). To account for the dilution through terrigenous input TOC fluxes need to be calculated rather than using the total amount of TOC in a sediment record (described in section 3.5.5). Decomposition of OM which reduces TOC is a more complex matter. OM degradation is controlled by several factors including sedimentation rate/bulk sediment accumulation, lithology, oxygenation of bottom water and sediments, bioturbation and the composition/reactivity of organic matter (Emerson, 1985; Müller and Suess, 1980; Canfield, 1989; Stein, 1991; Wefer et al., 1999; Meyers and Terranes, 2001). For example, the higher the OM input and the better OM

reservation, i.e. low oxygenation, low bioturbation with shallow penetration depth, high sedimentation rate and fine-grained sediments, the higher the TOC.

The C/N ratio has been commonly used to characterise the type/source of OM, algal or land plant (e.g. Müller, 1977; Jasper and Gagosian, 1990; Stein, 1991; Meyers, 1994; Schubert and Calvert, 2001), in a variety of settings, e.g. estuarines (Leng and Lewis, 2017), lakes (Meyers and Lallier- Vergès, 1999), terrestrial settings (Scheffer and Schachtschabel, 1984) and marine sediments (Stein, 1991). Organic matter of aquatic organisms (zooplankton, phytoplankton, diatoms) contains less carbon and more protein and hence they have lower C/N ratios than OM of higher land plants, which comprises more carbon-rich components, such as lignin (figure 3.7) (Meyers and Lallier-verges, 1999; Meyers 1997). Typical values for marine OM are between 4 and 10 (Meyers and Lallier-Vergés, 1999), with an average value of ~6 for zoo- and phytoplankton, which can increase to ~10 by preferential decomposition of protein-rich components as particles sink through the water column (Emery and Uchupy, 1984; Stein, 1991). In contrast, C/N ratios of land plants are higher (>15; Scheffer and Schachtschabel, 1984; Meyers and Lallier-Vergés, 1999).

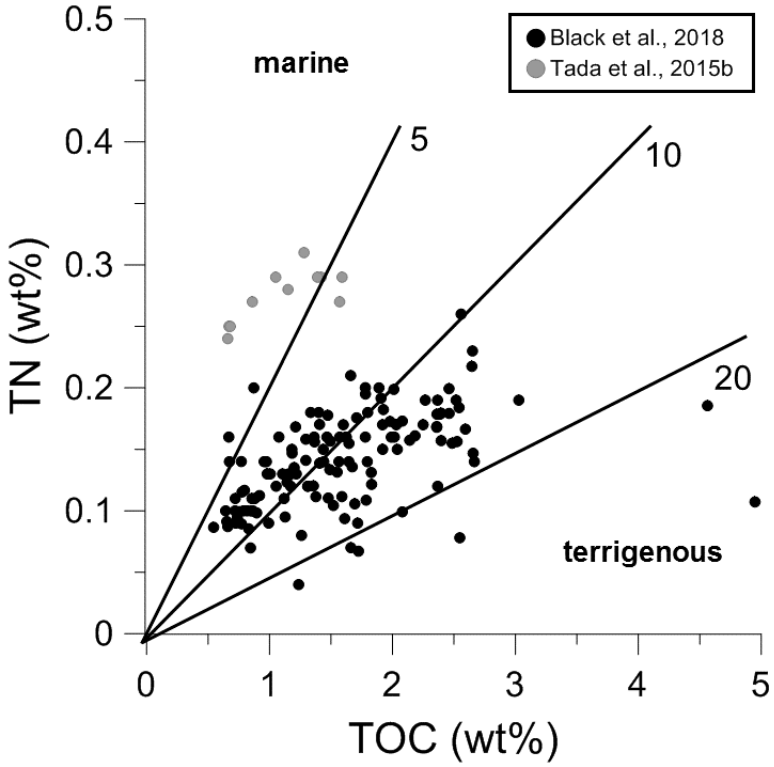

Figure 3.7. Total organic carbon (TOC) versus total nitrogen (TN) of Site U1427 for the upper 140 m (Black et al., 2018) and shipboard data of the investigated interval (Tada et al., 2015b). Lines (5, 10, 20) are for orientation (after Stein, 1991).

Shipboard measurements for TOC (11 data points, 0.7-1.6 wt%, average 1.1 wt%) and TN (0.2-0.3 wt%, average 0.3 wt%) were used to calculate C/N ratios (range 2.7-5.8, average 4.1) and plotted in figure 3.7. All shipboard data indicate marine OM as the predominant organic carbon source. More recently, Black et al. (2018) determined TOC and TN for the upper 140 m of Site U1427 (134 analyses, ~1 m spacing), from which C/N ratios were calculated (~4.2-26), suggesting a mixed marine-terrigenous origin of OM (figure 3.7). Given the shipboard lithological description (section 3.2.2) it is expected there were higher contributions from marine OM during interglacials, when enhanced nutrient input via TWC inflow primed marine productivity and higher terrigenous OM contributions and reduced marine productivity during glacials (chapter 2, section 2.4).

Another proxy able to decipher the source of organic carbon is the isotope ratio of bulk organic carbon. Like the example of oxygen, presented in chapter 2 (section 2.2), carbon has two different stable isotopes. While these isotopes share the same chemical characteristics (same amount and arrangement of electrons and protons), they differ in their physico-chemical properties due to their different number of neutrons (e.g. oxygen: ^{16}O, ^{17}O and ^{18}O; carbon: ^{12}C, ^{13}C) and hence their mass. This mass difference can be detected in a mass spectrometer and the relative contributions of the heavier (^{18}O, ^{13}C) over the lighter (^{16}O, ^{12}C) isotope can be calculated, with the resulting ratio expressed in the delta-notation (δ):

$$\delta R_{sample}\,[‰\,VPDB] = \left(\frac{R_{sample} * R_{standard}}{R_{standard}}\right) * 1000 \qquad \text{(eq. 3.1)}$$

where R denotes the isotope ratio ($^{13}C/^{12}C$, $^{18}O/^{16}O$) presented in the unit permil (‰) and reported against the Vienna Pee-Dee Belemnite (VPDB) standard (Coplen, 1994).

The isotope ratios of organic carbon ($\delta^{13}C_{org}$) can be influenced by C-source dynamics (terrigenous, marine), surface water CO_2, diagenesis and remineralisation and marine productivity (Maslin and Swann, 2006). In simple terms, the OM of marine plankton has $\delta^{13}C_{org}$ values between –20 and –22 ‰ (Jasper and Gagosian, 1993; Meyers, 1994), although great scatter is possible and latitudinal differences occur, e.g. marine OM average $\delta^{13}C_{org}$ in the tropics is –18 ‰ while in polar regions it is ~ –20 ‰ (Stein, 1991; Tyson, 1995; Hedges et al., 1997; Hayes, 2001). In contrast, $\delta^{13}C_{org}$ of terrigenous material generally have lower values, as low as ~–30 ‰ (figure

3.8). The vast majority of land plants (95 %) use the C_3 photosynthetic pathway, which produces OM with a lower isotope signature of on average –27 ‰, whilst land plants from arid regions (C_4-plants), such as Savannah grasses, have an average $\delta^{13}C_{org}$ of ~–12 ‰ (Stein, 1991; Meyers, 1994; Tyson, 1995; Hedges et al., 1997; Wagner et al., 2003).

In marine algae, $\delta^{13}C_{org}$ also varies in relation to changes in marine productivity as a result of the preferential take up of the light ^{12}C in marine plankton. The remaining C-pool available for subsequently formed marine OM is enriched in ^{13}C, resulting in higher $\delta^{13}C_{org}$ values (Maslin and Swann, 2006). Therefore, in a marine OM dominated system, higher (lower) $\delta^{13}C_{org}$ values indicate times of high (low) marine productivity, but at sites likely to be affected by additional variations in source dynamics, such as in the Japan Sea, the interpretation of $\delta^{13}C_{org}$ values can be challenging.

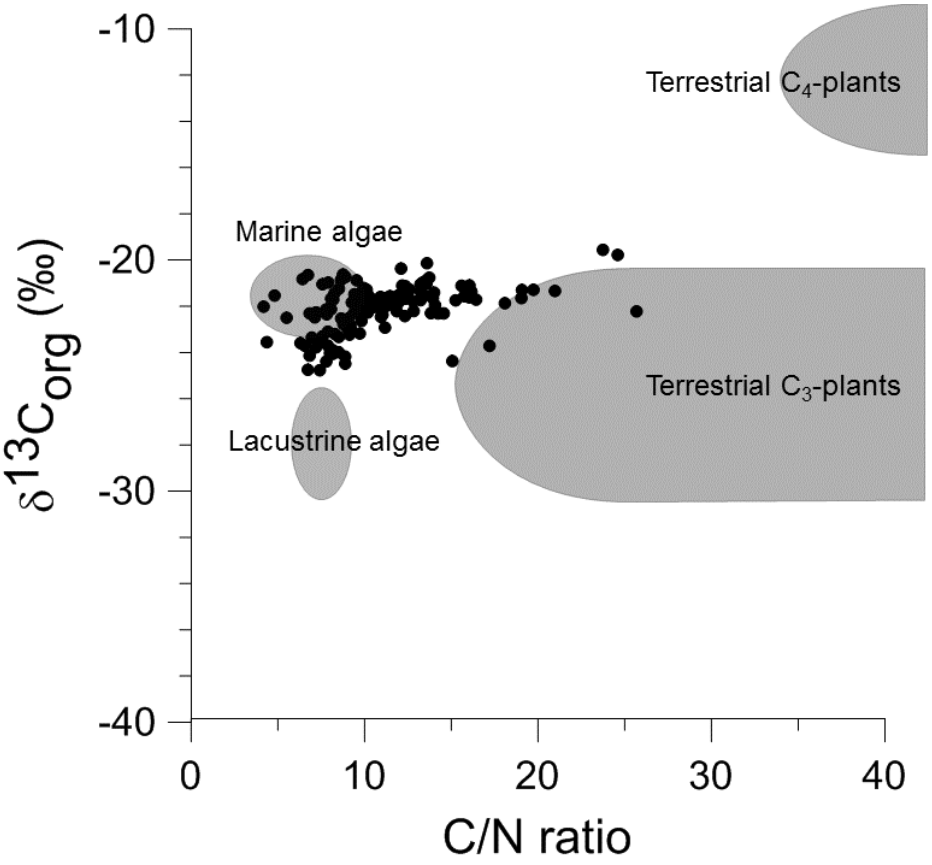

Figure 3.8. Cross-plot of C/N ratios versus $\delta^{13}C_{org}$ (after Meyers and Lallier-Vergés, 1999). Shaded areas indicate the location of marine and lacustrine algae as well as land plant organic matter in terms of their $\delta^{13}C_{org}$ and C/N ratios as described in Meyers (1994), Meyers and Lallier-Vergés (1999) and IAEA (2013). Black dots represent the C/N ratios and $\delta^{13}C_{org}$ results gathered by Black et al. (2018) from the upper 140m sediment cores of Site U1427.

A comparative cross-plot of $\delta^{13}C_{org}$ and C/N ratios, following the example of Meyers and Lallier-Vergés (1999), can be useful for interpreting bulk sediment organics parameters (figure 3.8). Shipboard $\delta^{13}C_{org}$ data for Site U1427 were not gathered, but analyses carried out in the upper 140m sediment cores show $\delta^{13}C_{org}$ values range between ~–25 and –19 ‰ (figure 3.8) (134 analyses; Black et al., 2018).

All 517 samples were analysed for their TOC and TN content every ~0.9 m, which increased to ~0.4 m at depths >385 m CCSF-D. About 300 milligrams (mg) of bulk sediment were decarbonated following the “rinse method” described in Brodie et al. (2011), which includes acidification of samples (~50-100 ml of 5 % hydrochloric acid, HCl) and repeated rinsing using deionised water (DI) until the pH was indistinguishable from DI, before drying at low temperature (~50 ºC) and grinding the material to a power sample (Brodie et al., 2011; Melanie Leng, pers. coms.). For analysis, 25-40 mg of powdered sample was analysed in an Element Analyser Isotope Ratio-Mass Spectrometer (EA-IRMS) at the National Environmental Isotope Facility (Keyworth). The device combusts the samples, cleans and dries the released gasses of contamination, and then measures TOC and TN in its EA component before transferring the sample gas into the attached IRMS to determine the $\delta^{13}C_{org}$ value. Three in-house standards with known $\delta^{13}C$, TOC and TN were used for quality control (“BROC2”, “SOILB”, “SOILA”) and show relative standard deviations (rsd.) of <0.09 for $\delta^{13}C$, <0.71 for TOC and <0.46 for TN. Seven outliers with high rsds. were identified and not used in this thesis.

3.5.3 Terrestrial organic particles $\delta^{13}C_{org}$ endmember model

Another way to investigate the amount of terrigenous input is by establishing an average $\delta^{13}C_{org}$ endmember value for terrigenous material in this setting. At Site U1427 land plant particles, including leaves, were identified on-board suggesting riverine input. The $\delta^{13}C_{org}$ of such land plant particles was analysed to derive a local terrestrial endmember value, which enables estimating the terrestrial contribution to the bulk sedimentary organic matter (section 3.5.2).

Variations in the contributions of C_3- and C_4-plants can have an impact since their typical $\delta^{13}C_{org}$ values differ (section 3.5.2). For this endmember model no differentiation between C_3- and C_4-plant OM could be made, based on the small size of the particles used, however, evidence from literature suggest a shift from

predominantly C_3- to C_4-plants or vice versa is unlikely, and instead evidence implies vegetation during glacials and interglacials were dominated by C_3-plants throughout the investigated time splice (chapter 5, section 5.4.2).

Defining the average $\delta^{13}C_{org}$ value for the endmember model was made by analysing the $\delta^{13}C_{org}$ composition of terrestrial plant matter particles isolated per light microscope from the >150 µm fraction of seven samples (table 3.2). These samples had shown an abundance plant matter of woody and leafy pieces with a fibrous or cellular structure (see chapter 5, figure 5.5, for example photographs).

Hole	Core	Section	Depth (cm)	Depth (m CCSF-D)
A	51	1	71	376
A	68	6	15	446
B	39	4	55	312
B	45	2	113	340
B	51	2	118	369
B	58	2	134	402
C	46	2	52	349

Table 3.2. Samples used in $\delta^{13}C_{org}$ endmember model.

The plant particles weighed between 0.01 and 0.27 mg, and were acidified in tin capsules to remove any potential particulate carbonates that may have stuck to the organics (Brodie et al., 2011). This method involves filling the tin capsule with 5 % HCl before drying the samples on a hot plate (~<70 ºC). Once dried, the capsules were left to cool before folding them for analyses as described in section 3.5.2. Analysis show 1std of +/-0.7‰ on repeat analyses.

3.5.4 Carbonate content ($CaCO_3$)

The production of calcium carbonate in the oceans is dominated by planktonic calcareous primary producers such as coccolithophores, calcareous dinoflaggelates and foraminifera, as well as benthic organisms such as molluscs, ostracods, bivalves and benthic foraminifera (Milliman, 1993). As the distribution of suspended calcium carbonate in the surface waters of the oceans resembles that of primary productivity (Rühlemann et al., 1999), $CaCO_3$ content of sediments can be used to as a proxy for primary productivity (e.g. Wefer et al., 1999). The interpretation of $CaCO_3$ is however complex because of the influence of dilution through terrigenous input and/or biosiliceous productivity decoupled from carbonate productivity, and by the influence

of dissolution of $CaCO_3$ during transport/sinking through the water column and post-depositional within the sediments (Wefer et al., 1999). To eliminate the effect of dilution, $CaCO_3$ accumulation rates (fluxes) were calculated (section 3.5.5).

Dissolution of $CaCO_3$ is primarily controlled by the carbonate-ion saturation of the surrounding water (Broecker and Peng, 1993). In surface ocean waters carbonate is oversaturated, but with depth it becomes undersaturated and carbonate dissolution begins at the lysocline (Berger, 1968). At greater depth the carbonate supply and dissolution balance each other and $CaCO_3$ content drops to zero (Rühlemann et al., 1999) and this depth defines the CCD (Bramlette, 1961). Another control on $CaCO_3$ dissolution is the remineralisation of organic matter in the sediments, which produces carbonate corrosive CO_2 gas (Emerson and Bender, 1981; Rühlemann et al., 1999). Therefore, the high sedimentation rates, fine-grained lithology and bathymetrical position above the CCD, combined with low TOC contents should guarantee best carbonate preservation at Site U1427 (see sections 3.2, 3.5.2).

In total 329 bulk sediment samples had a direct TIC measurement using a JENA multi-EA 4000 HT system 1500. For analysis, ~50 mg ground and homogenised sample material was weighed into a sample boat and placed into the JENA auto sampler. The device automatically acidifies samples by adding 400 µl of 40 % phosphoric acid in an oxygen environment/carrier gas and heating in the attached furnace to ~100 ºC for full digestion and release of the contained TIC as CO_2 gas. The released gas is cleaned, dried and analysed using a non-dispersive, optic infrared absorption carbon detector (C-NDIR). (Jezierski, 2015; Analytic Jena AG, 2012). Two in-house (1.2 % and 6 % TIC content) and one round robin material (called 81404) with known $CaCO_3$ contents were used for quality control and show rsd. of on average 0.1 (range 0.0-0.4).

From the TIC analyses $CaCO_3$ contents were quantified by calculating the molar mass of $CaCO_3$:

$$stoichiometric\ coefficient = \frac{CaCO_3 molar\ mass}{C\ atomic\ weight} = \frac{[40*12*(3*16)]}{12\frac{g}{mol}} = \frac{100\ g/mol}{12\ g/mol} \quad \text{(eq. 3.2)}$$

$$= 8.33$$

Using the stoichiometric coefficient the $CaCO_3$ content was calculated from TIC, assuming all TIC is bound to calcium carbonates (calcite, aragonite):

$$CaCO_3(wt\%) = (TC - TOC) * 8.33 = TIC * 8.33 \quad \text{(eq. 3.3)}$$

For completeness equation 3.3 also shows the calculation of TIC from TC (total carbon) and TOC (calculations after Bernard et al., 1995).

Shipboard ten $CaCO_3$ analyses were carried out across the investigated interval, ranging between 4.0 and 16.4 wt% $CaCO_3$ (average 10.0 wt%) and Black et al. (2018), measuring $CaCO_3$ in the upper 140 m sediment cores, present values between near nil and ~25 wt%.

3.5.5 Mass accumulation rates and fluxes

Sediment mass accumulation rates and fluxes for TOC and $CaCO_3$ contents were calculated to eliminate the effect of dilution through terrigenous input (see sections 3.5.2, 3.5.4). While the contents of TOC and $CaCO_3$, or in fact any proxy, is prone to the effects of dilution, fluxes on the other hand consider the weight or amount deposited over a certain area and over a certain unit of time. An example of a flux unit is gram per square centimetre over one-thousand years, g/cm2/ka.

In order to calculate a flux, the bulk sediment mass accumulation rate (MAR) must be calculated first. Here MARs were calculated using the results of 55 shipboard dry density measurements (Tada et al., 2015b) and multiplying them with average values of newly calculated sedimentation rates, which are based on the revised age model presented in this thesis (chapter 4, section 4.3.2). Bulk average MARs were calculated for each section respective sedimentation rate following previous ODP/IODP publications (Zachos et al., 2004; März et al., 2013):

$$bulk\ MAR\ [g/cm^2ka] = DD * linear\ SR \quad \text{(eq. 3.4)}$$

where DD is the dry density (g/cm^3) and linear SR is a linear sedimentation rate (cm/ka) assumed between age markers in an age model. Equation 3.4 assumes a linear sedimentation rate (between age markers). While such linear/constant sedimentation rates are unlikely true, this is a commonly applied way to estimate MARs. The fluxes for $CaCO_3$ and TOC were then calculated for each sample using the MARs (März et al., 2013) (equation 3.5):

$$Flux\ [g/cm^2ka] = bulk\ MAR * proxy\ content\ /\ 100 \quad \text{(eq. 3.5)}$$

For reference, each SR interval had fluxes calculated too, using an average TOC/$CaCO_3$ content for each of the intervals (see chapter 5, figure 5.10).

3.5.6 Rock-Eval pyrolysis

Rock-Eval (RE) pyrolysis is a method developed by the hydrocarbon exploration industry to determine the source-rock potential and thermal maturity of black shales but it has also been applied to recent marine sediments to determine the origin of OM, i.e. marine/terrigenous (Stein, 1991; Stax and Stein, 1994; Pimmel and Claypool, 2001; Kim et al., 2006; Baudin et al., 2015). Additionally, RE is used to gain information about non-reactive/inert OM, such as coal and/or reworked material within the samples (Espitalié, 1977; Tissot and Welte, 1984). The results of RE can give greater confidence in the interpretation of the bulk sediment organics and organics endmember model (sections 3.5.2, 3.5.3).

The classic bulk-rock RE pyrolysis method by Lafargue et al. (1998) is applied in this study. The steps in this method are sample heating to 300 ºC for 3 minutes, which releases volatile hydrocarbons (HC) and is determined as the S_1-peak. The temperature is then increased to 650 ºC at a rate of 25 ºC/min, which releases further HCs by degradation/pyrolysis of non-volatile (inert) OM and defines the S_2-peak. The temperature is then increased to 850 ºC and the temperature of maximum residue HC release characterises T_{max}, which indicates the maturity of the contained OM, with more mature OM needing higher activation energies to pyrolise and release HCs (Espitalié et al., 1977). Typical T_{max} for immature marine OM range around 400-430 °C, with higher values indicating more mature (oil window) or overmature OM conditions (Espitalié et al., 1977; Peters, 1986; Pimmel and Claypool, 2001). For young and shallow buried marine sediments T_{max} <400 ºC or even <300 ºC have been reported (Liebezeit and Wiesner, 1990; Wagner and Dupont, 1999). In a final step the sample is cooled to ~390 ºC while releasing trapped CO_2 gas from TOC (S_3-peak) (Espitalié et al., 1977). The total amount of released HCs and CO_2 gasses are detected by flame ionisation detectors (FID) and infrared detectors respectively. For more details on the method please see Lafargue et al. (1998) or Killops and Killops (2005).

Normalising the S_2- and S_3-peaks to TOC allows the calculation of Hydrogen Index (HI) and Oxygen Index (OI):

$$HI\ [mgHC/gTOC] = \frac{S2 - peak}{TOC} \times 100 \tag{3.6}$$

$$OI\ [mgCO_2/gTOC]\ = \frac{S3-peak}{TOC} \times 100 \quad (3.7)$$

with the TOC from RE (S_3-peak) being used, not the TOC of bulk sediment organic analyses (section 3.5.2), although the data gathered by the two methods show close resembles (r^2 of 0.86 across all 36 samples of this study, see below).

A cross-plot of HI versus TOC can help to identify the dominant source of OM. In marine sediments, algal material is HC-rich (HI >400 mgHC/gTOC), while the OM of land plants is relatively HC-poorer (HI <400 mgHC/gTOC; Stein, 1991; Wagner and Dupont, 1999; Killops and Killops, 2005). A simultaneous increase in both HI and TOC therefore implies an increased marine (algal) productivity, a typical pattern in marine sediments (Bertrand and Lallier-Vergés, 1993; Meyers and Lallier-Vergés, 1999).

One complication is related to mineral matrix effects (e.g. Wagner and Dupont, 1999; Disnar et al., 2003), when analysing TOC-poor samples (<1 wt% TOC; Wagner and Dupont, 1999). HI values tend to decrease with decreasing TOC values because of the increasing influence of the mineral matrix, especially in the presence of clay minerals such as illite (Disnar et al., 2003, and references within). Testing for the presence of the mineral matrix effects can be done by analysing a TOC versus S_2 yield cross-plot. A linear correlation curve that passes through the origin of the axes indicates no noticeable matrix effect and hence no alteration of the HI values (Disnar et al., 2003).

Another way to analyse RE-data is cross-plotting OI and HI in a pseudo-van Krevelen-diagram (Espitalié et al., 1977). This approach differentiates between three types (origins) of OM according to their position in the cross-plot (figure 3.9). Bacterial and land plant OM can be HC-rich (type I) or HC-poor but rich in carbohydrates e.g. wood and vascular plants (type III), while marine algae OM is enriched in protein and therefore has a higher H/C ratio than vascular plants (type II) (Peters and Simoneit, 1982; van Krevelen, 1984; Meyers and Lallier-Vergés, 1999; Meyers and Teranes, 2001). Post-depositional oxidation of OM, i.e. reworking and/or transport, leads to a reduction in HI and an increase in OI values, potentially shifting the values of type I and II OM to values closer to those of type III (land plant) material (figure 3.9) (Meyers and Lallier-Vergés, 1999).

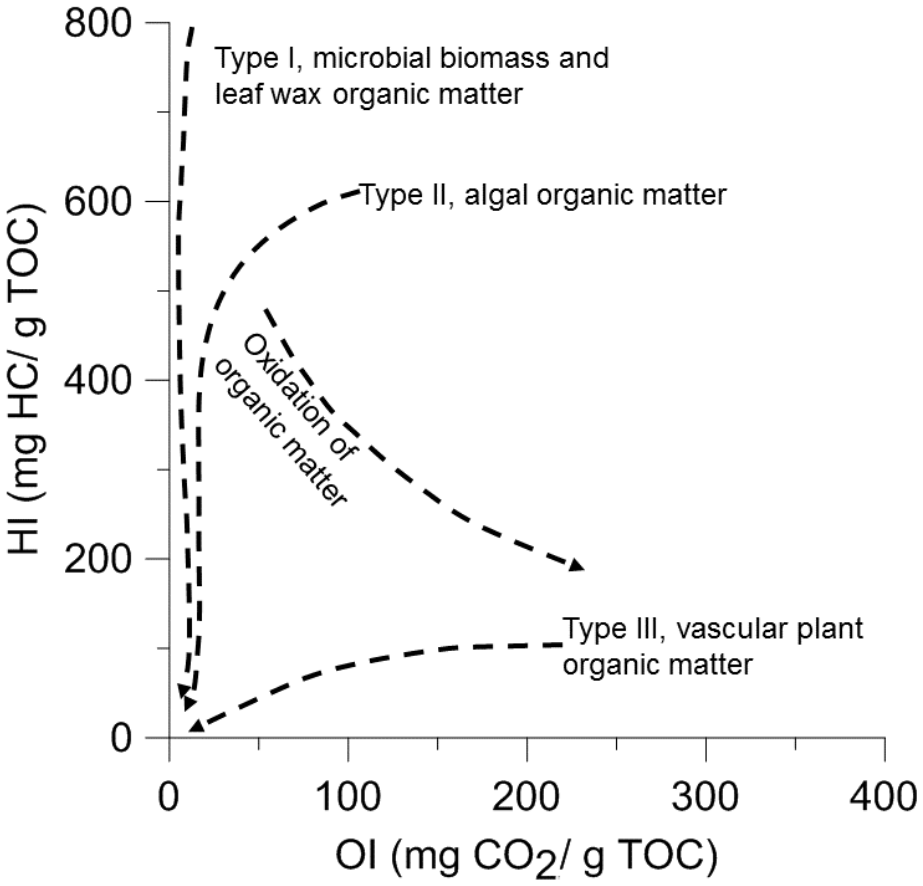

Figure 3.9. Pseudo-van Krevelen diagram with OM origins (scattered lines; Meyers and Lallier-Vergés, 1999). The Oxidation of OM line indicates the pathway type I and II OM would take if undergoing oxidation (lowering HI while increasing OI; Meyers and Lallier-Vergés, 1999) and following a path that brings it closer to resembling type III OM.

No shipboard RE analyses were carried out. In total 35 samples were analysed as in-kind contributions by the French Institute of Petroleum (IFP Energies Nouvelles) in Rueil-Malmaison (France) on a Rock-Eval 6 device for T_{max}, TOC, S_1-, S_2- and S_3-peaks which allowed calculating HIs and OIs. The samples cover glacial onsets and terminations, focussing on two intervals with pronounced differences in TOC and $\delta^{13}C_{org}$ values at 345-375 m and 465-525 m (see chapter 5, section 5.3.5). For analyses decarbonated, ground samples were measured using the Classic Bulk-Rock method by Lafargue et al. (1998). One in-house standard with known TOC, T_{max} and S_2-peak was used for quality control (standard marine source rock, IFP) and showed rsds. of 0.03 for TOC, 1.07 for T_{max} and 0.28 for S_2-peak.

3.5.7 Foraminifera in the Japan Sea

Foraminifera are single-celled marine organisms, living either planktonic (floating in the photic zone) or benthic (living on and within the upper layers of sediments) and

most foraminifera secrete a calcite shell (or test), consisting of multiple connected chambers which are species-specific in their alignment/coiling and number, as well as aperture(s)/opening(s) and surface ornamentations, such as spines, that are characteristic for individual species (e.g. Bé, 1977; Loeblich and Tappan, 1988; Rönnfeld, 2008). The fossil shells preserves these species-characteristic features, which allows their identification (see Murray, 1991, for a review). Foraminifera can be used to reconstruct palaeoceanographic conditions via species counts (assemblage studies) and/or via analyses of stable isotope ratios (see Pearson, 2012, for a review, and chapter 2, section 2.2). In this thesis the $\delta^{18}O$ and $\delta^{13}C$ records are established using the most abundant benthic genus *Uvigerina* and the two most abundant planktonic foraminifera species *G. bulloides* and *N. pachyderma* (sinistral coiling variety) in the sediments of Site U1427 (see section 3.2.5) (Domitsu and Oda, 2005; Tada et al., 2015b; Sagawa et al., 2018; Gallagher et al., 2018). Their high and near constant abundance suggests the possibility for the creation of a continuous isotope proxy record.

Foraminifera of the genus *Uvigerina* spp. often dominate assemblages in the Japan Sea (Das et al., 2018). The Uvigerinidae (family) are shallow infaunal, dwelling in the uppermost centimetres of sediments, and are most abundant in areas of high surface water productivity such as upwelling areas and/or areas where continental erosion occurs, and are often associated with dysoxic to anoxic conditions (e.g. Jorissen et al., 2007; Das et al., 2018, and references within). *Uvigerina* prefer muddy sediments and live in shelf to bathyal environments, in ~100->4500 m water depth (Murray, 1991). The interpretation of the resulting $\delta^{18}O$ record of *Uvigerina* spp. ($\delta^{18}O_{\textit{Uvigerina}\ \text{spp.}}$) is based on the widely applied assumption that *Uvigerina* calcify their shells in equilibrium with the surrounding sea water (Shackleton, 1974; Fontanier et al., 2006; Stern and Lisiecki, 2014). In this study the same approach as shipboard and in recent publications of the upper ~250 m of Site U1427 was applied (Tada et al., 2015b, Sagawa, 2018), isolating a single *Uvigerina* spp. morphotype (hispid, elongated, strong costae) that probably belongs to the species *Uvigerina peregrina* (Boersma, 1984).

The planktonic foraminifera species *G. bulloides* and *N. pachyderma* (s) are the most abundant planktonic species in the Japan Sea at present (Kheradyar, 1992; Tada et al., 2015 a, b). At present, the right coiling variety *N. pachyderma* (d) dominates the sediments under the influence of the inflow of warm, nutrient-rich

waters of ECSCW/TWC, while *N. pachyderma* (s) is being associated with the cooler water masses in the central and northern Japan Sea (Domitsu and Oda, 2005; Gallagher et al., 2018). Shifts in the predominant coiling ratio have been observed during the Pleistocene and are thought to be associated with changes in the TWC inflow over G-IG cycles, and at times of more restricted TWC inflow *N. pachyderma* (s) dominated over the right coiling variety (Domitsu and Oda, 2005; Gallagher et al., 2018).

G. bulloides is characteristic for upwelling regions in the Japan Sea (Kheradyar, 1992), and the typical indicator of nutrient-rich, low-saline waters around the Tsushima Strait and associated with enhanced contributions of ECSCW to the TWC (chapter 2, section 2.4; Domitsu and Oda, 2005; Gallagher et al., 2018 and references within). In the Japan Sea two morphotypes exist, a thick-walled and a thin-walled variety (Domitsu and Oda, 2005). Assemblage studies of planktonic foraminifera at 51 sites along the Western coast of Japan, found the thin-walled morphotype predominantly in the southern Japan Sea and in sediments deposited during interglacials, suggesting they may be related to warm TWC waters (Domitsu and Oda, 2005). In contrast, the thick-walled morphotype was more commonly found at central locations along the Japanese coast. Gallagher et al. (2018) present an assemblage study in the upper ~180 m of sediments at Site U1427, and described the thick-walled type from glacials and interglacials alike, appearing in association with warm water indicating species such as *Globigerinoides ruber*, and during periods of enhanced summer monsoon precipitation, suggesting that ECSCW inflow was possible at these times and sea-level stands.

The thick-walled morphotype dominates the sediments of Site U1427 and has previously been used by Sagawa et al. (2018) in the creation of stable isotope records for the upper interval and is used in this study to enable future merging of the isotope records of Site U1427.

3.5.8 Grain-size distribution

The sample preparation for the foraminiferal calcite stable isotope analyses includes steps during which grain-size fractions are acquired (wet- and dry-sieving, figure 3.5). The resulting grain-size fractions of >150 µm, 150-63 µm and <63 µm, were collected, dried and weighed. Where some material was lost during the laboratory process, as it was not the main parameter, data were not used in the

grain-size distribution analysis. Varying contributions of coarser/finer fractions can provide information about (i) the prevailing energy regime at the time sediment was deposited, (ii) about changes in the main riverine input source (McCave, 2002), and (iii) possibly provide insights into dissolution if assuming the coarse/sand grain-size fraction of 63 µm to 2 millimetres is mainly made up of planktonic foraminifera, as it is in the open ocean (Fischer and Wefer, 1999). Given the control of prevailing water body energy on the grain-size distribution, variations (coarsening/fining) may additionally hold information on distance to land and sea-level fluctuations in southern Japan Sea settings such as Site U1427, via interruptions to the inflow of the TWC (see chapter 2, section 2.4).

3.5.9 (Semi-quantitative) facies description

A semi-quantitative, light-microscopic facies description was done on selected samples that contributed to the foraminiferal $\delta^{18}O_{Uvigerina\ spp.}$ record to support the results of the bulk sediment geochemical analyses. Details of the facies description can be found in appendix A and photographic examples are available in section 5.3.4, however these are limited in their resolution and estimated scale as they were solely produced to provide a visual aid.

In 112 samples the contained particles (>150 µm) were identified and counted. Samples were selected by showing the largest difference in TOC (section 3.5.2) and being located at suspected glacial-interglacial transitions, then gaps between samples were filled in. Seven samples, containing abundant land-plant derived organic matter, were identified to be used in the creation of the terrestrial organic $\delta^{13}C_{org}$ endmember model (section 3.5.3). The abundance of such large (>150 µm) land-plant material in itself is a useful information as it suggests high TOC values may not be directly linked to marine productivity only but reflect a mixed terrigenous-marine TOC signal.

3.5.10 Stable isotope analyses ($\delta^{18}O$, $\delta^{13}C$) on foraminiferal calcite

Stable isotope records ($\delta^{18}O$, $\delta^{13}C$) of planktonic and benthic foraminiferal calcite can be used to reconstruct oceanic currents, carbon storage (in oceans), primary productivity and changes in global ice-volume and/or temperature (e.g Raymo et al., 1997; Elderfield et al., 2012; see also chapter 2, section 2.3.2). The $\delta^{18}O$ foraminiferal calcite of the shell is controlled by temperature and the oxygen isotope composition of the surrounding sea water at the time of calcification, which is

primarily controlled by global ice-volume and water salinity (chapter 2, section 2.2; e.g. Emiliani, 1955; Ruddiman, 2001d; Lisiecki and Raymo, 2005; Maslin and Swann, 2006).

At deep water sites, planktonic foraminifera $\delta^{18}O$ values are influenced by local effects such as sea surface temperature and possible salinity fluctuations, while benthic foraminiferal $\delta^{18}O$ values are mainly controlled by global ice-volume/temperature, which makes them ideal to correlate across sites and very useful for the generation of chemo-stratigraphic age models (see figure 2.4; Emiliani, 1955; Lisiecki and Raymo, 2005; Ravelo and Hillaire-Marcel, 2007). Typically, there is an inverse relationship between temperature and $\delta^{18}O$ in foraminiferal calcite, for most foraminifera a temperature decrease of 1 ºC leads to a $\delta^{18}O$ increase between +0.2 and +0.25 ‰ (Maslin and Swann, 2006; Ravelo and Hillaire-Marcel, 2007; Raymo et al., 2018 and references within). In Elderfield et al. (2010) a transfer function of +0.25 ‰/ºC was used for *Uvigerina spp*..

The relationship between sea water salinity and foraminiferal $\delta^{18}O$ is in general a 2 ‰ change in salinity results in a 1 ‰ change in $\delta^{18}O$ (Broecker, 1989). While salinities in the open ocean are fairly constant (~35 ‰), the modern TWC salinity at the TSS varies with seasons between ~31-34.6 ‰ (section 2.4.1), suggesting that modern annual salinity variations in the Japan Sea can impact on $\delta^{18}O$ records of planktonic and perhaps shallow-water benthic foraminifera, such as at Site U1427. This needs to be considered, as in this study, a benthic $\delta^{18}O_{\textit{Uvigerina spp.}}$ record is established in order to improve the age model of Site U1427 through a comparison with an open ocean reference stack (Lisiecki and Raymo, 2005).

The stable carbon isotope ($\delta^{13}C$) data is commonly produced alongside the measurement for $\delta^{18}O$ of a sample. Carbon has two isotopes which occur in different abundances on Earth ^{12}C (98.89 %) and ^{13}C (1.11 %) (Nier, 1950), and are present in solids such as calcite and organic matter as well as in gaseous phases such as CO_2, CH_4. Carbon isotope records are of interest in palaeo-climatology because they provide information on the carbon cycle (Emiliani, 1955), though the records can be a mix of signals from marine productivity, ocean circulation and carbon storage in the oceans (Maslin and Swann, 2006), making them challenging to interpret.

The $\delta^{13}C$ of marine calcite is primarily controlled by the dissolved inorganic carbon in the water from which it precipitates, which is controlled by a process called

the biological pump. The biological pump (re-)distributes dissolved inorganic carbon and nutrients in the oceans, effectively mixing deep and shallow water pools, via upwelling and pathways of phytoplankton in the ocean, and playing a key part in the drawdown and release of CO_2 into the atmosphere. Phytoplankton preferentially utilises the light ^{12}C isotope, leaving the surrounding (surface) ocean waters enriched in ^{13}C (e.g. Park and Epstein, 1960; Wefer et al., 1999). After death, the phytoplankton sinks through the water column and becomes embedded in the sediments. Part of the phytoplankton remineralises in the water column and can be decomposed in the sediments if oxygen is available, releasing the light ^{12}C back into the surrounding deep waters. Therefore, high marine productivity and high remineralisation rates lead to greater differences between surface and deep water masses, leaving the photic zone (deep waters) relatively depleted (enriched) in nutrients, ^{12}C and CO_2 (figure 3.10).

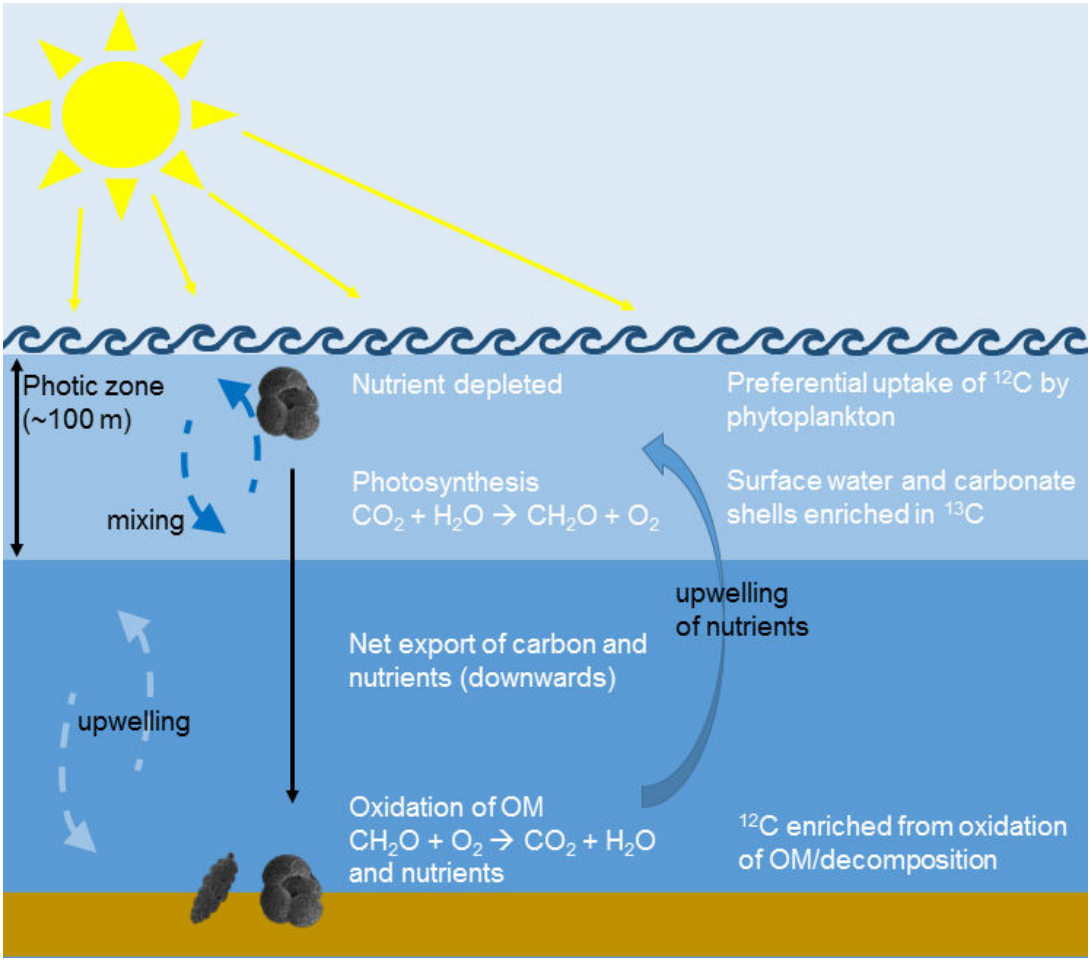

Figure 3.10. Schematic illustration of the biological pump in the oceans (modified after Ruddiman, 2001e).

The pathways of carbon in the ocean is however more complex than this. Carbon released from OM decomposition/remineralisation, together with nutrients, can be transported back to the photic zone via upwelling currents, increasing nutrients and lowering $\delta^{13}C$ in the surface waters (Mackensen and Licari, 2003, and references within). Hence, planktonic and benthic foraminiferal $\delta^{13}C$ is a mix of surface productivity (nutrient availability), remineralisation of OM and oxygen availability in the water column (e.g. Wefer et al., 1999; Maslin and Swann, 2006).

In this study, the planktonic isotope records were added to verify the identification of glacials and interglacials, particularly in the intervals between 300-395 m and ~460-525 m (see chapter 6, section 6.1). While the initial aim was to create planktonic $\delta^{18}O$ records with a similar resolution and at the same depths as $\delta^{18}O_{\textit{Uvigerina spp.}}$, this could not be achieved due to the absence of the selected planktonic species shells at certain depths. In order to increase the resolution, it has been tested in the framework of this thesis whether the two planktonic species' isotope records show such similarity that they may be merged into a single $\delta^{18}O_{planktonic}$ and $\delta^{13}C_{planktonic}$ record, hence increasing temporal resolution.

In total 210 samples were analysed for benthic isotope records (including 36 duplicates showing rsds. of ~0.08 ‰ on for both $\delta^{18}O_{\textit{Uvigerina spp.}}$ and $\delta^{13}C_{\textit{Uvigerina spp.}}$ (maximum rsd. $\delta^{18}O$ = 1.08 ‰ and $\delta^{13}C$ = 1.05 ‰), evenly spaced (1 m CSF-A) between 250-345 m (CCSF-D) and doubled (0.5 m CSF-A) below 345 m as a result of increased complexity of the proxy records (see subsequent chapters 4, 5 and 6). In addition to the down-core samples at Site U1427, a surface sample of the nearby site KR15-10, Site WB10 (section 3.3) was used to gather modern reference values.

For the planktonic foraminiferal records, 80 samples were analysed from the intervals 300-395 m and 460-525 m selecting samples that had a result for *Uvigerina spp*. isotope analysis and sufficient amounts of both or either *G. bulloides* and/or *N. pachyderma* (s) to allow for the isotope analysis and a diagenesis study (see section 3.5.11). Of those samples 41 contain *G. bulloides*, allowing 6 duplicate analyse and showing an average rsd. of 0.09 ‰ for $\delta^{13}C$ and $\delta^{18}O$, with maxima rsd. of 0.2 ‰ for both. Further 41 samples contain *N. pachyderma* (s), with sufficient amount of shells allowing 1 duplicate and showing an average rsd. of 0.02 ‰ for $\delta^{13}C$ and $\delta^{18}O$, with maxima rsd. of 0.02 ‰. In 27 samples, isotope values for both *G. bulloides* and *N. pachyderma* (s) were measured (both species present) allowing to compare the

isotopic offset in $\delta^{18}O$ and $\delta^{13}C$ between the two species. The average interspecies $\delta^{13}C$ and $\delta^{18}O$ offsets are 0.6 ‰ and <0.1 ‰ respectively. This offset in $\delta^{18}O$ is smaller than the maximum standard deviation and, since both records show similar trends and patterns (determination coefficient of $r^2 = 0.36$), they could be combined into a single $\delta^{18}O_{planktonic}$ record with a higher temporal resolution by normalising the records, i.e. setting the average $\delta^{18}O$ of each record to be zero, *c.f.* Bassinot et al. (1994) (chapter 6, section 6.3.1; Takuya Sagawa, pers. coms.). The interspecies offset in $\delta^{13}C$ is larger than the maximum standard deviation so the planktonic $\delta^{13}C$ records should not be merged (Takuya Sagawa, pers. coms.).

Each foraminiferal isotope analysis required ~50-100 micro-grams (µg) carbonate corresponding to 8-15 cleaned *Uvigerina spp.*, 5-30 *G. bulloides* and 6-40 *N. pachyderma* (s) shells. There is no standardised preparation protocol which in the past led to some issues in the comparability of records (Jones, 2014; Schonfeld, 2012, and references within). In order to enable a comparison and possible future merging of the isotope records from the upper ~250 m (Sagawa et al., 2018 and unpublished data) and lower ~250 m (this study) of Site U1427, the same laboratory protocol as used by Sagawa et al. (2018 and pers. coms.) was applied. The protocols only differ in the ultrasonic cleaning which Sagawa et al. did on crushed shells while here whole shells were cleaned.

After freeze-drying, deionised water (DI) was added and the samples were put on an orbital shaker for a few hours to disintegrate. Wet sieving using DI water was applied to remove the <63 µm grain-size fraction. The coarse fraction was then dried at low temperature (<50 ºC) and dry sieved on 150 µm mesh to gather the >150 µm fraction for isolation of the foraminifera shells (see figure 3.6). Whole, non-discoloured, white shells were isolated using a binocular light microscope, and cleaned in Eppendorf vials using a few drops of DI water and agitation in an ultrasonic bath for 20-30 seconds. As soon as the foraminifera had settled the DI water was removed and replaced, repeating this step several times until the water looked clean and there were no particles stuck to the outside of the shells. After cleaning the shells were dried at <50 ºC temperature. Analyses were undertaken at the NERC Isotope Geosciences Laboratories (Keyworth) using an IsoPrime dual inlet isotope ratio mass spectrometer plus multi-preparation device. A review of the basic measurement principle can be found in Hoefs (2004). In an automated process the foraminifera were treated with 90 ºC anhydrous phosphoric acid, which leads to the

release of CO_2 and other gaseous phases. The CO_2 gas is cleaned, removing other gaseous phases, and passed into the MS, which determines the isotope composition of the material. The computerised process automatically calculates deviations to the VPDB-scale (Vienna-PeeDee belemnite; international reference standard) through comparison of a laboratory standard (Carrara marble, KCM) against an international reference standard (white marble of unknown origin) (IAEA, 2013). In a final step the Craig correction (Craig, 1957) was applied to account for the rare occurrence of the ^{17}O isotope (chapter 2, section 2.2). All foraminiferal isotope data is reported in the δ-notation against VPDB (see section 3.5.2).

3.5.11 Diagenesis inspection of foraminifera shells

One complication impacting all marine calcite-based stable isotope records, including foraminifera, is their potential for post-depositional diagenetic alteration, which can modify the original palaeoenvironmental signals ($\delta^{18}O$, $\delta^{13}C$; e.g. D'Hondt and Arthur, 1996; Pearson et al., 2001; Wilson et al., 2002; Sexton et al., 2006; Sexton and Wilson, 2009). The effects of diagenesis are best documented in the "cool-tropics paradox" (D'Hondt and Arthur, 1996; Wilson and Opdyke, 1996). In early oxygen isotope records of the Cretaceous, based on tropical planktonic foraminiferal calcite, suggested sea surface temperatures (SST) would have been similar to today or even cooler during this greenhouse period (D'Hondt and Arthur, 1996). This stood in contradiction to other lines of evidence that all pointed towards much higher Cretaceous temperatures in a greenhouse world (e.g. Huber et al, 1995). In comparison, the planktonic $\delta^{18}O$ records even suggested cooler tropical SSTs than at higher latitudes, with extratropical Cretaceous SSTs indicating temperatures much higher temperatures than modern (Huber et al, 1995).

It became evident that what led to these cool tropical SSTs was diagenetic alteration of the foraminifera shells, impacting on the $\delta^{18}O$ records. The planktonic foraminifera used to generate the tropical $\delta^{18}O$ records had undergone diagenesis in the form of partial dissolution and replacement of the original organically produced calcite with inorganically precipitated calcite while embedded in the sediment giving them a frosty appearance under the light microscope (Schrag, 1999). The new diagenetic calcite records the $\delta^{18}O$ signal of the surrounding bottom water, which is much colder than the surface water, which the original foraminiferal calcite records, especially in tropical settings. The Cretaceous SST contradictions were overcome

when $\delta^{18}O$ records based on well preserved (glassy) Cretaceous planktonic foraminifera produced much higher SST estimates (Norris and Wilson, 1998; Pearson et al., 2001; Wilson and Norris, 2001; Wilson et al., 2002; Sexton et al., 2006; Edgar et al., 2013; 2015).

The effect of diagenesis on planktonic foraminifera $\delta^{18}O$ records has since been well studied (e.g. Pearson et al., 2001; Wilson et al., 2002; Sexton et al., 2006; Edgar et al., 2015), as these organisms precipitate their original calcite in warmer water masses (containing lower $\delta^{18}O$ values) than the post-depositional, diagenetic calcite, which contains higher $\delta^{18}O$ values. In addition, warm water planktonic foraminifera also have thinner shell-walls and larger pores than those of cooler waters, leading to them being even more susceptible to diagenetic alteration (Kozdon et al., 2011). As a result, the addition of diagenetic calcite layers pushes planktonic $\delta^{18}O$ records towards higher values (e.g. D'Hondt and Arthur, 1996; Kozdon et al., 2011; Edgar et al., 2015), suggesting lower temperatures.

The effect of diagenesis on benthic foraminifera $\delta^{18}O$ records is less well studied. Benthic foraminiferal records are considered to be less susceptible to the effects of diagenetic alteration since they, in general, produce more heavily calcified shells and both the original foraminiferal and diagenetic calcites are precipitated in similar waters conditions in terms of temperature and $\delta^{18}O$ (Sexton and Wilson, 2009; Edgar et al., 2015), making benthic foraminifera more robust $\delta^{18}O$-recorders (e.g. Schlanger and Douglas, 1974; Matter, 1974; Edgar et al., 2013; 2015). The $\delta^{13}C$ records experience less impact of diagenetic alteration as it has a smaller relationship with temperature (e.g. Maslin and Swann, 2006), and oxygen can exchange easier than carbon when in contact with water (Melanie Leng, pers. coms.).

Diagenetic shell alterations can sometimes be identified using a light microscope, showing as e.g. round holes in shells caused by dissolution or as discolouration to yellowish shades caused by heavy encrustation. Often, however, it is not possible to identify diagenetic alterations on visual inspection as this does not pick up on shell internal diagenetic alterations, such as recrystallisation and other effects which are not uniformly distributed within shells (Kozdon et al., 2011). As a result, higher magnification using scanning electron microscopy (SEM) is needed. Examples of the appearance of diagenetic alteration in SEM studies are given in publications for

benthic (e.g. Lamb and Miller (1984; Casazza, 2012; Edgar et al., 2013) and planktonic foraminifera (e.g. Fox and Wade, 2013; Edgar et al., 2015).

Diagenetic alteration has three main manifestations: (i) dissolution of the primary shell calcite, (ii) encrustation of surfaces with secondary (inorganic) calcite layers, and (iii) recrystallisation within the shell walls. Dissolution can create holes, remove the final chamber and make the shells more fragile by stripping away calcite layers, leading to fragmentation (Collen and Burgess, 1979) and crumbling when cleaned using ultrasonic agitation (Pearson et al., 2015). The outer surfaces can appear rough instead of smooth and pores can be enlarged (Fox and Wade, 2013). Diagenetic calcite overgrowths can precipitate on inner and outer shell surfaces and as infills to the shells, and they can obscure surface ornamentations such as pores, apertures and costae, which can prevent species identification (Pearson and Burgess, 2008; Fox and Wade, 2013). Recrystallisation is the replacement of the original micro-granular calcite crystals in the wall structure (within the shell walls) with larger, blocky crystals of inorganic, diagenetic calcite (Lamb and Miller, 1984; Pearson and Burgess, 2008, Fox and Wade, 2013; Voigt et al., 2016).

For the study of diagenesis using the SEM, well-preserved shells of *Uvigerina spp*., *G. bulloides* and *N. pachyderma* (d) were prepared from the surface sample (section 3.3), assuming they would have undergone the least diagenetic alteration due to their recent deposition. Eight down-core samples containing sufficient amounts of *Uvigerina spp*., *G. bulloides* and/or *N. pachyderma* (s) to allow isotope analysis and diagenesis study were selected from geochemical and grain-size extremes, e.g. high/low TOC and $CaCO_3$ contents and coarse/fine-grained sediment matrix., and from the contained shells the worst-preserved ones were selected (see appendix B, table I). This approach ensured the endmembers, best and worst preserved, could be analysed and compared.

The foraminiferal shells were prepared as for the stable isotope analysis (section 3.5.10) and for each sample 3-5 shells were then mounted on adhesive SEM stubs (where possible aperture facing up) and gold coated. The SEM images were taken on a JEOL ESM XL30 high vacuum electron microscope with secondary electron detector scanning at Newcastle University. For benthic foraminifera, images were taken using 20 kV voltage, and magnifications of 110-150x for surfaces and up to 3700x for internal wall structures. For planktonic foraminifera, images were taken

using 10 kV, and magnifications of 150-250x for surfaces and up to 5000x for internal wall structures.

Two samples were additionally analysed using energy dispersive x-ray (EDX) spectroscopy at Newcastle University on a HITACHI S2400 device with Oxford Instruments Inca ultra-thin window x-ray detector, using 20 kV voltage and magnifications of up to 5000x. This was to investigate surface areas that looked particularly encrusted with potentially diagenetic calcite layers. While EDX yields poor-quality imaging, it can give a qualitative to semi-quantitative evaluation of the contained elements in a sample through relative comparison of peak heights. This allows differentiation between primary and secondary calcites, as the latter are enriched in magnesium (Mg, Rosenthal and Boyle, 1993; Martin and Lea, 2002; Sexton et al., 2006). For these analyses the SEM stubs containing the shells were carbon coated to improve surface conductivity.

Imaging followed the approach by Fox and Wade (2013) investigating the external surfaces and ornamentation (at low and high resolution) before cracking the shells open using either a glass plate (*Uvigerina spp., N. pachyderma (s)*) or a picking needle (*G. bulloides*), to investigate the internal surfaces and wall-structure in cross-sections in high-resolution. The fragments were then inspected for alteration of the internal surfaces and wall-structure in cross-sections, for which the gold coating was repeated. The imaging results of the combined SEM/EDX study are illustrated in appendix B.

3.5.12 Trace element analysis on benthic foraminifera, Mg/Ca ratios

Deciphering temperature/ice volume from local salinity effects on foraminifera-based $\delta^{18}O$ records requires an additional proxy for either temperature or salinity, such as Mg/Ca ratios (Rosenthal, 2007; Sosdian and Rosenthal, 2009; Elderfield et al., 2012; Raymo et al., 2018). It has been shown that the $\delta^{18}O_{Uvigerina\ spp.}$ records of Site U1427 are affected by strong local salinity fluctuations (chapter 2, section 2.4; Sagawa et al., 2018), overriding the global temperature/ice volume-signal during glacials (chapter 2, sections 2.2, 2.4). As discussed, this makes the identification of G-IG cycles challenging and potentially inhibits comparison with open ocean $\delta^{18}O$ reference stacks, used to improve the site's age model (section 3.5.10, chapter 4).

One widely applied proxy for the determination of palaeo-ocean temperatures is the ratio of magnesium (Mg) to calcium (Ca; Mg/Ca ratios) of foraminiferal calcite

(Nürnberg, 1995; Rosenthal et al., 1997; Elderfield and Ganssen, 2000; Toyofuku et al., 2000; Sosdian and Rosenthal, 2009; Elderfield et al., 2010; Elderfield et al., 2012; Raymo et al., 2018). The substitution of Ca by Mg into calcite ($CaCO_3$) is temperature dependent, and with increasing temperature more Ca is replaced by Mg (Katz, 1973; Nürnberg et al., 1996; Rosenthal et al., 1997; Fischer and Wefer, 1999; Lear et al., 2000, 2002; Anand et al., 2003; Elderfield et al., 2006; Rosenthal, 2007), increasing Mg/Ca ratios by about 9% Mg per 1 ºC temperature increase (Nürnberg et al., 1996; Lea et al., 1999; Elderfield and Ganssen, 2000), and showing a 0.1 mmol/mol increase per 1 ºC in *Uvigerina* spp. following Elderfield et al. (2010, 2012).

Determining the Mg/Ca ratios in foraminiferal shells can be hindered by contamination such as adhesive clay and/or organic matter, and by diagenetic calcites which can affect the relationship between Mg/Ca ratios and temperature (section 3.5.11). The addition of diagenetic calcite overgrowths increases Mg/Ca ratios by contamination with Mg-enriched diagenetic calcite coatings (Rosenthal and Boyle, 1993; Martin and Lea, 2002; Sexton et al., 2006). Therefore, the presence of diagenetic calcite coatings must be investigated and a thorough pre-analysis cleaning procedure must be applied and adapted accordingly.

The cleaning protocol leading to reliable Mg/Ca records is the main crux when comparing Mg/Ca records with each other, as there is no standardised cleaning protocol. The most commonly applied procedures are the cadmium (Cd-) cleaning protocol (Boyle and Keigwin, 1985), the magnesium (Mg-) cleaning protocol (Barker et al., 2003), and adaptations of these to fit specific sample material.

The Mg-cleaning protocol includes clay removal, oxidation and leaching of the sample material to remove contamination by clay, silicates and organic matter (Barker et al., 2003). It does not include a cleaning step that would remove diagenetic calcite coatings on the shells. For such cases the Cd-cleaning protocol after Boyle and Keigwin (1985) is better suited as an additional reductive cleaning step is thought to reduce the amount of diagenetic calcite coatings (Boyle and Keigwin, 1985; Martin and Lea, 2002). The more rigorous Cd-cleaning was initially developed to measure cadmium in foraminiferal calcite, which occurs at much lower concentrations than magnesium (Boyle, 1981; Boyle and Keigwin, 1985). Subsequently, it was applied to prepare samples for analyses of other element/Ca ratios to reconstruct other physical and chemical ocean water properties and was

often modified during this process (e.g. Russell et al., 1994; Rosenthal et al., 1997; Marchitto et al., 2000).

This Cd-cleaning protocol is however not without criticisms either because of the lower solubility of (Mg-rich) diagenetic calcite overgrowths compared to foraminiferal calcite (Brown and Elderfield, 1996). This aggressive cleaning protocol therefore leads to greater loss of material, including calcite, and it potentially alters the foraminiferal calcite Mg content and hence the Mg/Ca ratios (Brown and Elderfield, 1996; Yu et al., 2007; Rosenthal, 2007; Greaves, 2008). The lower Mg/Ca ratios obtained may be interpreted as a sign of cleaner shells but, as described above, this may not be seen as a criteria for robust cleaning, but instead may be due to preferential dissolution (*op. cit.*).

The foraminiferal Mg/Ca palaeothermometry proxy has been successfully applied as a quantitative estimate of palaeo-ocean temperatures in a wide range of palaeoenvironmental studies (e.g. Nürnberg, 1995; Rosenthal et al., 1997; Rosenthal, 2007; Elderfield and Ganssen, 2000; Lea et al., 1999; Lea, 2003; Elderfield et al., 2012; Toyofuku et al., 2000), but has not been applied in the Japan Sea due to the poor preservation of foraminifera shells found in previously drilled, deeper sites. The shallow-water Site U1427 (section 3.2), with its significantly better preservation of shells, provides a unique opportunity to create Mg/Ca records. At this site, the Cd-cleaning protocol was applied to generate a Mg/Ca record for the upper ~250 m in sediment core (Sagawa, unpublished data), whereas here the Mg-cleaning protocol after Barker et al. (2003), with slight alterations as described in Elderfield et al. (2012), was used. This was done because (i) the diagenesis study (section 3.5.11 and appendix B) revealed no evidence of Mg-rich diagenetic coatings on the shells, making reductive cleaning redundant, (ii) few samples provided sufficient calcite for both stable isotope and trace element determination, hence, omitting the aggressive and calcite dissolving reductive cleaning step allowed more samples to be analysed, and (iii) the aim of the Mg/Ca record is to gather relative palaeo-temperature differences to clarify the identification of glacials and interglacials. Even though different cleaning protocols result in different measured Mg/Ca the relative changes are not affected by the cleaning protocol (Rosenthal et al., 2004). To confirm the suitability of this procedure, duplicate analyses will be made by Japanese colleagues (Takuya Sagawa, Kanazawa University) using the Cd-cleaning protocol (results pending).

A total of 57 down-core samples, evenly spaced across two intervals (300-395m and 460-525 m) were analysed. All samples contributing to the $\delta^{18}O_{Uvigerina\ spp.}$ record (section 3.5.10), had sufficient numbers of *Uvigerina spp.* to allow for Mg/Ca, isotope and SEM analysis, and were located at geochemical extremes, suggesting a spread across glacials and interglacials alike. One surface sample (section 3.3) was determined for modern Mg/Ca values to test the applied temperature calibration (Sagawa et al., in prep, see below). Subsequent analyses were undertaken within the frame of a European Consortium for Ocean Research Drilling (ECORD) Research Grant and carried out with pioneers of foraminiferal Mg/Ca palaeothermometry at the Godwin Laboratory for Palaeoclimate Research at the University of Cambridge.

Each analysis required ~300 µg uncleaned calcite which is approximately 10-30 *Uvigerina* spp. shells of >250 µm, the same grain-size fraction and genus as used for the upper ~250 m of Site U1427 (Takuya Sagawa, unpublished data). At an average calcite recovery rate>50 % ~150-200 µg cleaned calcite were used for each analysis. The same morphotype as for isotope analyses (section 3.5.7) was isolated, counted and weighed before being crushed between two glass plates to open the chambers. The first cleaning step removes clays. It uses DI water and ultrasonic agitation and is the most crucial for Mg/Ca determination because large contamination signals can arise from high Mg concentration in clays (Barker et al., 2003; Lea, 2003; Rosenthal, 2007), especially in the analyses of thin-walled species (Greaves, 2008). The second step oxidises and removes organic matter using hydrogen peroxide, with sodium hydroxide added in order to maintain a high pH to minimise calcite dissolution. Then remaining coarse silicates are removed using a fine brush under a microscope. The efficiency of this and the above steps can best be tested under microscopic inspection as the calcite should be glassy and completely colourless and without dark particles sticking to any surface. A final step of a weak leach using 0.001 M nitric acid removes secondary Mn-rich overgrowths (Boyle, 1983; Rosenthal, 2007), before the samples are dissolved in nitric acid.

Analyses were carried out on an Agilent inductively coupled plasma-optical emission spectrophotometer (ICP-OES). For quality control two reference solutions were analysed with the samples, one internal standard (Soln R3) and one international external standard (JCt-1). These both showed instrumental reproducibility, expressed as rsd. below 0.5 %. The accuracy of Mg/Ca determinations has been established by interlaboratory studies (Greaves et al., 2008;

Rosenthal et al., 2004) and was confirmed here by replicate analyses of standard JCt-1 where results agree with those published elsewhere (Hathorne et al., 2013). Reproducibility between samples was tested on seven duplicates, which were split before cleaning and showed rsd. below 5 %. Following the Cambridge laboratory protocol (Elderfield et al., 2012) an intensity ratio calibration after de Villers et al. (2002) was carried out, measuring each sample twice. In an initial run a diluted subsample was analysed to determine Ca concentration, then the samples were diluted to constant Ca-concentrations of 100 ppm to determine the Mg/Ca ratios (*c.f.* de Villers et al., 2002). A set of contamination-indicating elements (Al, Ba, Fe, K, Mn, Na, Si, Ti, Zn) were monitored simultaneously during each run. High concentrations of these elements, originating from imperfect cleaning or malhandling during cleaning/dissolution, indicates samples are also likely to be contaminated by Mg from a non-foraminiferal calcite source (*c.f.* Barker et al., 2003). Three samples showed high concentrations of contamination-indicating elements and were repeated, but still showed high levels of contamination and were not used in the interpretation. Overall, slightly higher than usual iron concentrations occurred in all down-core samples and the surface sample, which is typical for Japan Sea sediments and suggests these elevated values reflect a local, Japan Sea influence rather than a cleaning protocol issue (Tada et al., 2015a,b; Mervyn Greaves, pers. coms.).

3.5.13 Temperature estimates from foraminiferal Mg/Ca ratios

The Mg/Ca data are crucial for the corroboration of glacials and interglacials defined by the $\delta^{18}O_{Uvigerina\ spp.}$ record (see chapters 4 and 6). Neither the surface sample (section 3.3) nor the down-core foraminifera shells (section 3.5.11) showed diagenetic calcite overgrowths, which was confirmed by little sign of contamination-indicating elements in the Mg/Ca analyses (section 3.5.12). Hence, it was found that the Mg-cleaning protocol leads to trustworthy Mg/Ca ratios and can be used in the calculation of relative temperature changes.

In order to estimate palaeo-water temperatures from the Mg/Ca ratios a calibration equation is needed. Instead of an anticipated temperature-depth transect for the area near Site U1427 (see section 3.3, figure 3.5), preliminary data from 16 core-top sampling sites across a depth and bottom-water temperature transect in the Japan Sea (rose bengal stained *Uvigerina spp*., >150µm, 147-656 m water depth, 0.44-4.28 ºC bottom water temperature range, constant salinity 34.09-34.33 ‰;

Kimoto and Sagawa, unpublished data) were used to generate a Mg/Ca-temperature calibration (figure 3.11).

Linear and exponential calibration equations in the given temperature range are very similar, and so the linear regression (best fit) was applied:

$$\text{Temperature} = \left(\frac{Mg}{Ca} - 0.637\right) / 0.089\ [°C] \qquad \text{(eq. 3.8)}$$

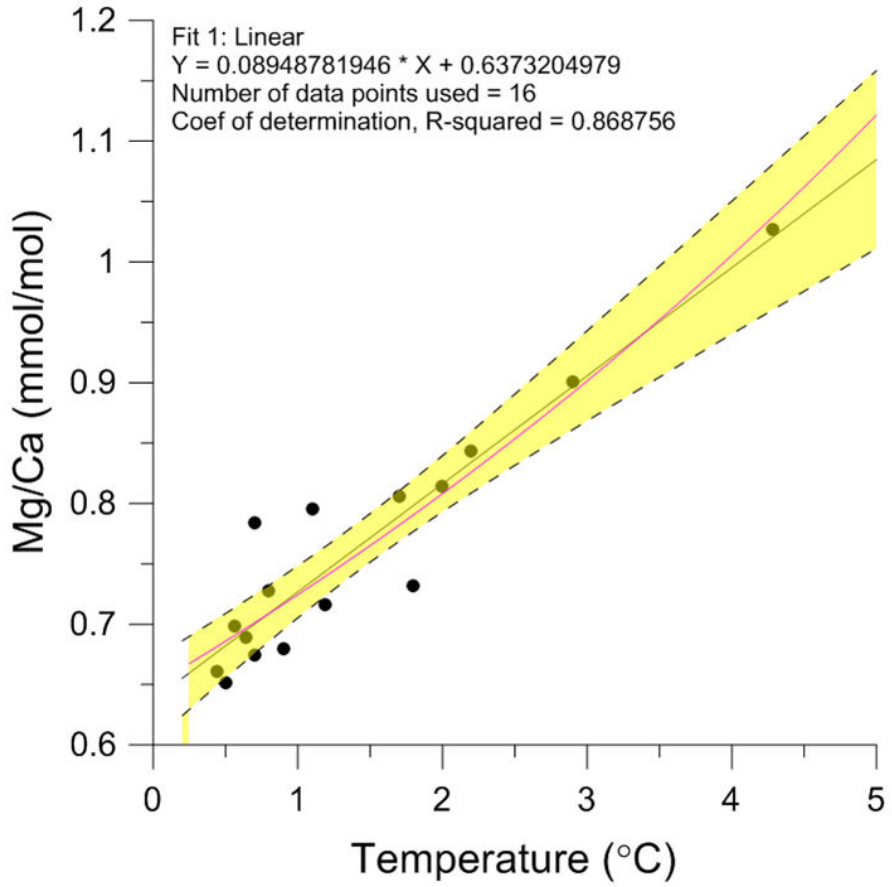

Figure 3.11. Core-top calibration data by Kimoto and Sagawa (unpublished data) and own calculation of a best fit (linear regression line, black) with 95 %-confidence intervals (yellow area). For comparison the best fit exponential regression line is shown as well (pink).

The calibration equation was tested by comparing the Mg/Ca-derived bottom-water temperature at the surface sample site (+1.2 °C) with in-situ measured bottom-water temperature (+1.74 °C, Sagawa et al., 2015). This offset can be explained by the combined error ranges of the in-situ temperature measurement and the Mg/Ca preparation and analysis on one hand, and the difference of the water masses used in the measurements on the other hand, with the latter potentially having the largest influence on the offset. The in-situ measured bottom water temperature is a snapshot

of the temperature in lowermost water column during a summer day on 4th July 2015 (Sagawa et al., 2015), while the Mg/Ca-based temperature estimate is a record of the water circulating in the uppermost sediment column, the habitat of *Uvigerina* spp., covering several years (lifespan of an *Uvigerina*, timespan contained in each 1 cm-wide sediment sample). Therefore it can be expected that the summer in-situ temperature measurement returns a higher value than the long-term foraminifera-based Mg/Ca temperature estimate.

An issue resulting from the application of this core-top calibration is that some down-core Mg/Ca data of Site U1427 fall out of the calibration range. The Mg/Ca range of the core-top calibration is ~0.6-1.1 mmol/mol, while the down-core Mg/Ca range is 0.7-1.6 mmol/mol (see chapter 6, section 6.3.4), leading to potential errors that cannot be corrected for. Despite the potential underestimation of absolute temperatures as a result of Mg/Ca and temperature data of Site U1427 being out of the calibration range, the core-top calibration by Kimoto and Sagawa remains the best fit available at present, as it is specifically designed for the *Uvigerina* spp. of the Japan Sea and using the same preparation technique, i.e. grain-size fraction and morphotypes. While the difficulties in the core-top calibration affects absolute temperatures, which should be treated with some caution, the relative changes over G-IG cycles should not be affected and therefore the Mg/Ca temperature estimates still allow the differentiation between glacials and interglacials, needed within the framework of this study.

Chapter 4: Revised Age Model

4.1 Introduction

Fundamental to the successful of any palaeoenvironmental study is a solid age model. Only this enables comparisons with other sites and palaeoenvironmental studies, allowing us to put the findings in a wider context. Recent studies published from Site U1427 have improved the shipboard age model for the upper ~250 m (Tada et al., 2015b; Kamikuri et al., 2017; Gallagher et al., 2018; Sagawa et al., 2018; Tada et al., 2018; Saavedra-Pellitero et al., 2019) but chronological controls on the sediments below 350 m are still limited. Previous studies found sediments below 250 m encompass the MPT (Tada et al., 2015b; Sagawa et al., 2018) and as a result, this chapter aims to refine the existing age-depth constraints for the sediment interval >260 m, which is crucial for studying the MPT in the Japan Sea.

In order to increase the chronological control for sediments >260 m at Site U1427 this chapter aims to establish a foraminiferal calcite-based isotope chemo-stratigraphy, which is one of the most widely applied approaches in marine palaeoceanographic studies (see chapters 2 and 3). Establishing a foraminiferal $\delta^{18}O$ stratigraphy has so far been problematic in the Japan Sea as preservation of suitable microfossil material is hindered by post-depositional processes (chapter 2, section 2.4). At previously drilled deep water sites the isotope records are incomplete, often $\delta^{18}O$ lacking information from glacials caused by calcite dissolution due to the shallow CCD (chapter 2, section 2.4.4). Furthermore, if preserved, glacial $\delta^{18}O$ signals are often overprinted by local salinity (chapter 2, section 2.4.4). Site U1427 was selected to be drilled due to its shallow water position (in ~330m water depth) meaning it was positioned above the CCD throughout the MPT, and has continuous, high sedimentation rates which favour carbonate preservation (chapter 3, section 3.2). Previous studies have confirmed the excellent preservation of carbonate microfossils, showing only few foraminifera-barren zones (Tada et al., 2015b; Sagawa et al., 2018; Gallagher et al., 2018).

4.2 Methods

For details on the laboratory protocols and limitations please refer to chapter 3. See section 3.2.3 for the shipboard colour reflectance, b*, section 3.5.7 for the

description of the isolated benthic foraminifera, section 3.5.10 for the benthic foraminifera stable isotope analyses (particularly $\delta^{18}O_{Uvigerina\ spp.}$), and section 3.5.11 for the test on diagenetic alteration on the foraminifera shells.

4.3 Revision of the Age-Depth Relationship

4.3.1 Selection of age tie points from previous studies

During IODP Expedition 346 low resolution age tie points were identified based on biostratigraphy and the Brunhes-Matuyama palaeomagnetic reversal. From this a simple, shipboard age model was created for Site U1427 (figure 4.1a) (Tada et al., 2015b,c). The shipboard age model suggests the interval investigated here, 260-525 m CCSF-D, contains sediments deposited during the MPT (~1200-600 ka; chapter 2, section 2.3; Tada et al., 2015b).

Between 260-525 m seven age tie points, including one palaeomagnetic reversal, the Brunhes-Matuyama, at 781 ka, were identified on-board (table 4.1; Tada et al., 2015b). Neither the palaeomagnetic Jaramillio Subchron at 988-1072 ka *c.f.* Lisiecki and Raymo (2005) nor the Cobb Mountain, occurring at 1220-1240 ka *c.f.* Cohen and Gibbard (2011), were identified. These palaeomagnetic markers must be either located within a particularly difficult to interpret sediment section that contains large scatter in palaeomagnetic declinations and lack of core orientation or within a sediment void of which several occurred at greater depths due to sediment expansion (Tada et al., 2015b). Only robust age tie points were selected to use in the revised age model (see table 4.1).

Based on the shipboard age-depth model, sedimentation rates (SR) (figure 4.1b) were calculated as:

$$Sedimentation\ rate\ (cm/ka) = \left(\frac{(D_{deeper} - D_{shallower})}{(Age_{deeper} - Age_{shallower})}\right) / 10 \qquad \text{(eq. 4.1)}$$

where D denotes depth. The equation assumes a linear relationship/sedimentation rate between age tie points, which is a widely applied approach (Tada et al., 2015b,c), but it neglects the heavily bioturbated lithology, changes in the amount of terrigenous input over G-IG cycles and/or varying sediment densities/compaction, and hence results should be taken as estimates.

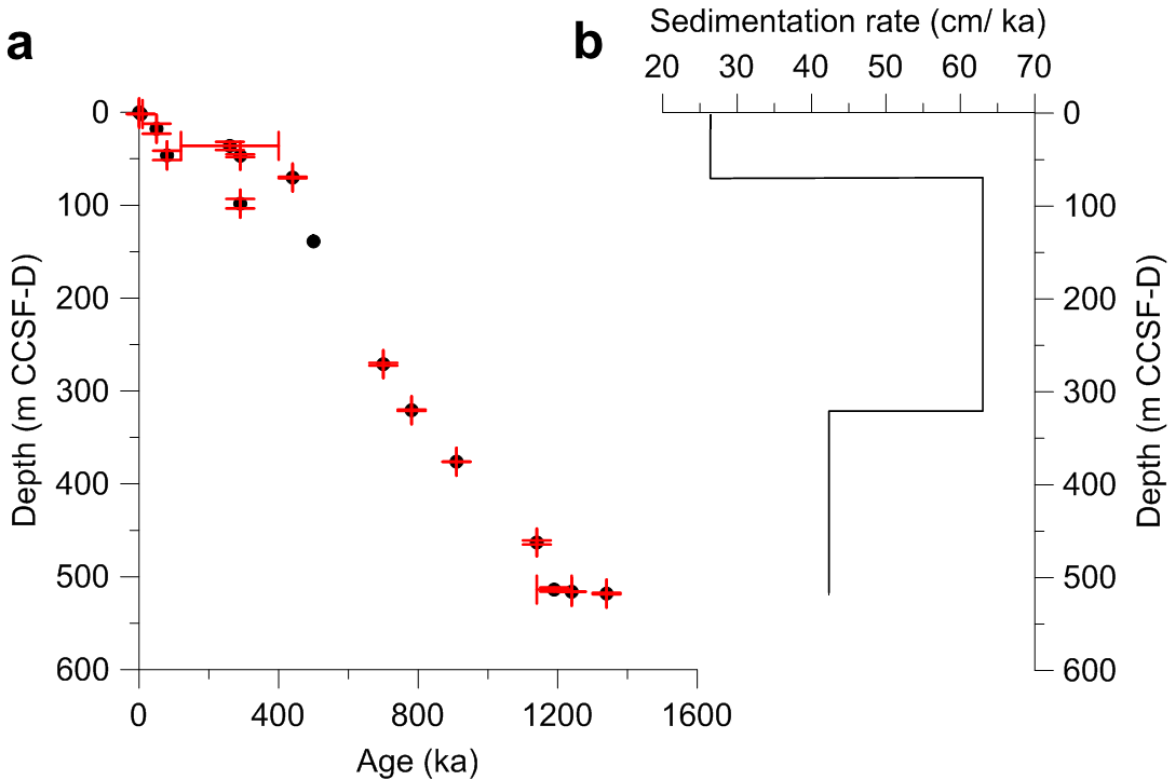

Figure 4.1. Shipboard age model for the entire core length of Site U1427 (after Tada et al., 2015b) and converted into the CCSF-D depth scale as used in this thesis. Figure 4.1a shows the depth-age relationship established on-board. Black dots represent shipboard age tie points (based on first and last occurrences of index fossils, coiling-ratio changes in planktonic foraminifera and palaeomagnetic markers), red bars indicate shipboard estimates of uncertainties in depth (vertical) and age (horizontal). Figure 4.1b shows sedimentation rates at Site U1427, as provided by Tada et al. (2015c).

A new benthic *Uvigerina* spp.-based $\delta^{18}O$ stratigraphy for the upper ~350 m of Site U1427 resolves some of the glacial periods (Sagawa et al., 2018). The age model presented in this thesis is based on a multi-faceted approach, combining age-depth markers with a correlation between the shipboard sediment colour reflectance index, b* (chapter 3, section 3.2.3) and $\delta^{18}O$ record of this thesis (higher (lower) $\delta^{18}O$ values corresponding to higher (lower) b* indices) and matching them to the LR04-stack for reference. The age model is confirmed by foraminiferal trace element analyses (chapter 6).

The b* record is interpreted as being driven by the abundance of biosilicious/ nannofossils-rich sediments, which correlate with high abundances of warm water radiolarian species, indicating a higher marine productivity (Tada et al., 2015b). The presence of warm water radiolarians indicate warmer seawater temperatures and are known to be closely linked to enhanced inflow of the TWC (chapter 2, section 2.4).

Following the current oceanographic model of the Japan Sea, such TWC ingressions occur predominantly during interglacial sea-level highstands (chapter 2, section 2.4; Oba et al., 1991; Tada 1994).

Based on the relationship between high (low) b* and higher (lower) sea-levels, and their associated ages meant that Sagawa et al. (2018) were able to link their benthic $\delta^{18}O$ record with glacial-interglacial cycles. As a result they were able to identify individual glacials and interglacials, and by comparing their record with the open ocean benthic foraminiferal $\delta^{18}O$ LR04 reference stack MIS 1-21 were identified (Sagawa et al., 2018).

Alongside the $\delta^{18}O$ record, Sagawa et al. (2018) also present a tephrochronology, where they correlate tephra layers between Sites U1426, U1427 and U1429 (figure 2.7). As a result of this tephrochronology, the revision of the age model presented here contains two tephrachronological layers, which were dated by correlation to Site U1426 and through previous studies of terrestrial-based sections where ages have been established. The tephra layer “Hkd-Ku” at 298.37m is dated to 756ka (Pickering et al., 1999) and the tephra layer “Ss-Pink” at 421.50-421.80m is dated to ~1050-1056ka (Tsuji et al., 2005), and are associated with the base and/or early stages of MIS 18 and MIS 30 respectively (Sagawa et al., 2018).

Stratigr. marker	Bioevent and epoch boundaries	Depth (m CCSF-A)	Depth (m CCSF-D)	Depth (+/- m)	Age (Ma)	Age (+/- Ma)	Age (ka)	Shipboard SR (m/ Ma)	Comments
Unit A1/A2		132.09	138.9		0.500		500	277.8	Tada et al., 2015b
PF	LO *N.k.* group	259.40	271.15	1.48	0.700	0.000	700	630.1	Tada et al., 2015b
Tephra	Hkd-Ku		298.37		0.756		756		Sagawa et al., 2018
PM	Bottom of C1n (B.M. bd)	308.96	320.72	0.75	0.781	0.000	781		Tada et al., 2015b
CN	LO *R.a.*	364.37	376.12	0.03	0.910	0.000	910	423.4	Tada et al., 2015b
Tephra	Ss-Pink		421.80		1.053		1053		Sagawa et al., 2018
CN	Bc *R.a.*	451.30		2.23	1.140	0.000	1140		Large error in depth; Tada et al., 2015b
PF	*N.p.* (d to s)	502.03		2.15	1.190	0.050	1190		Large error in depth; Tada et al., 2015b
CN	LO *G.*	504.33	516.08	0.15	1.240	0.000	1240		Tada et al., 2015b
CN	LO *H.s.*	506.29		0.75	1.340	0.000	1340		Outlier according to Tada et al., 2015b

Table 4.1. Compiled age tie points for the investigated interval of Site U1427 (after Tada et al., 2015b and Sagawa et al., 2018). All depths and ages are converted to the CCSF-D depth scale and to thousands years (ka) respectively. Errors in depth and age are given as "Depth (+/- m)" and "Age (+/- Ma)" in the respective columns. Shipboard sedimentation rates ("shipboard SR (m/Ma)") complement the table. The age tie points highlighted in red were not used in this thesis due to their large associated errors or being identified as outliers (see comments column).

Legend of stratigraphic marker types: Bt = Bottom, CN = calcareous nannofossils, d to s = dextral to sinistral coiling change, LO = last occurrence, PF = planktonic foraminifera, PM = palaeomagnetic, T = top of bed, tephra = tephra layer. Legend of bioevents: *N.k.* group = *Neogloboquadrina kagaensis* group, *R.a.* = *Reticulofenestra asanoi, N.p.* = *Neogloboquadrina pachyderma, G.* = *Gephyrocapsa, H.s.* = *Heliocosphaera sellii,* B.M. bd. = Brunhes/ Matuyama boundary.

4.3.2 Revised age-depth relationship

Based on the selected age tie points, presented in table 4.1, a new age-depth relationship was compiled (figure 4.2a). This allowed calculation of new SRs , which in general follow the shipboard trend, displaying highest SR of up to ~90cm/ka above 320 m, and a SR fluctuating between 30 and 50 cm/ka at greater depths (figure 4.2b, table 4.2; after equation 4.1). The true SR may have been more variable however, changing between age tie points that cannot be proven or disproven using the data gathered here. Tada et al. (2015b) suggested that SR may have changed over G-IG cycles with the variable amounts of terrigenous input. Further age tie points, perhaps generated in the future, would certainly create a more detailed picture of SR changes.

Depth interval (m CCSF-D)	Sedimentation rate (cm/ka)
138.90 - 271.15	66.13
271.15 - 298.37	48.61
298.37 - 320.72	89.4
320.72 - 376.12	42.95
376.12 - 421.80	31.94
421.80 - 516.08	50.42
516.08 - 540.27	48.37

Table 4.2. Calculated sedimentation rates with associated depth intervals as inferred from the revised age model.

4.3.3 Age estimates for analysed samples

Using the above revised age, depth and sedimentation rate framework (figure 4.2, table 4.1) allows for an interpolated age estimate for each analysed sample:

$$Sample\ age\ (ka) = \left(\frac{Age_{SR\ deeper} - \left(D_{SR\ deeper} - D_{sample}\right)}{SR_{deeper}\left(\frac{cm}{ka}\right)}\right) \qquad \text{(eq. 4.2)}$$

Not considering the effect of the heavy bioturbation the sediments have undergone (see chapter 3, section 3.2.2) the sample age estimates reveal the sediments date between ~1256 ka (~529 m) and 687 ka (~263 m), encompassing the MPT. Using an average SR of 50 cm/ka, each 1 cm thick sediment sample comprises sediments deposited over on average 20 years, with ~1-2 ka spacing between them, based on average sample spacing of 40 and 100 cm, respectively. The ages for all samples are presented in appendix A. However, there is significant uncertainty associated with each of these ages since they are calculated based on the

assumption of linear sedimentation rates and anchored by only six actual age markers over the studied ~275 m of sediment (table 4.1).

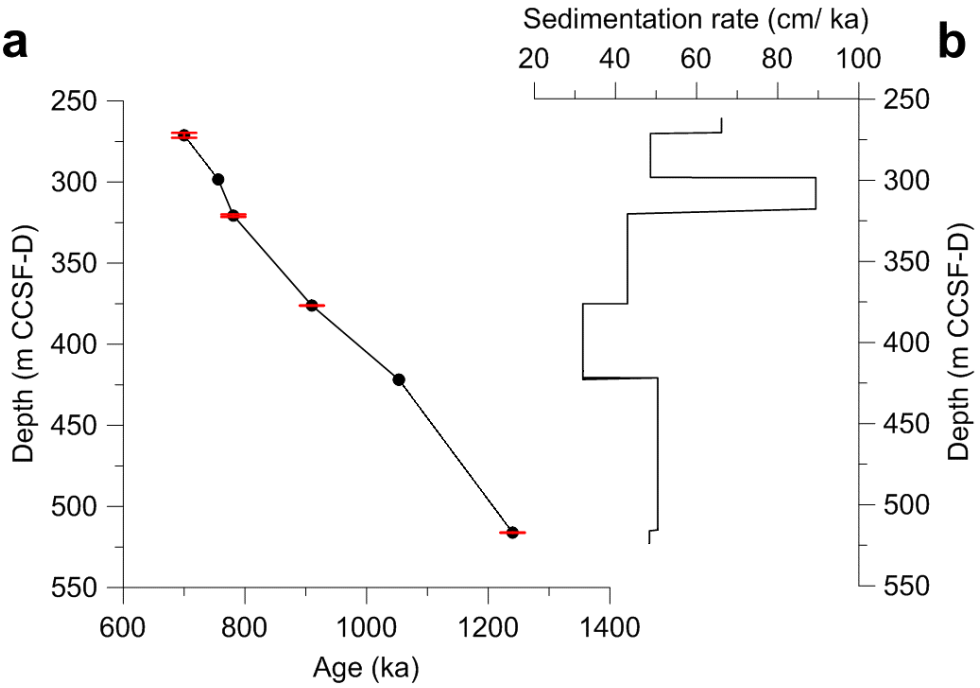

Figure 4.2. Revised age-depth-relationship (fig. 4.2a) and newly calculated sedimentation rates (fig. 4.2b) for the investigated interval of Site U1427. Black dots in figure 4.2a represent the selected age tie points (table 4.1), with red bars indicating their respective uncertainties in depth as given by Tada et al., (2015 b) and Sagawa et al. (2018). The uncertainties in age were set to be cero in Tada et al. (2015b) and are not provided for the two tephra layers in Sagawa et al. (2018), hence no error bars are shown.

For completeness, a sample age was also estimated for the surface sample (chapter 3, section 3.3), which encompasses the uppermost 1 cm of sediment and is deposited under a sedimentation rate of ~10-25 cm/ka (Sagawa et al., 2015). Using the above equation and assumptions the surface sample contains particles accumulated over the last 40-100 years.

4.3.4 Section summary and discussion

The assessment of the reliability of the available geochronological markers for the sediment interval 260-525 m of Site U1427 increased confidence in the MPT coverage of the selected sediment core section, dating approximately 1256-687 ka (section 4.3.3). Neither the Jaramillio Subchron nor the Cobb Mountain were identified must be located within a particularly difficult to interpret sediment sections or sediment voids (section 4.3.1). Newly calculated SRs are constant and show rates of ~30-90 cm/ka (average ~50 cm/ka).

Individual age for all samples used in this thesis have been calculated based on the outlined approach using equation 4.1, but this geochronology relies on the robustness of the approach for samples that lie out of or below the splice (chapter 3, section 3.2.1) and on a linear interpolation between age tie points, assuming no further changes in SR (figure 4.2a). The assumption of a linear relationship between age tie points is a widely applied approach and has previously been applied to Site U1427 (Tada et al., 2015b; Gallagher et al., 2018; Sagawa et al., 2018). This assumption may however not be fully applicable to Site U1427. It is likely that sedimentation rates varied more frequently than suggested, with the variable amount of terrigenous input and marine productivity over G-IG cycles.

The revision of the age tie points and addition of tie points from recent publications reveals further changes in SR where previously a linear relationship was considered (compare figures 4.1b and 4.2b). This points towards more frequent changes in the SR than suggested by any of the age models. In addition, the shipboard report suggests that SR may have changed over G-IG cycles as a result of the variable amounts of terrigenous input (Tada et al., 2015b). This would imply SR were higher (lower) during glacials (interglacials) when detrital input is thought to have increased (reduced). This idea is supported by the recent findings of Gallagher et al. (2018) who, combining their data with the SR of Sagawa et al. (2018), find higher SR during glacial maxima and at their terminations in the sediment records for the upper 180 m at Site U1427. This suggests that a simple linear interpolation between the six age tie points across the ~250 m sediment cores of the revised age model may not adequately estimate sample ages.

The linear SR between age tie points may also been affected by bioturbation as the sediments are frequently described as “heavily bioturbated” (Tada et al., 2015b). Bioturbation can disturb and mix marine sediments down to ~1 m and below if SR is low, and typically SR is ~1 cm/ka in deep-marine settings and ~10-100 cm/ka in coastal settings and shallow seas (Ruddiman, 2001c). Through mixing of the sediment, bioturbation reduces the temporal resolution of climate signals (Anderson, 2001) and attenuates and potentially shifts the climate signals (Loewemark et al., 2008). It is however likely this effect has been attenuated at Site U1427 due to the high SR. As bioturbation could have reached down to ~1 m in sediments (*op. cit.*) and depth uncertainties in age datums is less than 1 m, in theory, the maximum

uncertainty in calculated sample ages is 2 m, which is between 2.24 ka (at highest SR of 89.4 cm/ka) and 6.26 ka (at lowest SR of 31.94 m/ka).

Through the issues it is difficult to estimate the exact maximum resolution of the sediment records at Site U1427 that encompass the MPT. The theoretical temporal resolution of the proxy records, based on an average SR 50 cm/ka, assuming a linear SR between age tie points and given the sample available for this PhD (~0.5-1 m spacing; chapter 3, section 3.5.1), is ~1-2 ka. In theory, this resolution would allow studying the palaeoenvironmental and –oceanographic changes on millennial timescales and reliably resolve G-IG cycles, both in the 41-ka and 100-ka worlds, and capture the change in frequency which characterises the MPT.

Each G-IG cycle would contain at least 10 (100-ka world) and at most 40 (41-ka world) samples, varying depending on sample resolution of the analysis (chapter 3, section 3.5), SR and cycle duration. In addition, there is a general issue with uncertainty in the precise timescale of short-lived (millennial and sub-millennial) palaeo-climate events, even in the most ideal archives, i.e. high SR and little bioturbation (see discussion in Kemp and Sexton, 2014; Tomašových et al., 2019). There have been recent attempts to quantify the level of uncertainty of palaeo-climate archive resolution using statistical models (e.g. Trauth, 2013; Dolman and Laepple, 2018).

In any case, the above is currently the best estimate for sample ages and provides the chronological framework for the palaeoenvironmental studies across the MPT in this study. The crux in increasing the resolution and allowing more precise dating of the sediments, lies in the establishment of a SR-independent link with age. One such way is through the creation of an isotope chemo-stratigraphy.

4.4 Isotope Chemo-Stratigraphy across the MPT

*4.4.1 Identification of glacials and interglacials using b**

The shipboard b* index (section 3.2.3) shows high amplitude and high frequency variability between 2 and 10, with lowest values occuring between 520-510 m and repeatedly dropping to a value of ~4 from 375 m upwards, each with a duration of ~5 m (figure 4.3). No such minima occur between ~510 and 375 m. As described in section 3.2.3, a coherence between the b* index and G-IG cycles was identified on-board and has since been applied to studies of the upper ~250 m of Site U1427

(Tada et al., 2015b; Miller and Dickens, 2017; Black et al., 2018; Itaki et al., 2018; Gallagher et al., 2018; Sagawa et al., 2018; Saavedra-Pellitero et al., 2019), with glacials being represented by b* minima and interglacials by b* maxima (Tada et al., 2015b). Based on this relationship between b* and G-IG cycles, glacials (indicated by low b*) are likely centred at ~520-510 m (~1250-1230 ka), 375-345 m (910-840 ka), ~320-310 m (~780-770 ka) and ~295-275 m (~750-708 ka) (figure 4.3a).

4.4.2 Benthic foraminiferal stable isotope records, $\delta^{18}O_{Uvigerina\ spp.}$ and $\delta^{13}C_{Uvigerina\ spp.}$

In order to confirm the glacials suspected by the b* index, the gathered $\delta^{18}O_{Uvigerina\ spp.}$ record is compared with b*. The benthic $\delta^{18}O_{Uvigerina\ spp.}$ record shows high frequency, high amplitude variability, with values ranging between +4.4 and +3.1 ‰ at depths for >260 m (figure 4.3a). Fluctuations in $\delta^{18}O_{Uvigerina\ spp.}$ appear less frequent from 375 m upwards, which is also apparent in the b* index (figure 4.3a). The most prominent feature in $\delta^{18}O_{Uvigerina\ spp.}$ is an excursion to lower values between 345 and 375 m, shifting from +3.9 to +3.3 ‰, concomitant with the change to lower b* values (section 4.4.1).

Another feature of the b*-$\delta^{18}O_{Uvigerina\ spp.}$ comparison is a shift to lower b* values concomitant with high $\delta^{18}O$ values, starting around 375 m and most pronounced between ~510 and 520 m (figures 4.3a and 4.4). As a result, the coherence between the $\delta^{18}O_{Uvigerina\ spp.}$ and b* records runs opposite and the differentiation of glacials and interglacials as done on-board and for the upper interval of Site U1427 (*op. cit.*) does not fit this interval (see figure 4.4).

This inconsistency between the two records could potentially be caused by diagenetic alteration of the foraminifera shells, since a similar emergence of higher than expected $\delta^{18}O$ values had previously been from planktonic foraminifera shells that had undergone post-depositional diagenetic alteration (see cool tropics paradox, chapter 3, section 3.5.11).

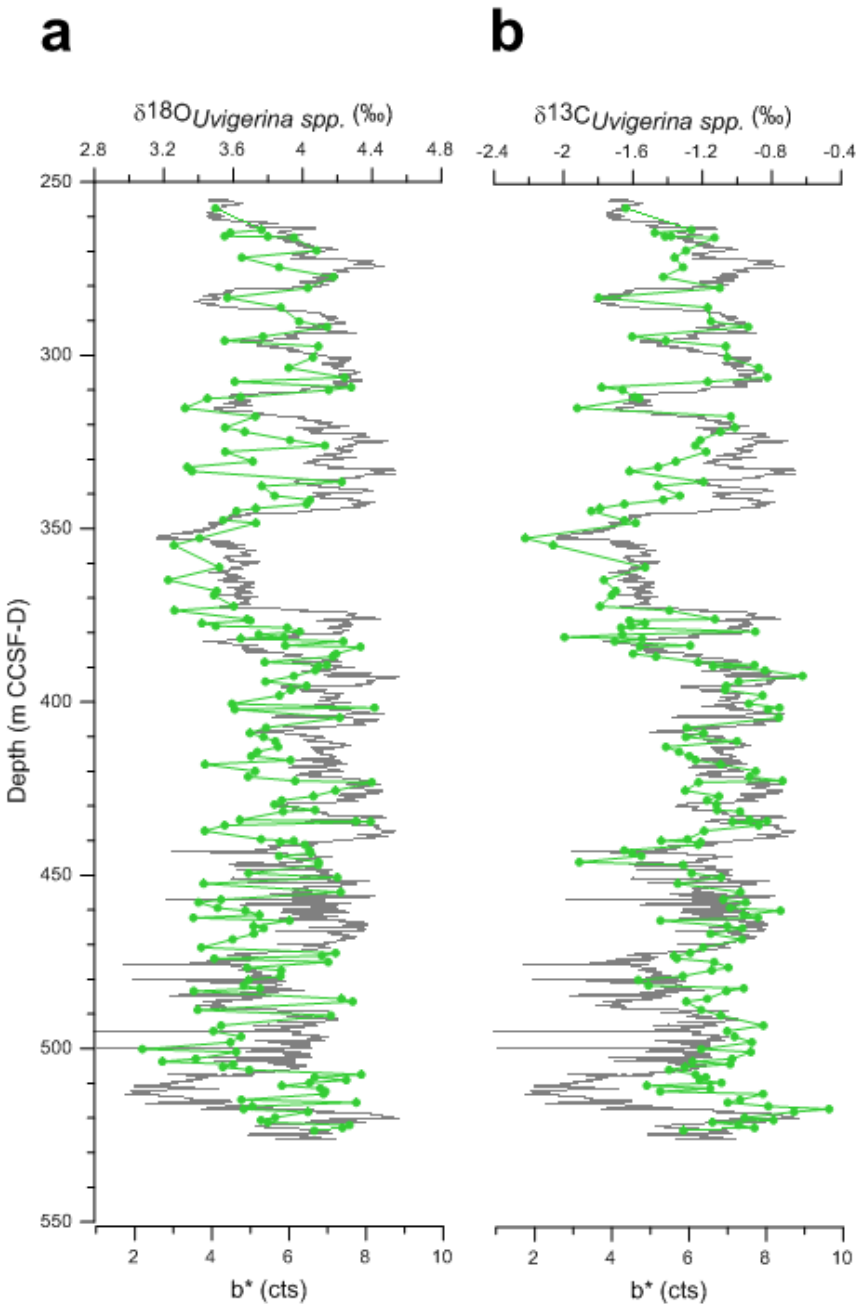

Fig. 4.3. Benthic foraminiferal stable isotope records of $\delta^{18}O_{Uvigerina\ spp.}$, fig. 4.3a, and $\delta^{13}C_{Uvigerina\ spp.}$, fig. 4.3b, plotted against depth in sediment core, with the b* index (grey) plotted in the background for reference. Most remarkable in these records is the pronounced perturbation at ~375-345 m and a deviation in the relationship between b* and $\delta^{18}O_{Uvigerina\ spp.}$ at 517-472 m.

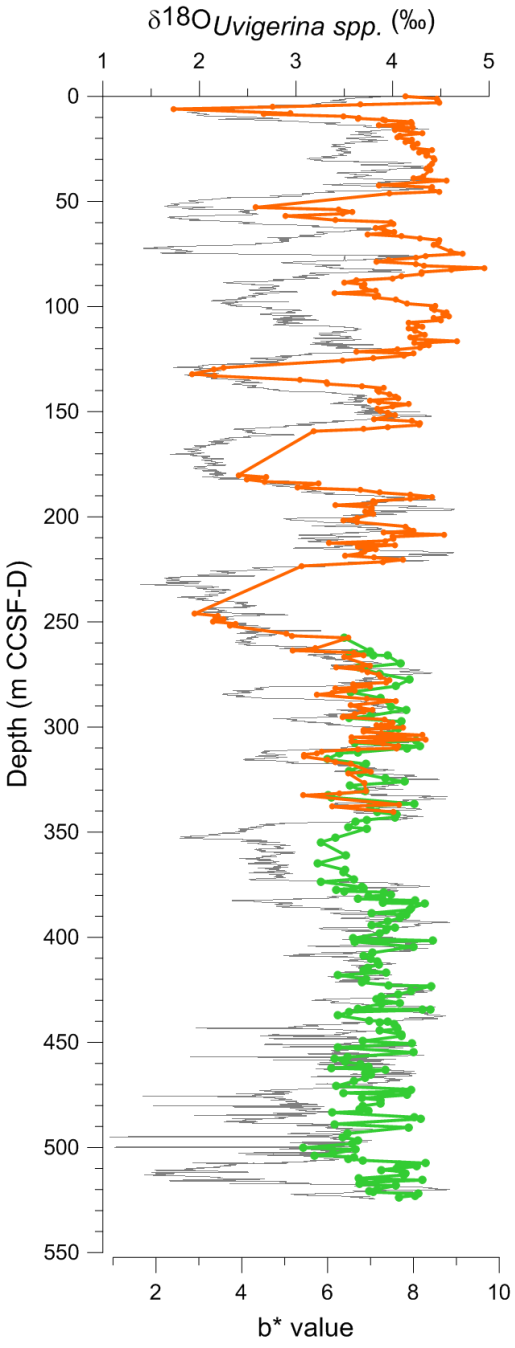

Figure 4.4. Compilation of *Uvigerina* spp.-based $\delta^{18}O$ records for the entire cored interval of Site U1427, using data generated in the framework of this thesis (green) and by Sagawa et al. (2018) (orange), with the b* index (grey) for reference.

To test the reliability of the $\delta^{18}O_{Uvigerina\ spp.}$ and $\delta^{13}C_{Uvigerina\ spp.}$ records with respect to potential diagenetic alteration of the tests *Uvigerina* spp. shells were investigated using combined SEM and EDX spectroscopy (chapter 3, section 3.5.11). The SEM analyses display a good preservation state with little signs of diagenetic alteration of the shells, showing micro-granular wall structures, open pore channels that extend

through shell walls, few shells with holes, and little signs of secondary overgrowths on surfaces (see appendix B). Where possible secondary overgrowths do seem to appear, EDX analyses does not show the chemical signature typical for diagenetic calcites, i.e. enhanced Mg-levels (*c.f.* Sexton et al., 2006; chapter 3, section 3.5.11). The good preservation implies $\delta^{18}O_{Uvigerina\ spp.}$ and $\delta^{13}C_{Uvigerina\ spp.}$ reflect the original palaeo-signals and hence excursions described above, comparing b* and $\delta^{18}O_{Uvigerina\ spp.}$, are closely linked palaeoenvironmental changes. Other possible explanations for the change in co-variance between b* and $\delta^{18}O_{Uvigerina\ spp.}$ are mis-identification of glacials/interglacials, or an improved glacial connection with the open ocean (see chapter 6).

The $\delta^{13}C_{Uvigerina\ spp.}$ record also shows high frequency and high amplitude variability, with values ranging between –2.2 and –0.5 ‰, which track b* throughout the record, showing higher (lower) ratios together with higher (lower) b* indices (figure 4.3b). The only exception to this is between ~520-510 m when $\delta^{13}C_{Uvigerina\ spp.}$ does not decrease as much as the b* values. Another feature, that is also seen in the b* and $\delta^{18}O_{Uvigerina\ spp.}$ records, are less frequent changes from maxima to minima together with higher amplitudes in variability at depths <375 m. This is shown in $\delta^{13}C_{Uvigerina\ spp.}$ by a pronounced drop in its mean minimum values, shifting from ~–1.2 ‰ at depths >375 m to less than ~–1.6 ‰ at depths <375 m.

The resolution of the isotope data equates to on average ~1-2 ka using the approach of section 4.3.3. Gaps in the data greater than 6 ka represent intervals of the sediment core where there were insufficient numbers or an absence of *Uvigerina spp*. shells in the sediments. These gaps are up to 15 ka in length and are most pronounced between 375-345 m, an interval where the lowest isotope and b* values occur. Whether the *Uvigerina spp.* reduction/absence in this interval is a primary signal of unfavourable conditions for the foraminifera to live in or a secondary one as a result of post-depositional dissolution is unclear.

4.4.3 Establishing marine isotope stages using $\delta^{18}O_{Uvigerina\ spp.}$

To establish an age model for Site U1427 beyond 350 m, a comparison between the $\delta^{18}O_{Uvigerina\ spp.}$ record with the LR04-stack was made, using the b* index to match the two records (figure 4.5) (chapter 3, section 3.4). The LR04-stack resolves glacials and interglacials as global averages and labels them as marine isotope stages (MIS), applying odd numbers to interglacials and even numbers to glacials, starting with MIS

1 as the present. The LR04-stack MIS nomenclature is used in this thesis and has recently been used in Sagawa et al. (2018) for the age model of the shallower part of Site U1427. In this thesis, the revised age model (section 4.3.2) was used as a temporal framework, with the relationship between b* and $\delta^{18}O_{Uvigerina\ spp.}$ used as an indicator for glacials/interglacials and in the comparison with the LR04-stack, which enabled the identification of MISs (figure 4.5). The effect of reduced glacial sea water salinity in reducing glacial $\delta^{18}O$ complicates MIS identification and has been described by numerous studies from the Japan Sea (see chapter 2, section 2.4), including Kido et al. (2007) who describe the phenomenon from a site nearby Site U1427 (MD01-2407, Oki Ridge, 932 m water depth, age: <640 ka) and by Sagawa et al. (2018) who analysed *Uvigerina spp*. in the upper ~350 m of Site U1427 (see also figure 4.5).

The most prominent feature in b* and $\delta^{18}O_{Uvigerina\ spp.}$ is a perturbation to lower values in both parameters between 345 and 375 m. During this interval the lowest $\delta^{18}O$ values occur, average ~+3.3 ‰, simultaneous with low b* around 2-3, indicating a prolonged glacial period. The interval dates between 866 and 910 ka according to the revised age model, which approximately corresponds to MIS 22-24 based on the LR04-stack boundaries (figure 4.5).

The globally supressed interglacial of MIS 23 (Clark et al., 2006; Elderfield et al., 2012; chapter 2, section 2.3) is centred somewhere between, but cannot be identified in either b* or $\delta^{18}O_{Uvigerina\ spp.}$. There is however a peak of higher $\delta^{13}C_{Uvigerina\ spp.}$ values between 360 and 370 m (figure 4.5b), the interpretation of which is difficult as there are several factors influencing the $\delta^{13}C$ record. These include ocean circulation, primary productivity, storage of carbon in carbonates and organic matter, and the Mackensen-effect, which postulates benthic foraminifera mainly precipitate their shell calcite when food is available, i.e. recrding preferentially high marine surface productivity events (Wefer et al., 1999; Maslin and Swann, 2006, for a review). The coherence between $\delta^{13}C_{Uvigerina\ spp.}$ and b* above 375 m points towards productivity as a main control on $\delta^{13}C_{Uvigerina\ spp.}$ during this time and at this site, as it is the main

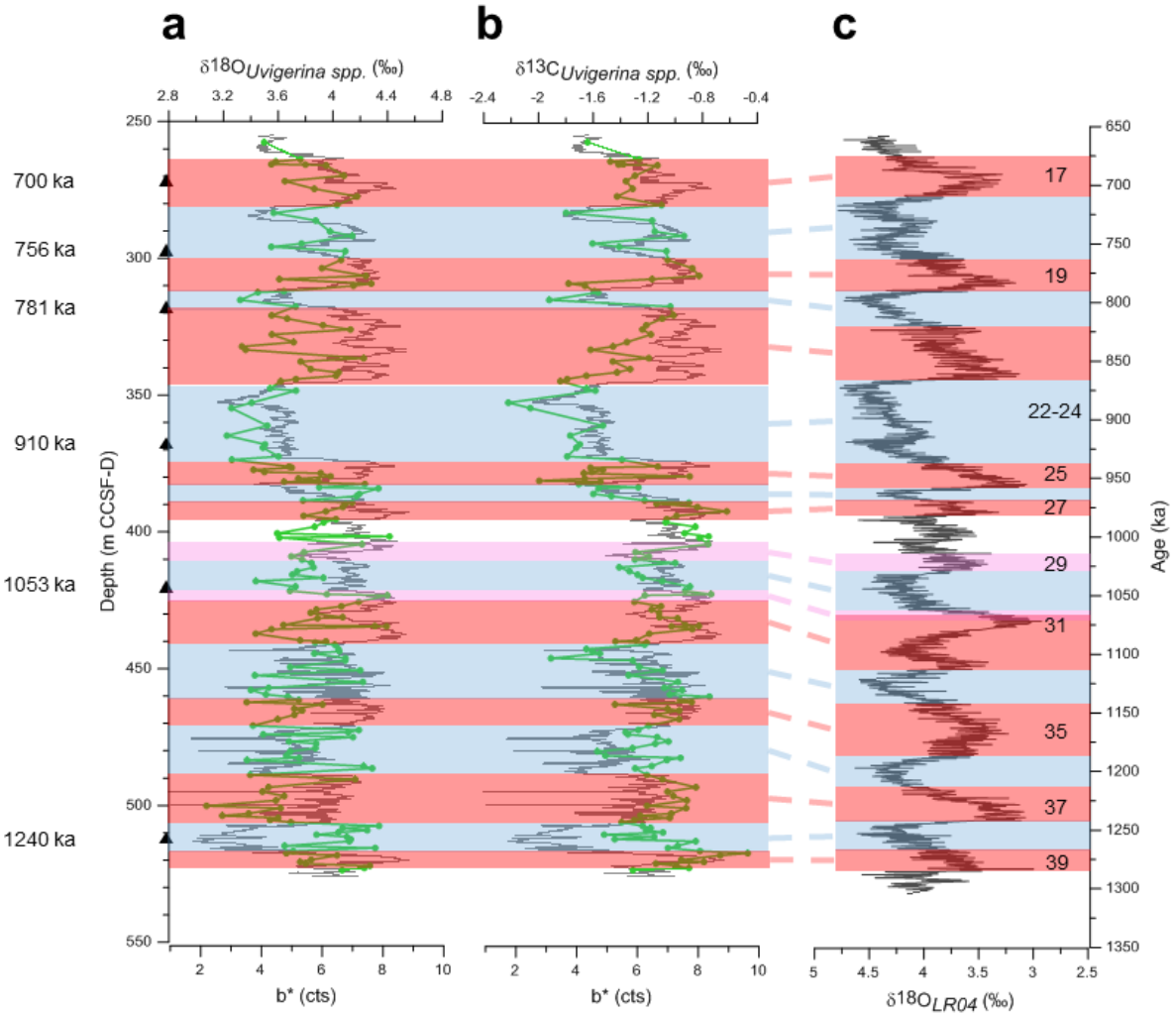

Figure 4.5. Summary plot showing $\delta^{18}O$ (fig. 4.5a) and $\delta^{13}C$ (fig. 4.5b) of *Uvigerina spp.* and an isotope-stratigraphy for the lower interval (>260m) based on the comparison with the LR04-stack (Lisiecki and Raymo, 2005; fig. 4.5c). The colour reflectance index (b*, grey line in the background of $\delta^{18}O$ and $\delta^{13}C$) and selected age points (black numbers and triangles next to the depth; section 4.3.2) are plotted for reference. Marine isotope stages are labelled by black numbers (black numbers next to age scale), with glacials (blue bars) and interglacials (red bars) after Lisiecki and Raymo (2005). Pink bars indicate the approximate positions of warm water radiolarian occurrences as found by Sagawa et al. (2018) and Itaki et al. (2018).

control on the b* index, resulting in b* to vary with the amount of biogenic silica in the sediments and being higher during interglacials and lower during glacials (see chapter 3, section 3.2.3). Primary productivity itself is controlled by the inflow of nutrient-rich waters of the TWC and restricted to interglacial sea-level highstands (see chapter 2, section 2.4). The $\delta^{13}C_{Uvigerina\ spp.}$ peak between 360 and 370 m might therefore indicate TWC inflow during an interglacial, i.e. MIS 23.

At depths <345 m the amplitudes in the foraminiferal isotope and b* records increase while the occurrences of fluctuations decrease. Using the same approach as described above (combination revised age-depth model/markers as a temporal framework and the b* index to match the LR04-stack with the $\delta^{18}O_{Uvigerina\ spp.}$ record) enabled identifying the glacials MIS 20 (~320-311 m) and MIS 18 (~300-280 m), as well as the interglacials MIS 21 (~345-320 m), MIS 19 (~311-300 m) and MIS 17 (starting at 280 m, upper end may be missing) (figure 4.5).

At depth >375 m it is more difficult to identify glacials and interglacials as fluctuations in b*, LR04-stack and $\delta^{18}O_{Uvigerina\ spp.}$ are more abundant, but their amplitudes are reduced and hence excursions are not as pronounced. This might be expected as the dampening of climate variability prior to the MPT in a 41-ka world, especially during glacials, has been documented previously (see chapter 2, section 2.3; e.g. Shackleton, 1976; Pisias and Moore, 1981). However, further glacials and interglacials were identified, namely glacials MIS 38, 36, 32, 30 and 26 and interglacials MIS 39, 37, 35, 27 and 25, as well as the interval MIS 33-31 (figure 4.5 and table 4.3).

MIS	Depth (m CCSF-D)	Duration (ka)	MIS	Depth (m CCSF-D)	Duration (ka)
17	<281		29	405 - 410	15
18	281 – 300.8	37	30	410 - 422	35
(19	300.8 - 311.5)		(31-33	422 – 439)	
(20	311.5 - 319.5)		(34	439 – 461)	
21	319.5 - 345	56	35	461 - 472	20
22-24	345 - 375	65	36	472 - 489	35
25	375 - 382	17	37	489 - 507	35
26	382 - 388	25	38	507 - 517	20
27	388 - 396	23	39	>517	

Table 4.3. Marine isotope stages with their corresponding depths in the sediment cores of Site U1427 (approximate beginning and end) and respective approximate durations based on the sample ages calculated above (section 4.3.3). MIS in brackets have large uncertainties in their depth/age estimates and have hence been skipped in duration estimates.

Based on the sample age estimates (section 4.3.3) durations of MIS were calculated (table 4.3) and show a tendency for longer G-IG cycles between MIS 39 and 35, averaging ~55 ka, followed by a tendency for shorter cycles between MIS 34

and 25, averaging ~40 ka, and a return to longer G-IG cycles emerging again from MIS 21 onwards, ~50 ka in length. The Emergence of longer, quasi 100 ka cycles followed by a lull in this frequency and the re-emergence and persistence of the 100 ka cycles from MIS 22 onwards has previously been described from the LR04-stack and from the southern hemisphere (Clark et al., 2006; Elderfield et al., 2012).

In the lowermost interval, MIS 36 to MIS 38 were identified based on the age-framework of the revised age model (section 4.3.2) and relatively pronounced excursions to low b* values. It seems, however, the relationship between b* and $\delta^{18}O_{Uvigerina\ spp.}$ during these glacials may have changed, suggesting relatively higher glacial $\delta^{18}O_{Uvigerina\ spp.}$ values than during the adjacent interglacials (see figure 4.5). This shift in the glacial $\delta^{18}O_{Uvigerina\ spp.}$-behaviour could be caused by a poor shell preservation, changes in local (glacial) hydrology, or an improved exchange with normal-saline open ocean waters during these glacials, investigated in chapter 6. One such period of high glacial $\delta^{18}O_{Uvigerina\ spp.}$ also occurs between 60 and 80 m at Site U1427 (figure 4.4; Sagawa et al., 2018).

In addition to the MIS identified using the above approach, the approximate positions of further glacials and interglacials were extracted from age markers identified in previous studies (section 4.3.1). The Ss-Pink tephra layer, dated to ~1050-1056 ka by Tsuji et al. (2005) and identified at 421.50-421.80 m by Sagawa et al. (2018), is associated with MIS 30 (Sagawa et al., 2018). Sagawa et al. (2018) furthermore identified warm water radiolarians present in the sediments just below this tephra layer, at ~425m, which must have originated from the East China Sea, having been transported into the Japan Sea during an interglacial sea-level highstands, and are therefore associated with the interglacial MIS 31 (figure 4.5). Further warm water radiolarians are present at ~410-405 m and at 407.5 m and have been associated with MIS 29 (figure 4.5) (Itaki et al., 2018).

4.4.4 Section summary and discussion

This section presented a near-continuous foraminifera-based $\delta^{18}O$ record for the Japan Sea, which is unique due to widespread glacial carbonate dissolution (see chapter 2, section 2.4). By combining tephrachronology, biostratigraphy and magnetostratigraphy (section 4.3) with the shipboard b* index (chapter 3, section 3.2.3) and the new $\delta^{18}O_{Uvigerina\ spp.}$ record, glacials and interglacials can be distinguished. The b* index, a proxy for marine productivity, has been shown to vary

with G-IG cycles, showing lower values during glacials and higher values during interglacials (e.g. Tada et al., 2015b; Sagawa et al., 2018; see also chapter 3, section 3.2.3). The $\delta^{18}O_{Uvigerina\ spp.}$ record also varies with G-IG cycles but here the contrasting influences of global ice-volume/temperature and local water salinity need to be disentangled. In the Japan Sea, in general, glacials are characterised by low foraminiferal $\delta^{18}O$ values due to low $\delta^{18}O$ values in the surrounding water (chapter 2, section 2.4), but occasional deviations from this trend have been found at some sites, including Site U1427 (Oba et al., 1991; Sagawa et al., 2018), suggesting the local $\delta^{18}O$-system is even more complex. However, it has been shown here that well-preserved foraminifera shells are found in the sediments of Site U1427 continuously, even though reduced in numbers during the more pronounced glacial intervals, such as at 375-345 m (figure 4.4 and 4.5).

Through comparison of $\delta^{18}O_{Uvigerina\ spp.}$ and b* with the LR04-stack (using also the revised age model, section 4.3), many of the MIS contained in the sediments can be identified (figure 4.5). In general, the interglacial $\delta^{18}O$ values of the LR04-stack and Site U1427 are similar, for example MIS 35 shows an average of ~+3.5 to +3.75 ‰ in the LR04-stack and ~+3.6-+3.4 ‰ at Site U1427, but the $\delta^{18}O$ values can vary greatly between these two records during glacials and within certain interglacials due to the local freshwater input affecting $\delta^{18}O_{Uvigerina\ spp.}$ at Site U1427. Gaps in the MIS identification exist, for example, during the pronounced glacial interval MIS 24-22, where the globally supressed interglacial MIS 23 was difficult to identify based on b* and $\delta^{18}O_{Uvigerina\ spp.}$ alone. Possibly the interglacial MIS 23 is located between 370 and 360 m, where $\delta^{13}C_{Uvigerina\ spp.}$ may indicate enhanced marine productivity, a typical feature for interglacials in the Japan Sea. Further gaps exist between MIS 35 and 27, where low amplitude variabilities in the records reduced the certainty in glacial and interglacial identification.

In sediments older than MIS 25 the relationship between $\delta^{18}O_{\ Uvigerina\ spp.}$ and b* appears to be different. While glacials above MIS 25 are characterised by low b* and $\delta^{18}O$ values caused by reduced marine productivity and freshwater input impacting on the $\delta^{18}O$ record (see chapter 2, section 2.4 and chapter 3, section 3.2.3), below MIS 25 glacials seem characterised by low b* with high $\delta^{18}O$ values. This a-typical relationship is most pronounced during MIS 39-36. Therefore below MIS 25 the identification of glacials and interglacials is based more on the consistency between

b* and age tie points with the LR04-stack. Potential causes for this glacial $\delta^{18}O$ patterns, such as hydrological or sea-level changes, are investigated in chapter 6.

4.5 Summary and Conclusions

This chapter established a revised and extended age model for IODP Site U1427 based on new data compared to data previously published (Lisiecki and Raymo, 2005; Tada et al., 2015b; Gallagher et al., 2015; Sagawa et al., 2018; Itaki et al., 2018; Tada et al., 2018). The revised age-depth relationship and newly calculated sedimentation rates show a continuously high sedimentation rate between 30 and 90 cm/ka, being highest between 260 and 320 m (figure 4.2). Using the revised age-depth relationship shows the sediment interval 260-530 m spans the MPT, encompassing 1256-687 ka, although significant uncertainty is associated with calculated ages (see section 4.3).

The revised age-depth relationship allowed calculating the theoretical maximum temporal resolution of proxy records, which is ~1-2 ka with each sample comprising ~20 years of particle deposition, based on the sediment samples available for this study at a spacing of ~50-100 cm and the revised sedimentation rates. However, heavy bioturbation may have affected or perhaps destroyed the ability of these sediments to record changes on very short, e.g. millennial timescales. For this reason, it is certainly difficult to identify monsoon-related DOC events in the proxy records (see chapter 2, sections 2.3, 2.4). Furthermore, the laminated sediment, typically associated with DOC-monsoon events in the Japan Sea, are absent at Site U1427. Often used to correlate between sites in the Japan Sea, the absence of such laminated layers has made the sediments of Site U1427 difficult to correlate with other site in the basin (Irino et al., 2018; Sagawa et al., 2018; Tada et al., 2018).

The good calcite preservation at Site U1427 enabled the creation of a near-continuous benthic foraminiferal $\delta^{18}O_{\textit{Uvigerina spp.}}$ record, which is the first from the Japan Sea to cover the MPT, at high-resolution with on average 6 ka gaps between samples with high continuity allowing the resolution of interglacials and glacials alike. By comparing the generated $\delta^{18}O_{\textit{Uvigerina spp.}}$ record with the b* index and the LR04-stack most of the contained glacials and interglacials could be identified, allowing to establish an isotope chemo-stratigraphy across MIS 39-17 (figure 4.5), with only few MIS missing between MIS 35-27 and MIS 23. Using the revised age-depth

relationship enabled calculation of lengths of G-IG cycles. This shows a change from relatively long cycles during MIS 39-36, on average 55 ka in length, to shorter cycles during MIS 35-25 being on average ~40 ka in length, back to prolonged G-IG cycles during MIS 21-17, lasting ~50 ka on average. A similar trend of longer, to shorter, to prolonged G-IG cycles across the MPT has been described in other studies and records of the MPT, including the global LR04-stack (Clark et al., 2006; Elderfield et al., 2012).

In addition, the benthic $\delta^{18}O_{Uvigerina\ spp.}$ record revealed two distinct intervals (i) an isotopic perturbation at 375-345 m, coinciding with MIS 24-22 and characterised by a prolonged period of very low $\delta^{18}O$ values, and (ii) an interval of high glacial $\delta^{18}O_{Uvigerina\ spp.}$ values between MIS 39 and at least MIS 36 (perhaps MIS 25), a behaviour that deviates from the Japan Sea-typical behaviour (see chapter 2, section 2.4), but has been found on one occasion also in the shallow section of Site U1427 (figure 4.4; Sagawa et al., 2018). It is thought that the described phenomenon of low glacial $\delta^{18}O$ values has prevailed in the Japan Sea during the majority of glacials of the Quaternary, though its onset is still in debate, varying between 2500 and 1600 ka (Tada, 1994; Kitamura, 2007; Hoiles et al., 2012). Therefore it is unclear what might have caused the apparent shift from high to low glacial $\delta^{18}O$ values across the MPT and it will be explored further in the subsequent chapters.

Chapter 5: Palaeoenvironmental Reconstruction across the MPT (MIS 39-17)

5.1 Introduction

The revised age model for Site U1427 (chapter 4) demonstrates (i) continuously high sediment accumulation across the sediment interval ~260-520 m and (ii) the interval is spanning MIS 39-17, which includes the MPT. This enables detailed palaeoenvironmental and -oceanographic studies of the MPT in the Japan Sea.

The sediment cores of Site U1427 show sedimentation rates of up to ~90 cm/ka but heavy bioturbation limits potential millennial-scale palaeo-climate signals in the records (see chapter 4). The high sedimentation rates at this site are thought to be the result of good preservation of marine carbonates, but in addition, it is also influenced by terrestrial processes due to its close proximity to land (Tada et al., 2015b). Sites in close proximity to land have the potential for much higher sedimentation rates than those further offshore, and may provide an opportunity for high-resolution palaeo-studies, but, on the other hand, the close proximity to land likely leads to complications in the interpretation of the proxy records due to the varying sources and contributions of sediment particles as input from land and/or from marine productivity. At Site U1427 terrestrial organic matter is likely making up a significant contribution to the sediments, especially during glacials (Tada et al., 2013). This terrestrial organic matter can originate from the Asian hinterland, being transported to the Japan Sea via the strong winds of the East Asian winter monsoon, but some proportion of it has also arrived at Site U1427 via local freshwater runoff (rivers, lakes) as the shipboard party identified large and well-preserved plant remains (leaves, bark) in the sediments (Tada et al., 2015b).

At open ocean sites the main control on sedimentation are marine processes such as marine primary productivity and typical sedimentation rates vary between 0.2-1 cm/ka at low primary productivity sites and some 100cm/ka in high-productivity areas (Stein, 1991). At sites nearer to continents the relatively higher terrigenous contributions to the sediment can be expected, and, additionally, the marine component of the signals can be biased by local influences such as freshwater input changing the chemistry of the ocean water, and these biases may change over time. This complication of disentangling the mixed marine-terrigenous signals led to ocean

drilling programs focus on far offshore sites. Despite these issues, recently many near-continent sites have been drilled because of their potential for high sedimentation rates and for high-resolution palaeo-archives.

In order to understand the depositional environment of Site U1427, i.e. the processes on land and in the ocean, a multi-proxy approach is used in this study. A multi-proxy approach combines palaeoenvironment proxies, which are traditionally interpreted as being mainly controlled by the same process (e.g. Wefer et al., 1999), therefore complementing each other and increasing the confidence in the interpretation. This approach is especially helpful in complex settings with mixed sediments and signals of different origins, such as at Site U1427.

This chapter aims to decipher the varying contributions of terrigenous input and marine productivity to the sediments of Site U1427 across the MPT. A focus will be on the palaeoenvironmental reconstruction of the two intervals identified in chapter 4 (section 4.5), MIS 39-36 and 24-22. The interval of MIS 24-22 is distinct in its very low b* values (chapter 3, section 3.2.3), which coincide with low benthic foraminiferal oxygen isotope values ($\delta^{18}O_{Uvigerina\ spp.}$, chapter 4, section 4.4.2). In contrast, before MIS 24 and most pronounced during MIS 39-36, low b* values seem to coincide with high $\delta^{18}O_{Uvigerina\ spp.}$ values, thus suggesting a reverse relationship between the two records. This chapter will investigate the palaeoenvironmental changes that may have contributed to this changed relationship between b* and foraminiferal $\delta^{18}O$.

Challenges are expected, as the majority of analytical tools for the investigation of past climatic and palaeoceanographic changes, proxies, were developed in open ocean settings, mostly from the North Atlantic, and these may not work in the same way in marginal seas such as the Japan Sea, and at Site U1427.

Specific objectives of this chapter are:

1) To create proxy records that help decipher times of high marine palaeo-productivity from high terrigenous input by:
    a. producing a visual coarse sediment description in support of bulk sediment analyses, and
    b. producing multi-proxy records that help decipher the origin of organic matter in the sediments (terrigenous, marine), using carbon to nitrogen ratios, carbon isotope signature, and parameters generated through Rock-Eval pyrolysis;

2) To estimate the varying amounts of terrigenous and marine contributions to the sediments by creating an endmember model for terrigenous-derived organic matter in this setting;
3) To explore the palaeoenvironmental conditions through the whole of the sediment record across the MPT, MIS 39-17.

5.2 Methods

For details on the laboratory protocols and limitations please refer to chapter 3, section 3.5.2 for bulk sediment organic parameters and section 3.5.3 for the terrestrial organic matter carbon isotope endmember model, to section 3.5.4 for carbonate content, section 3.5.6 for Rock-Eval pyrolysis, section 3.5.8 for the grain-size distribution and section 3.5.9 for a facies description. The calculation of bulk sediment mass accumulation rates and fluxes are in section 3.5.5. All data can be found in appendix A.

The marine isotope stages (MIS) and age tie points, as identified and used in chapter 4 (see section 4.4.3), and the sediment colour reflectance (b*, section 3.2.3), are shown together with new sediment data for reference. MIS are displayed as coloured bars on the far left of figures, as are the age tie points (presented as triangles and numbers to the left of figures). The b* index (Irino et al., 2018) is shown as a light grey line running in the background of new data.

5.3 Results

5.3.1 Bulk sediment organic parameters ($\delta^{13}C_{org}$, TOC, TN, C/N ratios)

Comparative plots of bulk sediment organic parameters, namely total organic carbon content (TOC), total nitrogen content (TN) the ratio of TOC and TN (C/N ratio) and the isotope ratio of bulk sediment organic matter ($\delta^{13}C_{org}$), together with the b* index are shown in figure 5.1. All four sediment organic parameters show coherent trends over G-IG cycles of lower glacial and higher interglacial values. In general they follow the trends and patterns of the b* index.

The TOC values fit well with the shipboard analyses values (figure 5.1a). The TOC record shows highest amplitude fluctuations between MIS 39 and 36, ranging between 0.5 and 2.0 wt% (average of ~1.2 wt%) and lowest values occurring during the glacial MIS 38. Between MIS 35 and 25 TOC increases (range 1.0-3.1 wt%,

average ~1.8 wt%), before dropping to values around ~0.7 wt% during the interval MIS 24-22. The only exception to these low values is a TOC-peak of 1.0-1.5 wt% between ~370 and 360 m. In the uppermost ~100 m of the investigated interval, between 345 and 260 m, TOC variations are increased in amplitude, varying between ~0.5 and 2.0 wt%, similar to the variation extents between MIS 39 and 36 but with less frequent minima/maxima.

The high coherence of TOC with b* (figure 5.1a) suggests similar driving mechanisms or they are responding to similar environmental forcing. Shipboard analyses found a link between b* and marine productivity, with high b* values occurring in biogenic silica-rich, nannofossils-rich sediments (chapter 3, section 3.2.3). The abundance of nannofossils suggests high marine productivity and, alongside high TOC values, corresponds to high productivity phases. Both records, TOC and b*, indicate higher marine productivity during interglacials and lower productivity during glacials.

The TN data fall below the shipboard results (figure 5.1b), ranging between ~0.05 and 0.35 wt% (average 0.2 wt%). TN contents below 0.1 wt% should however be treated with caution due to reduced accuracy of TN results at such low TN concentrations (Melanie Leng, pers. coms.). Just like for TOC, there is a coherence of TN with b* as both records show higher (lower) values during interglacials (glacials) (figure 5.1b). The relationship between b* and TN is clear between MIS 39 and 31, but becomes less pronounced between MIS 31-25. The interval MIS 24-22 is expressed by a distinct shift with reduced TN content (average ~0.1 wt%), although these may not be reliable values because of the low TN concentration. Then there is a peak in TN between ~370 and 360 m, where TN content doubles (up to ~0.2 wt%). From MIS 21 onwards the G-IG variations become more pronounced again and TN ranges between ~0.05 and 0.3 wt% with an average of ~0.1 wt%.

Using TOC and TN contents, C/N ratios are calculated and they vary between 3.3 and 15.0 (average 10.0), lying above the values of nine shipboard data points (2.7-5.8, average 4.1), which is probably due to the discrepancy in TN values (see above) (figure 5.1c). C/N ratios are higher (lower) during interglacials (glacials) between MIS 39 and MIS 25. Glacial values are lower during MIS 39 and 36 (~7.0) than during glacials between MIS 35 and 25 (~10), while interglacial values are similar (~12). From MIS 25 the relationship between C/N ratios and G-IG cycles continues but

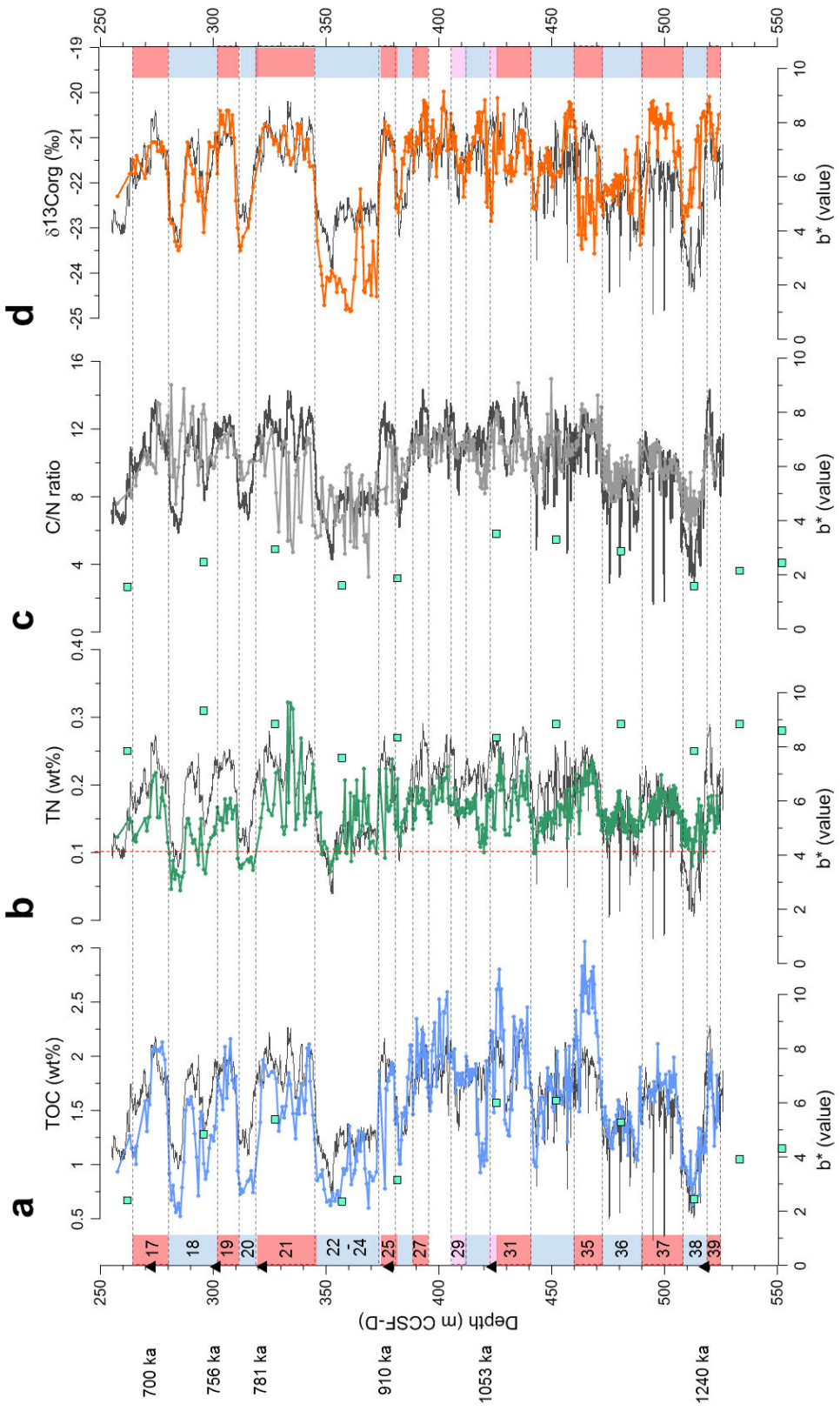

Figure 5.1. Bulk sediment organic parameters TOC (fig. 5.1a), TN with quantification limit (red, dashed line) (fig. 5.1b), C/N ratios (fig. 5.1c) and $\delta^{13}C_{org}$ (fig. 5.1d) against depth in sediment core, together with b*, which is related to marine productivity (chapter 3, section 3.2.3). The figure also shows shipboard data for TOC, TN and C/N ratios calculated here from the shipboard data (turquoise squares).

is less pronounced due to high variability in C/N, showing high frequency variations across glacials and interglacials alike and a range of ~4-14 (figure 5.1c).

The $\delta^{13}C_{org}$ data show higher (lower) values during interglacials (glacials), and a high coherence with the b* index (figure 5.1d), indicating $\delta^{13}C_{org}$ is strongly related to variations between marine productivity and terrestrial organic matter input, with interglacials experiencing relatively higher marine productivity, while during glacials the input of terrigenous-derived organic matter is relatively higher (see chapter 3, sections 3.2.3, 3.5.2). Most pronounced G-IG cyclicity and coherence with b* through large variations are present during MIS 39-36 (–23.5 to –20 ‰) and during MIS 24-17 (~–25 to –20.4 ‰). During MIS 24-22 the $\delta^{13}C_{org}$ data are as low as ~–25.0 ‰ but between 370 and 360 m a single, well-defined peak shows values of up to –22.0 ‰. Both the distinct shift in the proxy records and the peak between 370-360 m, have also been described in TOC and TN data. The interval MIS 35-25 is characterised by more frequent, but smaller fluctuations (–22.5 to ~–20.5 ‰), consequently making it harder to find a visual coherence with the b* index, and the strong coherence between relatively lower (higher) $\delta^{13}C_{org}$ values during glacials (interglacials) is not always persistent.

5.3.2 Carbonate content ($CaCO_3$)

The carbonate content ($CaCO_3$) has been calculated from total inorganic carbon (TIC, chapter 3, section 3.5.4) and shows values between ~0.0 and 26.0 wt% (average ~9.0 wt%), fitting well to the nine shipboard data points (range 4.0-16.4 wt%, average 10.0 wt%) (figure 5.2). $CaCO_3$ varies over G-IG cycles showing higher (lower) values during interglacials (glacials). During MIS 39-36 there is a high coherence with $CaCO_3$ and b* over G-IG cycles ($CaCO_3$ varying between 3 and 15 wt%), which is not always persistent during MIS 35-28 ($CaCO_3$ range ~10-15 wt%), but it reappears during MIS 27-17 ($CaCO_3$ range ~9-26 wt%). The lowest $CaCO_3$ values occur during the glacials MIS 26 and MIS 24-22 (<5 wt%) and highest $CaCO_3$ values occur during interglacials MIS 25 and 21 (>20 wt%). While widespread dissolution events have been attributed to low glacial $CaCO_3$ contents at deep water sites in the Japan Sea (see chapter 2, section 2.4), Site U1427 is thought to have been located above the CCD throughout the lower Pleistocene to Holocene (Tada et al., 2015b), an assumption that is supported by recent findings of well-preserved

calcite shells, like those of foraminifera (Gallagher et al., 2018; Sagawa et al., 2018) and coccolithophores (Saavedra-Pellitero et al., 2019).

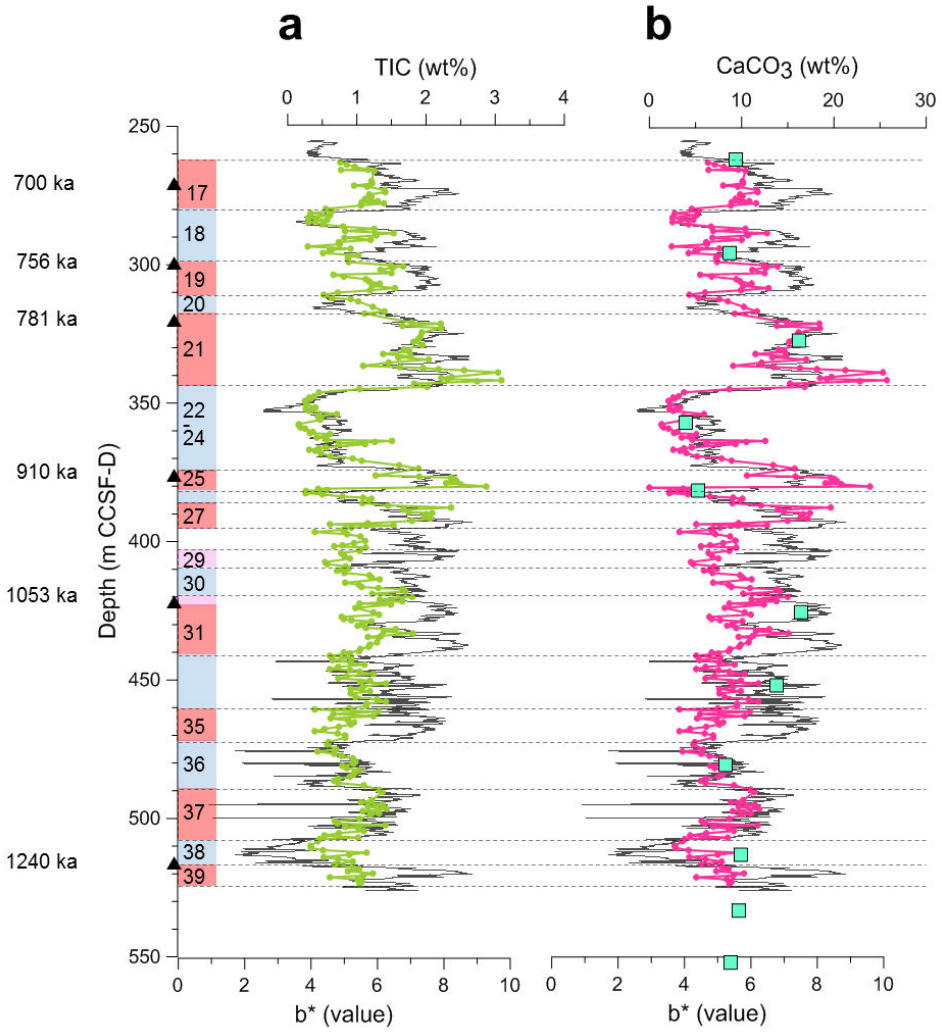

Figure 5.2. Measured TIC (fig. 5.2a) and calculated $CaCO_3$ contents (fig. 5.2b) versus depth in sediment core, together with shipboard $CaCO_3$ data (fig. 5.2b, turquoise squares).

5.3.3 Grain-size distribution

The overall very fine grained sediments (Tada et al., 2015c) were subdivided into >150 µm, >63 and <63 µm grain-size fractions in the preparation for foraminiferal isotope analyses (chapter 3, sections 3.5.8, 3.5.10) to generate the grain-size distribution presented in figures 5.3a and b. The fine fraction, <63 µm, makes up the majority of the sediment, on average 78.0-99.8 wt%, while the coarsest fraction, >150 µm, has an average contribution of just 0.7 wt%. The grain-size becomes coarser (finer) during interglacials (glacials), which is also evident in a low-resolution shipboard grain-size record produced in the framework of the lithological description (chapter 3, section 3.2.2; Tada et al., 2015c). The glacial (interglacial) fining

(coarsening) is most apparent during MIS 39-36 and from MIS 25 upwards, while a clear trend is lost during the mid-section (MIS 35-26).

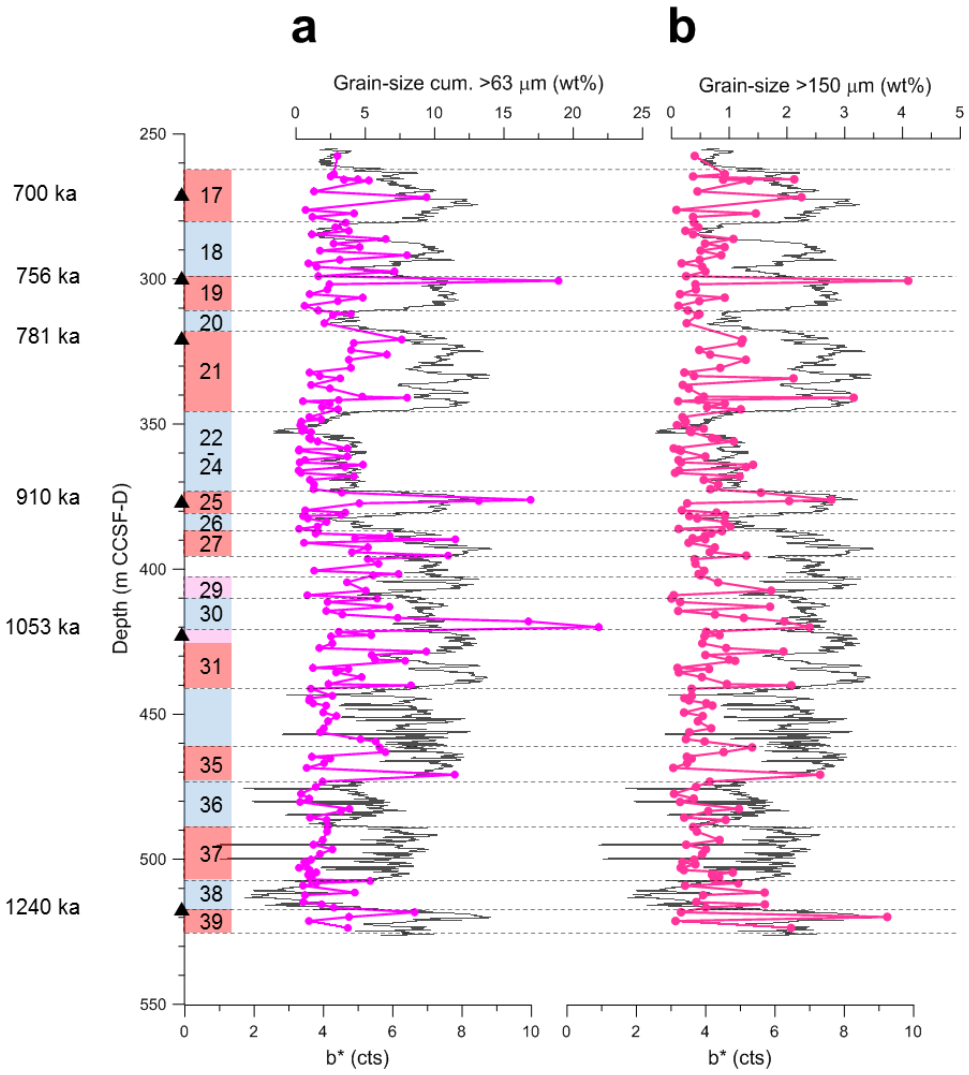

Figure 5.3. The cumulative grain-size fractions >63 µm (fig. 5.3a) and >150 µm fraction (fig. 5.3b).

Shipboard findings suggest a close relationship between grain-size and terrigenous input, displaying a negative correlation with smaller grain-sizes occurring together with higher terrigenous input (chapter 3, section 3.2.2; figure 5.4). Six pronounced intervals of very fine-grained, siliciclastic-rich sediments, were identified on-board (chapter 3, figure 3.3; reprinted below figure 5.4). These fine-grained, terrigenous input-dominated intervals occur according to the revised age model predominantly during glacials (figure 5.4d), namely MIS 38, 26, 24-22, 20 and 18.

A prolonged interval of fine-grained and siliciclastic-dominated sediments occurs during MIS 24-22 (figure 5.4). Here, the shipboard lithology describes the sediments

as laminated which implies a reduction or absence of bioturbation, linked to a reduction of oxygen levels (Tada et al., 2015c).

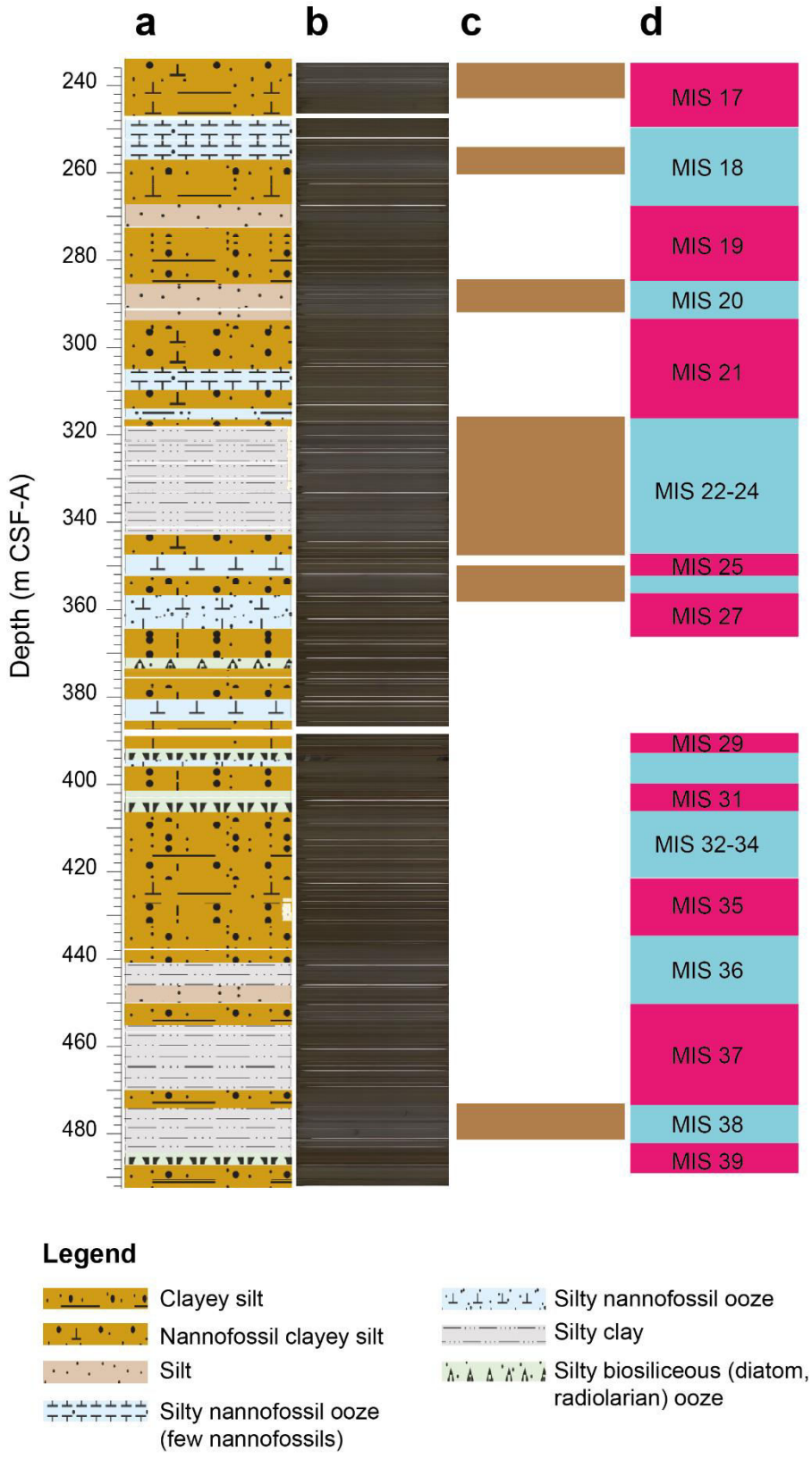

Figure 5.4. Correlation between shipboard lithology (fig. 5.4a), core section photographs (fig. 5.4b) with siliciclastic-rich intervals (fig. 5.4c) as described on-board (Tada et al., 2015c). Note: depth scale is CSF-A.

5.3.4 Semi-quantitative facies analysis

The full results of the semi-quantitative facies analysis of the >150 µm grain-size fraction can be found in appendix A but the most important findings are

(i) sediments contain an abundance of various marine and terrigenous materials, including marine biogenic carbonates such as foraminifera shells, ostracods, echinoid and bivalve fragments, and marine non-carbonates such as sponge spiculae, peloids (agglutinated, mixed, fine-sand sized particles). Non-marine particles include rock and mineral fragments as well as land-derived organic matter. Particles of uncertain origin include pieces of mica, gypsum crystals and diatoms.

(ii) sediments tend to contain more marine biogenic fragments during interglacials, while glacials are characterised by enhanced abiogenic, siliciclastic components in a finer-grained matrix, a relationship which has also been described by the shipboard party (Tada et al., 2015c).

Most remarkably, foraminifera, which otherwise occur throughout the core and often dominate the coarsest grain-size fraction, are reduced in numbers of both planktonics and benthics during MIS 24-22. Few of the shells show round holes, thought to be a sign of beginning dissolution rather than remobilisation and transport, which would have caused abrasion fragmentation of the shells (Melanie Leng, pers. coms.). Six samples during this interval (two in MIS 22 at 352 m, two in MIS 22 between 355 and 359 m, and two in MIS 24 at ~367 m) do not contain any foraminifera shells. This is confirmed by the shipboard report (Tada et al., 2015c), which describes the interval as foraminifera shell scarce or “barren”, and it coincides with lowest $CaCO_3$ content (section 5.3.2). Apart from rare foraminifera, the coarse fraction of MIS 24-22 is dominated by terrigenous material such as quartz grains as well as rock and mineral fragments and, unusual for a marine sediment, large pieces of land-plant organic matter (example photographs in figure 5.5a). Such large organic matter pieces occur throughout the cores and vary in shape (rounded outlines to elongated particles), size (~63-150 µm in length) and colour (orange, red, brown and black) but have in common the cellular structure, made up from the rigid cell walls, that strongly suggests their higher land plant origin. At some depths, sediments even contained pieces of leaves (Ann Dunlea, pers. coms.), confirming the terrigenous origin of these particles.

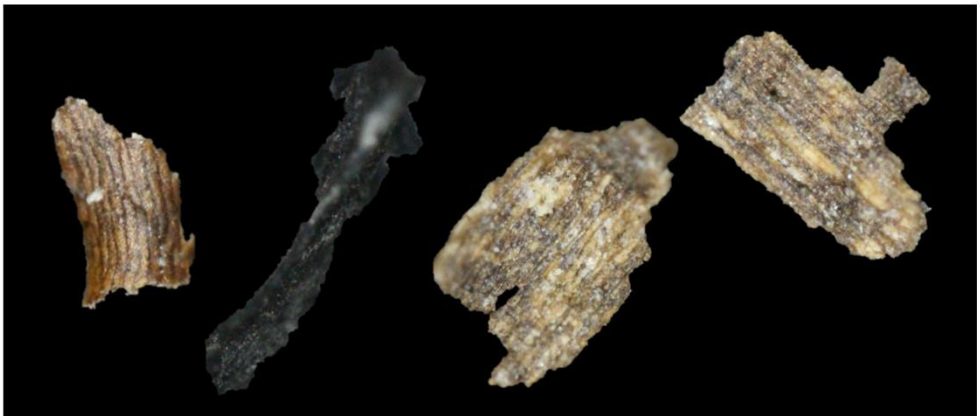

Figure 5.5. Examples of terrestrial land plants remains in varying states of preservation but mostly with cell structure visible. Photographs are for illustration and are not to scale.

Another feature of the sediments is the presence, often abundance, of sponge spiculae, also described in the shipboard report (Tada et al., 2015b). Sponge spiculae can be made up of either carbonate or biogenic silica (Koltun, 1966; Flügel, 2004a). A dissolution test using diluted HCl acid showed no response of the spiculae to the acid treatment, suggesting the sponge spiculae found here are of non-carbonate, biosiliceous material. Biosiliceous sponges are preferentially found in deep water settings (Dohrmann et al., 2008, and references herein) and are also well-known from the Japan and East China Seas and Northwest Pacific (Van Soest et al., 2012). Sponges in general prefer quiet water conditions with low sedimentation rates (Flügel, 2004a), which is not a given at the shallow-water, high sedimentation rate Site U1427. Biosiliceous sponges however are known to disintegrate after death (Flügel, 2004a) and their spiculae may settle autochthonous at the same location or be transported some distance. An example is the spiculae transport of over 700 km in the Southern Ocean (Koltun, 1966, Popova, 1986). At Site U1427 sponge spiculae occur preferentially during interglacials (MIS 39, 37, 27, 25, 21, 17) with some occurrences during glacials (MIS 38, 22, 18), which could indicate a link between spiculae occurrences and the TWC inflow during sea-level highstands.

Another biosiliceous component are rare occurrences of abundant large, centric diatoms (example photographs in figure 5.6d). Before MIS 25 the presence of large, centric diatoms in samples coincides with shipboard findings of abundant to dominant diatoms in the sediments, including few to rare occurrences of freshwater diatoms (specimen *Fragilaria* and *Cyclotella*; Tada et al., 2015b) and during glacials and interglacials alike (figures 5.6b-d). According to the shipboard report the identified

freshwater specimen indicate running water and/or lake origin (Tada et al., 2015b). However, the identification of diatoms on genus level (not species) is difficult, as species of the same genus/order can occur in both terrestrial freshwater and in low-saline coastal waters, an example being the order of Thalassiosirales, to which the genus *Cyclotella* belongs (Sancetta, 1982). After MIS 25 large, centric diatoms found in the coarse fraction (>150 µm) during the facies analysis coincide with common to few diatoms in bulk sediment and in an assemblage where freshwater diatoms are common (Tada et al., 2015b; figure 5.6). After MIS 25 the large, centric and freshwater diatoms occur during glacials only.

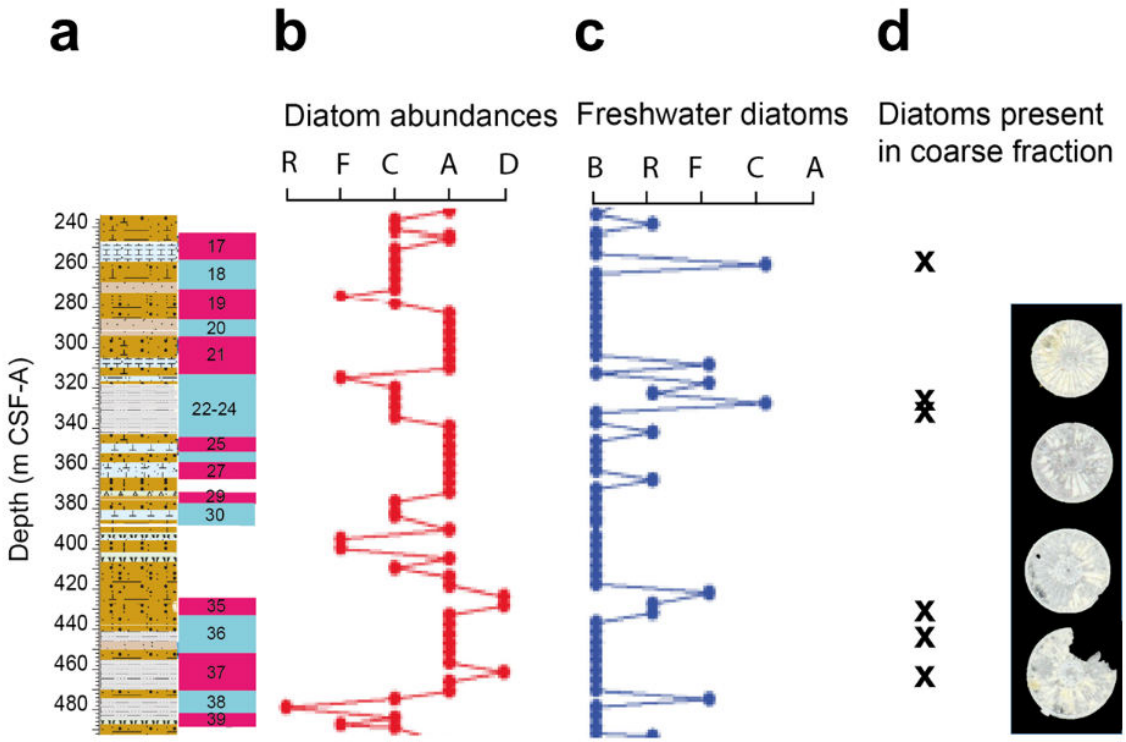

Figure 5.6. Shipboard total diatom (fig. 5.6b) and freshwater (fig. 5.6c) abundances from bulk sediment smear slides (R = rare, F = few, C = common, A = abundant, D = dominant; following Tada et al., 2013). Occurrences of large, centric diatoms in the >150 µm grain-size fraction and photographic examples (for illustration purposes, not to scale) (fig. 5.6d). For reference marine isotope stages are shown in fig. 5.6a (copy of figure 5.4). Figure modified from Tada et al. (2015b). Note: depth scale is CSF-A.

In a large number of samples a light, platy mineral is often abundant in the coarse fraction (figure 5.7). The mineral is present in two varieties as individual platy crystals and loosely packed aggregates of spherical shape. A selection of these minerals were analysed using EDX spectroscopy to semi-quantitatively estimate their chemical composition (chapter 3, section 3.5.11). The EDX results show that the minerals

mainly consist of calcium, sulphur and oxygen (figure 5.7a), and therefore could be gypsum. Compact gypsum spheres/rosettes, as shown in figures 5.7b and c can form in arid environments, clay pits, evaporative marine sediments and in marine sediments themselves (Bain, 1990, and references within; Pirlet et al., 2010; Lin et al., 2016). Although the formation processes differ between environments, they have in common the fundamental of weathering or oxygenation of sulphides such as pyrite and free Ca^{2+}-ions to precipitate carbonate around a nucleus (Flügel, 2004b). In the case of a fine grained matrix such as clay surrounding the nucleus, the growing aggregates push away the clay and get their round shape from this process. Shipboard XRD and smear slide analyses show minor but constant amounts of pyrite present in the sediments almost throughout the entire interval (Tada et al., 2015b), hence allowing for gypsum formation to take place and suggesting that pyrite contained in the sediments could have oxidised to form the gypsum.

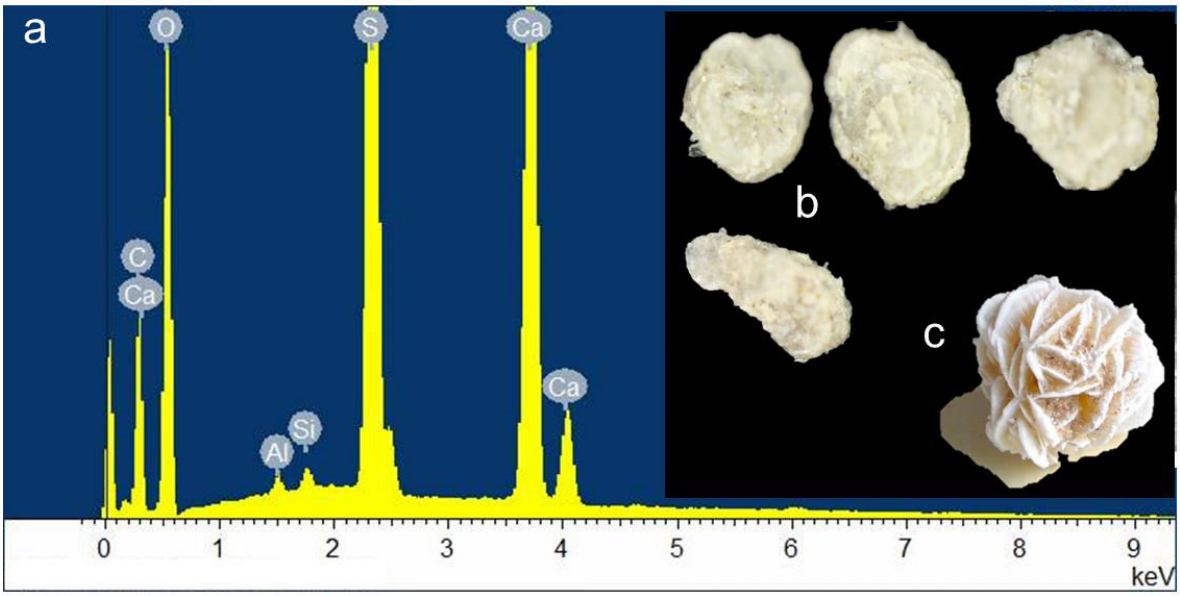

Figure 5.7. EDX spectrum of the light minerals found (fig. 5.7a) and high-resolution light microscope image of example coarse-fraction grains (fig. 5.7b) and gypsum roses for comparison (fig. 5.7c; unimelb.edu.au/science communication/2012/08/26/the-crystal-cave-of-giants; 09/01/2020). Photographs are for illustration and are not to scale.

Another characteristic of the coarse fraction is the presence of large mica fragments. Usually in marine sediments this is explained through the erosion of strata on land and riverine transport to the marine deposition site, and hence the higher the mica content, the higher the terrigenous riverine input is likely to be. At Site U1427 this would imply increased precipitation over Japan, most likely related to a stronger summer monsoon. There is a coherence between the presence of mica in the coarse

fraction and G-IG cycles but it changes across the MPT. Before MIS 25 mica occurs during both glacials and interglacials but from MIS 25 onwards mica predominantly occurs during interglacials, while during glacials mica is mostly absent from the sediment coarse fraction. If the main input mechanism was by riverine runoff this would suggest little precipitation/runoff difference across G-IG cycles before MIS 25, while during MIS 24-17 glacials would be characterised by pronounced dryer climate, i.e. less runoff and riverine mica input. The sedimentation rates, which could be affected by the reduced riverine input of terrestrial material, including mica, may not respond to this mechanism at Site U1427, as contributions of aeolian-derived terrestrial material would continue or even increase in this scenario.

At Site U1427 there is another possible input mechanism for mica to the sediments. Ikehara (1991) describe mica-rich surface sediments belonging to submerged, former continental strata located east of Oki Islands (figure 5.8). These deposits are located in around 200 m water depth, similar to Site U1427, and in close proximity to the investigated site. The mica deposits are furthermore positioned underneath the TWC that flows around the Oki Islands and continues to Site U1427 (Talley et al., 2006; Tada et al., 2015b). As a result it is possible for the TWC to cross over the mica deposits, picking up particles and delivering them to the site. This process may be promoted by upwelling through Ekman transport, which is known from the area around Oki Islands and Site U1427 (Park and Kim, 2010). Through the upwelling-associated turbulent water flow and mixing of the water column, the particles' residence time within the water column and hence their transport distance may be extended. If the main mica input mechanism was delivery from the Oki Island mica deposits, then the absence of mica during glacials of MIS 24-17 would suggest reduced or absent TWC inflow, preventing the transport of mica to the site, while the same mechanism was possible during glacials before MIS 24. The possibility of an additional marine mica source complicates the traditional palaeoenvironmental interpretation of increasing (decreasing) amounts of mica in the sediments as indicator of enhanced (decreased) riverine input and/or precipitation.

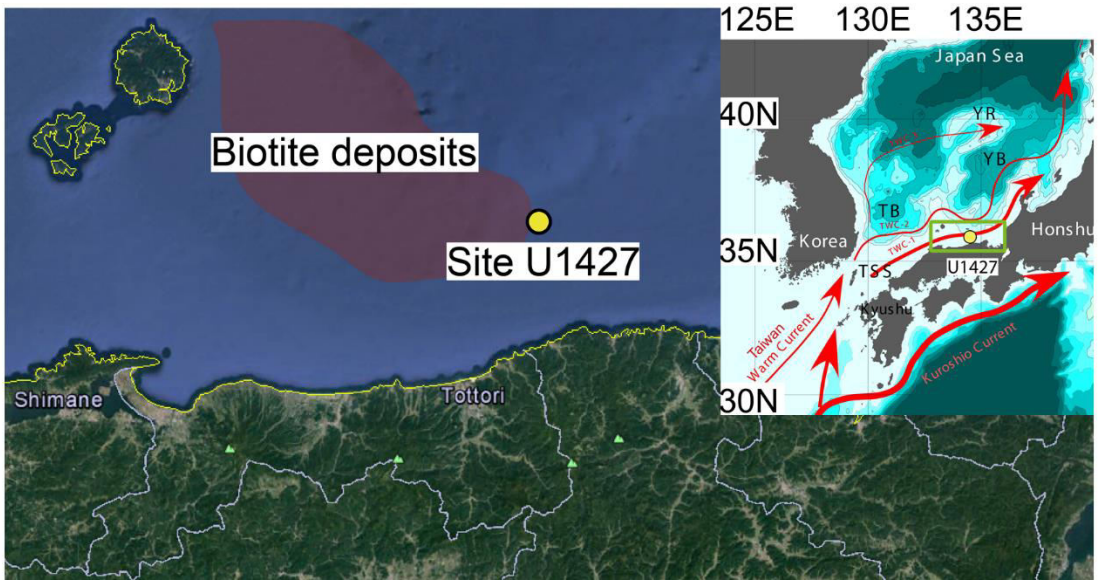

Figure 5.8. Satellite image showing the approximate position of mica/ biotite deposits east of Oki Islands (purple area; Ikehara, 1991, after Yokota et al., 1990) and Site U1427 (yellow circle). Insert gives a broader overview of the surrounding areas (green box; altered after Tada et al., 2015b).

5.3.5 Rock-Eval pyrolysis of bulk sediments

Rock-Eval pyrolysis (RE) parameters were analysed in samples from MIS 39-35 and MIS 27-19 for comparison (chapter 3, section 3.5.6). Throughout the analysed sediments the temperatures of maximum residue hydrocarbon (HC) release (T_{max}), a descriptor of thermal maturity, which increases gradually over depth intervals of hundreds of meters but not at the short depth scales studied here, are below 430 ºC (396-426 °C), characterising the organic matter (OM) contained in these young marine sediments (as expected) as “immature”, i.e. not having been in depths/temperatures of the HC-generating window (figure 5.9a) (Espitalié et al., 1977; Peters, 1986; Stein et al., 1991; Pimmel and Claypool, 2001). Caution must however been taken when interpreting these T_{max} data because TOC (figure 5.1a) and S_2-peaks (figure 5.9c) are generally very low, leading to potential mis-assignments of T_{max} during the pyrolysis cycle. This limitation of the technique is seen, for example, in T_{max} swings with unrealistically elevated signatures, approaching 430 ºC and suggesting close to oil window maturity, in an extremely TOC-depleted interval between 375 and ~360 m (MIS 24-22, figure 5.9c).

The other four RE parameters range between S_1-peak 0.15-0.61 mg HC/g sediment, S_2-peak 0.32-8.71 mg HC/g sediment, oxygen index (OI) 111-302 mg CO_2/g TOC and hydrogen index (HI) 127-375 mg HC/g TOC. The S_1-peak is very low and close to zero, indicating little to no free HCs in these sediments (figure 5.9b).

Therefore, most of the OM in these sediments is bound to the kerogen-fraction, releasing HCs only after thermal breakdown – defining the S_2-peak. All four parameters, S_1-, S_2-peaks, HI, OI, generally show increases (decreases) during interglacials (glacials) (figures 5.9b-e).

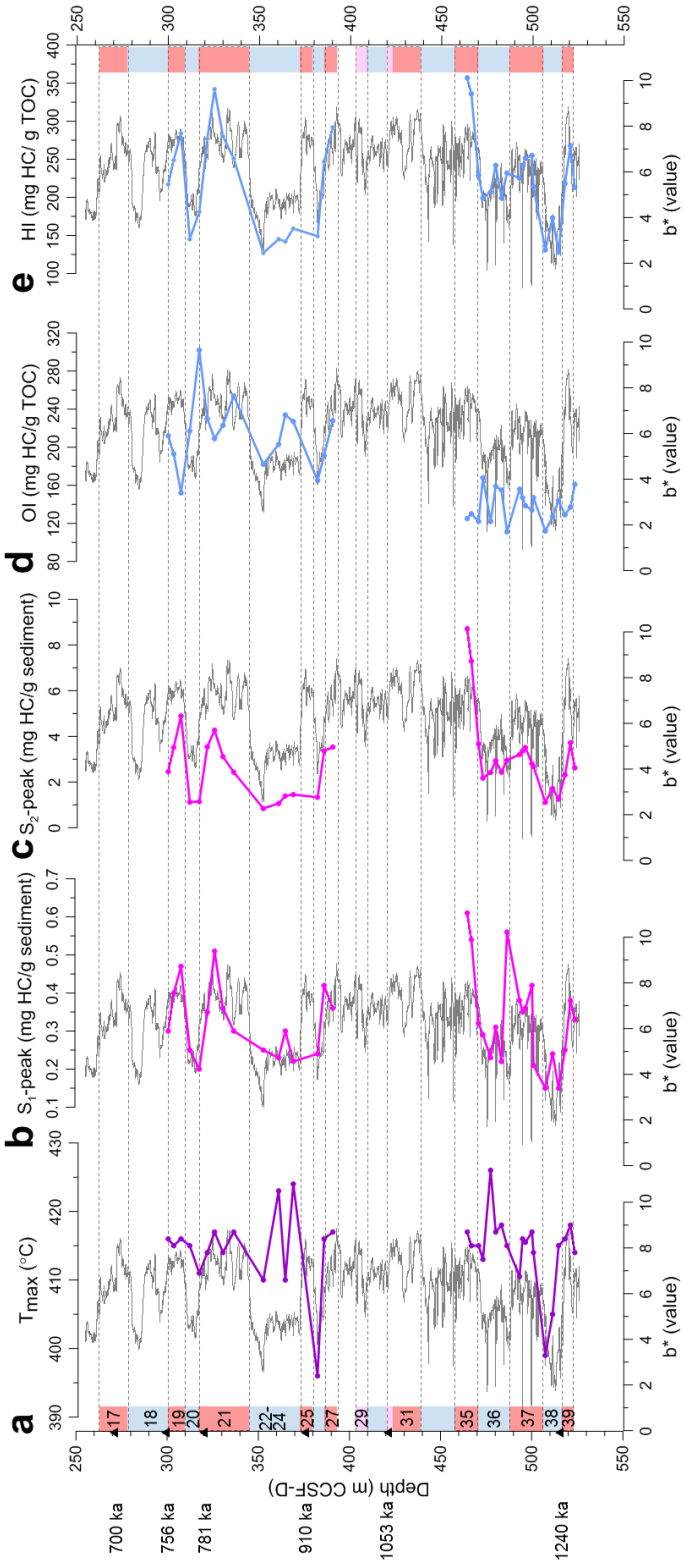

Figure 5.9. Rock-Eval Pyrolysis parameters T_{max} (fig. 5.9a), S_1-peak (fig. 5.9b), S_2-peak (fig. 5.9c), OI (fig. 5.9d) and HI (fig. 5.9e) versus depth in sediment cores.

5.4 Deciphering Sources of Organic Matter

Despite it only makes up a small proportion in marine sediments, organic matter (OM) plays an important role in reconstructing past environments and oceanography because of its links with past marine productivity and input of terrigenous OM (see chapter 3, section 3.5.2). The complexity of Site U1427 means a multi-proxy approach is needed for the interpretation of the different and potentially varying sources of OM, i.e. terrigenous input and/or marine produced particles. As a result, there are sometimes inconsistent and contradictory interpretations of individual palaeo-records between traditional indicators of marine productivity (TOC, $\delta^{13}C_{org}$, $CaCO_3$) and those that trace the terrestrial/marine origin of carbon (C/N ratios, $\delta^{13}C_{org}$, HI, kerogen-type RE parameters) (see below).

5.4.1 Sediment accumulation and marine fluxes

TOC and $CaCO_3$ can be used to estimate past marine organic and carbonate productivity (chapter 3, sections 3.5.2, 3.5.4) and, combined with the b* index (chapter 3, sections 3.2.3), they can allow estimating past marine OM, carbonate and biogenic silicate productivity (Tada et al., 2015b). As TOC and $CaCO_3$ vary with b* over G-IG cycles, showing higher (lower) values during interglacials (glacials), this suggests that there is enhanced (reduced) marine productivity during interglacials (glacials) (figures 5.1a and 5.2b). However, dilution of the $CaCO_3$ and TOC signals by greater terrigenous input is an important consideration at this site, as well as decomposition and dissolution (chapter 3, sections 3.5.2, 3.5.4). The amount of terrigenous input is likely to have varied over G-IG cycles (Tada et al., 2015b) and so this needs to be considered in the context of variations in $CaCO_3$ and TOC over G-IG cycles.

A way to adjust for the effects of dilution is the transformation of contents into fluxes, i.e. the amount that sinks to a given area of seafloor over a certain time (chapter 3, section 3.5.5). Fluxes of TOC and $CaCO_3$ were calculated from bulk sediment mass accumulation rates (MAR) using equations 3.4 and 3.5 (chapter 3, section 3.5.5) and are presented in appendix A and figure 5.10. The calculated MARs (figure 5.10a) are high in sediments younger than MIS 20 (<320 m; range 50-110 g/cm2/ka) and lower before MIS 20 (>320 m; 30-65 g/cm2/ka), and peak (highest) across MIS 20 and 19 when sedimentation rates (SR) are highest (up to 90 cm/ka, chapter 4, section 4.3.2). Between MIS 39-21 MAR are relatively constant (range

~40-65 g/cm^2/ka), showing lowest values (~30 g/cm2/ka) during MIS 30-25. These bulk sediment MARs are much higher than typical examples from the open ocean. Examples from the Pleistocene show accumulation rates of <1.5 g/cm^2/ka in the South Atlantic (Zachos et al., 2004b) and around 0.5 g/cm^2 ka in the Indian Ocean (Sykes and Ramsey, 1995). Quaternary records of the Japan Sea show MARs range from ~3 g/cm^2/ka at IODP Site U1430 (Shen et al., 2017), to 4.1 g/cm^2/ka at ODP Site 797 (Tamaki et al., 1990; Irino and Tada, 2000) and 6.9 g/cm^2/ka (ODP Site 798; Dunbar, 1992) respectively (see figure 2.7 for site locations in the Japan Sea). Site U1427 shows about ~10-fold higher sediment MARs than these deep water settings, demonstrating once more the constant and high amounts of sediment accumulating at this site. This suggests that Site U1427 must have in addition to marine productivity high contributions of material from land.

Despite these high MARs, the bulk sediment geochemical records are very complex to interpret, especially during MIS 39-25 (section 5.3.1). Therefore, sampling was increased to the highest possible resolution of one sample per ~40 cm, based on samples available for this study. However, this did not increase the definition of G-IG cycles or have a significant impact on new signals emerging. In theory, given the high SRs, it should have been possible to record millennial-scale variabilities as the 40 cm resolution, which has 1-2 ka spaces between samples (see chapter 4). However, the heavy bioturbation (Tada et al., 2015b, c) seems to have destroyed the archives of Site U1427 for this high resolution through mixing of the sediments and attenuating the contained palaeo-signals.

The calculated fluxes of TOC and $CaCO_3$ (figures 5.10b,e) look very much alike the TOC and $CaCO_3$ contents (figures 5.1a, 5.2b), just shifted in a few places due to the few age markers in the age model that result in low resolution of SR and MAR records (chapter 4, section 4.3.2), used to calculate the fluxes. For reference, both individual sample fluxes and average fluxes across SR/MAR intervals are presented in figures 5.10b/d and 5.10c/e respectively. Individual sample fluxes have coherences with b* over G-IG cycles, showing higher (lower) values during interglacials (glacials). Most deviations from this relationship occur at times of very high or low MAR/SR, such as during MIS 20 and 21, likely being the result of the perturbations in MAR/SR (figure 5.10).

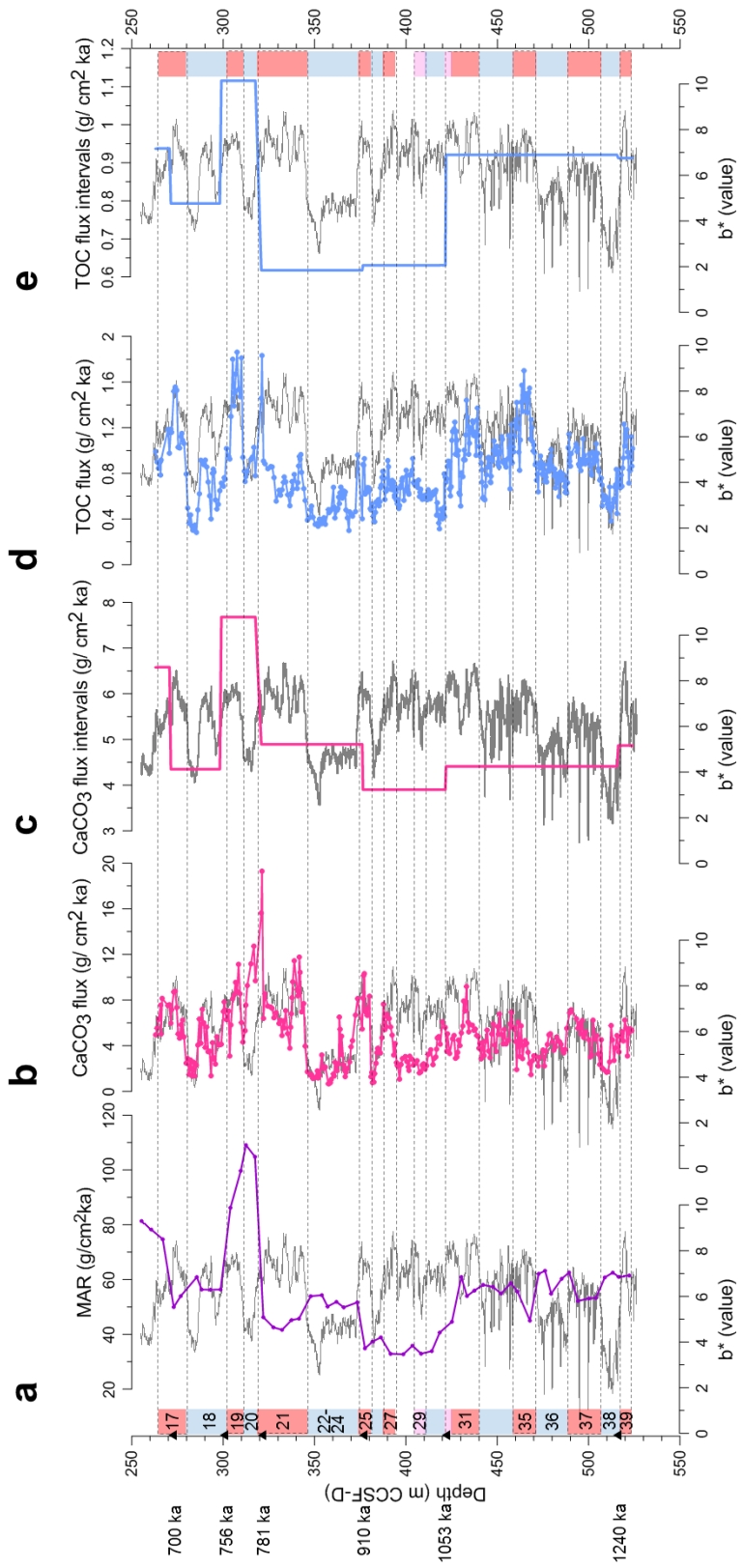

Figure 5.10. Bulk sediment mass accumulation rates (fig. 5.10a) and fluxes of $CaCO_3$ (fig. 5.10b) and TOC (fig. 5.10d). Seven changes in the sedimentation rates were identified (chapter 4, section 4.3.2) and, since these are having a strong influence on the fluxes, average fluxes are shown for each SR section (fig. 5.10c and e).

The $CaCO_3$ flux individual samples shows coherence with b*, which is most pronounced during MIS 39-36 and MIS 27-17, varying predominantly between ~2 and 12 g/cm^2/ka (figure 5.10b), comparable to the $CaCO_3$ flux of 0-1.5 g/cm^2/ka from the Sea of Okhotsk, across the same interval (Nürnberg and Tiedemann, 2004) and above the $CaCO_3$ fluxes of the Japan Sea Site ODP 798 of ~0-3 g/cm^2/ka (Stein and Stax, 1992a; figure 2.7). The relatively higher CaCO3 fluxes at Site U1427 compared to Site 798 is likely the result of its position above the CCD and relatively better carbonate preservation (Tada et al., 2015b; chapter 3, section 3.2).

The $CaCO_3$ flux of Site U1427 shows a steady reduction in the $CaCO_3$ flux across MIS 35-27, from values of ~8 to ~2 g/cm^2/ka, then G-IG cycles become more pronounced. Two features stand out from the record across MIS 27-17, a prolonged period of low $CaCO_3$ fluxes across MIS 24-22 with values around 2 g/cm^2/ka, and very high $CaCO_3$ fluxes across MIS 21-19 with values of up to 20 g/cm^2/ka (figures 5.10b, c). The reduced $CaCO_3$ flux across MIS 24-22 might be related to either reduced marine productivity producing less carbonates, or by post-depositional dissolution of carbonates. Dissolution makes carbonate shells, originally >63 µm, brittle and disintegrating into smaller carbonate fragments (then <63 µm). Therefore, dissolution can be expressed as reduced $CaCO_3$ content and increased fine-fraction, which is the case across MIS 24-22 (see grain-size distribution in figure 5.3). However, carbonate dissolution was probably low given the site's position above the CCD (chapter 3, section 3.2) and fine-grained sediments which reduce pore water circulation and diagenetic processes. Additionally, recent findings of well-preserved carbonate shells at Site U1427 (Gallagher et al., 2018; Sagawa et al., 2018; Saavedra-Pellitero et al., 2019) and well-preserved foraminifera shells across MIS 24-22 found in this study (chapter 4, section 4.4.2) make extensive dissolution less likely.

Across MIS 24-22 the $CaCO_3$ flux based on individual samples (figure 5.10b) shows values around 1-2 g/cm^2/ka, only between 370 and 360 m values nearly tripling to ~6 g/cm^2/ka. Since $CaCO_3$ fluxes are higher during interglacials this peak may indicate the position of MIS 23, which could not be identified based on the foraminiferal isotope stratigraphy generated in chapter 4 (section 4.4.4).

Well pronounced are also enhanced $CaCO_3$ fluxes across MIS 20-19 (figures 5.10b, c). During the glacial MIS 20 $CaCO_3$ flux is high while the content is low, suggesting high $CaCO_3$ input led to the high flux but at the same time a high level of

dilution through terrigenous input led to the content to be low. At this time TOC flux is as high as during MIS 21, suggesting continued high marine productivity (figure 5.10d). $\delta^{13}C_{org}$ shows lower values than during MIS 21, but still higher than during the glacials of MIS 24/22. As $\delta^{13}C_{org}$ is influenced by both marine productivity and the kind of terrigenous OM input (see chapter 3, section 3.5.2) it is hard to decipher the origin of the elevated values. However, in combination with enhanced TOC and $CaCO_3$ fluxes, continued marine productivity is the most likely cause of the enhanced $CaCO_3$ flux during MIS 20.

The TOC flux shows higher (lower) values during interglacials (glacials), especially prominent during MIS 39-31 and MIS 20-17 (figure 5.10d, e). The overall range of the TOC flux is ~0.3-1.8 g/cm^2/ka, which is above TOC fluxes calculated for ODP Site 798, ranging between 0.02-0.5 g/cm^2/ka (Stein and Stax, 1992a,b; figure 2.7). The overall higher TOC fluxes at Site U1427 compared to Site 798 likely reflect higher terrigenous OM input rather than better OM preservation, since Site U1427 should be better ventilated than Site 798 allowing for greater OM degradation.

One feature of the record is the high TOC flux during the lower part of MIS 35, simultaneously with high b* and, unusual for an interglacial at Site U1427, low $CaCO_3$ flux (figure 5.10d). The high TOC flux and high b* could indicate enhanced marine productivity, however this is not mirrored in the $CaCO_3$ flux. Higher TOC fluxes could also originate from enhanced OM preservation, although there is no change in lithology towards finer grained sediments or reduced bioturbation (figure 5.4), which would not suggest improved OM preserving conditions (figure 5.4). Another possible mechanism for enhanced TOC fluxes could be greater input of land-plant OM. Shipboard smear slide analyses show freshwater diatoms are present in the sediments during MIS 35 (section 5.3.4 and figure 5.6) which are assumed to have originated from lake or running water environments (Tada et al., 2015b), indicating enhanced terrigenous input at this time. The implied riverine input could have delivered OM to Site U1427 but at the same time also nutrients, priming marine productivity and increasing TOC fluxes. Therefore, the TOC flux increase during the lower part of MIS 35 could have originated from OM input from either marine or terrigenous sources, or a combination of both.

The interval MIS 30-21 is characterised by reduced TOC fluxes during interglacials, decreasing from up to 1.6 g/cm^2/ka during MIS 35 to <0.8 g/cm^2/ka during MIS 24/22, while glacial fluxes remain at a similar level, around 0.3-0.6 g/cm^2/ka (figure 5.10d). The prominent MIS 24-22 interval does not stand out significantly in the TOC flux, although fluxes remain close to the lowest values of ~0.3 g/cm^2/ka throughout this section, values similar to those found in the Sea of Okhotsk of ~0.0-0.2 g/cm^2/ka (Nürnberg and Tiedemann, 2004).

The low TOC fluxes during MIS 24-22 may imply either reduced OM input or reduced OM preservation. Reduced OM preservation is unlikely since the high SRs at Site U1427 favour good OM preservation through quickly removing OM from the sediment surface. In addition, the finer grained sediments across MIS 24/22 would make it hard for oxygen to penetrate the sediments and the laminated lithology suggests reduced oxygenation and low/absent bioturbation (see figure 5.4). Shipboard lithological data suggests higher siliciclastic contributions compared to marine particles. This is reflected in the findings of facies analysis carried out here, which suggests relatively more terrigenous particles, such as rock fragments and quartz grains across MIS 24/22 (section 5.3.4 for summary, appendix A).

On the other hand, the low $CaCO_3$ and TOC fluxes across MIS 24/22 (figure 5.10b, c) could imply reduced marine carbonate and OM productivity, or post-depositional alteration of both signals, i.e. OM decomposition reducing TOC and creating environments corrosive to carbonates. The b* index, closely related to marine biosiliceous productivity (chapter 3, section 3.2.3), is low as well, but crucially is not affected by the above processes of carbonate dissolution and OM degradation, suggesting reduced marine productivity is the most likely cause low TOC fluxes across MIS 24/22.

Within MIS 24-22 a peak of higher TOC fluxes occurs at 370-360 m of up to 0.6 g/cm^2/ka, indicating either enhanced OM input or better OM preservation. Since OM preservation is assumed to be at its best during MIS 24-22 (see above) this TOC flux peak more likely reflects enhanced OM input. Simultaneously a peak in $CaCO_3$ fluxes occurs providing support for enhanced overall marine productivity and OM export, although the sources of the OM cannot be differentiated by these proxies. Since OM content in the sediments tends to be higher during interglacials, the peak in these fluxes likely occurred during the MIS 23 interglacial, which could previously not be distinguished in the revision of the age model (chapter 4, section 4.4).

5.4.2 Recorders of terrigenous input 1, C/N ratios

A useful tool in to disentangle the varying contributions of marine and terrigenous OM is the application of C/N ratios (section 5.3.1). As described in chapter 3 (section 3.5.2) C/N ratios of 4.0-10.0 typically refer to OM originating from aquatic phytoplankton, while terrestrial plant material has C/N ratios higher than that (>15; Scheffer and Schachtschabel, 1984; Meyers and Lallier-Vergés, 1999).

The determined C/N ratios range from 3.3 to 15.0 with an average 10.0 (figure 5.11) and tend to be lower during glacials (around or below 10.0) and relatively higher during adjacent interglacials, usually being above 11.0 (figure 5.1c). Low C/N ratios are common in the Japan Sea. For example, at ODP Site 798, a deep water site in the Yamamoto Basin just north of Site U1427, C/N ratios range between ~2.0 and 15.0 over the last 1.5 Ma (Stein, 1991) and around 5.0-12.0 across the MPT (Stein and Stax, 1992a, b), showing values of up to 30.0 and an average of 10.0 in records covering the Miocene to Quaternary period (Stax and Stein, 1994). At ODP Site 798 the low C/N ratios have been interpreted as representing the dominance of marine-derived OM and mixed marine-terrigenous OM when C/N ratios approach their maxima of ~30. Such high, clearly terrigenous values are not observed at Site U1427. A recent publication by Black et al. (2018), investigating the sediments of the upper 250 m of Site U1427, C/N ratios vary between 4.0 and 32.0 (see chapter 3, figure 3.6). While the majority of C/N ratios gathered here for the lower 250 m fall within the range presented by Black et al. (2018) there are no C/N values above 15.0 in the lower 250 m (figure 5.11).

The simplified interpretation of the overall low C/N ratios on their own would suggest marine-derived OM dominates the sediments. Additionally, C/N ratios suggests the relative contribution of marine OM was higher during glacials due to the lower C/N ratios, while the terrestrial contribution was relatively higher during interglacials due to the higher C/N ratios (figure 5.1c). Some of the highest amounts of marine-derived OM and lowest C/N ratios would appear to have been deposited during the glacials of MIS 22, 24, 36 and 38 and interglacial MIS 21 (figure 5.11).

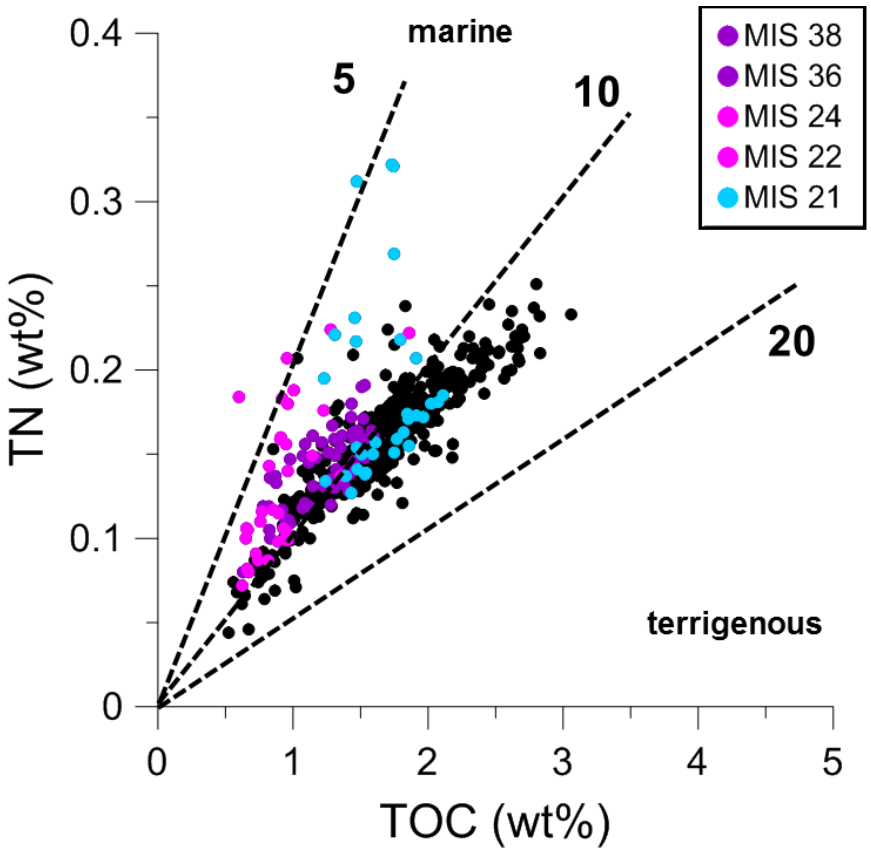

Figure 5.11. Cross-plot showing C/N data (black dots) plotting dominantly in the zone of marine-derived organic matter. MIS 21, 22, 24, 36 and 38, shown as examples, apparently contain highest contributions of marine-derived OM. C/N ratio lines (5, 10, 20) are for orientation (after Stein, 1991).

This interpretation of higher (lower) marine OM contributions during glacials (interglacials) is in stark contradiction to the prevailing palaeoceanographic models, which expect enhanced marine productivity and therefore higher marine OM contributions to the sediments during interglacials as a result of enhanced nutrient supply via the TWC inflow (see chapter 2, section 2.4) (Tada, 1994; Oba et al., 1991).

The apparent higher marine productivity during glacials from the exclusive interpretation of the low C/N ratios is misleading. It seems C/N ratios are not exclusively controlled by varying contributions of marine- and terrigenous-derived OM, but by additional processes that can affect C/N ratios. Such processes can include (i) various sources of OM (perhaps also not constant over time), (ii) low TOC values (<0.3 wt%) impacting the TN measurement (Meyers, 1997) and reducing C/N ratios (Meyers and Teranes, 2001), (iii) input of nutrients and enhanced marine productivity may not, as assumed, exclusively be controlled by the inflow of nutrient-rich TWC waters, but in addition by terrigenous nutrient input via dust or riverine

runoff from the nearby continents, and/or (iv) changes in the OM preservation. Low TOC values may not have affected the C/N ratios either, as TOC is continuously >0.5 wt% (figure 5.1a). Variations in OM sources can also be traced using $\delta^{13}C_{org}$ (section 5.3.1). $\delta^{13}C_{org}$ varies with G-IG cycles and in general C/N ratios follow G-IG cycles, although suggesting the reverse relationship with marine productivity of enhanced glacial productivity as inferred from low C/N ratios (figure 5.1c). From MIS 26 upwards the G-IG trends are weaker expressed suggesting the influence of varying sources of OM is likely to be small during this interval. Varying sources of nutrients (TWC, dust, riverine input) might have primed marine OM production at times at which the TWC could not enter the Japan Sea, priming marine OM productivity and leading to signals deviating from the trend of higher/lower interglacial/glacial productivity as suggested by the palaeoceanographic models (see chapter 2, section 2.4). This additional nutrient input cannot be studied with the methods applied in this work. The possibility of changes in OM preservation having led to the deviation of C/N ratios from the anticipated G-IG behaviour, as suggested by the palaeoceanographic models seems the most likely cause.

Changes in the preservation of OM can alter C/N ratios. Diagenetic alteration can especially affect algal OM, as cellulose-rich terrigenous OM is less degradable than algal OM (Meyers, 1994). In the anaerobic decomposition of carbon-rich components of OM carbon is remineralised and carbon is released from the sediments as CO_2 and CH_4 and diffuses away. Nitrogen however is converted to ammonium (NH_4^+) and becomes adsorbed to interlayers of clay minerals, becoming inorganically bound in the sediments (Müller, 1977; Waples and Sloan, 1980; Stein, 1991; Meyers, 1997; Meyers and Lallier-Vergés, 1999; Schubert and Calvert, 2001). This extra amount of inorganically bound nitrogen increases the amount of TN in the material (Müller, 1977; Meyers, 1994) and can lead to difficulties in the interpretation of TN and C/N ratios, especially in OM-poor sediments where it may become the major proportion of TN (Müller, 1977; Stein, 1991; Schubert and Calvert, 2001). It has been estimated that the sediments in the Japan Sea could contain ~0.035 wt% inorganically bound nitrogen (Irino and Tada, 2000). The addition of inorganically bound N increases TN contents and reduce C/N ratios, leading to an overestimation of the marine contribution to OM in the sediments.

The main clay mineral phase that nitrogen adsorbs to in low oxygen environments is illite where nitrogen substitutes for potassium in the crystal structure of illite

(Schubert and Calvert, 2001). Shipboard data describe enhanced amounts of illite in the sediments at depths that correspond to MIS 38-35 and MIS 24-21 (figure 5.12a) and elevated NH_4^+ values in the sediments of Site U1427 that would suggest OM decomposition in an oxygen-reduced environment (Tada et al., 2015b). Comparing the shipboard illite record with the C/N ratios (figure 5.12b) shows that often higher illite counts occur in tandem with lower C/N ratios, and vice versa. Examples of this are during MIS 38 (high illite, low C/N ratios), MIS 31-25 (low illite, high C/N ratios), and most pronounced during MIS 24-21 (high illite, lowest and most variable C/N ratios, figure 5.12).

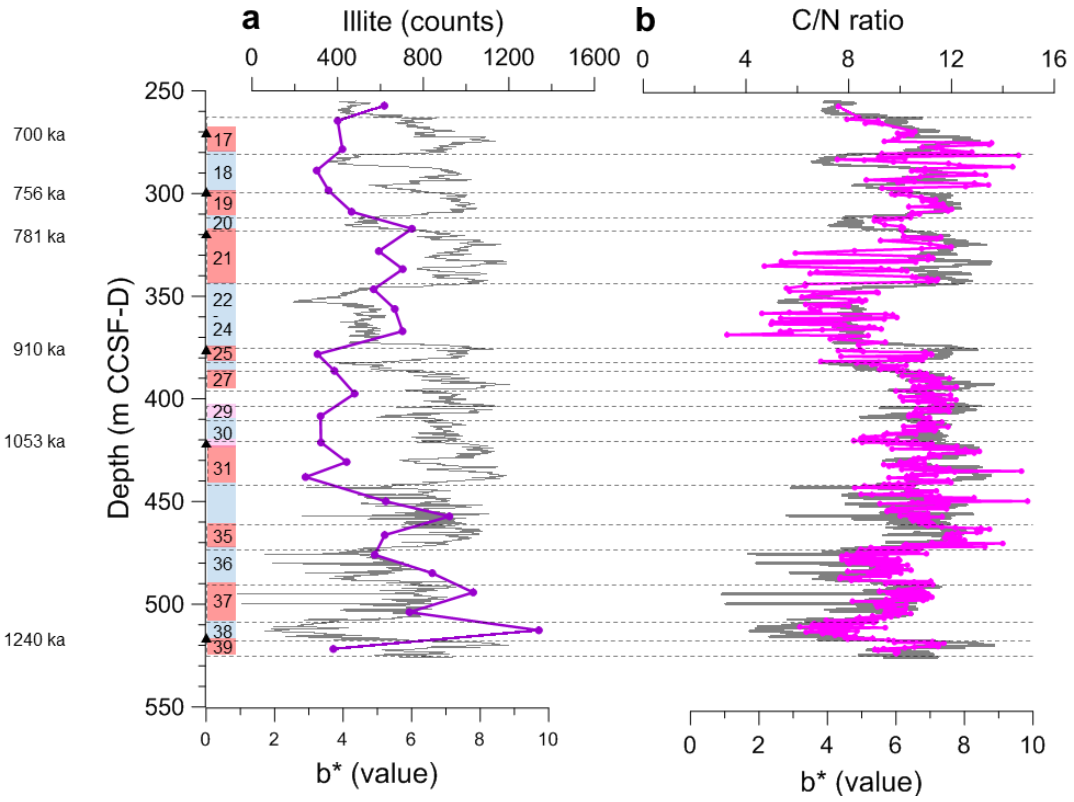

Figure 5.12. Comparison of illite record (fig. 5.12a, shipboard XRD data, Tada et al., 2015b) and calculated C/N ratios (fig. 5.12b).

During the two high-illite intervals of MIS 38-~35 and MIS 24-21 the C/N ratios behave somewhat differently. During MIS 24-21 illite is high and C/N ratios are low, which strongly points towards inorganically bound nitrogen in the system. This is supported by the shipboard lithological description, which describes the sediments as only slightly bioturbated or even laminated (345-375 m) suggesting low oxygen levels that would be needed for the anaerobic decomposition of OM in the sediments (Schubert and Calvert, 2001) and leading to enrichment of TN through inorganically bound nitrogen and low C/N ratios.

In contrast, during MIS 38-35 (~450-520 m) illite is high while C/N ratios follow the G-IG cycles, apparently unaltered by the effects of inorganically bound nitrogen. One can speculate that bioturbation could have played a role. The shipboard lithology describes the sediments as heavy bioturbated, at least between ~480-504 m, below which no bioturbation data has been logged. The presence of strong bioturbation implies relatively well oxygenated sediments, allowing organisms to thrive and burrow. Therefore, the heavily bioturbated sediments would limit the formation of a low-oxygen environment needed for the anaerobic decomposition of OM (Schubert and Calvert, 2001), and as a result nitrogen-enrichment through inorganically bound nitrogen would be limited. Furthermore, the OM flux (TOC flux, section 5.4.1) is higher during MIS 38-35 compared to MIS 24-22 suggesting inorganically-bound nitrogen might also make up a smaller proportion of total nitrogen contained in the sediments. While during MIS 24-22 when the TOC flux to the sediments is low, a greater proportion of total nitrogen would be present as inorganically-bound nitrogen, hence having a higher influence on the C/N ratios.

Looking at the possible input mechanism of clay (including illite) points to climatic differences between MIS 38-35 and MIS 24-22. Clay minerals, including illite, mainly enter the marine system through aeolian and/or riverine input (Griffin et al., 1968; Wefer et al., 1999). Across MIS 24/22 the climate across Asia has been suggested to have become more arid compared to pre-MIS 24, together with a strengthening in the EAWM and enhanced dust transport across Asia, as inferred from numerous marine and terrestrial records of Eurasian loess-paleosol sequences, pollen assemblages and dust input to the Asian seas (e.g. Raymo et al., 1997b; Heslop et al., 2002; Dodonov, 2005; Hoogakker et al., 2006; Wan et al., 2007; Kitaba et al., 2012; Zhai et al., 2020). This arid climate, combined with a glacial sea-level lowstand and associated cut-off of the nutrient supplying TWC, could have led to the high illite contents with simultaneous reduced marine productivity.

In contrast, the high illite contents of MIS 38-35 appear not to have altered the C/N ratios much. Another difference of MIS 38-35 from MIS 24-22 are relatively enhanced marine productivity and wetter climate. The wetter climate suggests a mechanism different from aeolian dust input for the origin of illite during this interval. In the East China Sea, illite-rich sediments occur at the river mouths of the Yangtze and Yellow Rivers (riverine input) and reflect the geochemical composition of loess deposits in the hinterland through which they cut (e.g. Griffin et al., 1968; Nie et al.,

2015). This suggests the possibility of illite being transported to Site U1427 by strong river runoff, when precipitation over the Yangtze and Yellow river source areas was high. Strong river runoff would enhance the TWC inflow in to the Japan Sea (chapter 2, section 2.4; Oba et al., 1991), which could have picked up illite from the sediment load and transported it to Site U1427. Since the TWC is considered the main input mechanism of nutrients to the Japan Sea (chapter 2, section 2.4) the strong TWC inflow would have primed marine productivity and OM production. The enhanced marine productivity, possibly in combination with also increased terrigenous OM input washed in from the nearby land, would have increased TN in the sediments and enhanced mixing of the water column, reducing the amount of inorganically bound nitrogen and its impact on C/N ratios.

In short, the interpretation of C/N ratios at Site U1427 is complicated and should be done with great care as C/N ratios are influenced by a combination of the amount and source of OM input, oxygenation (OM degradation) of the sediments as well as inorganically bound nitrogen and the amount of illite in the sediments. Although very challenging to interpret, C/N ratios can make a valuable contribution the interpretation of palaeo-productivity and input proxy records. Applying this proxy combination suggests that enhanced illite contents at Site U1427 reflects either arid climate with enhanced aeolian input through strong winds of an enhanced EAWM, or the opposite, wet climate with high amounts of riverine runoff and high marine productivity (strong EASM). Regardless of the input process, periods of enhanced illite contents are linked with enhanced terrigenous input, most pronounced during MIS 38-~35 and MIS 24-21 (figure 5.12).

5.4.3 Recorders of terrigenous input 2, $\delta^{13}C_{org}$ record and associated endmember model

To get more clarity on the counteracting effects of terrigenous input and marine productivity, further proxy records are needed to help to decipher the origin of OM, i.e. terrigenous or marine. One such proxy is $\delta^{13}C_{org}$ (figure 5.1d), which allows differentiation between marine OM (typically ~–20 to –22 ‰) and terrestrial land plants, with the majority of terrestrial land-plants belonging to C_3-plants and showing $\delta^{13}C_{org}$ values <–22 ‰, and aridity-tolerating C_4-plants typically showing values around –12 ‰ (see chapter 3, section 3.5.2). Typically, C/N ratios and $\delta^{13}C_{org}$ run opposite, with e.g. high C/N and low $\delta^{13}C_{org}$ indicating terrestrial origin of OM.

At Site U1427 $\delta^{13}C_{org}$ varies between ~–25 and –20 ‰ with an average of –21.7 ‰, suggesting a mix of marine and terrigenous OM sources. $\delta^{13}C_{org}$ shows a strong coherence with b* over G-IG cycles as the result of a strong link with marine productivity (figure 5.1d; see also chapter 3, sections 3.2.3, 3.5.2), becoming more positive/higher during interglacials implying relatively more marine-derived OM components, while glacials are characterised by lower $\delta^{13}C_{org}$ values indicate reduced marine and enhanced contributions of terrigenous-derived OM to the sediments. This interpretation fits to the interpretation of the TOC and $CaCO_3$ fluxes (section 5.4.1) and the palaeoceanographic models that suggest enhanced marine productivity during interglacials and relatively more terrigenous-derived material deposited in the Japan Sea during glacials (Oba et al., 1991; Tada, 1994; Saavedra-Pellitero et al., 2019) (see chapter 2, section 2.4).

The G-IG cycles in $\delta^{13}C_{org}$ are most pronounced during MIS 39-36 and MIS 26-17. An exception occurs during the mid-section of MIS 36, which shows slightly higher/more positive $\delta^{13}C_{org}$ values suggesting enhanced marine productivity during this glacial (figure 5.1d). At the same time $\delta^{18}O_{\textit{Uvigerina spp.}}$ shows lower values which suggests either a period higher glacial temperatures or enhanced freshwater input (figure 4.4; see also chapter 3, 3.5.10), which cannot differentiated based on $\delta^{18}O$ and $\delta^{13}C_{org}$ values alone. Further proxy records, e.g. foraminiferal Mg/Ca ratios and temperature estimates, are being used in chapter 6 to support this evidence.

During MIS 39-27 the difference between glacial and interglacial $\delta^{13}C_{org}$ values becomes gradually smaller, reducing from about –20 to –23.5 ‰ (at MIS 39-35) to –20 to –22 ‰ (at MIS 29-27) (figure 5.1d). While the interglacial values remain relatively stable around –21 ‰, glacial $\delta^{13}C_{org}$ values gradually increase from ~–23 to ~–21.5 ‰. This gradual glacial $\delta^{13}C_{org}$-increase could be caused by higher contributions of marine OM, typically having values of –22 to –20 ‰ (see chapter 3, section 3.5.2) or by a change in the source of the terrigenous OM, i.e. a change from low $\delta^{13}C_{org}$ C_3-plants with typical $\delta^{13}C_{org}$ values below –22 ‰ to a greater proportion of aridity-tolerating C_4-plant OM with typical values around –12 ‰ (chapter 3, section 3.5.2).

To investigate the possible change from OM dominated by C_3- to C_4-plants a cross-plot of C/N versus $\delta^{13}C_{org}$ can be very useful (chapter 3, section 3.5.3, figure 3.7), although care must be taken in this case due to the issues surrounding the

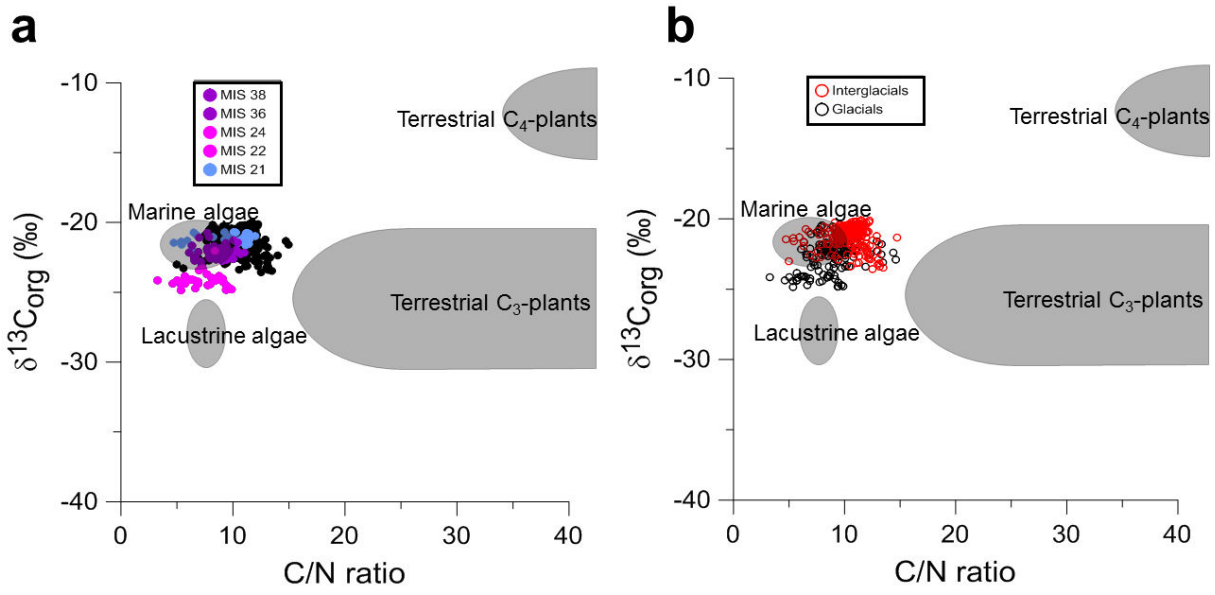

Figure 5.13. Cross-plot of $\delta^{13}C_{org}$ and C/N ratios showing all data (black dots) and additional differentiation into MIS 38, 36, 24-22 and 21 (fig. 5.13a) and glacials/interglacials (fig. 5.13b). Shaded areas indicate typical values for marine and lacustrine algae as well as terrestrial C_3- and C_4-plants (after Meyers, 1994 and Meyers and Lallier-Vergés, 1999).

interpretation of C/N ratios: While the C/N differences between glacials and interglacials have likely been affected by an inorganic contribution of N (section 5.4.2), the overall C/N ratios (across all glacials and interglacials) may be less skewed. The interpretation of this cross-plot suggests the sediments are dominated by marine-derived OM, with minor terrigenous (C_3-plant and/or lacustrine algae) contributions (figure 5.13a). Splitting the data into glacials MIS 38, 36, 24, 22 and data outside these intervals (including MIS 35-27) shows (i) the marine component is lowest during MIS 24/22 and some data points plot close to values characteristic for lacustrine algae, indicating enhanced terrigenous or indeed freshwater input at this time (figure 5.13a). Freshwater input can also be inferred from shipboard diatom data, which suggested freshwater diatoms being washed-in during MIS 24-22 (figure 5.6). (ii) Compared with MIS 24-22 during MIS 38/36 relatively more marine-derived OM is contained in the sediments with few data points having C/N ratios >10, plotting towards the field of C_3-plant OM. (iii) The OM of interglacial MIS 21 (figure 5.13a), which potentially contains high amounts of inorganically bound nitrogen that reduced C/N ratios (figure 5.12), does not differ much from other interglacials in its OM composition (figure 5.13b), containing predominantly marine-derived OM. This indicates some inorganically bound nitrogen is constantly present in the sediments of Site U1427, as previously been suggested from deep waters sites in the Japan Sea

(Irino and Tada, 2000). (iv) The data presented here do not suggest a change from predominantly C_3- to C_4-plant OM as no shift towards much higher/more positive $\delta^{13}C_{org}$ occurs in the data.

Further evidence that contradicts a change from C_3- to C_4-plant OM-dominance across the MPT comes from the interpretation of previous proxy records (sections 5.4.1, 5.4.2), which compared to MIS 24/22 suggested a wetter climate during MIS 35-27 to which C_3-plants are better adapted (see above and chapter 3, section 3.5.2). The suggested wetter climate is also mirrored in the $\delta^{18}O_{\textit{Uvigerina spp.}}$ record (figure 4.5), which is highly variable during this interval as a result of local freshwater input events overriding the global ice volume signal/temperature (see chapter 2, section 2.4 for details).

Previous studies on the development in the Asian monsoon system also suggest wetter conditions developing across the MPT, including MIS 38-25. For example, mineralogical and facies studies of loess-paleosol sequences from the CLP suggest a significant precipitation increase and EASM strengthening starting around 1200 ka (An et al., 1990; Han et al., 2012; Meng et al., 2018), which has recently been shown to affect interglacials (Sun et al., 2010) and, more significantly, glacials, beginning around the termination of MIS 38/37 (Li et al., 2017; Meng et al., 2017) or MIS 36 (Peng et al., 2020). Vegetation-based evidence confirms the wet climate from ~MIS 38 onwards, as inferred from pollen and spore assemblages in sediments samples from outcrops on the Okinawa Islands (southern Japan) (Fujiki and Ozawa, 2008).

Across MIS 39-17 high rainfall has been suggested for the interglacials MIS 37, 35, 31, 29 and 25 with up to 450-490 mm annual mean precipitation on the CLP, while precipitation was lowest during MIS 38 and 22 with ~30 mm/a as reconstructed from a loess magnetic susceptibility record of the central CLP (Peng et al., 2020). The low precipitation reconstructed for MIS 38 and 22 is confirmed by loess-paleosol sequences of the CLP which indicate stronger EAWM winds and sparser vegetation coverage (Guo et al., 1998). The reconstructed rainfall further suggests highly variable precipitation across MIS 35-31 with much more precipitation during interglacials during than glacials (interglacials ~360-450 mm/a, glacials 150-210 mm/a) and relatively stable precipitation across MIS 30-26, especially during glacials, of ~330-420 mm/a (Peng et al., 2020). The stable wet conditions are mirrored in an expansion in evergreen broadleaved-tree dominated temperate warm forest between 1000 and 800 ka, approximately MIS 28-20 (Fujiki and Ozawa, 2008). These findings

from literature fit well with findings of Site U1427, from this and other studies. The precipitation increases fits well with the timing of the sudden increase in and elevated values of illite found by the shipboard party across MIS 38-31 (figure 5.12a). Illite is a clay mineral, which is likely to have been delivered to the site via riverine runoff, although local ocean current systems may have played a role too (section 5.3.4).

From MIS 25/24 onwards glacial precipitation is reduced to minima of 50-100 mm/a, with lowest reconstructed precipitation on the CLP of ~30 mm/a during MIS 22 (Peng et al., 2020). The reduction in glacial precipitation is mirrored in the CLP vegetation coverage, which reflects a semi-desert landscape (Guo et al., 1998) and in the Japanese vegetation cover. For example, Kitaba et al. (2012), who investigated vegetation/pollen records in Osaka Bay, central Japan, found evidence for a wet climate and the dominance of C_3-plants during glacials and interglacials alike between 39 and MIS 25, and a shift towards dryer glacial conditions from MIS 24 onwards. Their data suggests that interglacial vegetation cover was dominated by a deciduous broadleaved forest, including beech trees and oaks , throughout the interval MIS 39-17, but glacial vegetation shifted from dominating Taxodiaceae (cedars, redwood tress) to dominating Pinaceae (including sub-boreal pines and firs) from MIS 22 onwards, indicating cooler and dryer glacials (Kitaba et al., 2012).

Despite the shift in glacial vegetation dominance, all these plants are C_3-plants, which contradicts the idea that high glacial $\delta^{13}C_{org}$ values across MIS 39-25 might have originated from a shift to aridity-tolerating, higher $\delta^{13}C_{org}$-yielding C_4-plants. Instead, high glacial $\delta^{13}C_{org}$ values across MIS 39-25 most likely originate from enhanced marine productivity. In contrast, across MIS 25-17 glacial $\delta^{13}C_{org}$ values become as low as ~–25 ‰, especially during MIS 24-22 (figure 5.1d). These values are close to the values typically expected for pure C_3-plant OM of the dominant plants described by Kitaba et al. (2012), for example, Taxodiaceae OM typically has average $\delta^{13}C_{org}$ values of ~–25.4 ‰ (Smith and Epstein, 1971), cedars ~–26.4 ‰ (Chikaraishi et al., 2004), Pinaceae have on average ~–30.8 ‰ and oaks typically ~–28.9 ‰ (both Smith and Epstein, 1971). This δ13Corg evidence suggests a change in the amount of glacial productivity/terrigenous input across the investigated interval. Across MIS 39-25 glacial marine productivity seems to have been relatively higher than during MIS 24-17, when the relative contribution of terrigenous-derived OM must have been higher.

To quantify the amount of marine/terrigenous OM in the sediments and to determine the local $^{13}C/^{12}C$ ratio, the generation of a $\delta^{13}C_{org}$ endmember model can be useful. For this quantification the average $\delta^{13}C_{org}$ value of terrigenous-derived OM was analysed (chapter 3, section 3.5.3), with the results of terrestric OM showing $\delta^{13}C_{org}$ values of –26.9 to –24.8 ‰, with an average of –25.8 ‰ (table 5.1).

Hole	Core	Sect	Depth (cm)	Depth (m CCSF-D)	$\delta^{13}C_{org}$ (‰)
B	51	2	118	369	–24.8
A	51	1	71	376	–25.6
C	46	2	52	349	–26.4
A	68	6	15	446	–25.7
B	39	4	55	312	–26
B	58	2	134	402	–25.1
B	45	2	113	340	–26.9

Table 5.1. Results of terrigenous OM particle $\delta^{13}C_{org}$ analyses of seven selected samples rich in terrigenous OM particles.

Using the average $\delta^{13}C_{org}$ value as an endmember for 100% terrigenous OM and assuming value of –20 ‰ for 100% marine-derived OM, as it is the highest measured $\delta^{13}C_{org}$ value, i.e. closest to 100 % marine. This approach makes sure that all measured $\delta^{13}C_{org}$ values fall within the calculation range and enables estimating the relative contributions of marine/terrigenous OM to each analysed sediment sample (figure 5.14). Based on the estimates the sediments contain between about a third (~30.7 %) and nearly fully marine-derived OM (98.7 %), on average ~75.7 %. At ODP site 798, nearby Site U1427 (figure 2.7), it was estimated that 50-80% is marine-derived OM (Stein and Stax, (1992a), suggesting a greater sensitivity of Site U1427 to changes in the marine and terrestric realms. However, there is large uncertainty associated with these estimates arising from the range of $\delta^{13}C_{org}$ values measured in the terrigenous OM particles.

The uncertainty associated with the approach is shown here for the example of the lowest $\delta^{13}C_{org}$ value recorded, –25 ‰ at MIS 22 (see figure 5.14). If using the lowest $\delta^{13}C_{org}$ value of the terrigenous OM particles, –26.9 ‰, in the calculation of marine OM contributions at MIS 22 then the estimate would be that around 27.5 % of sample OM are of marine origin. In contrast, if using the highest values of terrigenous

OM particles in the calculation of the same sample, –24.8 ‰, then it would be estimated that only 4.2 % of OM is marine OM. For comparison, using the average terrigenous OM value of –25.8 ‰ $\delta^{13}C_{org}$ for the same sample leads to an estimated 30 % of the sample OM being of marine origin (figure 5.14). While values closer to that of marine OM, i.e. closer to –20 ‰, have smaller uncertainty, the above calculation for OM with values closest to that of terrigenous OM has shown that the uncertainty in estimating the OM origin using the endmember approach can be as much as 23 %. Therefore, the following interpretation, which uses the average terrigenous particle $\delta^{13}C_{org}$ value, needs to be taken cautiously.

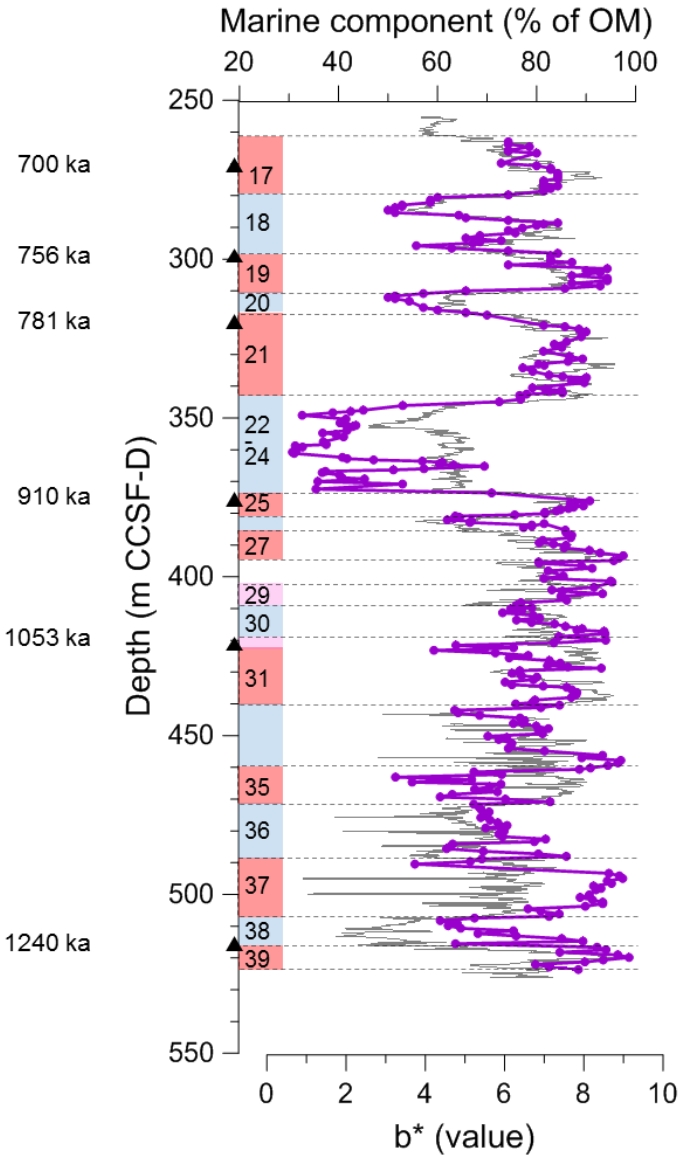

Figure 5.14. The $\delta^{13}C_{org}$ endmember model showing the estimated amount of marine OM contributions to the bulk sediment $\delta^{13}C_{org}$ record (shown in figure 5.1d).

The endmember model data follows G-IG cycles, showing a higher marine component during interglacials (generally ~90 %) and less marine-derived OM during glacials where the terrigenous component is correspondingly higher. Across MIS 39-36 the G-IG cycles are well expressed but during MIS 35-27 they become less pronounced. This attenuation of the G-IG cycles in the $\delta^{13}C_{org}$ endmember is mainly due to a steady increase in the glacial marine OM contribution, which increases from ~65 % during MIS 38/36 to ~70-75 % during MIS 30/28, while the interglacial contribution remains constant around 90 % (figure 5.14). A likely cause for this glacial marine OM increase across MIS 35-27 could be the enhanced precipitation (see above, Kitaba et al., 2012; Peng et al., 2020), which would have increased the contribution of nutrient-rich ECSCW to the TWC, ultimately leading to enhanced marine productivity in the Japan Sea (see chapter 2, section 2.4). This mechanism of primed marine productivity through TWC inflow should however not have been possible at glacial sea-level lowstands, as the shallow sills (~120 m maximum) would have prevented the TWC from entering the basin according to the palaeoceanographic model (chapter 2, section 2.4) (e.g. Oba et al., 1991; Tada, 1994; Tada et al., 1999). The seemingly absence of a sea-level mechanism on marine productivity across MIS 35-27 need to be investigated (see chapter 6).

The lowest marine OM contributions are found during the glacials MIS 24 and 22 (~30 %). During this interval a peak occurs between ~360 and 370 m where marine OM contributions more than double, increasing to nearly 70 %. This may be another indication for the position of the interglacial MIS 23, which could not be identified in the revision of the age model based on the benthic foraminiferal $\delta^{18}O$ and b* records (chapter 4, section 4.4). The low $\delta^{13}C_{org}$ values during MIS 24-22 are a prominent feature of the $\delta^{13}C_{org}$ record and endmember model. The inferred enhanced terrigenous input would suggest either enhanced riverine runoff or the opposite, enhanced dry climate eroding material, both would increase the amount of terrigenous OM delivered.

Colder and drier glacial climates across MIS 24-22, compared to glacials across MIS 39-25, can be inferred from local pollen records and precipitation reconstructions (see above; Kitaba et al., 2012; Peng et al., 2020), but MIS 24/22 is also pronounced in $\delta^{13}C$ records from other, globally distributed locations. For example, an overall 3 ‰ mean ocean $\delta^{13}C$ decrease is inferred from foraminiferal $\delta^{13}C$ across sites in the Atlantic and equatorial Pacific (Raymo et al., 1997b), and is suggested to have

originated from a large one-off input of ^{13}C-depleted terrestrial OM eroded from the exposed shelves during very low sea-level stands and a more arid climate, as inferred from pollen and dust records (Raymo et al., 1997b, and references within; Hoogakker et al., 2006). It has also been suggested that changes in the global ocean-atmosphere carbon-cycle may have played an important role during the MPT (see chapter 2, section 2.3), by removing atmospheric CO_2 and exporting and storing it in the oceans (Broecker, 1982; Raymo et al., 1997b; Chalk et al., 2017; Farmer et al., 2019b). This atmospheric CO_2 decrease is thought to have allowed the ice sheets to expand during MIS 24-22 (Elderfield et al., 2012; Rohling et al., 2014) and ultimately controlled the onset of the 100-ka G-IG cycles (Farmer et al., 2019b).

In summary, the $\delta^{13}C_{org}$ record and endmember model show that the sediments contain a mix of marine-/terrigenous-derived OM, containing on average ~75 % marine-derived OM. There are strong G-IG cycles in the $\delta^{13}C_{org}$ record between MIS 39-36, which become weaker expressed during MIS 35-27, likely caused by glacial increase of marine-derived OM shifting $\delta^{13}C_{org}$ values towards interglacial values. Previous pollen studies and precipitation reconstructions for the CLP also suggest subsequently wetter climate during this interval. However, marine productivity in the Japan Sea is linked to the inflow of nutrient-rich TWC waters, which should have been prevented to enter the basin during glacial sea-level lowstands (chapter 2, section 2.4), so marine productivity during MIS 35-27 is seemingly decoupled from the control of eustatic sea-level fluctuations. Further investigations into the possible effect of sea-level fluctuations across the MPT on Site U1427 are made in chapter 6. Across MIS 24-27 well-pronounced G-IG return to the $\delta^{13}C_{org}$ records, fitting again to the palaeoceanographic model and general climatic trends.

5.4.4 Recorders of terrigenous input 3, Rock-Eval pyrolysis

For greater clarity on the origin of OM in the sediments and to overcome the contradicting interpretations of C/N ratios (section 5.4.2) and $\delta^{13}C_{org}$ (section 5.4.3) analyses, Rock-Eval pyrolysis (RE) was undertaken to provide an independent proxy for the OM origin. RE was applied to samples from the intervals MIS 39-35 and MIS 27-19, which have been suggested to work differently due to a possible change in the palaeoceanography of the Japan Sea and/or climatic changes (see sections 5.4.1-5.4.3).

Analysis of a cross-plot of RE-derived TOC and HI values can help to differentiate between marine/algal and terrigenous-/non-algal derived OM (figure 5.15). The low HI values of <400 mgHC/gTOC would traditionally be interpreted as sediments dominated by terrigenous-derived OM. However, in immature marine sediments, such as at Site U1427 characterised by T_{max} of ~390-430 ºC (figure 5.9a), marine algal-dominated OM can show lower HIs, in the range of 200-400 mgHC/gTOC (Stein et al., 1989; Stein, 1991). Similarly low HI values are also found at other sites in the Japan Sea, for example, from sites near the TSS, which show HI values of 0-~250 mgHC/gTOC (Kim et al., 2007) and/or ODP site 798, which shows HI of ~100-500 mgHC/gTOC (Stein and Stax, 1992a,b). The interpretation of these low HI values as originating from a high marine/algal OM component fits with the estimated ~75 % average marine-derived OM based on the $\delta^{13}C_{org}$ endmember model (section 5.4.3).

Lowest HI/TOC ratios occur during glacials MIS 24/22 and MIS 38, while part of MIS 36 shows slightly higher HI/TOC ratios, plotting closer to those of interglacial values. The low HI/TOC ratios during the glacials MIS 38, 36, 24 and 22 compared to relatively higher interglacial values imply higher terrigenous-derived, non-algal OM contributions to the sediments at these times, while interglacials and part of MIS 36 have relatively higher HI/TOC ratios and hence contain relatively more marine-algal OM (figure 5.15; Meyers and Lallier-Vergés, 1999; Stein et al., 1991; Wagner and Dupont, 1999; Killops and Killops, 2005). This contradicts the interpretation of C/N ratios, which have suggested higher (lower) terrigenous OM contributions during interglacials (glacials) (section 5.4.2), but fits well to the G-IG cycles seen in the $\delta^{13}C_{org}$ data (section 5.4.3).

Possible reasons for the conflicting interpretations of C/N and HI/TOC is in the reliability of these data. As discussed in section 5.4.2 C/N ratios are altered at least in some parts of the sediment cores by inorganically bound nitrogen, reducing C/N ratios and making the record less reliable. HI values on the other hand need to be interpreted cautiously in particular in settings with young, TOC-poor (~<1 wt%) marine sediments, deposited in close proximity to land, such as Site U1427 (glacial TOC as low as ~0.5 wt%; figure 5.1a). In such settings HI values can be affected by so called mineral matrix effects, which can hinder a meaningful interpretation of HI (Katz 1973; Espitalié et al., 1984; Stein 1991; Wagner and Dupont, 1999).

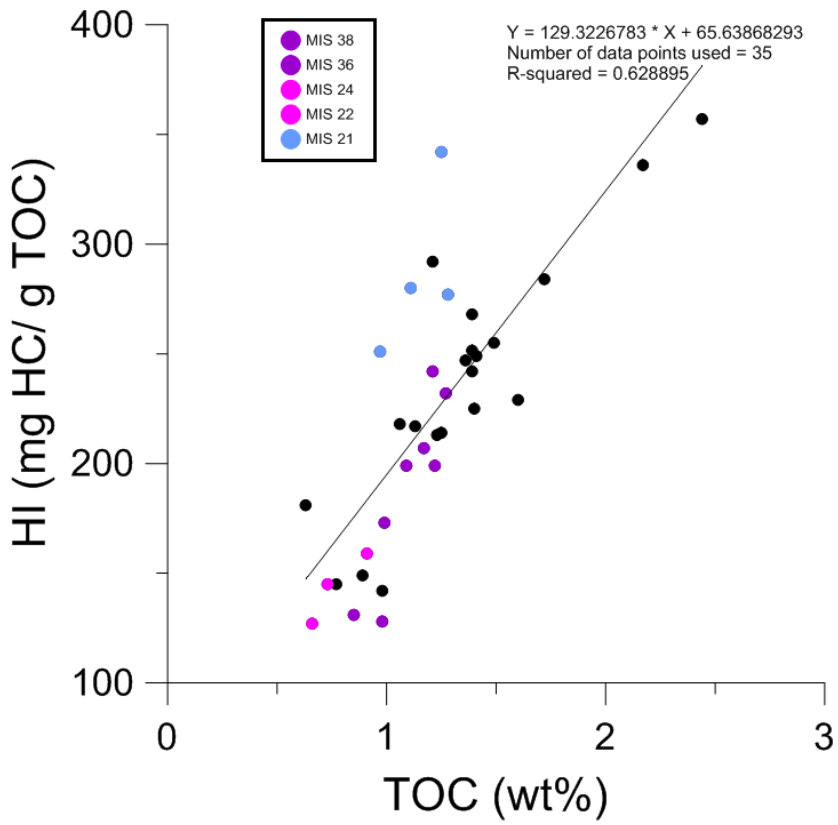

Figure 5.15. Cross-plot of RE-derived TOC versus HI across MIS 39-35 and MIS 24-22. Black dots represent interglacial data, while pink/purple dots highlight glacials MIS 38, 36, 24 and 22.

Mineral matrix effects can be caused by the input of fresh plant matter, which leads to retardation during the RE pyrolysis and/or input of heavily oxidised OM, such as reworked fossil material eroded from an old strata and transported, burned OM (charcoal) and/or fresh marine algal OM that has been heavily oxidised during sinking in the water column and exposure on the sea floor (Thomas Wagner, pers. coms.). When HC-rich algal OM is oxidised its HI decreases while its OI increases (Espitalié et al., 1977; Peters, 1986; Meyers and Lallier-Vergés, 1999), which shifts the values closer to those typically associated with terrigenous OM and leads to an underestimation of the marine OM component.

While the input of burned OM to the (northern) Japan Sea is thought to have been relatively stable across the investigated interval and only increased during MIS 21 (Lu et al., 2018), the OM degradation and/or reworking need to be tested. A way to test for possible mineral matrix effects is a cross-plot of S_2-peak versus TOC (figure 5.16). Should a well-fitting correlation curve through the data trend towards the origin of the axes, there are no noticeable mineral matrix effects on the HI values (Disnar et al., 2003). The RE data of Site U1427 is trending towards the origin, and a well-

fitting, linear regression with an r^2 of >0.9 cutting the x-axis at ~0.5 wt% TOC, excluding mineral matrix effects may have played a major role, suggesting therefore these HI values can be assumed trustworthy (Figure 5.16). This supports the concordant interpretation of $\delta^{13}C_{org}$ and HI of enhanced terrigenous-derived OM contributions during glacials, most pronounced during MIS 38 and 24/22, and relatively higher marine-derived OM during interglacials.

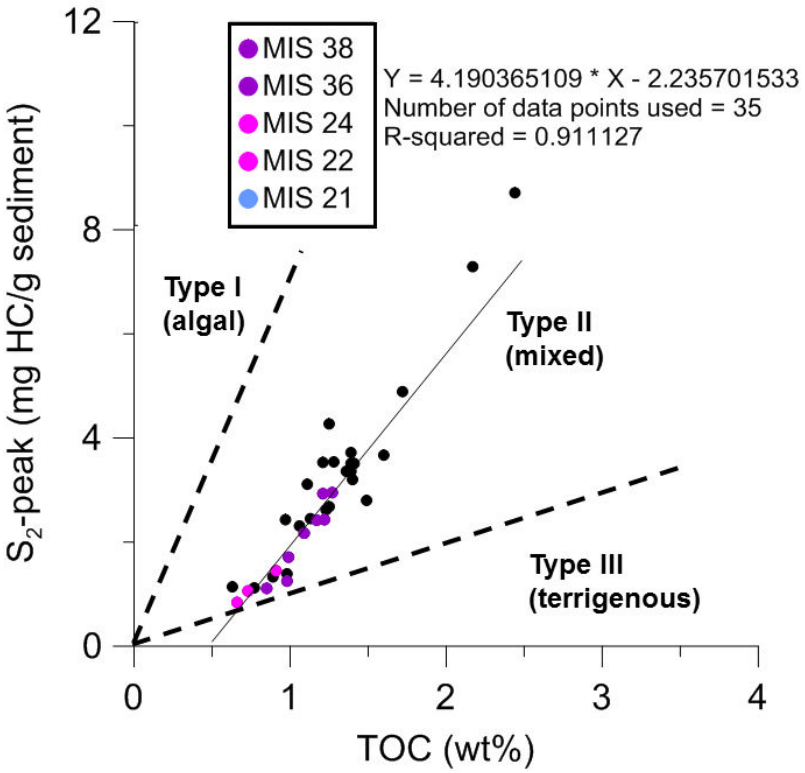

Figure 5.16. Cross-plot of RE-derived TOC and S_2-peaks. Dashed lines subdivide the plot into predominantly algal (type I), mixed algal-terrigenous (type II) and terrigenous (type III) OM (after Langford and Blanc-Valleron, 1990), with data plotting predominantly in the field of mixed terrigenous-algal OM and the data of some glacials (MIS 38, 24, 22) close to the field of predominantly terrigenous-derived OM.

An S_2-peak/TOC cross plot can also be used to investigate OM, allowing differentiation between algal- and terrigenous-derived OM (after Langford and Blanc-Valleron, 1990; figure 5.16). It suggests the OM is predominantly mixed algal-terrigenous-derived with some of the glacial data (MIS 38, 36, 24 and 22) containing predominantly terrigenous-derived OM.

Another way to investigate the OM origin is using a pseudo-van Krevelen diagram of HI versus OI (Espitalié et al., 1977; Meyers and Lallier-Vergés, 1999; Meyers and Teranes, 2001; see also chapter 3, section 3.5.6). In this plot the data plots between the fields of type II (algal) and type III (terrigenous, vascular plants) OM, signifying

again a mix of marine and terrigenous material (figure 5.17). The glacials MIS 38, 36, 24 and 22 show lowest HI (<200 mg HC/g TOC) and moderate OI (100-250 mg CO_2/g TOC) values, while the interglacial data show higher HI (up to 400 mg HC/g TOC) and OI values (up to ~300 mg CO_2/g TOC), suggesting either (i) higher amounts of vascular land plant OM contributions during the glacials (and relatively higher algal OM contributions during the interglacials) or (ii) the glacial values have been altered through the effect of oxidation (degradation/ diagenesis/ mineral matrix effects). The range of OI values at Site U1427 sits within OI range of ~50-500 presented from other sites in the Japan Sea (Stein and Stax, 1992a,b; Kim et al., 2007).

To differentiate between higher vascular plant contributions and OM degradation an oxidation-line of OM can be useful (see figure 5.17). This line follows the path algal OM would take during increasing degrees of oxidation/degradation, reducing its original HI and increasing its OI (Espitalié et al., 1977; Peters, 1986; Meyers and Lallier-Vergés, 1999). The glacial data predominantly plot below the oxidation line while interglacial data, as an example MIS 21 highlighted in figure 5.17, plot closer to or above the line. If the glacials did originally contain more algal OM, as suggested by the C/N ratios (section 5.4.2), oxygenation would have shifted their values roughly along the oxidation line to their current place in figure 5.17. However, evidence against widespread oxygenation comes from the shipboard lithology, which describes the sediments as laminated during MIS 24-22 (see chapter 3, section 3.2.2), indicating reduced oxygenation of the sediments and absent bioturbation or very high sedimentation rates, although this is contradicted by the calculated sedimentation rates in this interval, being around 40 cm/ka (figure 4.2b). The RE-data that tested for possible mineral matrix effects on HI values and which are related to oxygenation/degradation of OM, showed no noticeable alterations (figure 5.16). From this evidence it can be inferred that the low HI during MIS 24/22 do not reflect heavily oxidised OM and do not represent a diagenetically altered signal, but instead reflect enhanced contributions of terrigenous-derived OM from vascular land plants.

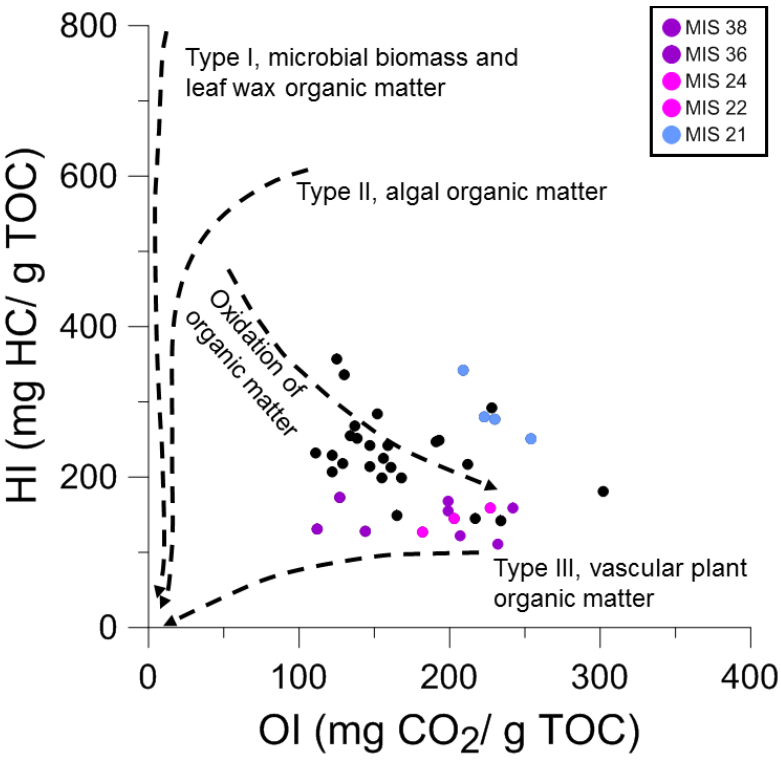

Figure 5.17. Pseudo-van Krevelen diagram (after Espitalié et al., 1977; Meyers and Lallier-Vergés, 1999; Meyers and Teranes, 2001), including "oxidation of organic matter"-line after Meyers and Lallier-Vergés (1999).

Outside MIS 24/22 and including the pronounced glacials of MIS 38/36 the sediments are well bioturbated and C/N ratios are unaltered by the effects of high illite contents (section 5.4.2), both indicating better oxygenated sediments than during MIS 24/22. Relatively higher HI/OI values across the analysed interglacials means data is plotting closer to values characteristic for algal OM (type II) than the data of MIS 24/22. This could either mean OM deposited during interglacials has not been affected by diagenesis or the sediments originally contained relatively more algal OM, yielding higher HI values than those of MIS 24/22. The potential for diagenetic alteration in these sediments is higher due to the better oxygenation, suggesting that originally high HI values from higher marine-derived OM input is the more likely cause. This interpretation of RE data of higher marine OM input during interglacials and relatively more terrigenous-derived OM during glacials is concomitant with the $\delta^{13}C_{org}$ interpretation (section 5.4.3).

5.5 Summary and Conclusions

The analyses of the geochemical and sedimentological proxy records (section 5.3) has shown these marine sediments are a complex mix of marine production and

constant terrigenous background sedimentation. In this and previous studies, such as the shipboard report (see chapter 3, sections 3.2 and 5.3.3, 5.3.4) as well as in recent studies of the upper 250 m of Site U1427 (Sagawa et al., 2018; Gallagher et al., 2018; Black et al., 2018) it has been shown that changes in the sediment composition occur with G-IG cycles. The sediments contain higher amounts of $CaCO_3$, TOC and more marine-/algae-derived OM during interglacials indicting enhanced marine productivity. In contrast, glacials have relatively higher terrigenous input, such as siliciclastic and C_3 land-plant particles and potentially mixed in lacustrine algae OM and freshwater diatoms (sections 5.3.4, 5.4.1, 5.4.2, 5.4.3). At Site U1427, nutrient input and hence primary productivity is likely to be influenced by monsoonal precipitation (Tada et al., 2015b) and additionally by riverine input from the nearby land (section 5.4.1).

There are sub-orbital timescale palaeo-signals emerging from the proxy records, where marine productivity/terrigenous input deviate from their anticipated behaviour across G-IG cycles. An example is MIS 36, which shows higher $\delta^{13}C_{org}$ values indicating enhanced marine productivity during its mid-section (see section 5.4.3). Since nutrient-supply and marine productivity in the Japan Sea are controlled by EASM precipitation intensity, besides eustatic sea-level fluctuations (see chapter 2, section 2.4), the enhanced marine productivity during MIS 36 implies enhanced nutrient input either controlled by a higher glacial sea-level or a strengthening in the EASM (on sub-orbital timescales) or both.

The calculated bulk sediment mass accumulation rates at Site U1427 are much higher than in the open ocean or at deep water sites in the Japan Sea (section 5.4.1), implying constant and high contributions from land in addition to marine productivity. Although sediment accumulation is high and in theory could have recorded (sub-) millennial-scale variabilities (chapter 4, section 4.3.3), increasing the marine productivity/terrigenous input records of TOC, TN, $\delta^{13}C_{org}$ to their maximum temporal resolution of ~0.4 m spacing (samples available for this study; see chapter 3, section 3.5.2) across MIS 39-25 did not lead to the emergence of new palaeo-signals. Therefore, while sub-orbital-scale signals could be contained within the sediments, the heavy bioturbation across most of the investigated interval (Tada et al., 2015b, c) likely has affected the archive in some intervals for millennial-scale variability, and certainly for sub-millennial-scale variability (see section 5.4.1), including those associated with DOCs, which are centennials in length and millennials apart (chapter

2). This is supported by the shipboard lithology, which shows the millimetre- to centimetre-scale dark/light sediment alternations, typically associated with DOCs in the Japan Sea, are absent across the MPT at Site U1427.

The multi-proxy approach chosen here has proved indispensable to decipher the origin of OM in the sediments, i.e. marine production or terrigenous input. In this complex setting all proxy records need to be interpreted very carefully and some of the traditional marine proxy records have been brought close to their limits of being interpretable, e.g. C/N ratios (section 5.4.2).

The most remarkable features of the proxy records are (i) the shift from pronounced G-IG cycles during MIS 39-36 to less pronounced glacials during MIS 35-27, and (ii) a distinct shift/perturbation during MIS 24-22 and the re-emergence of clear G-IG cycles after this perturbation (MIS 24-17). (i) The interval MIS 39-36 is characterised by mixed terrigenous-marine/algal OM with pronounced G-IG cycles of increased marine productivity (terrigenous input) during interglacials (glacials), based on a number of large pieces of terrestrial land plants (section 5.3.4), relatively high illite content (section 5.4.2), $\delta^{13}C_{org}$ values (section 5.4.3) and RE (section 5.4.4) analysis. Based on the $\delta^{13}C_{org}$ estimates the sediments deposited during glacials MIS 38 and 36 contain ~65 % marine-derived OM while the interglacials across MIS 39-17 contain closer to ~90% (figure 5.14). During the subsequent interval MIS 35-27 the marine OM component gradually increases during glacials, reaching up to ~75 % during MIS 30, while the interglacial values remain similar (figure 5.14), attenuating the differences between glacials and interglacials in proxy records including b*, which makes it difficult to identify MIS (see chapter 4, section 4.4).

Overall, this increase in glacial marine productivity and marine OM input could be linked to the climate becoming wetter (see section 5.4.3), which increased nutrient input from land. The main source for nutrients to the Japan Sea is however thought to be the TWC inflow and the glacial increase in marine productivity conflicts with the palaeoceanographic model that suggests a glacial near isolation of the Japan Sea and cut-off of the TWC inflow (see chapter 2, section 2.4). Further indications for continued TWC inflow during at least some of the glacials of MIS 39-27 could be inferred from mica particles in the coarse fraction (section 5.3.4), which was hypothesised to originate either from riverine input or from the mica deposits near Oki

Islands, transported to Site U1427 via the TWC (figure 5.8; Ikehara, 1991). Speculatively, since mica is present through glacials and interglacials alike across MIS 39-25 TWC has been proposed to have prevailed in this interval, flowing across the shallow, southern Japan Sea as far as Site U1427. This hypothesis will be further addressed in chapter 6.

(ii) The interval MIS 24-22 is characterised by low marine productivity as inferred from low $CaCO_3$ and TOC fluxes (section 5.4.1) and low marine OM contributions of ~30 % based on the $\delta^{13}C_{org}$ endmember model (section 5.4.3), and relatively higher terrigenous input based on the siliciclastic-rich lithology (figure 5.4, section 5.3.4), enhanced sediment mass accumulation rates (figure 5.10) and higher contributions of vascular land-plant OM (section 5.4.4). There are also indications for freshwater input at this time, e.g. the presence of freshwater diatoms (Tada et al., 2015b; see figure 5.6), high illite contents (figure 5.12a), RE data being close to values typical for lacustrine algae (figure 5.13), and low $\delta^{18}O_{\textit{Uvigerina spp.}}$ values indicating a freshwater imprint on the $\delta^{18}O$ record (see chapter 4, figure 4.5). Interestingly, mica, which was found in the sediments during interglacials and glacials alike across MIS 39-25 and suggested to be transported to Site U1427 via TWC inflow, is absent from the sediments during glacials from MIS 24-22 onwards (section 5.3.4). This is an intriguing find in terms of potential changes in the glacial palaeoceanography of the Japan Sea across the MPT and is investigated further in chapter 6.

Two further features of the sediments are a productivity peak within MIS 24-22, occurring at ~370-360 m (see figures 5.1d, 5.10b, d, 5.14), which likely indicates the position of MIS 23 that could not be identified in the chemo-stratigraphy of chapter 4, and the return of pronounced productivity G-IG cycles from MIS 21 onwards, continuing to the most recently deposited sediments (MIS 16-1; see Sagawa et al., 2018; Gallagher et al., 2018; Black et al., 2018).

Chapter 6: Palaeoceanographic Reconstruction of the Shallow, Southern Japan Sea across the MPT (MIS 39-17)

6.1 Introduction

Based on previous chapters the intervals MIS 39-36 and 24-17 are prominent features of the palaeoceanographic record from Site U1427. Comparison of the benthic foraminiferal isotope record, $\delta^{18}O_{Uvigerina\ spp.}$, with the shipboard colour reflectance (b*, Tada et al., 2015b) and an open ocean reference stack (LR04-stack, Lisiecki and Raymo, 2005) across MIS 39-17 suggests there was a fundamental change in the relationship of b* and the LR04-stack with $\delta^{18}O_{Uvigerina\ spp.}$ around MIS 25/24 (chapter 4, figures 4.4, 4.5). In the LR04-stack glacials are characterised by higher/more positive $\delta^{18}O$ values than interglacials (see chapter 3, section 3.4). In contrast, glacial $\delta^{18}O$ values from the Japan Sea are lower/more negative due to restricted exchange with the open ocean and continued (if reduced) freshwater input from EASM/precipitation and runoff from the surrounding landmasses, reducing the waters salinity and $\delta^{18}O$ (see chapter 2, section 2.4).

Most intriguingly glacials before MIS 25, most pronounced during MIS 39, 36 and 26, have relatively high $\delta^{18}O$ values compared with interglacials (see chapter 4, section 4.4). This chapter aims to explore the palaeoceanography of the Japan Sea across the MPT and possible causes for these glacial $\delta^{18}O$-shifts. The causes for this shift in glacial $\delta^{18}O$ could be (i) a misinterpretation of the $\delta^{18}O$ record, i.e. interglacials have been mistaken for glacials, (ii) diagenetic alterations of the foraminiferal calcite, (iii) a change in the amount of freshwater input, i.e. significantly reduced (or absent) during glacials, and/or (iv) a palaeoceanographic reorganisation across the MPT. In order to establish what might have caused the $\delta^{18}O$ behaviour changes a revised palaeoceanographic model for the shallow, southern Japan Sea across the MPT will be created based on these findings.

Specific objectives of this chapter are:

1) To test the validity of the benthic $\delta^{18}O$ anti-/ in-phase behaviour with the open ocean records through:
    a. Verifying the reliability of the $\delta^{18}O_{Uvigerina\ spp.}$ by analysing possible diagenetic alteration of the foraminifera shells.

b. Verifying the identification of glacials/ interglacials through the application of a salinity-independent temperature proxy, i.e. trace element analysis.

2) To test the hypothesis of palaeoceanographic changes having led to the in-/out of phase $\delta^{18}O$-behaviour with the open ocean by producing planktonic foraminiferal stable isotope records ($\delta^{18}O$, $\delta^{13}C$) and see if the isotope behaviour-change continues through the water column;
3) To establish what might have caused the $\delta^{18}O$ behaviour changes through the creation of a revised palaeoceanographic model for the shallow, southern Japan Sea based on the findings of this thesis.

6.2. Methods

Details on the laboratory protocols and limitations please refer to chapter 3. Section 3.5.7 for foraminifera used in this work, details of the stable isotope analyses (section 3.5.10) and diagenesis study (section 3.5.1). Trace element work is described in section 3.5.12, with the approach for Mg/Ca-based temperature estimates outlined in section 3.5.13.

For reference, the MIS and age tie points (see section 4.4.3), and the b* index (section 3.2.3), are shown together with new sediment data. MIS are displayed as coloured bars on the far left of figures, as are the age tie points (presented as triangles and numbers to the left of figures). The b* index (Irino et al., 2018) is shown as a light grey line running in the background of new data.

6.3 Results

6.3.1 Foraminiferal $\delta^{18}O$ records ($\delta^{18}O_{Uvigerina\ spp.}$, $\delta^{18}O_{Bull}$, $\delta^{18}O_{Pach}$, $\delta^{18}O_{planktonic}$)

The $\delta^{18}O_{Uvigerina\ spp}$ record has been presented in chapter 4 (figures 4.3a, 4.4, 4.5) and is shown here for comparison (figures 6.1a). The $\delta^{18}O_{Uvigerina\ spp.}$ values range between +3.1 and +4.4 ‰ and show two prominent features: (i) across MIS 39-25, most pronounced during MIS 39-36, $\delta^{18}O_{Uvigerina\ spp.}$ follows the pattern of the LR04-stack, showing high $\delta^{18}O$ values during glacials, which is unusual for $\delta^{18}O$ of the Japan Sea (see chapter 2, section 2.4). Only after MIS 25 the Japan Sea-typical behaviour of glacial $\delta^{18}O$ values appears in the record, showing lighter glacial

$\delta^{18}O_{Uvigerina\ spp.}$ values compared with the LR04-stack (see figure 4.4). (ii) Persistent low $\delta^{18}O_{Uvigerina\ spp.}$ values occur across MIS 24-22 (figure 6.1a).

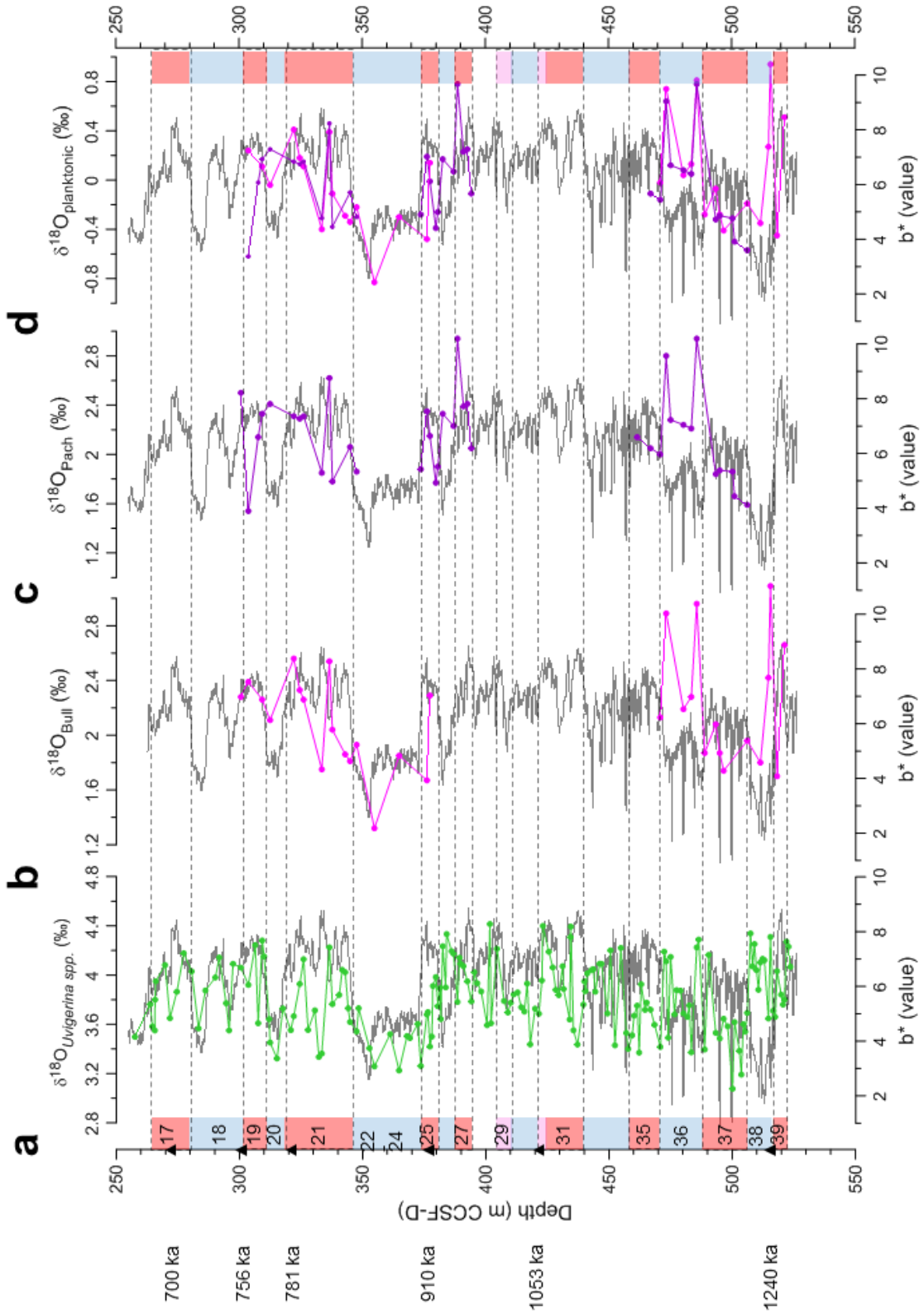

Figure 6.1. Summary plot of foraminiferal $\delta^{18}O$ records, showing benthic (*Uvigerina spp.*; fig. 6.1a), planktonic (*G. bulloides*; fig. 6.1b; *N. pachyderma* (s); fig. 6.1c) and the merged planktonic record (fig. 6.1d).

The $\delta^{18}O$ records of the planktonic species *G. bulloides* (range +1.3 to +3.1 ‰, average +2.2 ‰; figure 6.1b) and *N. pachyderma* (s) (range +1.5 to +2.9 ‰, average +2.2 ‰; figure 6.1c) do not show a significant $\delta^{18}O$-offset between the species of <0.1 ‰, hence they were combined to a single record by normalising the records, i.e. setting the average to zero ($\delta^{18}O_{planktonic}$; figure 6.1d), to provide higher resolution (see also chapter 3, sections section 3.5.7, 3.5.10). The record covers the intervals of MIS 39-36 and MIS 24-22 and shows high glacial and relatively lower interglacial $\delta^{18}O$ values before MIS 25, most pronounced during MIS 39-36, and, in contrast, low glacial/high interglacial $\delta^{18}O$ values across MIS 25-17. A pattern that has also been identified in $\delta^{18}O_{Uvigerina\ spp.}$ record (figures 6.1a, 4.4).

Overall, the numbers of foraminifera shells contained in the sediments, including *Uvigerina spp*., *G. bulloides* and *N. pachyderma*, are reduced during MIS 24-22 (see appendix A), implying unfavourable conditions, likely associated with reduced marine productivity, as suggested by enhanced terrigenous/reduced marine contributions to the sediments during this interval (see chapter 5).

6.3.2 Foraminiferal $\delta^{13}C$ records ($\delta^{13}C_{Uvigerina\ spp.}$, $\delta^{13}C_{Bull}$, $\delta^{13}C_{Pach}$)

The benthic foraminiferal $\delta^{13}C_{Uvigerina\ spp.}$ record has been presented in chapter 4 (figure 4.3b) and is shown here for comparison (figures 6.2a). The $\delta^{13}C_{Uvigerina\ spp.}$ ranges from –2.2 to –0.5 ‰, average of –1.2 ‰, varying with G-IG cycles and in general showing higher (lower) values during interglacials (glacials). Lowest $^{13}C_{Uvigerina\ spp.}$ values occur during MIS 24-22, being on average ~–1.8 ‰. The amplitude of the variations over G-IG cycles are weaker expressed during MIS 39-25, and become more distinct during MIS 25-17. In contrast to the $\delta^{18}O_{Uvigerina\ spp.}$ record, $\delta^{13}C_{Uvigerina\ spp.}$ does not show a change in its behaviour across MIS 39-17 but seems to continue to follow the same pattern across G-IG cycles throughout the interval. The planktonic $\delta^{13}C$ records were not combined due to their significant interspecies offset of on average 0.6 ‰, which is outside the analytical error (chapter 3, section 3.5.10; figure 6.2d). Both planktonic $\delta^{13}C$ records do however show similar trends and patterns over G-IG cycles, most pronounced during MIS 39-36, showing lower (higher) values during interglacials (glacials), ranging from –1.9 to 0.0 ‰ (average –0.6 ‰) and –1.2 to +0.7 ‰ (average 0.0 ‰) for $\delta^{13}C_{Bull}$ and $\delta^{13}C_{Pach}$ respectively (figures 6.2b, c).

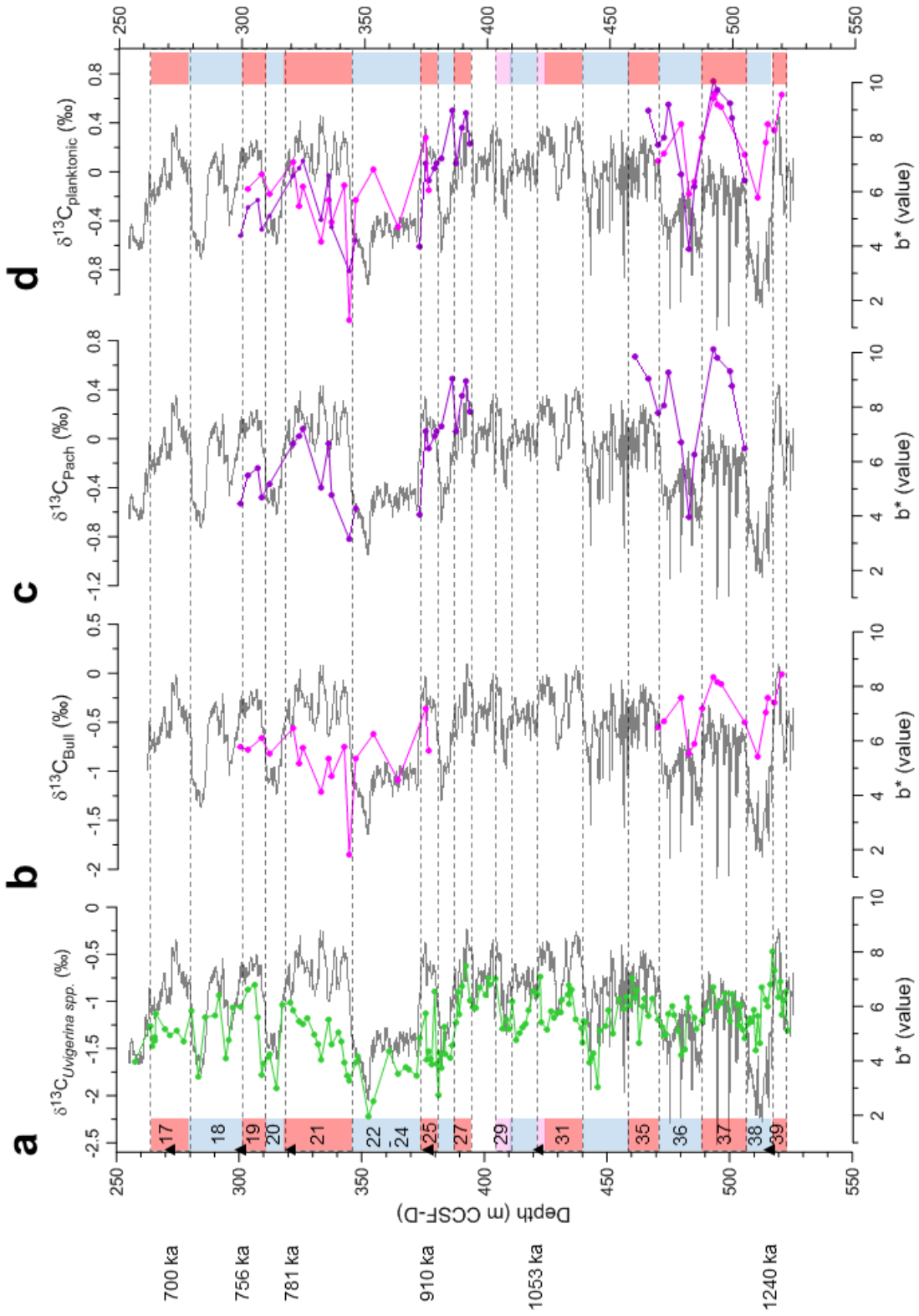

Figure 6.2. Summary plot of foraminiferal $\delta^{13}C$ records showing benthic (*Uvigerina spp.*; fig. 6.2a) and planktonic (*G. bulloides*; fig. 6.2b; *N. pachyderma* (s); fig. 6.2c) and the merged planktonic record (fig. 6.2d).

Two exceptions for the G-IG trends occur during mid/late MIS 36 and mid-MIS 22 where both planktonic records indicate high glacial $\delta^{13}C$ values while benthic $\delta^{13}C$

values either do not show elevated values by the same degree or are reduced. Since the $\delta^{13}C$ composition of foraminifera shells reflects the $^{13}/^{12}C$-changes in the available C-pool, the higher values could be a result of enhanced marine productivity, preferentially consuming ^{12}C and enriching the C-pool in ^{13}C, or it could be a result of changes in the ocean C-pool (see chapter 3, section 3.10). A simplified differentiation between these two mechanisms can be made by comparing the planktonic with the benthic $\delta^{13}C$ records. If benthic and planktonic $\delta^{13}C$ records trace each other, than changes in the oceanic C-reservoir are the most likely the cause for $\delta^{13}C$ changes. However, if the planktonic and benthic $\delta^{13}C$ records diverge, i.e. $\delta^{13}C_{planktonic}$ increases while $\delta^{13}C_{benthic}$ decreases/remains at a similar level, then productivity is the more likely cause for the $\delta^{13}C$ shift (Maslin and Swann, 2006).

In both cases, MIS 36 and 22, the coherence between benthic and planktonic $\delta^{13}C$ is not quite clear due to the low resolution of the planktonic $\delta^{13}C$ records. It appears that in both cases the benthic $\delta^{13}C_{\textit{Uvigerina spp.}}$ showing lower values while the $\delta^{13}C_{Planktonic}$ values increase, which could suggest marine productivity as the most likely cause (figure 6.2a, d). A minor increase in marine productivity could also be inferred from $\delta^{13}C_{org}$ and $CaCO_3$ content with both indicating slightly enhanced marine OM contributions or, perhaps, input of less $\delta^{13}C$-depleted terrigenous OM (figures 5.1d, 5.2b). At the same time TOC fluxes remain low, suggesting if at all only a meagre change in marine productivity (figure 5.10d). A likely source for nutrients for the productivity during MIS 22, when the Japan Sea was isolated from the open ocean circulation, could be from nearby land and/or exposed shelves, being the result of the great sea-level fall of ~120 m during MIS 22 (e.g. Bintanja et al., 2005; Elderfield et al., 2012; Rohling et al., 2014; see chapter 2, section 2.3).

On a global scale, lower benthic $\delta^{13}C$ values have been reported from open ocean sites during MIS 22, and suggested to be associated with the combination of increased global aridity and a large scale erosion-event that redistributed ^{13}C-depleted carbon (~–18 ‰) from exposed shelves back into the ocean realm (Shackleton, 1977; Raymo et al., 1997). This hypothesis has however been doubted as benthic foraminiferal $\delta^{13}C$ values have been found to predate changes in sea-water $\delta^{18}O$, suggesting changes in the oceanic carbon reservoir occurred prior to the sea-level fall (Elderfield et al., 2012). Due to the low resolution of the $\delta^{18}O$ records of Site U1427 this lead/lag relationship cannot be tested and, in addition, the Japan Sea

would have been isolated from global oceanic circulation patterns caused by the sea-level lowstand. It is likely, however, that local, Japan Sea circulation patterns have contributed to the low benthic $\delta^{13}C$ values.

Benthic foraminiferal $\delta^{13}C$ values are influenced by a complex set of parameters, such as the isotope composition of the available C-pool, which is influenced by surface water productivity, ocean circulation and remineralisation of organic matter (chapter 3, section 3.5.10). It is possible, that the foraminiferal $\delta^{13}C$ values became lower by the addition and combined effects of the input of ^{12}C-enriched/light terrigenous matter, as suggested by bulk sediment organic parameters and Rock-Eval data (see chapter 5), and a stagnant water column, under which bottom waters became even more enriched in ^{12}C as a result of capturing ^{12}C released from OM remineralisation (see chapter 3, section 3.5.10 for background information).

6.3.3 Foraminiferal diagenesis survey

Foraminiferal shells can be affected by post-depositional processes, such as dissolution and/or overgrowth with secondary, diagenetic calcite crusts, which both can impact on $\delta^{18}O$ and $\delta^{13}C$ records (see chapter 3, section 3.5.11). A diagenetic study (sections 6.3.2, 6.3.3) was undertaken on selected shells that appeared poorly preserved under light microscope ("frosty", slightly discoloured; *c.f.* Edgar et al., 2015). For comparison, well-preserved, modern shells were studied as well (chapter 3, section 3.3). A combination of high-resolution SEM and EDX analysis was undertaken (chapter 3, section 3.5.11).

Overall the shells (benthic and planktonic) appear well preserved (appendix B), implying that the palaeo-records ($\delta^{18}O_{Uvigerina\ spp.}$, $\delta^{18}O_{Plankctonic}$, $\delta^{13}C_{Uvigerina\ spp.}$, $\delta^{13}C_{Bull}$, $\delta^{13}C_{Pach}$) reflect the original environmental conditions and giving confidence in the foraminiferal calcite-based Mg/Ca temperature estimates (section 6.3.4). The preservation of foraminifera at Site U1427 is therefore much better than at deep water sites in the Japan Sea, as suggested by shipboard light microscopic observations (Takuya Sagawa, pers. coms.), and in other north Pacific marginal basins, such as the Bering Sea (Detlef et al., 2020).

6.3.4 Foraminiferal calcite trace element analysis and temperature estimates

The benthic foraminiferal $Mg/Ca_{Uvigerina\ spp.}$ spans MIS 39-35 and MIS 27-19, ranging between 0.9 and 1.6 mmol/mol with an average of 1.25 mmol/mol (figure

6.3a). The modern Mg/Ca value, derived from analysis of the surface sample (chapter 3, section 3.3), is 0.74 mmol/mol. Although the down-core record has gaps due to absence of shells, it has a coherence with b* throughout, showing lower (higher) $Mg/Ca_{Uvigerina\ spp.}$ ratios during glacials (interglacials) when b* is low (high). The derived down-core palaeo-water temperature estimates (chapter 3, section 3.5.13) range between +2.6 and +11 °C (figure 6.2b), being higher (lower) during interglacials (glacials).

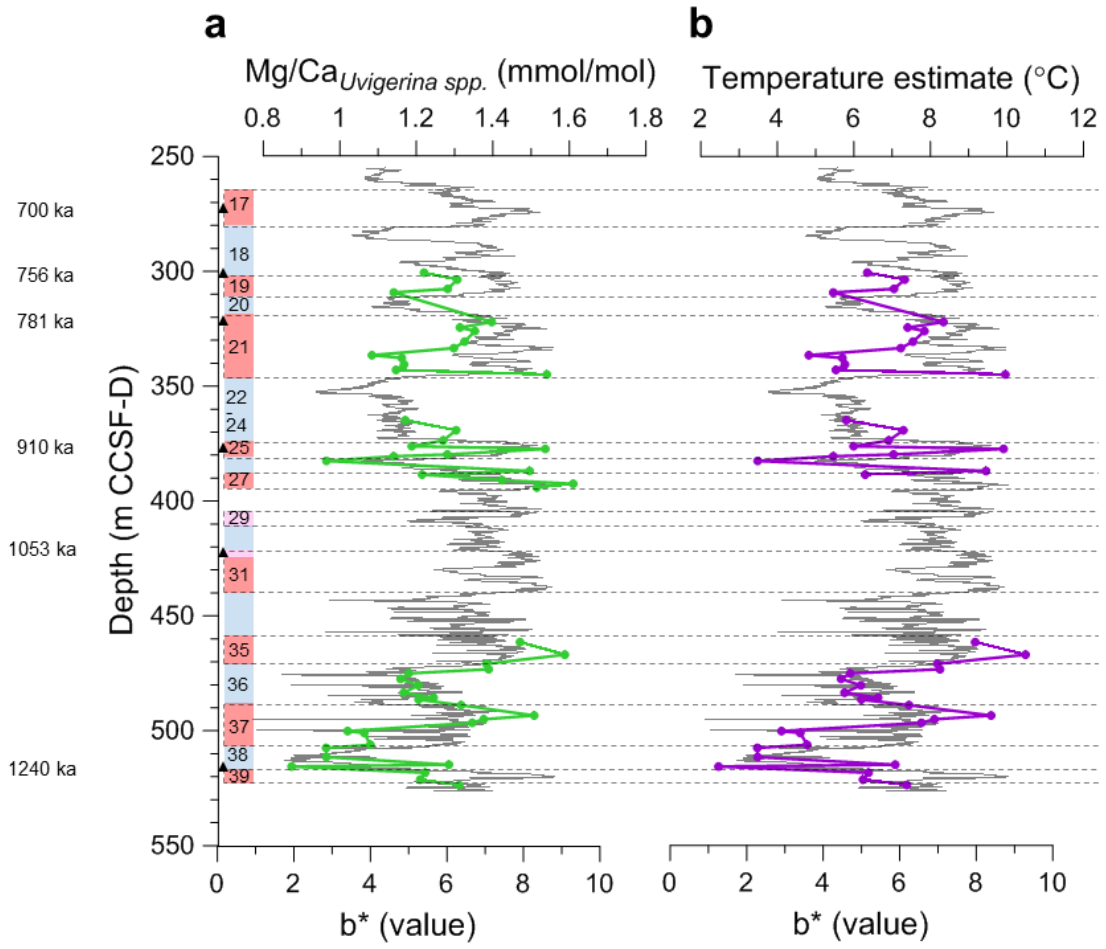

Figure 6.3. Benthic foraminiferal Mg/Ca ratios (fig. 6.3a) and calculated temperature estimates (fig. 6.3b).

6.4. Palaeoenvironmental Signals of the Isotope Records, $\delta^{18}O$

6.4.1 Reliability of isotope records

The most intriguing feature of the benthic and planktonic $\delta^{18}O$ records is the shift in glacial $\delta^{18}O$ values around MIS 25, most pronounced in the high-resolution $\delta^{18}O_{Uvigerina\ spp.}$ record (figures 6.1a, b, c). Glacials in $\delta^{18}O_{Uvigerina\ spp.}$ across MIS 39-25

are characterised by relatively higher glacial than interglacial $\delta^{18}O$ values. For example, glacials MIS 38 and 36 show $\delta^{18}O$ values of up to +4.4 ‰ (average MIS 38 of +4.1 ‰, MIS 36 of +3.9 ‰), while interglacials MIS 39, 37 and 35 show $\delta^{18}O$ of as low as about +3.1 ‰ (average MIS 39 of +4.0 ‰, MIS 37 of +3.5 ‰, MIS 35 of +3.4 ‰) (figure 6.1a). Glacials across MIS 24-17, in contrast, are characterised by relatively lower $\delta^{18}O$ values than interglacials, typical for the Japan Sea (see chapter 2, section 2.4). For example, the glacials of MIS 24-22 and 20 show ^{18}O values of as low as +3.2 ‰ (average MIS 24-22 of +3.5 ‰, MIS 20 of +3.8 ‰), while interglacials of MIS 21 and 19 show ^{18}O values of up to +4.2 ‰ (average MIS 21 of +3.8 ‰, MIS 19 of +4.0 ‰). This signature of low-$\delta^{18}O$ glacials continues upwards to the most recent sediments (figure 4.4) (Sagawa et al. 2018).

One possible cause for the shift to Japan Sea unusual high glacial $\delta^{18}O$ values is diagenetic alteration of foraminifera shells. The addition of diagenetic calcite layers or recrystallisation of shells can lead to higher $\delta^{18}O$ (see cool-tropics paradox; chapter 3, section 3.5.11), although the effect of this would expected to be smaller in benthic foraminifera than in planktonics, since benthic foraminifera have thicker shell walls, with less ornamentation/surface area and they precipitate their shells in similar conditions as those in which diagenesis would take place. For the shallow infaunal genus *Uvigerina spp.* the effect of diagenesis on $\delta^{18}O$ records should be minimal as the original calcite and the post-depositional diagenetic calcite potentially could be formed in the same water mass (Shackleton, 1974; Fontanier et al., 2006; Edgar et al., 2013; Stern and Lisiecki, 2014). Furthermore, it has been argued that even the effect of strong diagenetic alteration and the addition of diagenetic calcite on benthic $\delta^{18}O$ records (using *Uvigerina* spp., *Cibicidoides*) is negligible if the secondary calcite was precipitated at shallow burial depths (<300 m) and if additionally foraminifera were embedded in fine-grained sediments and when diagenesis took place under similar conditions to where the foraminifera lived (Pearson et al., 2001; Sexton and Wilson, 2009; Edgar et al., 2013 Edgar et al., 2015). All of which applies to Site U1427 as sediments consist of a fine-grained matrix and the foraminifera originated from sediment/burial depths (<300 m). In addition, sediments at U1427 become finer during glacials, which makes strong diagenetic alteration of shells specifically during glacials and causing the higher $\delta^{18}O_{\textit{Uvigerina spp.}}$ values, less likely (Tada et al., 2015c and chapter 5, section 5.3.3)

Despite the different sensitivity to diagenetic alteration, both the benthic and planktonic foraminifera $\delta^{18}O$ records indicate a glacial $\delta^{18}O$-switch at MIS 25. While diagenetic alteration could lead to higher glacial $\delta^{18}O$ values in planktonic foraminifera as described from MIS 39 and 36, it would only have affected shells deposited during glacials while those deposited during interglacials seem unaffected, showing relatively lower $\delta^{18}O$ values (see figure 6.1), making diagenesis a less plausible cause. As the results of the diagenesis survey showed little evidence for diagenetic alteration (section 6.3.3; appendix B) the isotope data are thought to be reliable and should reflect palaeoenvironmental signals.

6.4.2 Verification of glacials and interglacial identification, Mg/Ca temperature estimates

Another possible cause for the shift from high to low glacial $\delta^{18}O$ values is a misidentification of the glacials. In the Japan Sea glacials are usually associated with low $\delta^{18}O$ values (chapter 2, section 2.4) but isotope data for MIS 39-25 shows most glacials have higher $\delta^{18}O$ values than adjacent interglacials (figure 6.1, 6.4a). The b* index, in contrast, used in the identification of glacials/interglacials (chapter 4, section 4.4), continues to show lower (higher) values during glacials (interglacials) throughout the investigated section, supporting the nature and presence of the high-$\delta^{18}O$ glacials.

Increased confidence in the identification of glacials and interglacials is inferred from temperature estimates, calculated from foraminiferal *Uvigerina spp.* Mg/Ca ratios (section 6.3.4). These temperature estimates are likely inaccurate in their absolute water temperature values and need to be taken cautiously (see chapter 3, section 3.5.13). However, their relative changes over G-IG cycles should not be affected and therefore the record still allows the anticipated differentiation between glacials and interglacials.

The derived down-core palaeo-bottom water temperature estimates (chapter 3, section 3.5.13) range between +2.6 and +11 °C (figure 6.2b), being higher (lower) during interglacials (glacials). This palaeo-temperature range, from an assumed palaeo-water depth of ~300-200 m (considering past sea-level lowstands of maximum about –120 m and local tectonic developments, see section 3.2) fits to previous studies of Japan Sea temperature across the MPT. For example, SSTs were suggested to have been below 18 °C, as inferred from a switch in dominant

coiling direction of *N. pachyderma* (Kheradyar, 1992), and temperatures may have ranged between ~+5 and +15 °C, as inferred from organic temperature proxies recorded at Site U1425 (central Japan Sea; Wittkopp, 2017). The bottom water temperatures recorded in this study are lower than the SSTs (*op. cit.*), which is to be expected given the greater water depth. However, the similarity between previous temperature studies and this work increases confidence in the gathered temperature record and, in addition, it suggests a well-mixed water column that transferred SST signals to the shallow bottom waters at Site U1427. This well-mixed water column would also explain the freshwater imprint on the sea floor dwelling benthic foraminiferal $\delta^{18}O_{Uvingerina\ spp.}$ record (figure 6.1a, 6.4a). Ultimately, the Mg/Ca-based temperature estimates confirm the identification of both high- and low-$\delta^{18}O$ glacials (section 4.4).

Exceptions to the Mg/Ca trends occur during interglacials MIS 37 and 21 when Mg/Ca ratios and resulting temperature estimates remain low for part of the stages. Changes in the oceanic Mg and Ca composition can be ruled out, as both elements have residence times in the oceans longer than the analysed records (Mg 13 Ma, Ca 1 Ma, Broecker and Peng, 1982). Diagenesis can be ruled out as well because the addition of a secondary (Mg-rich) inorganic coating would lead to higher Mg/Ca ratios (Sexton et al., 2006) but in any case no signs of diagenetic coatings were found on the foraminifera shells (section 6.3.3, appendix B). Partial dissolution, however, can cause lower Mg/Ca ratios (see chapter 3, section 3.5.12), but Site U1427 is thought to have been above the CCD for the timescale the sediments cover (Tada et al., 2015) and the presence of foraminifera shells throughout the investigated section suggests the same. Therefore, post-depositional alteration of the shells is less likely in this setting to have led to the low Mg/Ca ratios.

It could be that the exceptions from the Mg/Ca trend over G-IG cycles during the early stages of MIS 37 and 21 are the result of a size effect, caused by the wide size-range selected (>250µm) (Mervyn Greaves, pers. coms.). The facies description shows larger *Uvigerina spp*. shells being present in the sediments, indicating larger than usual shells may have been selected for analyses (appendix A). It has been argued that lower Mg/Ca ratios can be a consequence of larger foraminiferal shells analysed, and it is therefore recommendable to reject the low Mg/Ca-samples for further palaeoenvironmental interpretations (Elderfield et al., 2012; Mervyn Greaves, pers. coms.).

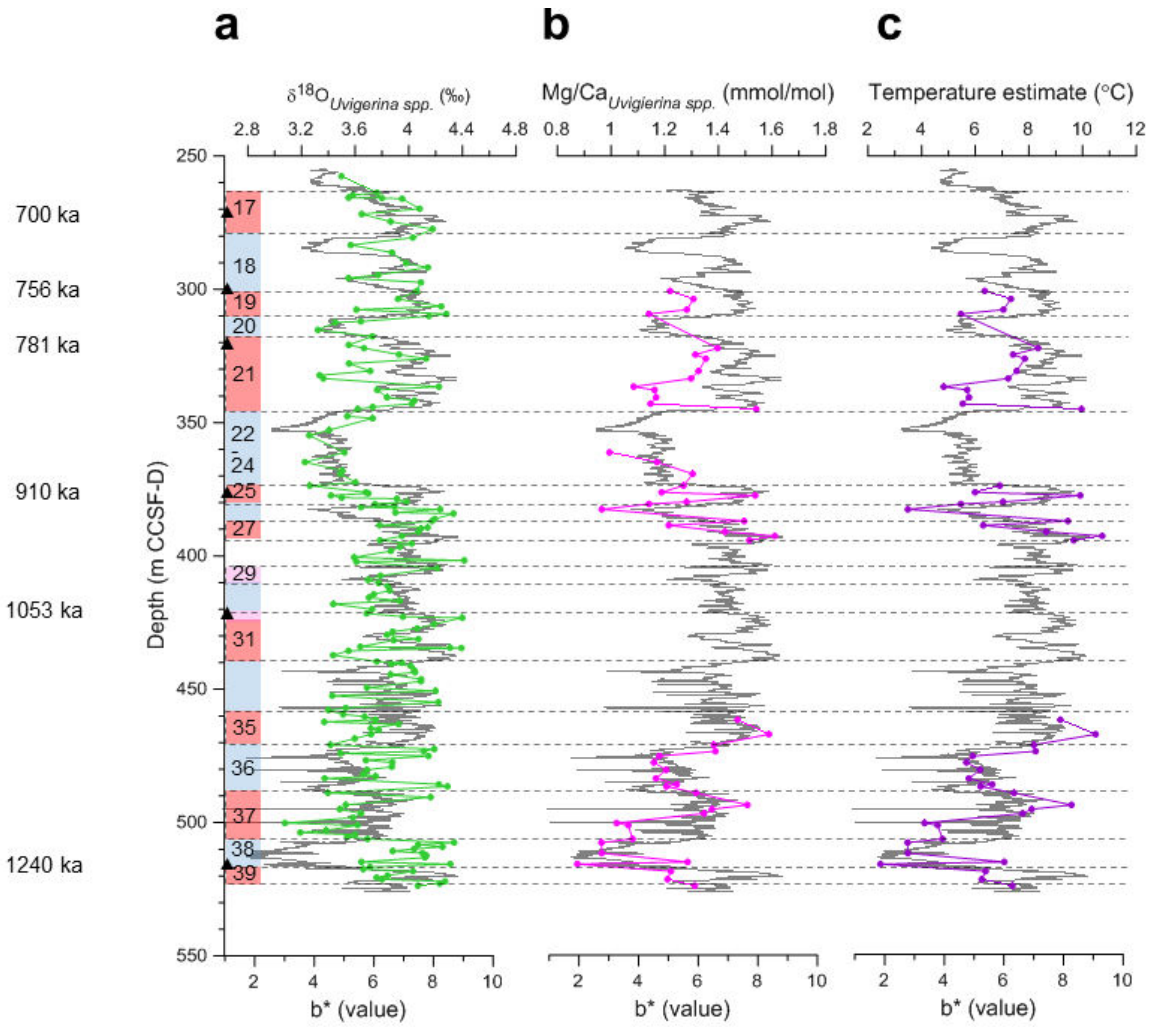

Figure 6.4. Summarising plot of benthic $\delta^{18}O$ (fig. 6.4a) in direct comparison with benthic Mg/Ca record (fig. 6.4b) and estimated temperatures (fig. 6.4c).

6.4.3 Possible causes for the switch in glacial $\delta^{18}O$

Having excluded unreliable palaeo-signals (section 6.4.1) and/or misidentification (section 6.4.2) as reasons for the switch from predominantly high $\delta^{18}O$ glacials across MIS 39-25 to low $\delta^{18}O$ glacials from MIS 25 to present, other processes that could have led to high glacial $\delta^{18}O$ values are (i) changes in the hydrological cycle or (ii) changes in the palaeoceanography of the shallow, southern part of the Japan Sea.

The combination of the restricted water mass exchange with the open ocean during glacial sea-level lowstands with reduced precipitation, i.e. dryer climate and/or a weaker EASM, and perhaps also increased evaporation, could lead to higher glacial sea water salinity and higher $\delta^{18}O$ values. Typically however, the glacial isolation of the Japan Sea leads to the formation of a freshwater lens and lower $\delta^{18}O$

values, as the result of continued input of freshwater from surrounding landmasses and precipitation over the basin, and a lack of water mass mixing with the open ocean (chapter 2, section 2.4).

Speculatively, under glacial palaeoceanographic conditions with reduced freshwater input/increased evaporation sea water salinity and $\delta^{18}O$ values could increase. As a mathematical example to show what can be done with the data, during MIS 38 and 26 $\delta^{18}O$ would be expected to be ~+3.4 ‰ if assuming a consistent coherence between b* and $\delta^{18}O$ as during MIS 24-22, i.e. amount of change in b* leads to the same amount of change in $\delta^{18}O$ across the glacials. During MIS 38/26 the $\delta^{18}O$ records show however values of ~+4.2 ‰, a difference of ~+1 ‰ to the expected $\delta^{18}O$ value above. It has been shown that for a +1 ‰ change in $\delta^{18}O$ of calcite the sea water salinity would need to increase by 2 ‰ (*c.f.* Broecker and Denton, 1990). At present Site U1427 is being emerged in Japan Sea proper water, which prevails at all water depths >300 m in the Japan Sea, and is characterised by a relatively constant salinity of 34.06-34.08 ‰ (chapter 2, section 2.4.1). The palaeo-water depth of Site U1427 was likely between 200 to 300 m (depending on sea-level stand) (chapter 3, section 3.2). During sea-level lowstands the water column above the site would have been shallower, making the site more sensitive to influences of surface water parameters. The modern interannual surface salinity variations of the TWC at the TSS range from 34.6 to 31 ‰ (*c.f.* Lee, 2007), showing that a 2 ‰ change in surface water salinity is possible in the Japan Sea and suggesting a 2 ‰ salinity change at site U1427 may be possible during glacial sea-level lowstands, even if only part of the surface salinity signal was transported to the sea floor. While this cannot be tested from the data generated here, it is clear that the freshwater imprint, which usually overrides the influence of ice-volume/temperature signal and drives the unusual low glacial $\delta^{18}O$ in the Japan Sea, is absent from the $\delta^{18}O_{\textit{Uvigerina spp.}}$ record during MIS 38 and 26.

Crucially, the mechanism of increased glacial $\delta^{18}O$ values through increased water salinity and being the combined result of restricted exchange with open ocean waters and reduced precipitation/increased evaporation, contradicts the palaeo-climatic interpretations of this time-slice. As described in chapter 5, climate was becoming progressively wetter from MIS 38 onwards leading to enhanced freshwater input during glacials and interglacials alike (chapter 5, section 5.4.3). The enhanced

freshwater input should have lowered the glacial $\delta^{18}O$ values throughout this section. It therefore seems unlikely reduced precipitation was the cause of high $\delta^{18}O$ glacials between MIS 39 and 25.

To follow on the second mechanism proposed in this section, a possible connection between the shallow, southern Japan Sea and the open ocean, may be a more plausible cause for the high $\delta^{18}O$ glacials (see next section). The most prominent high-$\delta^{18}O$ glacials are MIS 38, 36 and 26 (on average $\delta^{18}O$ is ~+4.2 ‰) show $\delta^{18}O$ values similar to those of the LR04-stack across the same MISs (~+4.25 to +4.5 ‰; chapter 4, figure 4.5c). This similarity of glacial $\delta^{18}O$ values suggests similar processes have controlled the presence of these values in both records. In the open ocean the LR04-stack $\delta^{18}O$ values are thought to be mainly controlled by global ice-volume/temperature (see chapter 2, section 2.2 and chapter 3, section 3.4) and, in order for the glacial $\delta^{18}O$ values of Site U1427 to be controlled by the same processes, a better glacial connection with the open ocean would need to be proposed for glacials before MIS 25 (although some local freshwater input and its influence on $\delta^{18}O$ cannot be excluded).

6.4.4 Sea-level and East Asian summer monsoon (precipitation) fluctuations across the mid-Pleistocene transition

A better glacial connection between the shallow, southern Japan Sea and the open ocean, i.e. East China Sea, Yellow Sea and North-west Pacific Ocean, before MIS 25 is likely, given globally higher glacial sea-levels. Before MIS 25 eustatic sea-level fluctuations over G-IG cycles were small, having an average global glacial sea-level drop around ~–60 to –80 m between ~2700 and 1200 ka (*c.f.* Sosdian and Rosenthal, 2009), compared to the late Pleistocene to recent glacials, which show average eustatic sea-level drops are up to –120m +/-32 m due to the development of the large Northern Hemisphere ice sheets (*c.f.* Sosdian and Rosenthal, 2009).

While sea-level curves based on foraminiferal $\delta^{18}O$ are not available for the Japan Sea, they exists for other sites and global/regional sea-level models, I.e. sea-level reconstructions, have been developed based on these sites (see chapter 2, section 2.3.3). Some uncertainty does arise from the application of such global average sea-level curves and models that are based on locations far away from Site U1427. For example, local tectonics may have influenced the local sea-level developments, glacial isostatic adjustments can have dampened locally a global sea-level rise.

Nevertheless, as there is no sea-level curve from the Japan Sea, such global averages give the opportunity to estimate local sea-levels. Locally, at Site U1427 and surrounding areas are in a tectonically very active region with volcanic events having taken place in southern Japan and the Japanese Isles across the MPT, but no local uplift events could be identified (Yoon, 1997; Kitamura and Kawagoe, 2006; Itaki, 2016). The biggest tectonic events around the Tsushima Strait (TSS) are related to the opening of the Japan Sea, starting in the late Oligocene, with stress field changes (extensional to compressional) during the mid-Miocene and, although minor movements (minor faulting) took place after the mid-Miocene, the TSS area has been tectonically stable since the mid-Miocene, which is supported by modern seismological activity (Katsura and Nagano, 1976; Ishikawa and Tagami, 1991; Fabbri et al., 1996; Son et al., 2015; Claringbould et al., 2019). Although there is a possibility of sill depth changes related to deposition/erosion in the TSS, no large (tectonically induced) sill depth change is expected.

The sea-level estimates by Bintanja et al. (2005), Sosdian and Rosenthal (2009), Elderfield et al. (2012), Rohling et al. (2014) and Berends et al. (2019) were used in this thesis to estimate the water level over the TSS, hereafter referred to as sill depths, in a simplistic model by deducting the past sea-level stand from the modern water depth over the TSS sill (130 m; Oba et al., 1991). The respective TSS sill depth curves are presented in figure 6.5d. Based on the Elderfield et al. sea-level curve TSS sill depths were relatively stable during interglacials while glacial sill depths were greater across MIS 25-39 compared with MIS 24-17, when they regularly became as shallow as ~20 m (figure 6.5d). Greater glacial sill depths before ~MIS 25 can also be inferred from the sea-level curves by Rohling et al. (2014) and Berends et al. (2019) (both about 60 to 90 m), while the Bintanja et al. (2005)-based sill depths suggest that sills may have been as shallow as during MIS 24/22 during glacials before MIS 25 (as low as 40 m TSS sill depth) (figure 6.5d).

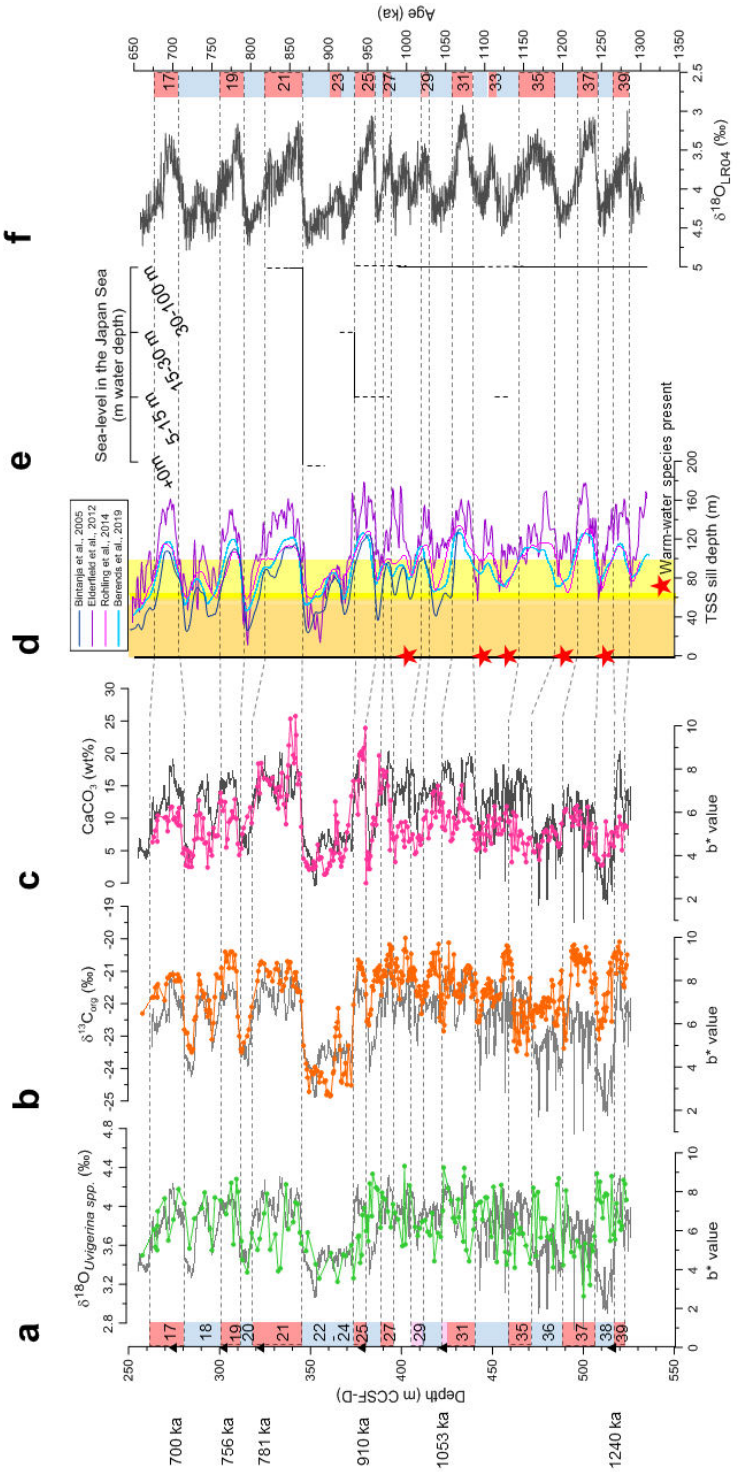

Figure 6.5. Benthic foraminiferal $\delta^{18}O_{Uvigerina\ spp.}$ record (fig. 6.5a), $\delta^{13}C_{org}$ (fig. 6.5b) and $CaCO_3$ (fig. 6.5c) compared with estimated TSS water depth fluctuations across MIS 39-17 (fig. 6.5d; based on Bintanja et al., 2005; Elderfield et al., 2012; Rohling et al., 2014; Berends et al., 2019) with glacial intrusions of warm water species (red stars; based on Kitamura et al., 2001; Tada et al., 2015b; Itaki et al., 2018). Orange indicates proposed mode 1 TSS sill water depth, yellow indicates proposed mode 2 TSS sill stands and white indicates mode 3 TSS sill stand. Fig. 6.5e shows local water depth estimates based on a study of the Omma Formation outcrops nearby Site U1427 (Kitamura, 2016). The LR04-stack (fig. 6.5f) and Site U1427 age tie points (black triangles and numbers, far left) and MIS (see chapter 4, fig. 4.4) are shown for reference.

The global sea-level/TSS sill depth reconstructions after Elderfield et al. (2012), Rohling et al. (2014) and Berends et al. (2019) fit well with data from the Japan Sea. For example, modelled TSS sill depths for the last glacial maximum, thought to have seen a similar sea-level fall as during MIS 24/22, indicate sea-levels of up to –134 m below present (Yokoyama et al., 2000; Bintanja et al., 2005; Lambeck et al., 2014), and suggesting 95 % of the TSS had dried up (Matsui et al., 1998; Tada et al., 1999). Overall, sea-level records from the Japan Sea that cover the MPT are pretty much limited to lithological and micropalaeontological assemblage studies on the Omma Formation outcrops near Kanazawa City and about ~200 km north-east of Site U1427, where the late stages of the MPT have been intensively studied, overall covering MIS 60-19 (approximate location see figure 3.1; e.g. Kitamura, 1991; Kitamura et al., 2001; Kitamura and Kawagoe, 2006; Kitamura and Kimoto, 2006; Hoiles et al., 2012; Kitamura 2016). The lithofacies inventory of these shallow-water deposits suggests TWC inflow during each interglacial sea-level highstand since MIS 56 at ~1700 ka. Based on lithofacies analysis, Kitamura (2016) suggests sediments were deposited in a fairly constant water depth of 30-100 m during MIS 39-27, while during the deposition of younger sediments until MIS 21 water depth was more variable, reducing to 5-30 m during MIS 27-23, aerial exposure of the area and the formation of a back marsh environment with trees and mammal footprints during MIS 22, and the return to 30-100 m water depth with the return of marine molluscs during MIS 21 (Kitamura, 2016; see figure 6.5e). These higher glacial sea-levels before MIS 25, globally and in the Japan Sea, might have enabled a better connection between the shallow southern part of the Japan Sea and the open ocean.

The TSS sill depth is one parameter influencing the inflow of the TWC, the other is the strength of the EASM and its associated freshwater runoff from the Yangtze and Yellow Rivers (see chapter 2, section 2.4). While the EASM strength varied over G-IG cycles, being relatively weaker during glacials (see chapter 2, section 2.4), the sea-level fall associated with glacials would have exposed large parts of the shallow East China Sea shelf and shifted the Yellow and Yangtze River mouths to positions much closer to the TSS (Park and Chu, 2006) (see chapter 3, figure 3.1). The closer proximity of the river mouths to the TSS during glacials may have compensated in part for the reduced glacial precipitation and shallower sills, at least at sea-level stands above those of the LGM and MIS 24-17, allowing some TWC inflow even

during glacials. This suggests that at sea-level stands above those of glacials across MIS 39-25 some inflow of the TWC may have been possible.

Evidence for a glacial connection and inflow of TWC warm waters before MIS 25 is also present in sediment-facies and micropalaeontological studies from Site U1427. First, mica occurs in the sediments during both glacials and interglacials between MIS 39-25 while after MIS 25 mica occurs predominantly during interglacials (chapter 5, section 5.3.4). The input mechanism for mica to Site U1427 is either via riverine runoff, i.e. mica is present at times of strong freshwater runoff, or via transport by the TWC when it is able to intrude the Japan Sea (chapter 5, section 5.3.4). If mica was brought to Site U1427 via rivers then this would imply constant freshwater runoff over glacials and interglacials, which would raise the question, why the freshwater imprint on $\delta^{18}O$ is absent during the pre-MIS 25 glacials. Alternatively, if mica was delivered via the TWC then this would imply the TWC could enter the basin during interglacials as well as glacials between MIS 39-35.

Further supporting evidence for a glacial connection with the open ocean to have existed across MIS 39-35 and having ceased from MIS 24 onwards is inferred from the relationship between illite and the TN content (chapter 5, section 5.4.3). Across MIS 24-22 C/N ratios are unreliable recorders of terrigenous/marine contributions due to additional inorganically bound N in the sediments, adsorbed to illite under oxygen-depleted environments (chapter 5, section 5.4.3). In contrast, during MIS 39-25 even though illite was present in the sediments, C/N ratios remain unaffected as a result of a higher oxygen levels preventing the adsorption of N to clay minerals (see figure 5.12). The proposed better oxygenation was likely achieved by enhanced mixing of the water column, which in the Japan Sea is a sign of TWC inflow and therefore implies a connection with the open ocean (see chapter 2, section 2.4).

The micropalaeontology of Site U1427 also suggests TWC inflow at certain times during glacials between MIS 39-25. For example, Itaki et al. (2018), who investigated the radiolarian assemblage across Site U1427, show warm water radiolarian species present during several interglacials as well as at least during the glacials of MIS 34, 32 and 28. Glacial deposits between these MISs and younger than MIS 28 also contain warm water radiolarians, but the sediments cannot be dated with great certainty based on Itaki et al. (2018). Itaki et al. (2018) link the presence of the warm water radiolarians to the warm waters of the ECS, where they originate and become

part of the TWC inflow, supporting the idea that during these glacials, MIS 34, 32, and 28, water masses from the open ocean entered the southern Japan Sea (see figure 6.5d). Similarly the warm water foraminifera *Globigerinoides ruber* (d'Orbigny, 1839), which also originates from the ECS and is associated with TWC intrusions to the Japan Sea, was identified in the facies of the Omma Formation during glacials MIS 38, 36 and 34 (Kitamura et al., 2001, Hoiles et al., 2012), and in the sediments of Site U1427 at depths corresponding to MIS 38 and 39 (Tada et al., 2015b) (see figure 6.5d).

There is also evidence in literature for a strengthening of the Kuroshio Current (KC) around MIS 39-25, which might have benefitted the TWC strength and hence its inflow. Pleistocene reefs at Ryuku Island (figure 2.7) expanded northwards between 1100 and 800 ka (Yamamoto, 2006). This northwards expansion has been suggested to be related to the KC strengthening across the MPT as a response to increased glacio-eustatic sea-level variations (Gallagher et al., 2015). The KC strengthening in combination with higher sea-levels before MIS 25 (see figure 6.5d) and enhanced EASM precipitation (see chapter 5) must have strengthened the TWC and enabled open ocean waters to reach Site U1427 in the shallow, southern part of the Japan Sea, affecting the sediments and proxy records even during glacial sea-level lowstands.

In summary, there is evidence from sea-level/sill depth estimates as well as studies of the sedimentary facies, micropalaeontology and geochemical proxies that suggest a glacial connection between Site U1427 in the shallow, southern Japan Sea and the open ocean, allowing the TWC to enter the basin during some glacials between MIS 39-25. This connection and the TWC inflow is most pronounced during the glacials MIS 38, 36, and 25 through high and persistent, open ocean-like benthic foraminiferal $\delta^{18}O$ values. Across MIS 34, 32 and 28 there is additional data suggesting this glacial connection when $\delta^{18}O_{\textit{Uvigerina spp.}}$ were relatively high and warm water species, originating from the ECS, occur in the sediments of Site U1427.

6.5 Revised Palaeoceanographic Model for the Shallow, Southern Japan Sea across the MPT

There are a number of studies that have examined the palaeoenvironment and palaeoceanography of the Japan Sea in response to eustatic sea-level fluctuations

and variable precipitation intensity across East Asia over the most recent G-IG cycles (e.g. Oba et al., 1991; Tada 1994; Kitamura et al., 1997; Tada et al., 1999; Kitamura et al., 2001; Kido et al., 2007; Hoiles et al., 2012; Oba and Irino, 2012; Gallagher et al., 2018; Saavedra-Pellitero et al., 2019). Palaeoceanographic modes for the Japan Sea suggested in these studies describe marine productivity in the Japan Sea as being primarily controlled by the inflow of nutrient-rich waters from the ECS (TWC, ECSCW) across the shallow sill the south (TSS; although local riverine nutrient input cannot be excluded), which in turn is controlled by variations in eustatic sea-level and the EASM intensity (see chapter 2, section 2.4). The palaeoceanographic modes have been developed from proxy records of deep water sites of the Japan Sea covering the most recent G-IG cycles only, none of them uses records reaching as far back as the MPT.

Tada et al. (1999) investigate lithological changes, i.e. dark-light sediment colour alternations, and foraminiferal isotope records over the last 200 ka or MIS 1-7 of deep water site ODP 797. Tada et al. suggest four palaeoceanographic modes for the Japan Sea depending on TSS sill depth. At sea-level lowstands of –90 m and TSS sill depth of 40 m the Japan Sea was nearly isolated, and through excess precipitation over evaporation during these glacials (Matsui et al., 1998) the water mass in the Japan Sea became stratified, leading to the development of euxinic deep waters, i.e. anoxic and hydrogen sulphide-enriched waters (Tada et al., 1999). Their proposed mechanism, mode 2, occurs during sea-level stands of –90 to –60 m (TSS sill 40-70 m) when the Japan Sea was still isolated, but not enough to form a low-salinity surface layer. The restricted TSS inflow during this mode consists of the TWC with variable contributions of nutrient-rich, low saline ECSCW, which would, when increased, lead to a stronger water column stratification and slightly enhanced marine productivity (Tada et al., 1999). Their third mechanism, mode 3, suggests that when sea-level was –60 to –20 m (TSS sill 70-110 m) there is significant inflow via the TSS and variable relative contributions of ECSCW to the TWC can be traced in palaeo-productivity records from the Japan Sea. At times of high ECSCW contributions to the TWC, marine productivity was high and water mass stratification increased leading to reduced deep water oxygenation and better OM preservation. Mode 4 occurs during sea-level highstands of –20 to +10 m (TSS sill 110-140 m) when TWC inflow was high and dominated over the relative contributions of ECSCW. Under these conditions the deep water ventilation improved but, as the TWC is

relatively depleted in nutrients compared with ECSCW (Horibe, 1981; Tada 1999), deep waters were well oxygenated but nutrient depleted, just like at present.

Similar deep water circulation modes and sea-/sill level stands were also suggested by Watanabe et al. (2007), who investigated deep water sediment fabrics over the last 160 ka and suggested a fifth mode, which is characterised by short-term anaerobic deep water conditions caused by upwelling events, and which occurs at sea-level stands of –90 to –30 m (TSS sill 40-100 m). Recently, a shallow-water perspective was added to these palaeoceanographic models based on coccolithophore assemblages of the most recent ~450 ka, i.e. MIS 1-11, of Site U1427 (Saavedra-Pellitero et al., 2019). Their proposed mode 1, occurring at sea-levels of –90 m (TSS sill <40 m), is characterised by low nutrient-input, low sea surface salinities and low (glacial) temperatures. During the mode 1 glacials the basin is suggested to have been completely isolated, inferred from low b* and low benthic foraminiferal $\delta^{18}O$ values (Sagawa et al., 2018). Their proposed mode 2, occurring at low (–90 to –60m; TSS sill 40-70 m) to intermediate sea-levels (–60 to –20 m; TSS sill 70-110 m), encompasses the 2nd and 3rd mode of Tada et al. (1999). This mode is characterised by increasing flow through the TSS, but due to intermittent sea-level lowering strong oscillations occur in the TWC inflow/restriction, which is mirrored in the species assemblage (Saavedra-Pellitero et al., 2019). Their proposed mode 3 occurs during high sea-levels of –20 to +10 m (TSS sill 110-140 m) when TWC inflow and marine carbonate productivity are highest.

The findings presented in previous chapters of this study in combination with the eustatic sea-level variations shown in figure 6.6 suggest three palaeoceanographic modes for the shallow, southern Japan Sea across the MPT. In the following the terms TSS and TWC inflow are used for the inflow through the southern Straits of the Japan Sea, not differentiating between inflows through the Tsushima or Korea Straits (see figure 2.7). At sea-level stands of >–80/–90 m below present and **TSS sill depth of less than 40-50 m** depending on the selected sea-level reconstruction (see figure 6.5b; Bintanja et al., 2005; Elderfield et al., 2012; Rohling et al., 2014; Berends et al., 2019) there is no evidence for TWC/ECSW inflow and marine productivity is reduced while the terrigenous input is relatively higher (see chapter 5). During this palaeoceanographic **mode** (**1**; see figure 6.5d), which encompasses glacials of MIS 24-17 only and starting around the time of the 900 ka-event (see appendix C),

foraminiferal $\delta^{18}O$ records at Site U1427 are characterised by the Japan Sea-typical low glacial values caused by freshening of the Japan Sea water mass as a consequence of the isolation of the basin (figure 6.6a). The reduced (surface) water salinity led to stratification of the water column and anoxic/dysoxic conditions at deeper-water sites (Tada et al., 1999; Kido et al., 2007). Ocean current strength was likely reduced during mode 1, as inferred from the fining of the sediments (chapter 5, section 5.3.3), which gives further support for the suggested isolation of the Japan Sea. The suggested mode 1 complements the established palaeoceanographic modes of the Japan Sea (chapter 2, section 2.4), and is similar in its expression as the modes 1 in Tada et al. (1999) and Saavedra-Pellitero et al. (2019).

At intermediate sea-level lowstands of ~–80 to –30 m and **TSS sill water depths of ~50-100 m** (figure 6.5d) another palaeoceanographic mode appears (**mode 2**), which dominates the glacials of MIS 39-25 and also occurs during the interglacials MIS 23 and 18 (figure 6.6b). At the TSS sill depths of mode 2 some degree of water-mass exchange and TWC inflow is present, but with varying contributions of low-saline waters as a result of varying contributions of ECSCW to the TWC and/or freshwater runoff from the surrounding landmasses. During mode 2 marine productivity in the shallow, southern Japan Sea is very sensitive to variations in the composition of the TWC, i.e. variations in the contributions of nutrient-rich, low saline ECSCW to the TWC.

An example for high ECSCW/freshwater runoff during mode 2 is MIS 23, a weakly expressed interglacial (see appendix C). At a TSS sill stand of around 80-95 m the $\delta^{18}O_{\textit{Uvigerina spp.}}$ record of MIS 23 shows the Japan Sea-typical low glacial values, indicating reduced exchange with the open ocean and an enhanced impact of freshwater input on the $\delta^{18}O$ record (figure 6.5a). Some degree of TWC inflow and/or nutrient input was however present, as inferred from enhanced marine productivity proxies (see figure 6.5b, c). Note, however, that a clear marine productivity signal is not present, but hints towards periods of higher/lower productivity are present in the collected proxy records, Most likely, the freshwater imprint on the $\delta^{18}O_{\textit{Uvigerina spp.}}$ record is caused by a combination of restricted, but present, exchange with the open ocean and increased contributions of ECSCW to the TWC. Although the nutrient input via TWC through the TSS is thought to be the main control on marine productivity in the Japan Sea (chapter 2, section 2.4), in this particular setting with

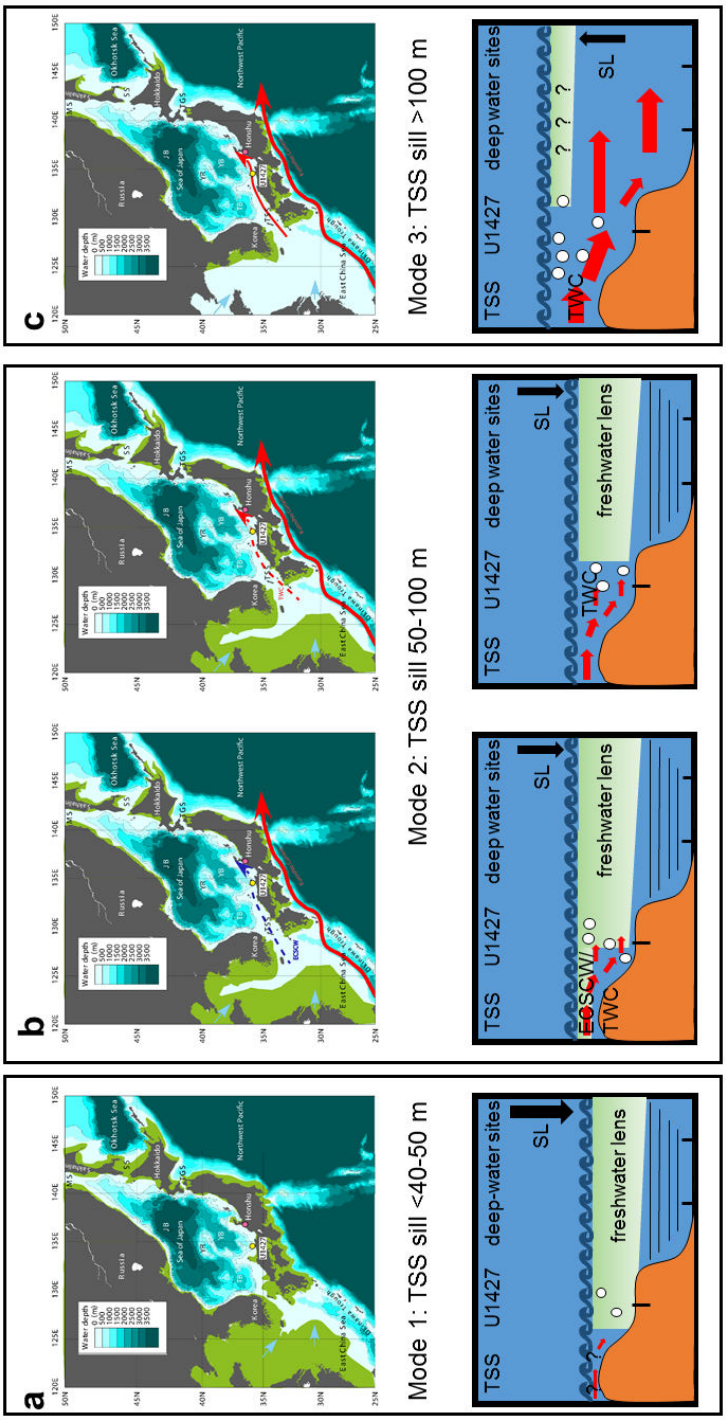

Figure 6.6. Revised palaeoceanographic modes for the shallow, southern Japan Sea across the MPT with major ocean currents (red and dark blue lines) as well as major freshwater sources (light blue arrows). The base map is from Tada et al. (2013) while palaeo-shorelines are redrawn for mode 1 from Saavedra-Pellitero et al. (2019) (sea-level –100 m; fig. 6.6a), for mode 2 from Tada et al. (2013) (for central to north Honshu, Hokkaido and Sakhalin) and Park and Chu (2006) (for southern Japan Sea, ECS and TSS area) (sea-level -75 m; fig. 6.6b), and for mode 3 from Saavedra-Pellitero et al. (2019) (sea-level –20 m; fig. 6.6c). TSS = Tsushima strait, SL = sea-level, TWC = Tsushima warm current, ECSCW = East China Sea coastal water. Schematic illustrations indicate primary productivity (white dots), drill sites (black vertical lines) and stratification of the water column (horizontal lines in bottom water).

close proximity to land input of nutrients and freshwater from the surrounding landmasses cannot be excluded. This combination of enhanced input of low-saline waters and nutrients led to low $\delta^{18}O_{Uvigerina\ spp.}$ values and primed marine productivity during MIS 23.

In contrast, during the glacial of MIS 38 the TSS sill water depth was shallower than during MIS 23, estimated to have been around ~60-70 m (figure 6.5d), which should have restricted the exchange with the open ocean, which should have led to a pronounced freshwater imprint on the $\delta^{18}O_{Uvigerina\ spp.}$ record, lowering $\delta^{18}O_{Uvigerina\ spp.}$ values. However, relatively higher $\delta^{18}O_{Uvigerina\ spp.}$ values suggest reduced freshwater imprinting (figure 6.5a). The reduced freshwater imprinting implies a better water-mass exchange with the open ocean and/or lower contributions of low-saline ECSCW to the TWC (figure 6.6b). Marine productivity and terrigenous input during MIS 38 were at similar levels as during MIS 23 as inferred from $\delta^{13}C_{org}$ (marine versus terrigenous OM proxy), TOC flux and Rock-Eval pyrolysis parameters (OI, HI) (chapter 5), which suggests similar nutrient-availability. The combination of marine productivity at levels similar to MIS 23 with relatively high glacial $\delta^{18}O_{Uvigerina\ spp.}$ values suggests exchange with the open ocean was possible, as was the inflow of the TWC, but the relative contribution of low-saline ECSCW to the TWC was reduced, reducing the impact of low-saline waters and leading to high glacial $\delta^{18}O$ values during MIS 38.

The comparison of MIS 38 and 23 demonstrates the sensitivity of the shallow, southern Japan Sea during mode 2 sea-level/TSS sill stands to variations in the contributions of ECSCW to the TWC, which is a result of variations in the EASM precipitation intensity. The EASM variations do not only affect the contributions of ECSCW to the TWC but also the amount of runoff from the surrounding landmasses and precipitation over the Japan Sea. The combination of these factors have played an important role in the shaping of the glacial of MIS 36. MIS 36, in general having high $\delta^{18}O_{Uvigerina\ spp.}$ values like MIS 38, but during its mid-section $\delta^{18}O$ values in both planktonic and benthic foraminifera are reduced (figure 6.5a, d). This $\delta^{18}O$ reduction is unlikely a result of more restricted conditions as it likely occurs together with a sea-level rise/TSS sill deepening, which would have improved the exchange with the open ocean (see Elderfield et al., 2012; figure 6.5d). Instead, the $\delta^{18}O$ reduction is more likely related to increased EASM precipitation starting around 1200 ka, as

inferred from Chinese loess-paleosol sequences (e.g. An et al., 1990; see chapter 5, section 5.4.3). As a result of the EASM strengthening the contribution of warm, low-saline, nutrient-rich ECSCW to the TWC increased, which resulted in lower $\delta^{18}O$ values and primed marine productivity (see figure 6.5). The increased contribution of warm ECSCW is supported by higher Mg/Ca-based temperature estimates (section 6.4.3) and the presence of remains of warm water species in the sediments (see figure 6.5d).

While sub-orbital scale variations in marine productivity and $\delta^{18}O$ frequently occur during mode 2, the more extreme TSS sill stands during modes 1 and 3 (see below) seem to make the palaeoceanography of the shallow, southern Japan Sea less sensitive to EASM variations. The proposed mode 2 is similar to mode 2 and 3 of Tada et al. (1999) and mode 2 of Saavedra-Pellitero et al. (2019). While the study of Tada et al. (1999) only covers the last ~85 ka and Saavedra-Pellitero et al. (2019) the last ~450 ka, this study extends back to the MPT and confirms the extension of mode 2 back to ~1200 ka. Furthermore, the proposed mode 2 of this study dominates during glacials of MIS 39-25, strongly suggesting a glacial connection between the open ocean and shallow, southern Japan Sea during the early stage of the MPT. In the later stage of the MPT, MIS 24-17, this glacial connection is absent and instead the Japan Sea-typical low glacial $\delta^{18}O$ values suggest the glacial isolation of the basin (see mode 1 above). Most importantly, previous studies suggested the glacial isolation of the Japan Sea was a feature of glacials of at least the last 1.7 Ma (e.g. Kitamura, 2007; see chapter 2, section 2.4), but the geochemical records of Site U1427, presented in this study, suggest a better glacial connection before MIS 25.

Another palaeoceanographic mode occurs at highest sea-level stands of less than –30 m and **TSS sill depths of >100 m** and dominates interglacials of MIS 39-17, potentially also occurring during some glacials of MIS 39-25, depending on the selected sea-level reconstruction (figure 6.5d). This palaeoceanographic **mode 3** is characterised by an exchange with the open ocean and unrestricted TWC inflow, as inferred from high, open ocean-like $\delta^{18}O_{\textit{Uvigerina spp.}}$ values and high marine productivity (figure 6.6c). Reduced $\delta^{18}O$ values during mode 3 are likely related to enhanced contribution of ECSCW to the TWC and hence linked to times of enhanced EASM precipitation. This mode is similar to modes 4 of Tada et al. (1999) and mode 3 of Saavedra-Pellitero et al. (2019).

Using the suggested palaeoceanographic modes to evaluate the sea-level reconstructions shown in figure 6.5d suggests the model by Bintanja et al. (2005) may not be a reliable tracer of past sea-level for the shallow, southern Japan Sea across the MPT. The sea-level curve by Bintanja et al. often indicates lower sea-levels/shallower TSS sill water depths than suggested by the geochemical records of Site U1427, e.g. during MIS 36 and 30. The sea-level reconstructions by Elderfield et al. (2012), Rohling et al. (2014) and Berends et al. (2020) show a better fit with the geochemical records of Site U1427 and suggested palaeoceanographic modes across the MPT. As a word of caution, the Tsushima Strait (TSS) sill-level reconstruction presented in this thesis should, however, not be used as a (global) sea-level reconstruction, as it is influenced by local influences, such as local tectonics in the TSS sill and local freshwater imprint on $\delta^{18}O$ records.

6.6 Summary and Conclusions

This chapter has shown that there is a change in the expression of glacials in both benthic and planktonic foraminiferal $\delta^{18}O$ records across the MPT. The Japan Sea-typical low-$\delta^{18}O$ glacials do not persist in the investigated interval, but are only present from MIS 24 and younger, and from there extend to the most recent sediments as shown by Sagawa et al. (2018) (figure 4.4). Most intriguingly, the low-$\delta^{18}O$ glacials do not continue across MIS 25-39, instead low b* indices, used as an aid in the identification of glacials and interglacials, often coincide with relatively higher $\delta^{18}O$ values, just like in the open ocean (figure 6.5). This behaviour is most pronounced during MIS 39-36 as well as during MIS 34, 33 and 26.

After having eliminated effects such as possible diagenetic alteration of the foraminifera shells (section 6.4.1) and age model uncertainties, the relatively higher glacial $\delta^{18}O$ values across MIS 39-25 were confirmed by foraminiferal Mg/Ca temperature estimates that suggest relatively lower temperatures during these glacials (section 6.4.2). Subsequently, potential palaeoenvironmental and palaeoceanographic causes were investigated (section 6.4.3), and it was concluded that the most likely cause for the glacial $\delta^{18}O$-switch are generally higher eustatic sea-level/TSS sill water depths before MIS 24 (section 6.4.4). However, influences of the variations in the EASM complicate the palaeoceanography in this setting, so that a revised palaeoceanographic model for the shallow, southern Japan Sea that covers the MPT was developed.

The suggested palaeoceanographic mode 1, active at TSS sill water depths of <40-50 m and encompassing glacials across MIS 24-17 only, restricts the exchange with open ocean waters and results in low $\delta^{18}O$ values and low marine productivity (figure 6.6a). During the suggested mode 2, which is active at TSS sill water depths of ~50-100 m and dominates during glacials of MIS 39-25 but also interglacials MIS 23 and 18, TWC inflow is generally possible and the influence of EASM precipitation on the palaeoceanography is highest (figure 6.6b). At times of low precipitation, $\delta^{18}O$ are high, often similar to the open ocean, while when precipitation increased, $\delta^{18}O$ reduce most likely due to the increased contributions of lower-saline ECSCW to the TWC. This EASM mechanism is suggested to fundamentally having played a role in shaping MIS 36. This is an example how monsoon/precipitation signals can be recorded in the sediments of Site U1427, specifically in $\delta^{18}O$ values and marine productivity, even though no direct rainfall proxy was applied. Crucially, the suggested mode 2 is active during glacials and interglacials alike, confirming previous suggestions of a possible glacial connection between the open ocean and the shallow, southern Japan Sea (section 6.5). Finally, during the suggested palaeoceanographic mode 3, active at maximum TSS sill water depths and dominating during interglacials of MIS 39-17, TWC inflow is unrestricted and high nutrient delivery primes marine productivity.

Chapter 7: Thesis Summary and Conclusions

7.1 Introduction

Recently recovered sediments from a shallow-water site in the southern Japan Sea, IODP Site U1427, promised high-resolution, continuous records of EAM variability across the last ~1300 ka (e.g. Tada et al., 2015b). Furthermore, due to its shallow-water position, the site promised to enable the creation of a foraminifera-based isotope chemo-stratigraphy, which could aid as a Rosetta stone for the entire Japan Sea region by linking its age model to other Japan Sea sites.

Complications in the interpretation of proxy records gathered at this site were to be expected due to its close proximity to land and due to the sensitivity of the Japan Sea to glacio-eustatic sea-level variations, which is a result of its shallow sills (see chapter 2, section 2.4). Since glacio-eustatic sea-level variations increased across the MPT, studying possible effects on the palaeoceanography of the Japan Sea was the specific focus of this study.

7.2 Key Outcomes of this PhD Project

7.2.1 Chronology for IODP Site U1427

The revised age model for the sediment interval ~260-525 m shows continuously high sedimentation rates between 30 and 90 cm/ka. Based on these, a revised age-depth relationship was generated, which forms the basis of age estimates for samples used in this thesis (table 4.1, figure 4.2). These age estimates have to be taken cautiously due to the assumed linear sedimentation rates between age tie points, of which there are six across the studied ~275 m sediment column (see table 4.1). The predominantly heavy bioturbation of the sediments puts an additional constraint on precise correlations (Tada et al., 2015c), but the age estimates support earlier findings that suggest the studied sediment interval encompasses the MPT (Tada et al., 2015b; Sagawa et al., 2018; Itaki et al., 2018).

Bulk sediment accumulation rates are high, up to 110 g/cm^{2}ka (chapter 5, section 5.4.1), and could in theory enable a maximum temporal resolution of ~1-2 ka based on the samples available for this study (each 1 cm thick and at spacing of ~50 to 100 cm between samples). This would allow investigations of millennial-scale variabilities in the proxy records, but the highest 1 ka resolution does not reveal new (additional)

palaeo-signals in comparison to a 2 ka resolution, suggesting the sediments of Site U1427 did not archive information on such short timescales.

It is likely that the homogenising/mixing effect of bioturbation on the sediments has affected the potential of these sediments to reliably record sub-orbital and millennial timescale changes in certain parts of the sediment record. Therefore, the above theoretical temporal resolution of 1-2 ka needs to be taken cautiously, and it is almost certain that bioturbation destroyed the archive of individual DOCs (see chapter 2). More importantly, the sediments at Site U1427 do not contain the millimetre- to centimetre-scale dark/light sediment alternations associated with DOCs at deep water sites from the Japan Sea. It would therefore be difficult even with higher temporal resolution to study the relationship between EASM variability and DOCs. This study demonstrates that the sediments of Site U1427 cannot be used as a Rosetta stone, i.e. providing a high-resolution chronological framework for testing the relationship between EASM variability and DOCs, or correlating this section to deep water sites in the Japan Sea (Sagawa et al., 2018; Itaki et al., 2018; Tada et al., 2018).

One clear advantage of Site U1427 is, however, its good calcite preservation, enabling an isotope chemo-stratigraphy to be established (chapter 4, section 4.4). This is achieved by the presented near-continuous benthic foraminiferal $\delta^{18}O$ record, which is the first to cover the MPT from the Japan Sea, encompassing MIS 39-17. In general, the $\delta^{18}O_{\textit{Uvigerina spp.}}$ patterns are in agreement with previously published records from the Japan Sea, showing lower glacial and higher interglacial values. These Japan Sea-specific patterns appear from MIS 24 onwards, and continue to the most recent sediments (Sagawa et al., 2018). Between MIS 39-36 and perhaps continuing to MIS 25, however, the $\delta^{18}O$ deviates from the Japan Sea-typical pattern, showing glacials that are characterised by an open ocean-like signature of relatively higher glacial and lower interglacial $\delta^{18}O$ values (see chapter 4, section 4.4). The most likely cause for this shift in glacial $\delta^{18}O$ values is a fundamental change in the glacial palaeoceanography of the shallow, southern Japan Sea across the MPT. Based on this hypothesis, revised palaeoceanographic modes have been proposed (see chapter 6 and below).

7.2.2 Palaeo-climatic and marine productivity changes across the MPT

The proxy records of Site U1427 prove challenging to interpret due to the Japan Sea's palaeoceanography and variable contributions of terrigenous material on orbital and sub-orbital timescales (see this study; Sagawa et al., 2018; Gallagher et al., 2018; Black et al., 2018). While bulk sediment mass accumulation rates are much higher at Site U1427 than in the open ocean or at deep water sites in the Japan Sea (see chapter 5, section 5.4.1), but their interpretation is not straightforward. Some traditional palaeoceanographic proxies have been brought to the limits of being interpretable in this setting (e.g. C/N ratios) and hence the applied multi-proxy approach has proved indispensable in deciphering the palaeo-signals and origins of material (e.g. terrigenous/marine organic matter).

Nutrient input to and marine productivity in the Japan Sea are controlled by a combination of eustatic sea-level variations and EASM intensity and, in addition, at Site U1427 likely by local riverine runoff (chapter 5, section 5.4.2). In general, marine productivity and terrigenous input vary with G-IG cycles across MIS 39-17, suggesting higher marine productivity during interglacials and relatively higher terrigenous contributions to the sediments during glacials (see chapter 5). Exceptions from this general trend occur, for example, during the glacial of MIS 36 when EASM precipitation intensity and marine productivity increase during its mid-section (see chapter 5, section 5.4). Another example is MIS 23, a weakly expressed interglacial in this record, which suggests marine productivity was lower than usual for an interglacial (chapter 5, section 5.4). Overall, the amplitude in change of marine productivity decreased between MIS 35 and 25 through enhanced glacial productivity while interglacial productivity remained at similar levels and their frequency remained high (see chapter 4, table 4.3; appendix C). Across the same interval, benthic $\delta^{18}O$ values are highly variable, likely caused by a strengthened and more variable EASM (see chapters 5 and 6). The combination of highly variable $\delta^{18}O$ values and reduced expression of glacials and interglacials in the productivity/input records makes the differentiation between glacials and interglacials in the interval MIS 39-25 challenging (see Chapter 4).

The above examples demonstrate the complexity of the palaeoceanography of the Japan Sea and contributions to its sediments, i.e. marine productivity and/or terrigenous input, especially in its shallow, southern part, including Site U1427. Eustatic sea-level and EASM intensity both affect marine productivity and $\delta^{18}O$

values at Site U1427, which often makes it difficult to decipher their contributions and to discern whether they are expressed in the same fashion in proxy records during glacials and interglacials.

7.2.3 Palaeoceanographic modes for the shallow, southern Japan Sea across the MPT

The enhanced marine productivity during several glacials across MIS 39-25 implies a novel mechanism of enhanced nutrient input, leading to new palaeoceanographic modes being proposed across the MPT (see chapter 6). While occasional glacial inflow of TWC waters has not been categorically excluded by previous studies (e.g. Tada et al., 1999; Saavedra-Pellitero et al., 2019), the presented study supports this idea with high-resolution geochemical records that indicate glacial TWC inflow may have persisted for entire cold stages, e.g. MIS 38 (see chapter 6, section 6.5).

This proposed mode, which is characterised by TWC inflow during glacials, dominated during glacials across MIS 39-25, at a time when glacial sea-levels were higher globally and in the Japan Sea (chapter 6, figure 6.5). Crucial for future EASM reconstructions, this glacial connection implies that EASM variability can be recorded at Site U1427 during glacials and interglacials across MIS 39-25, while previously it was presumed the EASM signals must be dampened during glacials due to the combined effect of near-isolation of the Japan Sea during sea-level lowstands and the reduced EASM precipitation intensity (see chapter 2, section 2.4).

The proposed mode 1 persisted during the most pronounced sea-level lowstands and shallowest TSS sill water depths of 40-50 m during glacials of MIS 24-17. It was characterised by little to no TWC inflow, as inferred from low marine productivity and likely little to no nutrients supplied by TWC cut-off, and by low $\delta^{18}O$ values as a result of the formation of a freshwater lens, which overrode the open ocean ice-volume/temperature signal.

The proposed palaeoceanographic mode 2 persisted at intermediate TSS sill stands of 50-100 m and dominated during glacials of MIS 39-25. It was characterised by a strong impact of monsoonal precipitation, i.e. EASM intensity variability. At times of low precipitation and weak EASM, foraminiferal $\delta^{18}O$ values were high, similar to the open ocean, and marine productivity was low. In contrast, at times of high precipitation, which led to enhanced contributions of low-saline, nutrient-rich ECSCW

to the TWC, glacial $\delta^{18}O$ values were low and marine productivity could increase due to enhanced nutrient supply. From these different modes it can be deduced that although there is no direct proxy record for the EASM, monsoon signals (precipitation) are contained in the sediments of Site U1427.

The third proposed palaeoceanographic mode persisted during interglacial sea-level highstands and maximum TSS sill stands across MIS 39-17. It was characterised by high $\delta^{18}O$ values, suggesting an unrestricted exchange with open ocean waters and high marine productivity as a result of high contributions of ECSCW to the TWC, caused by strong EASM precipitation.

The proposed improved glacial connection across the MPT has impacts on some age models for Japan Sea records, where the presence of warm water species, previously thought to have intruded only during interglacial sea-level highstands, was used to correlate interglacials (e.g. Hoiles et al., 2012). Such simplified age controls would need to be revised, at least if produced for locations in the southern Japan Sea.

7.3 Outlook and Future Work

In this study, the palaeoceanography of the shallow, southern Japan Sea was investigated across the MPT. The Japan Sea palaeoceanography is intrinsically linked with orbital- and sub-orbital- (millennial-) scale variations in the EASM and the EASM has been proposed as a possible important influence during the MPT (see chapter 2) (e.g. Oba et al., 1991; Tada, 2004). Sub-orbital scale lithological alternations have been identified in sediments of deep-sea sites across the Japan Sea and are thought to be linked with EASM variations, however, linking these sediments with global climate events has not yet been possible due to challenges in establishing high-resolution age models (see chapter 2, section 2.4).

In this study, a foraminiferal-calcite based isotope chemo-stratigraphy was established using sediments from a shallow-water site in the southern Japan Sea, IODP U1427. This site is under direct influence of the TWC, which strength and composition is linked with variations in the EASM (See chapter 2, section 2.4 and chapter 3, section 3.1, 3.2). This stratigraphy allows correlating the records of Site U1427 to sites across the world, however, linking it with deeper-water sites in the Japan Sea has been difficult due to the absence of characteristic dark/light sediment

alternations (Sagawa et al., 2018; Itaki et al., 2018; Tada et al., 2018), which were proposed to be traceable basin-wide and associated with orbital- and sub-orbital timescales (e.g. Tada, 2004; Tada et al., 2013).

A correlation attempt was made by Sagawa et al. (2018), linking their well-dated upper interval of Site U1427 (orbital-scale, $\delta^{18}O$ chemo-stratigraphy) with the deep water Site U1424 (northern Japan Sea, ~2800 m water depth) via sediment colour records based on core section photographs. This correlation proved difficult due to the faint colour changes in the upper ~250 m of sediments of Site U1427 (Sagawa et al., 2018). Such a correlation is even more difficult in the sediments deeper than 250 m, studied in this work, as colour variations are even fainter and millimetre-scale dark/light sediment alternations are not present or have been destroyed by heavy bioturbation (see chapter 3, section 3.2). Therefore, the stratigraphy of Site U1427 cannot be used as an anticipated regional chronological control. It would therefore be recommendable to drill a water depth transect in the southern Japan Sea, which should enable linking the isotope chemo-stratigraphy of Site U1427 with gradually deeper water sites based on their geochemical records and $\delta^{18}O$ patterns.

With respect to the proposed revised palaeoceanographic modes for the shallow, southern Japan Sea across the MPT and the suggested switch around MIS 25 from high, open ocean-like to low, Japan Sea-typical glacial $\delta^{18}O$ values (see section 7.2.4), a freshwater proxy would be very useful to support/reject this idea. It has been proposed that at sea-level/TSS sill stands of palaeoceanographic mode 2 the influence of the monsoon and riverine runoff from the nearby continent has had a great impact on the palaeoceanography, affecting the $\delta^{18}O$ record of Site U1427. Although the $\delta^{18}O$ is at times dominated by the freshwater signal, $\delta^{18}O$ is not a direct proxy for freshwater input as such. It would therefore be beneficial to have a direct proxy of freshwater input, such as the presence of freshwater diatoms in the sediments.

In addition, it would be useful to expand micropalaeontological studies, such as those of Gallagher et al. (2018) and Saavedra-Pellitero et al. (2019) for the upper 250 m of Site U1427, as these can trace warm water species intrusions during the glacials of MIS 39-25. Such intrusions are linked to the inflow of warm waters through the TSS and would hence provide greater certainty to the proposed glacial TWC inflow. These micropalaeontological studies would be especially useful if linked with

sites in the northern East China Sea, such as IODP Sites U1428 and U1429, which could be used for reference and to trace EASM variations, as these sites record the Yangtze/Yellow River discharge more directly and in high-resolution (e.g. Tada et al., 2013). If the same patterns appeared during glacials in the ECS and Japan Sea records, this would support the idea of the improved glacial connection across MIS 39-25. This is currently not possible as the proxy records published of those IODP sites either do not cover the MPT or are of insufficient resolution in this interval, i.e. ~1200-600 ka (Anderson et al., 2018; Beny et al., 2018; Clemens et al., 2018; Zhao et al., 2018; Anderson et al., 2019; Matsuzaki et al., 2019; Zhao et al., 2019; Zhou et al., 2019).

With respect to the difficulties in deciphering the marine productivity from the terrigenous input signal (see chapter 5) it would be interesting to undertake provenance studies of particles and to generate a $CaCO_3$ record that subdivides between carbonate in the >63 and <63 µm grain-size fractions. Assuming carbonates in the >63 µm fraction mainly consist of foraminifera and molluscs, while those <63 µm mainly consist of coccoliths, ostracod shells and other nanno-fossil remains, as well as DIC-derived carbonates, a better understanding of marine carbonate productivity could be achieved. This would be particularly helpful to decipher if or in which intervals $CaCO_3$ reflects a surface or bottom water signal. If $CaCO_3$ was mainly associated with the fine fraction, then it would likely represent a surface water signal and could be linked with the EASM and nutrient-input with greater certainty.

In conclusion, the sediments of Site U1427 hold exciting new insights into the expression of the MPT in a marginal basin but also reveal that in such settings the influence of regional factors, e.g. EASM, sills/straits and current systems, cannot be neglected and need to be recognised to correctly interpret the sedimentary record.

Chapter 8: References

Abe-Ouchi, A., Saito, F., Kawamura, K., Raymo, M.E., Okuno, J., Takahshi, K., Blatter, H. (2013) 'Insolation-driven 100,000-year glacial cycles and hysteresis of ice-sheet volume', *Nature*, 500, pp. 190-193.

Ahagon, N., Tanaka, Y., Ujiié, H. (1993) '*Florisphaera profunda*, a possible nannoplankton indicator of late Quaternary changes in sea-water turbidity at the northwestern margin of the Pacific', *Mar. Micropaleontol.*, 22, pp. 255–273.

An, Z., Tunghseng, L., Yanchou, L., Porter, S.C., Kukla, G., Xihao, W., Yingming, H. (1990) 'The long-term paleomonsoon variation recorded by the loess-paleosol sequences in central China', *Quat. Int.*, 7/8, pp. 91-95.

Analytic Jena AG (2012) *Multi EA4000, Elementary Analyzer - Operating Manual*, Jena: Analytic Jena AG.

Anand, P., Elderfield, H., Conte, M.H. (2003) 'Calibration of Mg/Ca thermometry in planktonic foraminifera from a sediment trap time series', *Paleoceanography*, 18(2), pp. PA000846.

Anderson, D.M. (2001) 'Attenuation of millennial-scale events by bioturbation in marine sediments', *Paleoceanography*, 16(4), pp. 352-357.

Anderson, C.H., Murray, R.W., Dunlea, A.G., Giosan, L., Kinsley, C.W., McGee, D., Tada, R. (2018) 'Climatically driven changes in the supply of terrigenous sediment to the East China Sea', *Geochem., Geophys., Geosys*., 19(8), pp. 2463-2477.

Anderson, C.H., Murray, R.W., Dunlea, A.G., Giosan, L., Kinsely, C.W., McGee, C.W., Tada, R. (2019) 'Aeolian delivery to Ulleung Basin, Korea (Japan Sea), during development of the East Asian Monsoon through the last 12 Ma', *Geological Magazine*, pp. 1-12.

Ao, H., Dekkers, M.J., Xiao, G., Yang, X., Qin, L., Liu, X., Qiang, X., Chang, H., Zhao, H. (2012) 'Different orbital rhythms in the Asian summer monsoon records from north and south China during the Pleistocene', *Glob. Planet. Change*, 80-81, pp. 51-60.

Barker, S., Greaves, M. and Elderfield, H. (2003) 'A study of cleaning procedures used for foraminiferal Mg/Ca paleothermometry', *Geochem., Geophys., Geosys.*, 4(9), p. 8407.

Basak, C., Fröllje, H., Lamy, F., Gersonde, R., Benz, V., Anderson, R.F., Molina-Kescher, M., Pahnke, K. (2018) 'Breakup of last glacial deep stratification in the South Pacific', S*cience*, 359, pp. 900–904.

Bassinot, F.C., Labeyrie, L.D., Vincent, E., Quidelleur, X., Shackleton, N.J., Lancelot, Y. (1994) 'The astronomical theory of climate and the age of the Brunhes-Matuyama magnetic reversal', *EPSL*, 126, pp. 91-108.

Bé, A.W.H. (1977) 'An ecological, zoological and taxonomic review of recent planktonic foraminifera', in: Ramsay, A.T.S. (ed.) *Oceanic micropalaeontology*, *volume 1*, London: Academic Press, pp. 1-100.

Bentov, S., and J. Erez (2006) 'Impact of biomineralization processes on the Mg content of foraminiferal shells: A biological perspective', *Geochem. Geophys. Geosyst.*, 7, pp. Q01P08.

Beny, F., Toucanne, S., Skonierczny, C., Bayon, G., Ziegler, M, (2018) 'Geochemical provenance of sediments from the northern East China Sea document a gradual migration of the Asian Monsoon belt over the past 400,000 years', *Quat. Sci. Rev*., 190, pp. 161-175.

Berends, C.J., de Boer, B., Dolan, A.M., Hill, D.J., van de Wal, R.S.W. (2019) 'Modelling ice sheet evolution and atmospheric CO2 during the late Pliocene', *Clim. Past*, 15, pp. 1603-1619.

Berger, W.H. (1968) 'Planktonic foraminifera: selective solution and paleoclimatic interpretation', *Deep-Sea Res.*, 15, pp. 31-43.
Berger, A. and Loutre, M.F. (1991) 'Insolation values for the climate of the last 10 million years', *Quat. Sci. Rev.,* 10(4), pp. 297-317.
Berger, W.H. and Jansen, E. (1994) 'Mid-Pleistocene climate shift: The Nansen connection', in: Johannessen, O.M., Muench, R.D., Overland, J.E. (eds.) *The polar oceans and their role in shaping the global environment*. Geophysical Monographs 84, Washington D.C.: American Geophysical Union, pp. 295-311.
Berger, W.H., Li, X., Loutre, M.F. (1999) 'Modelling northern hemisphere ice volume over the last 3 Ma', *Quat. Sci. Rev.*, 18, pp. 1-11.
Bernard, B.B., Bernard, H., Brooks, J.M. (1995) 'Determination of total carbon, total organic carbon and inorganic carbon in sediments', College Station (TX): TDI-Brooks International/ B&B Laboratories, 5pp.
Bertrand, P. and Lallier-Vergés, E. (1993) 'Past sedimentary organic matter accumulation and degradation controlled by productivity', *Nature*, 364, pp. 786-788.
Bintanja, R., van de Wal, R.S.W., Oerlemans, J. (2005) 'Modelled atmospheric temperatures and global sea levels over the past million years', *Nature*, 437, pp. 125-128.
Bintanja, R. and van de Wal, R.S.W. (2008) 'North American ice-sheet dynamics and the onset of 100,000-year glacial cycles', *Nature*, 454, pp. 869-872.
Birner, B., Hodell, D.A., Tzedakis, P.C., Skinner, L.C. (2016) 'Similar millennial climate variability on the Iberian margin during two early Pleistocene glacials and MIS 3', *Paleoceanography,* 31, pp. 203-217.
Black, H.D., Anderson, W.T., Alvarez-Zarikian, C.A. (2018) 'Data report: organic matter, carbonate, and stable isotope stratigraphy from IODP Expedition 346 Sites U1426, U1427, and U1429', in: Tada et al. (eds.) *Proc. IODP, volume 346*.
Boersma, A. (1984) *Handbook of common Tertiary Uvigerina*, New York: Microclimates Press, Plate 2 (p. 123) and Plate 2 (p. 156).
Bond, G., Heinrich, H., Broecker, W., Labyrie, L., McManus, J., Andrewes, J., Huon, S., Jantschik, R., Clasen, S., Simet, C., Tedesco, K., Klas, M., Bonani, G., Ivy, S. (1992) 'Evidence for massive discharges of icebergs into the North Atlantic ocean during the last glacial period', *Nature*, 360, pp. 245-249.
Boyle, E.A. (1981) 'Cadmium, zink, copper and barium in foraminifera tests', *Earth and Planetary Science Lett.*, 53, pp. 11-35.
Boyle, E.A. (1983) 'Manganese carbonate overgrowths on foraminifera tests', *Geochim. et Cosmochim. Acta*, 47, pp. 1815-1819.
Boyle, E. and Keigwin, L. (1985) 'Comparison of Atlantic and Pacific paleochemical records for the last 215,000 years: changes in deep ocean circulation and chemical inventories', *EPSL*, 76, pp. 135-150.
Bramlette, M.N. (1961) 'Pelagic sediments', in: Sears M. (ed.) *Oceanography*. Washington D.C.: American Association for the Advancement of Science, Special Publication 67, pp. 345-366.
Brasier, M.D. (1995) 'Fossil indicators of nutrient levels. 1: Eutrophication and climate change'. *Geological Society, London, Special Publications*, 83, pp. 113-132.
Briucaud, A., Morel, A., Prieur, L. (1981) 'Absorption by dissolved organic matter of the sea (yellow substance) in the UV and visible domains', *Limnol. Oceanogr.,* 26(1), pp. 43–53.
Brodie, C.R., Leng, M.J., Caford, J.S.L., Kendrick, C.P., Lloyd, J.M., Yongqiang, Z., Bird, M.I. (2011) 'Evidence for bias in C and N concentrations and δ13C composition of terrestrial and aquatic organic materials due to pre-analysis acid preparation methods'*, Chem. Geol.*, 282, pp. 67-83.

Broecker, W.S. (1982) 'Glacial to interglacial changes in ocean chemistry', *Prog. Oceanogr*. 11, 151–197.
Broecker, W.S. and Peng, T.-H. (1982) *'Tracers in the Sea'*, Cambridge: Cambridge University Press, 690pp.
Broecker, W.S. and Denton, G.H. (1990) 'What drives glacial cycles?', *Scientific American*, 262(1), pp. 49-56.
Broecker, W.S. (1991) 'The great ocean conveyer', *Oceanography*, 4(2), pp. 79-89.
Broecker, W.S. and Peng, T.-H. (1993) 'What caused the glacial to interglacial CO_2 change?', in: Heimann M. (eds.) *The global carbon cycle*, Amsterdam-Berlin-Heidelberg- London-New York: Springer, pp. 95-115.
Brohan, P., Kennedy, J.J., Harris, I., Tett, S.F.B., Jones, P.D. (2006) 'Uncertainty estimates in regional and global observed temperature changes: a new data set from 1850', *J. Geophys. Res. – Atmospheres*, 111(D12), pp. D12106.
Canfield, D.E. (1989) 'Sulfate reduction and oxic respiration in marine sediments: implications for organic carbon preservation in euxinic environments', *Deep-Sea Res.*, 26, pp. 121-138.
Casazza, L.R. (2012) 'Symbiosis in the fossil record: Eocene *Nummulites* and Pleistocene reefs of Egypt', PhD thesis, University of California, Berkley. 115 pp.
Chalk, T.B., Hain, M.P., Foster, G.F., Rohling, E.J., Sexton, P.F., Badger, M.P.S., Cherry, S.G., Hasenfratz, A.P., Haug, G.H., Jaccard, S.L., Martínez-García, A., Pälike, H., Pancost, R.D., Wilson, P.A. (2017) 'Causes of ice age intensification across the mid-Pleistocene transition', *Proc. Natl. Acad. Sci. USA*, 114, pp. 13114–13119.
Cheng, H., Edwards, R.L., Sinha, A., Spötl, C., Yi, L., Chen, S., Kelly, M., Kathayat, G., Wang, X., Li, X., Kong, X., Wang, Y., Ning, Y., Zhang, H. (2016) 'The Asian monsoon over the past 640,000 years and ice age terminations', Nature, 534, pp. 640-646.
Chikaraishi, Y., Naraoka, H., Pouson, S.R. (2004) 'Carbon and hydrogen isotopic fractionation during lipid biosynthesis in a higher plant (Cryptomeria japonica)', *Phytochem.*, 65(3), pp. 323-330.
Chough, S.K., Lee, H.J., Yoon, S.H. (2000) *Marine Geology of Korean Seas – Chapter 5: East Sea*. 2nd edt., Amsterdam: Elsevier, 173-197.
Claringbould, J.S., Sato, H., Ishiyama, T., Van Horne, A., Kawasaki, S., Abe, S. (2019) 'Cenozoic evolution of the Tsushima Strait and the Fukue Basin, southern Sea of Japan: An interplay of tectonics, palaeo-environment, and volcanism', *Japan Geoscience Union Meeting*, abstract SCG57-12, 26th-30th May 2019, Chiba, Japan.
Clark, P.U. and Pollard, D. (1998) 'Origin of the middle Pleistocene transition by ice sheet erosion of regolith', *Paleoceanography*, 13(1), PA2660.
Clark, P.U., Alley, R.B., Pollard, D. (1999) 'Northern hemisphere ice-sheet influences on global climate change', *Science*, 286, pp. 1104-1111.
Clark, P.U, Archer, D., Pollard, D., Blum, J.D., Rial, J.A., Brovkin, V., Mix, A.C., Pisias, N.G., Roy, M. (2006) 'The middle Pleistocene transition: characteristics, mechanisms, and implications for long-term changes in atmospheric CO_2', *Quat. Sci. Rev.*, 25, pp. 3150-3184.
Clemens, S.C., Prell, W.L., Sun, Y. (2010) 'Orbital-scale timing and mechanisms driving late Pleistocene Indo-Asian summer monsoons: reinterpreting cave speleothem $\delta^{18}O$', *Paleoceanography*, 25, pp. PA4207.
Clemens, S.C., Holburn, A., Kubota, Y., Lee, K.E., Liu, Z., Chen, G., Nelson, A., Fox-Kemper, B. (2018) 'Precession-band variance missing from East Asian monsoon runoff', *Nature Comms.*, 9, pp. 3364.

Cohen K.M. and Gibbard, P. (2011) 'Global chronostratigraphical correlation table for the last 2.7 million years', Subcommission on Quaternary Stratigraphy (International Commission on Stratigraphy), Cambridge: England.
Collen, J.D. and Burgess, C.J. (1979) 'Calcite dissolution, overgrowth and recrystallization in the benthic foraminiferal genus *Notorotalia*, *J. Paleontol.*, 53(6), p. 1343–1353.
Coplen, T.B. (1994) 'Reporting of stable hydrogen, carbon and oxygen isotopic abundances', *Pure Appl. Chem.*, 66(2), pp. 273-276.
Craig, H. (1957) 'Isotopic standards for carbon and oxygen and correction factors for mass spectrometric analysis', *Geochem. et Cosmochem. Acta*, 12, pp. 133-149.
Dansgaard, W, Johnsen, S.J., Clausen, H.B., Dahl-Jensen, D., Gundestrup, N.S., Hammer, C.U., Hvidberg, C.S., Steffensen, J.P., Sveinbjornsdottir, A.E, Jouzel, J., Bond, G. (1993) 'Evidence for general instability of past climate from 250-kyr ice core record', *Nature*, 364, pp. 218-220.
Das, M., Singh, R.K., Vats, N., Holburn, A., Mishra, S., Farooq, S.H., Pandey, D.K. (2018) 'Changes in the distribution of Uvigerinidae species over the past 775 kyr: Implications for the paleoceanographic evolution of the Japan Sea', *Palaeogeogr., Palaeoclimatol., Palaeoecol.*, 5017, pp. 201-213.
DeMenocal, P.B. (1995) 'Plio-Pleistocene African climate', *Science*, 270 (5233), pp. 53-59.
Denton, G.H. (2000) 'Does asymmetric thermohaline-icesheet oscillator drive 100000-yr cycles', *J. Quat. Sci.*, 15, pp. 301-318.
Detlef, H., Sosdian, S.M., Kender, S., Lear, C.H., Hall, I.R. (2020) 'Multi-elemental composition of authigenic carbonates in benthic foraminifera from the eastern Bering Sea continental margin (International Ocean Discovery Program Site U1343)', *Geochim. Cosmochim. Acta*, 268, pp. 1-21.
De Villers, S., Greaves, M., Elderfield, H. (2002) 'An intensity ratio calibration method for the accurate determination of Mg/Ca and Sr/Ca of marine carbonates by ICP-AES', *Geochem., Geophys., Geosys.*, 3, pp. GC000169.
D'Hondt, S. and Arthur, A. (1996) 'Late Cretaceous oceans and the cool tropic paradox', *Science*, 271, pp. 1838-1841.
Diester-Haas, L., Billup, K., Lear, C. (2018) 'Productivity changes across the mid-Pleistocene climate transition', *Earth-Sci. Rev.*, 179, pp. 372-391.
Ding, Z.L., Yu, Z.W., Liu, T.S. (1991) 'Progresses of loess research (part III, orbital time scale)', *Quat. Sci.*, 3, pp. 336-348 (in Chinese).
Disnar, J.R., Guillet, B., Keravis, D., Di-Giovanni, C., Sebag, D. (2003) 'Soil organic matter (SOM) characterization by Rock-Eval pyrolysis: scope and limitations', *Organic Geochem.*, 34, pp. 327-343.
Diz, P., Cobelo-García, A., Hernández-Almeida, I., Corbí, H., Bernasconi, S.M. (2020) 'Persistent east equatorial Pacific carbon storage at the mid Pleistocene transition', *Paleoc. Paleocli.*, 35(6), pp. PA003789.
Dodonov, A.E. (2005) 'The stratigraphic transition and suggested boundary between the early and middle Pleistocene in the loess record of northern Eurasia', in: Head, M.J. and Gibbard, P.L. (eds.) *Early–middle Pleistocene transitions: The land–ocean evidence*. London: Geological Society of London, Special Publication 247, pp. 209–219.
Dohrmann, M., Janusen, D., Reitner, J., Collins, A.G., Wörheide, G. (2008) 'Phylogeny and evolution of glass sponges (porifera, hexactinellida)', *Syst. Biol.*, 57(3), pp. 388-405.
Dolman, A.M. and Laepple, T. (2018) 'Sedproxy: a forward model for sediment-archived climate proxies', *Clim. Past*, 14(12), pp. 1851-1868.

Domitsu, H. and Oda, M. (2005) 'Japan Sea planktic foraminifera in surface sediments: geographical distribution and relationships to surface water mass' *Paleontol. Res.*, 9(3), pp. 255-270.
D'Orbigny, A.D. (1826) 'Tableau méthodique de la classe des Céphalopodes', *A. Sci. Nat.*, 7, pp. 96-169 and pp. 245-314.
D'Orbigny, A.D. (1839) 'Foraminifères', in: De la Sagra R. (ed.) *Histoire physique, politique et naturelle de l'ile de Cuba.* Paris: Royal Geographical Society, p. 82.
Dunbar, R.B., DeMenocal, P.B., Burckle, L. (1992) '26. Late Pliocene-Quaternary biosiliceous sedimentation rate at site 798, Japan Sea', in: Pisciotto, K.A., Ingle, J.C.Jr., von Breymann, M.T., Barron, J., et al. (eds.) *Proceedings of ODP, Scientific Results, volume 127/128*, pp. 439-455.
Duxbury, A.C., Duxbury, A.B., Sverdrup, K.A. (2005) *The world's oceans*, 8th ed., Boston: McGraw-Hill, p. 114.
Edgar, K.M., Pälike, H., Wilson, P.A. (2013) 'Testing the impact of diagenesis on the $\delta^{18}O$ and $\delta^{13}C$ of benthic foraminiferal calcite from a sediment burial depth transect in the equatorial Pacific', *Paleoceanography*, 28, pp. 468-480.
Edgar, K.M., Anagnostou, E., Pearson, P.N., Foster, G.L. (2015) 'Assessing the impact of diagenesis on $\delta^{11}B$, $\delta^{13}C$, $\delta^{18}O$, Sr/Ca and B/Ca values in fossil planktonic foraminiferal calcite', *Geochim. et Cosmochim. Acta*, 166, pp. 189-209.
Ehrenberg, C.G. (1861) *Über die Tiefgrund-Verhältnisse des Ozeans am Eingänge der Davisstrasse und bei Island*, Berlin: Abhandlungen der königlich Preussischen Akademie der Wissenschaft, pp. 131-139.
Elderfield, H. and Ganssen, G. (2000) 'Past temperature and $\delta^{18}O$ of surface ocean waters inferred from foraminiferal Mg/Ca ratios', *Nature*, 405, pp. 442-445.
Elderfield, H., Yu, J., Anand, P., Kiefer, T., Nyland, B. (2006) 'Calibrations for benthic foraminiferal Mg/Ca paleothermometry and the carbonate ion hypothesis', *E.P.S.L.*, 250, pp. 633-649.
Elderfield, H., Greaves, M., Barker, S., Hall, I., Tripati, A., Ferretti, P., Crowhurst, S., Booth, L. and Daunt, C. (2010) 'A record of bottom water temperature and seawater δ18O for the southern ocean over the past 440 kyr based on Mg/Ca of benthic foraminiferal *Uvigerina spp*.', *Quat. Sci. Rev.*, 29, pp. 160-169.
Elderfield, H., Ferretti, P. Greaves, M., Crowhurst, I.N., Mc Cave, I.N., Hodell, D., Piotrowski, A.M. (2012) 'Evolution of ocean temperature and ice volume through the mid-Pleistocene climate transition', *Science*, 337, pp. 704-709.
Emerson, S. and Bender, M. (1981) 'Carbon fluxes at the sediment water interface of the deep-sea: calcium carbonate preservation', *J. Mar. Res.*, 39, pp. 139-162.
Emerson, S. (1985) 'Organic carbon preservation in marine sediments', in: Sundquist, E.T. and Broecker, W.E. (eds.) *The carbon cycle and atmospheric CO_2: natural variations Archean to present*, Washington D.C.: American Geophysical Union, Geophys. Monogr. 32, pp. 78-89.
Emery, K.O. and Uchupy, E. (1984) *The geology of the Atlantic Ocean*, Berlin-Dordrecht-Heidelberg- London-New York: Springer, 1050pp.
Emiliani, C. (1955) 'Pleistocene temperatures', *Geology*, 63(3), pp. 538-578.
Espitalié, J., Laporte, L., Madec, M., Marquis, F., Leplat, P., Paulet, J., Boutefeu, A. (1977) 'Méthode rapide de caractérisation des roches mères, de leur potential pétrolier et de leur degré d'évolution', *Revue de l'Institut Français du Pétrole*, 32, pp. 23-42.
Espitalié, J., Nakadi, K.S., Trichet, J. (1984) 'Role of the mineral matrix during kerogen pyrolisis', *Org. Geochem.*, 6, pp. 365-382.
Fabbri, O., Charvet, J., Fournier, M. (1996) 'Alternate senses of displacement along the Tsushima fault system during the Neogene based on fracture analyses near the western margin of the Japan Sea', *Tectonophysics*, 257: 275-295.

Farmer, J.R., Goldstein, S.L., Haynes, L.L., Hönisch, B., Kim, J., Pena, L., Jaume-Seguí, Yehudai, M. (2019a) 'Data constraints on ocean-carbon cycle feedbacks at the mid-Pleistocene transition', *PAGES Magazine*,27(2), pp. 62-63.
Farmer, J.R., Hönisch, B., Haynes, L.L., Kroon, D., Jung, S., Ford, H.L., Raymo, M.E., Jaume-Seguí, M., Bell, D.B., Goldstein, S.L., Pena, L.D., Yehudai, M., Kim, J. (2019b) 'Deep Atlantic Ocean carbon storage and the rise of 100,000-year glacial cycles', *Nature Geosci.,* 12, pp. 355-360.
Flügel, E. (2004a) 'Fossils in thin sections: It is not that difficult', in: Flügel, E. (author) *Microfacies of carbonate rocks – analysis, interpretation and application*. Berlin-Dordrecht-Heidelberg-London-New York: Springer, p. 399-574.
Flügel, E. (2004b) 'Integrated facies analysis', in: Flügel, E. (author) *Microfacies of carbonate rocks – analysis, interpretation and application*. Berlin-Dordrecht-Heidelberg-London-New York: Springer, p. 646.
Fontanier, C., Mackensen, A., Jorissen, F.J., Anschutz, P., Licari, L., Griveaud, C. (2006) 'Stable oxygen and carbon isotopes of live benthic foraminifera from the Bay of Biscay: Microhabitat impact and seasonal variability', *Marine Micropaleontology*, 58, pp. 159-183.
Ford, H. and Raymo, M.E. (2020) 'Regional and global signals in seawater $\delta^{18}O$ records across the mid-Pleistocene transition', *Geology*, 48(2), pp.113-117.
Fox, L.R. and Wade, B.S. (2013) 'Systematic taxonomy of early-middle Miocene planktonic foraminifera from the equatorial Pacific Ocean: integrated ocean drilling program, site U1338', *J. Foraminiferal Res.*, 43(4), pp. 374-405.
Fujiki, T., and Ozawa, T. (2008) 'Vegetation change in the main island of Okinawa, southern Japan from late Pliocene to early Pleistocene', *Quat. Int.*, 184, pp. 75-83.
Fujine, K., Tada, R., Yamamoto, M. (2009) 'Paleotemperature response to monsoon activity in the Japan Sea during the last 160 kyr', *Palaeogeogr., Palaeoclim., Palaeoecol.,* 280, pp. 350-360.
Gallagher, J.S., Kitamura, A., Iryu, Y., Itaki, T., Kozifumi, I., Hoiles, P.W. (2015) 'The Pliocene to recent history of the Kuroshio and Tsushima currents: a multi-proxy approach', *P.E.P.S.*, 2(17), pp. DOI 10.1186/s40645-015-0045-6.
Gallagher, J.S., Sagawa, T., Henderson, A.C.G., Saavedra-Pellitero, M., De Vleeschouwer, D., Black, H., Itaki, T., Toucanne, S., Bassetti, M.-A., Clemens, S., Anderson, W., Alvarez-Zarikian, C., Tada, R. (2018) 'East Asian monsoon history and paleoceanography of the Japan Sea over the last 460,000 years', *Paleooc. Paleoclim.*, 33, 683-702.
Gamo, T. and Horibe, Y. (1983) 'Abyssal circulation in the Japan Sea', *J. Oceanogr. Soc. Japan*, 39, pp. 220-230.
Gamo, T., Nakayama, N., Takahata, N., Sano, Y., Zhang, J., Yamazaki, E., Taniyasu, S., Yamashita, N. (2014) 'The Sea of Japan and its unique chemistry revealed by time-series observations over the last 30 years', *Monogr. Environ. Earth Planets*, 2(1), pp. 1-22.
Ganopolski, A. and Calov, R. (2011) 'The role of orbital forcing, carbon dioxide and regolith in 100 kyr glacial cycles', *Clim. Past.*, 7, pp. 1415–1425.
Garlick, G.D. (1966) 'Oxygen isotope fractionation in igneous rocks', *E.P.S.L.*, 1, pp. 361-368.
Gradstein, F.M., Ogg, J.G., Schmitz, M.D., Ogg, G.M. (eds.) (2012) *The geological time scale 2012.* Amsterdam: Elsevier.
Gray, W.R., Rae, J.W.B., Wills, R.C.J., Shevenell, A.E., Taylor, B., Burke, A., Foster, G.L., Lear, C.H. (2018) 'Deglacial upwelling, productivity and CO2 outgassing in the North Pacific Ocean', *Nature Geosci.*, 11, pp. 340–344.

Greaves, M. (2008) 'Interlaboratory comparison study of calibration standards for foraminiferal Mg/Ca thermometry', PhD thesis, Southampton: Southampton University, Faculty of engineering, science and mathematics, school of ocean and earth science, 212pp.

Greaves, M., Caillon, N., Rebaubier, H., Bartoli, G., Bohaty, S., Cacho, I, Clarke, L., Cooper, M., Daunt, C., Delaney, M., DeMenocal, P., Dutton, A., Eggins, S., Elderfield, H., Garbe-Schoenberg, D., Goddard, E., Green, D., Groenveld, J., Hastings, D., Hathorn, E., Kimoto, K., Klinkhammer, G., Labeyrie, L., Lea, D.W., Marchitto, T., Martínez-Botí, M.A., Mortyn, P.G., Ni, Y., Nuernberg, D., Paradis, G., Pena, L., Quinn, T., Rosenthal, Y., Russell, A., Sagawa, T., Sosdian, S., Stott, L., Tachikawa, K., Tappa, E., Thunell, R., Wilson, P.A. (2008) 'Interlaboratory comparison study of calibration standards for foraminiferal Mg/Ca thermometry', *Geochem., Geophys., Geosys.*, 9(8), pp. GC001974.

Griffin, J.J., Windom, H., Goldberg, E.D. (1968) 'The distribution of clay minerals in the world ocean', *Deep-Sea Res.*, 15, pp. 433-459.

GRIP members (1993) 'Climate instability during the last interglacial period recorded in the GRIP ice core', *Nature*, 364, pp. 203-207.

Guo, Z., Liu, T., Fedoroff, N., Wei, L., Ding, Z., Wu, N., Lu, H., Jiang, W., An, Z. (1998) 'Climate extremes in loess of China coupled with the strength of deep-water formation in the North Atlantic', *Glob. Planet. Change*, 18, pp. 113-128.

Han, W., Fan, X., Berger, A. (2012) 'Tibet forcing of mid-Pleistocene synchronous enhancement of East Asian winter and summer monsoons revealed by Chinese loess record', Quat. Res., 78, pp. 174-184.

Hasenfratz, A.P., Jaccard, S.L., Martínez-García, A., Sigman, D.M., Hodell, D.A., Vance, D., Bernasconi, S.M., Kleiven, H.F., Haumann, F.A., Haug, G.H. (2019) 'The residence time of Southern Ocean surface waters and the 100,000 year ice age cycle', *Science*, 363, pp. 1080-1084.

Haq, B.U., Hardenbol, J., Vail, P.R. (1987) 'Chronology of fluctuating sea levels since the Triassic', *Science,* 235, pp. 1156-1167.

Hayes, J.M. (2001) 'Fractionation of the isotopes of carbon and hydrogen in biosynthetic processes', *Reviews in Mineralogy and Geochemistry*, 43(1), pp. 25–277.

Hays, J.D., Imbrie, J., Shackleton, N.J. (1976) 'Variations in the Earth’s orbit: Pacemakers of the ice ages', *Science*, 194(4270), pp. 1121-1132.

Head, M.,J. and Gibbard, P.L. (2005) 'Early-middle Pleistocene transitions: An overview and recommendation for the defining boundary', *Geological Society of London, Special Publications,* 247, pp. 1-18.

Hernández-Almeida, I., Sierro, F.J., Cacho, I., Flores, J.A. (2012) 'Impact of suborbital climate changes in the North Atlantic on ice sheet dynamics at the mid-Pleistocene transition', *Paleoceanogr. Paleoclimatol*., 27(3), pp. PA3214.

Heslop, D., Dekkers, M.J., Langereis, C.G. (2002) 'Timing and structure of the mid-Pleistocene transition: Records from the loess deposits of northern China', *Palaeogeogr., Palaeoclim., Palaeoecol.*, 185, pp. 133-1473.

Higgins, J.A., Kurbatov, A.V., Spaulding, N.E., Brook, E., Introne, D.S., Chimiak, L.M., Yan, Y., Mayewski, P.A., Bender, M.L. (2015) 'Atmospheric composition 1 million years ago from blue ice in the Allan Hills, Antarctica', *Proc. Natl. Acad. Sci. U.S.A.*, 112, pp. 6887–6891.

Hodell, D.A., Channell, J.E.T., Curtis, J.H., Romero, O.E., Röhl, U. (2008) 'Onset of “Hudson Strait” Heinrich events in the eastern North Atlantic at the end of the middle Pleistocene transition (~640 ka)?', *Paleoceanography*, 23, PA4218.

Hodell, D.A. and Channell, J.E.T. (2016) 'Mode transitions in northern hemisphere glaciation: Co-evolution of millennial and orbital variability in Quaternary climate', *Clim. Past*, 12, pp. 1805-1828.
Hoefs, J. (2004) 'Isotope fractionation mechanisms of selected elements', in: Hoefs, J. (ed.) *Stable Isotope Geochemistry*, *5ths revised edition*, Berlin-Dordrecht-Heidelberg- London-New York: Springer, pp. 31-76.
Hoiles, P.W., Gallagher, S.J., Kitamura, A., Southwood, J.M. (2012) 'The evolution of the Tsushima current during the early Pleistocene in the Sea of Japan: An example from marine isotope stage (MIS) 47', *Glob. Planet. Change*, 92-93, pp. 162-178.
Hönisch, B., Hemming, N.G., Archer, D., Siddall, M., McManus, J.F. (2009) 'Atmospheric carbon dioxide concentration across the mid-Pleistocene transition', *Science*, 324, pp. 1551–1554.
Hoogakker, B.A.A., Rohling, E.J., Palmer, M.R., Tyrrell, T., Rothwell, R.G. (2006) 'Underlying causes for long-term global ocean $\delta^{13}C$ fluctuations over the last 1.20 Myr', *E.P.S.L.*, 248, pp. 15-29.
Horibe, Y. (1981) *Preliminary report of the Hakuho Maru cruise KH-77-3 (Pegasus Expedition)*. Tokyo: Ocean Res. Inst., Univ. of Tokyo, 55pp.
Huber, B.T., Hodell, D.A., Hamilton, C.P, (1995) 'Middle-Late Cretaceous climate of the southern high-latitudes – Stable isotopic evidence for minimal equator-to-pole thermal gradients', *Geol. Soc. Am. Bull.*, 107, pp. 1164-1191.
IAEA, International Atomic Energy Agency (2013) 'Principles and applications volume 1: introduction: theory, methods, review', in: IAEA (ed.) *Environmental Isotopes in the Hydrological Cycle: Principles and Applications*, Vienna: IAEA, pp. 1-185.
Ichikura, M. and Ujiié, H. (1976) 'Lithology and planktonic foraminifera of the Sea of Japan piston cores', *Bull. Nat. Sci. Museum Tokyo,* Series C 2, pp. 151-178.
Ikehara, K. (1991) 'Modern sedimentation off San'In district in the southern Japan Sea', in: Takano, K. (ed.) *Oceanography of Asian Marginal Seas. Elsevier Oceanography Series 54.* Amsterdam: Elsevier Science Publishers, pp. 143-162.
Ikehara, K., Kikawa, K., Katayama, H., Seto, K. (1994) 'Late Quaternary paleoceanography of the Sea of Japan; a tephrochronological and sedimentological study', in: Juvigne, E.H. (ed.) Q*uaternary Environmental Changes.* Proc. Int. Geol. Congr., 29th (Part B), pp. 229–235.
Ikehara, K. and Itaki, T. (2007) 'Millennial-scale fluctuations in seasonal sea-ice and deep-water formation in the Japan Sea during the late Quaternary', *Palaeogeogr., Palaeoclim., Palaeoecol.*, 247(1-2), pp. 131-143.
Imbrie, J., Boyle, E., Clemens, S., Duffy, A., Howard, W., Kukla, G., Kutzbach, J., Martinson, D., McIntyre, A., Mix, A., Molfino, B., Morley, J., Peterson, L., Pisias, N., Prell, W., Raymo, M., Shackleton, N., Toggweiler, J. (1992) 'On the structure and origin of major glaciation cycles – 1. Linear responses to Milankovithc forcing', *Paleoceanography*, 7, pp. 701-738.
Imbrie, J., Boyle, E., Clemens, S., Duffy, A., Howard, W., Kukla, G., Kutzbach, J., Martinson, D., McIntyre, A., Mix, A., Molfino, B., Morley, J., Peterson, L., Pisias, N., Prell, W., Raymo, M., Shackleton, N., Toggweiler, J. (1993) 'On the structure and origin of major glaciation cycles – 2. The 100,000 year cycle', *Paleoceanography*, 8, pp. 699-735.
Ingle, J.C. (1975) 'Pleistocene and Pliocene foraminifera from the Japan Sea, leg 31, Deep Sea Drilling Project', in: Karig, D.E., Ingle, J.C., Bouma, A.H., Ellis, C.H., Haile, N., Koizumi, I., Ling, H.Y., MacGregor, I., Moore, J.C., Ujiie, H., Watanabe, T., White, S.M., Yasui, M. (eds.) *Initial Report of the Deep Sea Drilling Project, Volume 31*, pp. 693-701.

Ingle, J.C. Jr., Bristow, J.S., Bruckle, L.H., Charvet, J., Cragg, B.A., deMenocal, P., Dunbar, R.B., Follmi, K.B., Griffin, J.R., Grimm, K.A., Hamano, Y., Hirata, N., Holler, P., Isaacs, C.M., Kettler, R., Kheradyar, T., Krumsiek, K.A.O., Ling, H.-Y., Matsumoto, R., Muza, J.P., Parkes, R.J., Scott, S.D., Stein R., Sturz, A.A., Suyehiro, K., Pouclet, A., von Breymann, M.T. (1990) 'Site 798', *Proceedings of the Ocean Drilling Program, Initial Reports*, *volume 128*. College Station (Texas): Ocean Drilling Program, 116 p.

Inoue, Y. (1989) 'Northwest Pacific foraminifera as paleoenvironmental indicators', *Science Reports of the Institute of Geoscience*, *University of Tsukuba, Section B: Geological Sciences*, 10, pp. 57–162.

IODP detailed planning group members (2008) 'Asian monsoon and Cenozoic tectonic history: Report of the detailed planning group, May 2008', College Station (Texas): Integrated Ocean Drilling Program, 47 pp.

IODP (eds). (2011) *IODP Depth Scales Terminology.* Version 2.0, April 2011. College Station (Texas): Integrated Ocean Drilling Program, 20 pp.

IPCC members (2013) '*Climate change 2013: The physical science basis. Contribution of working group I to the fifth assessment report of the intergovernmental panel on climate change', Cambridge:* Cambridge University Press, 1535 pp.

IPCC members (2014) *'Climate change 2014: Synthesis report. Contribution of working groups I, II and III to the fifth assessment report of the intergovernmental panel on climate change*', 5th edn., Geneva: IPCC, 151 pp.

Irino, T., Tada, R., Ikehara, K., Sagawa, T., Karasuda, A., Kurokawa, S., Seki, A., Lu, S. (2018) 'Construction of perfectly continuous records of physical properties for dark-light sediment sequences collected from the Japan Sea during Integrated Ocean Drilling Program expedition 346 and their potential utilities as paleoceanographic studies', *Prog. Earth Planet. Sci.*, 5(23).

Ishikawa, N. and Tagami, T. (1991) 'Paleomagnetism and fission-track geochronology on the Goto and Tsushima Islands in the Tsushima Strait area: Implications for the opening mode of the Japan Sea'. J*ournal of Geomagnetism and Geoelectricity,* 43: 229–253.

Itaki, T., Ikehara, K., Motoyama, I., Hasegawa, S. (2004) 'Abrupt ventilation changes in the Japan sea over the last 30 kyr: evidence from deep-dwelling radiolarians', *Palaeogeogr., Palaeoclim., Palaeoecol.,* 208(3-4), pp. 263-278.

Itaki, T (2016) 'Transitional changes in microfossil assemblages in the Japan Sea from the late Pliocene to early Pleistocene related to global climatic and local tectonic events', *Progr. Earth Planet. Sci.*, 3(11), pp. 3-11.

Itaki, T., Sagawa, T. and Kubota, Y. (2018): 'Data report: Pleistocene radiolarian biostratigraphy, IODP expedition 346 site U1427', in: Tada, R., Murray, R.W., Alvarez Zarikian, C.A. and the expedition 346 scientists (eds.) *Proceedings of the Integrated Ocean Drilling Program 346*. College Station (Texas): Integrated Ocean Drilling Program, doi: 10.2204/iodp.proc.346.202.2018.

Jansen, E. and Sjøholm, J. (1991) 'Reconstruction of glaciation over the past 6 Myr from ice-borne deposits in the Norwegian Sea', *Nature*, 349, pp. 600-603.

Jansen, E., Fronval, T., Rack, F., Channell, J.E.T. (2000) 'Pliocene-Pleistocene ice rafting history and cyclicity in the Nordic Seas during the last 3.5 Myr', *Paleoceanography*, 15, pp. 709-721.

Jezierski, S. (2015) 'Determination of different carbon species in solids – using the real chemistry to obtain the right results', *Environmental Laboratory*, envirotech-online.com, pp. 10-11.

Jones, R.W. (2014) *Foraminifera and Their Applications*. Cambridge: Cambridge University Press, ISBN: 978-1-107-03640-6.

Jorissen, F.J., Fontanier, C., Thomas, E. (2007) 'Chapter seven: Paleoceanographical proxies based on deep-sea benthic foraminiferal assemblage characteristics', in: Hillaire-Marcel, C. and De Vernal, A. (eds.) *Developments in Marine Geology. V*olume 1, Amsterdam: Elsevier, pp. 263-325.
Jouzel, J., Masson-Delmotte, V., Cattani, O., Dreyfus, G., Falourd, S., Hoffmann, G., Minster, B., Nouet, J., Barnola, J.M., Chappellaz, J., Fischer, H., Gallet, J.C., Johnsen, S., Leuenberger, M., Loulergue, L., Luethi, D., Oerter, H., Parrenin, F., Raisbeck, G., Raynaud, D., Schilt, A., Schwander, J., Selmo, E., Souchez, R., Spahni, R., Stauffer, B., Steffensen, J. P., Stenni, B., Stocker, T.F., Tison, J.L., Werner, M., Wolff, E.W. (2007) 'Orbital and millennial Antarctic climate variablility over the past 800,000 years', *Science*, 317, pp.793-796.
Kamikuri, S.-S., Itaki, T., Motoyama, I., Matsuzaki, K.M. (2017) 'Radiolarian biostratigraphy from middle Miocene to late Pleistocene in the Japan Sea', *Paleontol. Res*., 21(4), pp. 397-421.
Kao, S.J., Horng, C.S., Hsu, S.C., Wei, K.Y., Chen, J., Lin, Y.S. (2005) 'Enhanced deepwater circulation and shift of sedimentary organic matter oxidation pathway in the Okinawa Trough since the Holocene', *Geophys. Res. Lett.*, 32, pp. L15609.
Kao, S.J., Wu, C.-R., Hsin, Y.-C., Dai, M. (2006) 'Effects of sea level change on the upstream Kuroshio Current through the Okinawa Trough', *Geophys. Res. Lett.*, 33, pp. L16604.
Karig, D.E., Ingle, J.C., Bouma, A.H., Ellis, C.H., Haile, N., Koizumi, I., Ling, H.Y., MacGregor, I., Moore, J.C., Ujiie, H., Watanabe, T., White, S.M., Yasui, M. (eds.) (1975) 'Initial Report of the Deep Sea Drilling Project, Volume 31', Ocean Drilling Program, College Station: Texas.
Katsura, T. and Nagano, M. (1976) 'Geomorphology and tectonic movement of the sea floor, northwest off Kyushu, Japan', *Journal of Oceanography*, 32: 139–150. (Japanese with English abstract).
Katz, A. (1973) 'The interaction of magnesium with calcite during crystal growth at 25–90 ºC and one atmosphere', *Geochim. et Cosmochim. Acta,* 37**,** pp. 1563-1586.
Keigwin, L.D. and Gobarenko, S.A. (1992) 'Changes in the distribution of Uvigerinidae species over the past 775 kyr: Implications for the paleoceanographic evolution of the Japan Sea', *Quat. Res*., 37, pp. 346-360.
Kemp, D.B. and Sexton, P.F. (2014) 'Time-scale uncertainty of abrupt events in the geologic record arising from unsteady sedimentation', *Geology*, 42(10), pp. 891-894.
Kender, S., Ravelo, A.C., Worne, S., Swann, G.E.A., Leng, M.J., Asahi, H., Becker, J., Detlef, H., Aiello, I.W., Andreasen, D., Hall, I.R. (2018) 'Closure of the Bering Strait caused mid-Pleistocene transition cooling', *Nature Comm.*, 9, pp. 5386.
Kheradyar, T. (1992) '27. Pleistocene planktonic foraminiferal assembages and paleotemperature fluctuations in Japan Sea, site 798', in: Pisciotto, K.A., Ingle, J.C.Jr., von Breymann, M.T., Barron, J. et al. (eds.) *Proceedings of the Ocean Drilling Program, Scientific Results*, *Volume 127/128, part 1*. College Station, Texas: ODP, pp. 457-470.
Kido, Y., Minami, I., Tada, R., Fujine, K., Irino, T., Ikehara, K. and Chun, J.-H. (2007) 'Orbital-scale stratigraphy and high-resolution analysis of biogenic components and deep-water oxygenation conditions in the Japan Sea during the last 640 kyr', *Palaeogeogr., Palaeoclimatol., Palaeoecol*., 247, pp. 32-49.
Killops, S. and Killops, V. (2005) *Introduction to Organic Geochemistry, 2nd Edition*, Oxford: Blackwell Scientific Publishing, 393pp.
Kim, I.-S., Park, M.-H., Ryu, B.-J., Yu, K.-M. (2006) 'Tephrostratigraphy and paleoenvironmental variation in late Quaternary core sediments of the

southwestern Ulleung Basin, East Sea (Sea of Japan)', *Island Arc*, 15, pp. 178-186.
Kim, J.-H., Park, M.-H., Tsunogai, U., Cheong, T.-J., Ryu, B.-J., Lee, Y.-J., Han, H.-C., Oh, J.-J., Chang, H.-W. (2007) 'Geochemical characterization of the organic matter, pore water constituents and shallow methane gas in the eastern part of the Ulleung Basin, East Sea (Japan Sea)', *Island Arc*, 16, pp. 93-104.
Kitaba, I., Harada, M., Hyodo, M., Katoh, S., Sato, H., Matsushita, M. (2011) 'MIS 21 and the mid-Pleistocene climate transition: Climate and sea-level variation from a sediment core in Osaka Bay, Japan', *Palaeogeogr., Palaeoclimatol., Palaeoecol.*, 299, pp. 227-239.
Kitaba, I., Hyodo, M., Katoh, S., Matsushita, M. (2012) 'Phase-lagged warming and the disruption of climatic rhythms during the Matuyama-Brunhes magnetic polarity transition', *Gondwana Res.*, 21, pp. 595-600.
Kitaba, I., Hyodo, M., Katoh, S., Dettman, D.L., Sato, H. (2012) '241 Cyclic vegetation changes during the mid-Pleistocene climate transition around Osaka Bay, southwest Japan', *Japan. J. Palynol., Special Issue*, 58, conference abstract, pp. 110.
Kitamura, A. (1991) 'Paleoenvironmental transition at 1.2 Ma in the Omma Formation, central Honshu, Japan', *Transac. Proc. Paleontol. Soc. Japan*, 162, pp. 767-780.
Kitamura, A., Kimoto, K., Takayama, T. (1997) 'Reconstruction of the thickness of the Tsushima Current in the Japan Sea during the Quaternary from molluscan fossils', *Palaeogeogr., Palaeoclimatol., Palaeoecol.,* 135, pp. 51-69.
Kitamura, A., Takano, O., Takada, H., Omote, H. (2001) 'Late Pliocene-early Pleistocene paleoceanographic evolution of the Sea of Japan', Palaeogeogr., Palaeoclimatol., Palaeoecol., 172, pp. 81-98.
Kitamura, A. and Kawagoe, T. (2006) 'Eustatic sea-level change at the mid-Pleistocene climate transition: new evidence from the shallow-marine sediment record of Japan', *Quat. Sci. Rev.*, 25, pp. 323-335.
Kitamura, A. and Kimoto, K. (2006) 'History of the inflow of the warm Tsushima Current into the Sea of Japan between 3.5 and 0.8 Ma', *Palaeogeogr., Palaeoclimatol., Palaeoecol.*, 236, pp. 355-366.
Kitamura, A. (2007) ' Paleoceanographic changes of the Sea of Japan during 3.5-0.8 Ma', in: Okada, H., Mawatari, S.F., Suzuki, N., Gautam, P. (eds.) *Origin and Evolution of Natural Diversity, Proceedings of International Symposium "The Origin and Evolution of Natural Diversity"*. 1–5 October 2007, Sapporo, pp. 187–194.
Kitamura, A. (2016) 'Constraints on eustatic sea-level changes during the mid-Pleistocene climate transition: Evidence from the Japanese shallow-marine sediment record', *Quat. Internat.*, 397, pp. 417-421.
Koizumi, I. (1992) 'Diatom biostratigraphy of the Japan Sea: Leg 127', in: Pisciotto, K.A., Ingle, J.C.Jr., von Breymann, M.T., Barron, J. et al. (eds.) *Proceedings of the Ocean Drilling Program, Scientific Results, Vol. 127/128*, Pt. 1, College Station, Texas: ODP, pp. 249-289.
Koizumi, I. (2013) 'Pacific', in: Elias, S.A. (ed.) *The Encyclopaedia of Quaternary Science.* Volume 1, Amsterdam: Elsevier, pp. 571-587.
Kölling, M., Bouimetarhan, I., Bowles, M.W., Felis, T., Goldhammer, T., Hinrichs, K.-U., Schulz, M., Zabel, M. (2019) 'Consistent CO_2 release by pyrite oxidation on continental shelves prior to glacial terminations', *Nature Geosci.*, 12, pp. 929-934.
Koltun, V.M. (1966) 'Sponge spiculae within the subsurface layer of sediments in the southern part of the Indian Ocean', in: *Geochemistry of Silica*. Moscow (Russia): Nauka, pp. 262-284.

Kozdon, R., Kelly, D.C., Kita, N.T., Fournelle, J.H., Valley, J.W. (2011) 'Planktonic foraminiferal oxygen isotope analysis by ion microprobe technique suggests warm tropical sea surface temperatures during the Early Paleogene', *Paleoceanography*, 26, pp. PA3206.

Kubota, Y., Kimoto, K., Tada, R., Oda, H., Yokoyama, Y., Matsuzaki, H. (2010) 'Variations of East Asian summer monsoon since the last deglaciation based on Mg/Ca and oxygen isotope of planktonic foraminifera in the northern East China Sea', *Paleoceanography*, 25(4), pp. PA001891.

Kukla, G. (1987) 'Loess stratigraphy in central China', *Quat. Sci. Rev.,* 6, pp. 191-219.

Kutzbach, J.E. and Guetter, P.J. (1989) 'Sensitivity of climate to late Cenozoic uplift in southern Asia and the American west: numerical experiments', *J. Geophys. Res.*, 94(15), pp. 18393-18407.

Lafargue, E., Espitalié, J., Marquis, F., Pillot, D. (1998) 'Rock-Eval 6 applications in hydrocarbon exploration, production and in soil contamination studies', *Revue de l'Institute Français du Pétrole*, 53(4), pp. 421-437.

Lamb, J.L. and Miller, T.H. (1984) 'Stratigraphic significance of Uvigerninid foraminifers in the western hemisphere', Exxon Company, USA: Harold Norman Fisk Memorial Papers, No. 66.

Lambeck, K., Rouby, H., Pucell, A., Sun, Y., Sambridge, M. (2014) Sea level and global ice volumes from the Last Glacial Maximum to the Holocene. Proceedings of the National Academy of Sciences of the United States of America, 111(43), pp. 15296–15303.

Langford, F.F. and Blanc-Valleron, M.-M. (1990) 'Interpreting Rock-Eval pyrolysis data using graphs of pyrolizable hydrocarbons vs. total organic carbon', *A.A.P.G. Bull.*, 74, pp. 799–804.

Laskar, J., Robutel, P., Joutel, F., Gastineau, M., Correia, A.C.M., Levrard, B. (2004) 'A long-term numerical solution for the insolation quantities of the Earth', *Astronomy and Astrophysics,* 428, pp. 261-285.

Lea, D., Mashiotta, T., Spero, H. (1999) 'Controls on magnesium and strontium uptake in planktonic foraminifera determined by live culturing', *Geochim. et Cosmochim. Acta*, 63(16), pp. 2369-2379.

Lea, D. (2003) 'Elemental and isotopic proxies of past ocean temperatures', in: Turkien, K. (ed.) *Treatise on Geochemistry*. Amsterdam: Elsevier, pp. 373-397.

Lear, C.H., Elderfield, H., Wilson, P.A. (2000) 'Cenozoic deep-sea temperatures and global ice volumes from Mg/Ca in benthic foraminiferal calcite', *Science*, 287, pp. 269-272.

Lear, C.H., Rosenthal, Y., Slowey, N. (2002) 'Benthic foraminiferal Mg/Ca-paleothermometry: A revised core-top calibration', *Geochem. et Cosmochem. Acta*, 66(19), pp. 3375-3387.

Lear, C.H., Billups, K., Rickaby, R.E.M., Diester-Haass, L., Mawbey, E.M., Sosdian, S.M. (2016) 'Breathing more deeply: deep ocean carbon storage during the mid-Pleistocene climate transition', *Geology*, 44(12), pp. 1035-1038.

Lee, S.H. and Choi, B.-J. (2015) 'Vertical structure and variation of currents observed in autumn in the Korea Strait', *Ocean Sci. J.*, 50(2), pp. 163-182.

Lee, K.E. (2007) 'Surface water changes recorded in Late Quaternary marine sediments of the Ulleung Basin, East Sea (Japan Sea)', *Palaeogeogr., Palaeoclim., Palaeoecol.*, 247, pp. 18–31.

Lee, E., Kim, S., Nam, S. (2008) 'Paleo-Tsushima water and its effect on surface water properties in the East Sea during the last glacial maximum: revisited', *Quat. Int.*, 176-177, pp. 3-12.

Leng, M.J. (ed.) (2006) 'Isotopes in palaeoenvironmental research', volume 10, Amsterdam-Berlin-Heidelberg- London-New York: Springer, 307pp.
Leng, M.J. and Lewis, J.P. (2017) 'C/N ratios and carbon isotope composition of organic matter in estuarine environments', in: Weckstrom, K. (ed.) *Applications of paleoenvironmental techniques in estuarine studies. Amsterdam-Heidelberg-New York:* Springer, pp. 213-237.
Li, Q., Wang, P., Zhao, Q., Tian, J., Cheng, X., Jian, Z., Zhong, G., Chen, M. (2008) 'Paleoceanography of the mid-Pleistocene South China Sea', *Quat. Sci. Rev.*, 27, pp. 1217-1233.
Li, J., Fang, X., Song, C., Pan, B., Ma, Y., Yan, M. (2014) 'Late Miocene–Quaternary rapid stepwise uplift of the NE Tibetan Plateau and its effects on climatic and environmental changes', *Quat. Res.*, 81(3), pp. 400-423.
Li, T., Liu, F., Abels, H.A., You, C.-F., Zhang, Z., Chen, J., Ji, J., Li, L., Li, L., Liu, H.-C., Ren, C., Xia, R., Zhao, L., Zhang, W., Li, G. (2017) 'Continued obliquity pacing of East Asian summer precipitation after the mid-Pleistocene transition', *E.P.S.L.*, 457, pp. 181-190.
Liebezeit, G. and Wiesner, M.G. (1990) 'Pyrolysis of recent marine sediments – 1. Biopolymers', *Org. Geochem.*, 16(4-6), pp. 1179-1185.
Lisiecki, L.E. and Lisiecki, P.A. (2002) 'Application of dynamic programming to the correlation of paleoclimate records'*, Paleoceanography*, 17(4), 1049, pp. PA000733.
Lisiecki, L.E. and Raymo, M.E. (2005) 'A Pliocene-Pleistocene stack of 57 globally distributed benthic $\delta^{18}O$ records', *Paleoceanography*, 20, pp. PA1003.
Loeblich, A.R. and Tappan, H.N. (1988) *Foraminifera genera and their classification*. New York: Van Nostrand Reinhold Company. 970 pp.
Loewemark, L., Konstantinou, K.I., Steinke, S. (2008) 'Bias in foraminiferal multispecies reconstructions of paleohydrographic conditions caused by foraminiferal abundance variations and bioturbational mixing: A model approach', *Marine Geology*, 256, pp. 101-106.
Lu, S., Irino, T., Igarashi, Y. (2018) 'Biomass burning history in East Asia during the last 4 million years recorded in elemental carbon variability at IODP site U1423', *Prog. Earth Planet. Sci.*, 5(53), pp. https://doi.org/10.1186/s40645-018-0206-5
Mackensen, A. and Licari, L. (2003) 'Carbon isotopes of life benthic foraminifera from the south Atlantic: sensitivity to bottom water carbonate saturation state and organic matter rain rates', in: Wefer, G., Mulitza, S., Ratmeyer, V. (ed.) *The South Atlantic in the Late Quaternary – Reconstruction of Material Budgets and Current Systems*. Amsterdam-Berlin-Heidelberg- London-New York: Springer, pp. 623-644.
Marchitto, T., Curry, W. and Oppo, D. (2000) 'Zink concentrations in benthic foraminifera reflect seawater chemistry', *Paleoceanography*, 15, pp. 299-306.
Martin, P. and Lea, D. (2002) 'A simple evaluation of cleaning procedures on fossil benthic foraminiferal Mg/Ca', *Geochem., Geophys., Geosys.*, 3(10), pp. 8401.
Martin-Garcia, G.M., Sierro, F.J., Flores, J.A., Abrantes, F. (2018) 'Role of the North Atlantic circulation in the mid-Pleistocene transition', *Clim. Past Discussions*, 14, pp. 1639-1651.
Martínez-Garcia, A., Rosell-Melé, A., Jaccard, S.L., Geibert, W., Sigman, D.M., Haug, G. (2011) 'Southern Ocean dust–climate coupling over the past four million years', *Nature*, 476, pp. 312-315.
März, C., Schnetger, B., Brumsack, H.J. (2013) 'Nutrient leakage from the North Pacific to the Bering Sea (IODP Site U1341) following the onset of Northern Hemispheric Glaciation?', *Paleoceanography*, 28, pp. 68-78.

Maslin, M., Seidov, D., Lowe, J. (2001) 'Synthesis of the nature and causes of rapid climate transitions during the Quaternary', in: Seidov, D., Haupt, B.J., Maslin, M. (edts.) *The Oceans and Rapid Climate Change: Past, Present, and Future*. Geophysical Monograph Series 126. Washington D.C.: American Geophysical Union, pp. 9-52.
Maslin, M.A. and Ridgwell, A.J. (2005) 'Mid-Pleistocene revolution and the "eccentricity-myth"', *Geol. Soc. London, Spec. Publ.*, 247, pp. 19-34.
Maslin, M.A. and Swann, G.E.A. (2006) 'Isotopes in marine sediments', in: M.J. Leng (ed.) *Isotopes in Palaeoenvironmental Research. V*olume 10. Amsterdam-Berlin-Heidelberg- London-New York: Springer, pp. 227-290.
Maslin, M.A. and Brierley, M. (2015) 'The role of orbital forcing in the early middle Pleistocene transition', *Quat. Int.*, 389, pp. 47-55.
Matsui, H., Tada, R., Oba, T. (1998) 'Low-salinity isolation event in the Japan Sea in response to eustatic sea-level drop during LGM', *Quat. Res.*, 37(3), pp. 221-233. (Japanese with English abstract).
Matsuzaki, K.M.M., Itaki, T., Tada, R., Kamikuri, S.-I. (2018) 'Paleoceanographic history of the Japan Sea over the last 9.5 million years inferred from radiolarian assemblages (IODP Expedition 346 Sites U1425 and U1430)', *Progr. Earth Planet. Sci.*, 5, https://doi.org/10.1186/s40645-018-0204-7.
Matter, A. (1974) 'Burial diagenesis of pelitic and carbonate deep sea sediments from the Arabian Sea', in: Whitmarsch, R.B., Weser, O.E., Ross, D.A. et al. (eds.) *Proceedings of the Ocean Drilling Program, Initial Report*, *volume 23*. College Station, Texas: ODP, pp. 891-921.
McCarroll, D. and Loader, N.J. (2005) 'Isotopes in tree rings', in: Leng, M.J. (ed.) *Isotopes in Palaeoenvironmental Research*. Amsterdam-Berlin-Heidelberg-London-New York: Springer, pp. 67-116.
McCave, I.N. (2002) 'Sedimentary settings on continental margins – an overview', in: Wefer, G., Billett, D., Hebbeln, D., Jørgensen, B.B., Schlüter, M., Van Weering, T.C.E. (eds.) *Ocean Margin Systems*. Amsterdam-Berlin-Heidelberg- London-New York: Springer, pp. 1-14.
McClymont, E., Sosdian, S.M., Rosell-Melé, A., Rosenthal, Y. (2013) ' Pleistocene sea-surface temperature evolution: Early cooling, delayed glacial intensification, and implications for the mid-Pleistocene', Earth-Sci. Rev., 123, pp. 173-193.
Meng, X., Liu, L., Wang, X.T., Baslam, W., Chen, J., Ji, J. (2018) 'Mineralogical evidence of reduced East Asian summer monsoon rainfall on the Chinese loess plateau during the early Pleistocene interglacials', *E.P.S.L.*, 486, pp. 61-69.
Meyers, P.A. (1994) 'Preservation of elemental and isotopic source identification of sedimentary organic matter', *Chem. Geol.*, 114, pp. 289-302.
Meyers, P.A. (1997) 'Organic geochemical proxies of paleoceanographic, paleolimnologic, and paleoclimatic processes', *Org. Geochem.*, 27(5/6), pp. 213-250.
Meyers, P.A. and Lallier, Vergès, E. (1999) 'Lacustrine sedimentary organic matter records of Late Quaternary paleoclimates', *J. Paleolim.*, 21, pp. 345-372.
Meyers, P.A. and Teranes, J.L. (2001) 'Sediment organic matter', in: Last, W.M. and Smol, J.P. (eds.) *Tracking Environmental Changes Using Lake Sediments – Volume II: Physical and Chemical Techniques.* Dordrecht: Kluewer, pp. 239-269.
Milanković, M.M. (1949) *Kanon der Erdbestrahlung und seine Anwendung auf das Eiszeitenproblem*. Belgrade: Royal Serbian Academy of Sciences, Special publication 132, p. 633.
Miller, C. and Dickens, G., (2017) 'Data report: reanalysis of interstitial water barium, iron, and sulfur concentrations at Sites U1426 and U1427', in: Tada, R., Murray, R.W., Alvarez Zarikian, C.A., and the Expedition 346 Scientists (eds.)

'*Proceedings of the Integrated Ocean Drilling Program,* 346'. College Station, TX: Integrated Ocean Drilling Program. 7pp.
Milliman, J.D. (1993) 'Production and accumulation of calcium carbonate in the ocean: Budget of a nonsteady state', *Glob. Biogeochem. Cycles*, 7(4), pp. 927-957.
Minami, I. (2003) 'Oxygen and carbon isotope variations of planktonic foraminifers in MD01-2407 core from Oki Ridge, the Japan Sea during the last 350 kyr', unpublished PhD thesis, University of Tokyo, p. 27. (Japanese with English Abstract).
Moore, C.M., Mills, M.M., Arrigo, K.R., Berman-Frank, I., Bopp, L., Boyd, P.W., Galbraith, E.D., Geider, R.J., Guieu, C., Jaccard, S.L., Jickells, T.D., La Roche, J., Lenton, T.M., Mahowald, N.M., Marañón, E., Marinov, I., Moore, J. ,K., Nakatsuka, T., Oschlies, A., Saito, M.A., Thingstad, T.F., Tsuda, A., Ulloa, O. (2013) 'Processes and patterns of oceanic nutrient limitation', *Nature Geosci*., 6, pp. 701-710.
Moreno, A., Cacho, I., Canals, M., Prins, M.A., Sanchez-Goni, M.F., Grimalt, J.O., Weltje, G.J. (2002) 'Saharan dust transport and high latitude glacial climatic variability: The Alboran Sea record', *Quat. Res.*, 58, pp. 318-328.
Mudelsee, M. and Statteger, K. (1997) 'Exploring the structure of the mid-Pleistocene revolution with advance methods of time-series analysis', *Geologische Rundschau*, 86, pp. 499-511.
Mudelsee, M. and Schulz, M. (1997) 'The mid-Pleistocene climate transition: Onset of 100 ka cycle lags ice volume build-up by 280 ka', *E.P.S.L.,* 151, pp. 117-123.
Mudelsee, M. and Raymo, M.E. (2005) 'Slow dynamics of the northern hemisphere glaciation', *Paleoceanography*, 20, pp. PA4022.
Muller, R.A. and MacDonald, G.J. (2000) 'Chapter 4 climate proxies', in: Muller, R.A. and MacDonald, G.J. (eds.) *Ice Ages and Astronomical Causes – Data, Spectral Analysis and Mechanisms*. Amsterdam-Berlin-Heidelberg- London-New York: Springer, pp. 105-141.
Müller, P.J. (1977) 'C/N ratios in Pacific deep-sea sediments: effect of inorganic ammonium and organic nitrogen compounds sorbed by clays', *Geochim. et Cosmochim. Acta*, 41, pp. 765-776.
Müller, P.J. and Suess, E. (1980) 'Productivity, sedimentation rate, and sedimentary organic matter in the oceans. 1. Organic matter preservation', *Deep Sea Res.*, 26, pp. 1347-1362.
Müller, J., Romero, O., Cowan, E.A., McClymont, E.L., Forwick, M., Asahi, H., März, C., Moy, C.M., Suto, I., Mix, A.C., Stoner, J. (2018) 'Cordilleran ice-sheet growth fueled primary productivity in the Gulf of Alaska, NE Pacific', *Geology*, 46(4), pp. G39904.
Murray, J.W. (1991) *Ecology and Palaeoecology of Benthic Foraminifera.* New York: Longman Scientific and Technical, 402pp.
Nie, J., Stevens, T., Rittner, M., Stockli, D., Garzanti, E., Limonta, M., Bird, A., Andò, S., Vermeech, P., Saylor, J., Lu, H., Breecker, D., Hu, X., Liu, S., Resentini, A., Vezzoli, G., Peng, W., Carter, A., Ji, S., Pan, B. (2015) 'Loess Plateau storage of Northeastern Tibetan Plateau-derived Yellow River sediment', *Nature Comms*., 6, pp. 9511.
Nier, A. O. (1950) 'A redetermination of the relative abundances of the isotopes of carbon, nitrogen, oxygen, argon and potassium', *Physical Rev.*, 77, pp. 789-793.
Nishiyama, K., Kawae, S., Sasaki, H. (1990) ' The Japan Sea proper water and the Japan Sea warm eddy', *Bull. Kobe Marine Observatory*, 209(1), pp. 10.

Nitani, H. (1972) 'On the deep and bottom waters in the Japan Sea', in: Shoji, D. (ed.) *Research in Hydrography and Oceanography*. Tokyo: Hydrographic and Oceanographic Department of Japan, pp. 151-201.
Norris, R.D. and Wilson, P.A. (1998) 'Low-latitude sea surface temperatures for the mid-Cretaceous and the evolution of planktonic foraminifera', *Geology*, 26, pp. 823–826.
Nürnberg, D. (1995) 'Magnesium in tests of Neogloboquadrina Pachyderma sinistral from high northern and southern latitudes', *J. Foramin. Res.*, 25(4), pp. 350-368.
Nürnberg, D., Bijma, J., Hemleben, C. (1996) 'Assessing the reliability of magnesium in foraminiferal calcite as a proxy for water mass temperatures', Geochim. et *Cosmochim. Acta*, 60(5), pp. 803-814.
Nürnberg, D. and Tiedemann, R. (2004) 'Environmental change in the Sea of Okhotsk during the last 1.1 million years', *Paleoceanography*, 19, pp. PA4011.
Oba, T., Kato, M., Kitazato, H., Koizumi, I., Omura, A., Sakai, T., Takayama, T. (1991) 'Paleoenvironmental changes in the Japan Sea during the last 85,000 years', *Paleoceanography*, 6(4), pp. 499-518.
Oba, T. and Irino, T. (2012) ' Sea level at the last glacial maximum, constrained by oxygen isotopic curves of planktonic foraminifera in the Japan Sea', *J. Quat. Sci.*, 27(9), pp. 941-947.
Ota, H. (1998) 'Geographic patterns of endemism and speciation in amphibians and reptiles of the Ryukyu Archipelago, Japan', *Res. Popul. Ecol.,* 40, pp. 189-204.
Paillard, D. (1998) 'The timing of Pleistocene glaciations from a simple multiple-state climate model', *Nature*, 391, pp. 378-381.
Park, R. and Epstein, S. (1960) 'Carbon isotope fractionation during photosynthesis', *Geochim. et Cosmochim. Acta*, 21(1-2), pp. 110-126.
Park, J. and Maasch, K.A. (1993) 'Plio-Pleistocene time evolution of the 100-kyr cycle in marine paleoclimate records', *J. Geophys. Res*., 98(1), pp. 447-461.
Park, S. and Chu, P.C. (2006) 'Thermal and haline fronts in the Yellow/East China Seas: Surface and subsurface seasonality comparison', *J. Oceanogr.*, 62(5), pp. 617-638.
Pearson, P.N., Ditchfield, P.W., Singano, J., Harcourt-Brown, K.G., Nicholas, C.J., Olsson, R.K., Shackleton, N.J., Hall, M.A. (2001) 'Warm tropical sea surface temperatures in the Late Cretaceous and Eocene epochs', *Nature*, 413, pp. 481-487.
Pearson, P.N. and Burgess, C. (2008) 'Foraminifer shell preservation and diagenesis: comparison of high latitude Eocene sites', in: Austin, W.E.N. and James, R.H. (eds.) *Biogeochemical Controls on Palaeoceanographic Proxies*. Special Publications volume 303, London: Geological Society of London, p. 59–72.
Pearson, P.N. (2012) 'Oxygen isotopes in foraminifera: overview and historical review', in: Ivany, L.C., Huber, B.T. (eds.) *Reconstructing Earth's Deep-Time Climate – The State of the Art in 2012*. The Paleontological Society papers, vol. 18, Cambridge: Cambridge University Press, p. 1-38.
Pearson, P.N., Evans, S.L., Evans, J. (2015) 'Effect of diagenetic recrystallization on the strength of planktonic foraminifer tests under compression', *J. Micropal.*, 34(1), pp. 59-64.
Pena, L.D. and Goldstein, S.L. (2014) 'Thermohaline circulation crisis and impacts during the mid-Pleistocene transition', *Science*, 345, pp. 318–322.
Peng, X., Ao, H., Xiao, G., Qiang, X., Qiang, S. (2020) 'The early-middle Pleistocene transition of Asian summer monsoon', *Palaeogeogr., Palaeoclimatol., Palaeoecol.*, 545, pp. 109636.

Peters, K.E. and Simoneit, B.R.T. (1982) 'Rock-Eval pyrolysis of Quaternary sediments from Leg 64, sites 479 and 480, Gulf of California', in: Curray, J.R., Moore, D.G., et al. (eds.) *Initial. Reports of DSDP expedition* 64. Washington D.C.: U.S. Government Printing Office, pp. 925-931.
Peters, K.E. (1986) *Guidelines for Evaluating Petroleum Source Rock using Programmed Pyrolysis*. Washington D.C.: American Association of Petroleum Geologists, 70(3), pp. 318-329.
Peterson, L.C. and Schimmenti, D.E. (2020) 'Data report: X-ray fluorescence scanning ofSite U1427, Yamato Basin, Expedition 346', in: Tada et al. (eds.) *Proc. IODP, volume 346*.
Pickering, K.T., Souter, C., Oba, T., Taira, A., Schaaf, M., Platzman, E. (1999) 'Glacio-eustatic control on deep-marine clastic forearc sedimentation, Pliocene–mid-Pleistocene (*c*. 1180–600 ka) Kazusa Group, SE Japan', *J. Geol. Soc. London*, 156, pp. 125-136.
Pimmel, A. and Claypool, G. (2001) *Introduction to ship-board organic geochemistry on JOIDES Resolution, technical note 30*. College Station, Texas: ODP, doi:10.2973/odp.tn.30.2001.
Pisias, N.G. and Moore, T.C. (1991) 'The evolution of Pleistocene climate: a data series approach', *E.P.S.L.*, 52, pp. 450-458.
Popova, I.M. (1986) 'Transportation of radiolarian shells by currents (calculations based on the example of the Kuroshio)', *Mar. Micropal.*, 11, pp. 197-201.
Porter, S.C. and An, Z. (1995) 'Correlation between climate events in the north Atlantic and China during the last glaciation', *Nature*, 375, pp. 305-308.
Qiu, B. (2001) 'Kuroshio and Oyashio currents', in: Steele, J.H., Thorpe, S.A., Turekian, K.K. (eds.) *Encyclopedia of Ocean Sciences*. London: Academic Press, pp. 1413–1425.
Ravelo, A. and Hillaire-Marcel, C. (2007) 'The use of oxygen and carbon isotopes of foraminifera in paleoceanography', in: Hillaire-Marcel, C. and De Vernal, A. (eds.) *Proxies in Late Cenozoic Paleoceanography*. Amsterdam: Elsevier, pp. 735-764.
Raymo, M.E., Ruddiman, W. and Froehlich, P.N. (1988) 'Influence of late Cenozoic mountain building on ocean geochemical cycles', *Geology*, 16(7), pp. 649-653.
Raymo, M.E. and Ruddiman, W. (1992) 'Tectonic forcing of late Cenozoic climate', *Nature*, 359, pp.117-122.
Raymo, M.E. (1997a) 'The timing of major climate terminations', *Plaeoceanography*, 12(4), pp. 577-585.
Raymo, M.E., Oppo, D.W., Curry, W. (1997b) 'The mid-Pleistocene climate transition: A deep sea carbon isotopic perspective', *Paleoceanography*, 12(4), pp. 546-559.
Raymo, M.E., Ganley, K., Carter, S. Oppo, D.W., McManus, J. (1998) 'Millennial-scale climate instability during the early Pleistocene epoch', *Nature*, 392, pp. 699-702.
Raymo, M.E., Kozdon, R., Evans, D., Lisiecki, L., Ford, H.L. (2018) 'The accuracy of mid-Pliocene δ^{18}O-based ice volume and sea level reconstructions', *Earth Sci. Rev.*, 177, pp. 291-302.
Rohling, E.J., Foster, G.L., Grant, K.M., Marino, G., Roberts, A.P., Tamisiea, M.E., Williams, F. (2014) 'Sea-level and deep-sea-temperature variability over the past 5.3 million years', *Nature*, 508-, pp. 477-482.
Rönnfeld, W. (2008) *Foraminiferen – Ein Katalog typischer Formen*. Tübingen: Institut für Geowissenschaften der Universität Tübingen. 146 pp (in German).
Rosenthal, Y. and Boyle, E. (1993) 'Factors controlling the fluoride content of planktonic foraminifers: An evaluation of its paleoceanographic applicability', *Geochim. et Cosmochim. Acta*, 57, pp. 335-346.

Rosenthal, Y., Boyle, E. and Slowey, N. (1997) 'Temperature control on the incorporation of magnesium, strontium, fluorine, and cadmium into benthic foraminiferal shells from Little Bahama Bank: Prospects for thermocline paleoceanography', *Geochim. et Cosmochim. Acta*, 61(17), pp. 3633-3643.
Rosenthal, Y., Perron-Cashman, S., Lear, C.H., Bard, E., Barker, S., Billups, K., Bryan, M., Delaney, M.L., deMenocal, P.B., Dwyer, G.S., Elderfield, H., German, C.R., Greaves, M., Lea, D.W., Marchitto, T.M.Jr., Pak, D.K., Paradis, G.L., Russell, A.D., Schneider, R.R., Scheiderich, K., Stott, L., Tachikawa, K., Tappa, E., Thunell, R., Wara, M., Weldeab, S., Wilson, P.A. (2004) 'Interlaboratory comparison study of Mg/Ca and Sr/Ca measurements in planktonic foraminifera for paleoceanographic research', *Geochem., Geophys., Geosys.*, 5(4), pp. GC000650.
Rosenthal, Y. (2007) 'Elemental proxies for reconstructing Cenozoic seawater paleotemperatures from calcareous fossils', in: Hillaire-Marcel, C. and De Vernal, A. (eds.) *Developments in Marine Geology*. Amsterdam: Elsevier, pp. 765-797.
Ruddiman, W.F., Raymo, M.E., Martinson, D.G., Clement, B.M., Backman, J. (1989) 'Pleistocene evolution: Northern hemisphere ice sheets and the north Atlantic ocean', *Paleoceanography*, 4(4), pp. 353-412.
Ruddiman, W.F. and Kutzbach, J.E. (1990) 'Late Cenozoic plateau uplift and climate change', Transactions of the Royal Society of Edinburgh - Earth and Environment 81, pp. 301-314.
Ruddiman, W.F. (2001a) 'Chapter 17: Humans and climate change', in: Ruddiman, W.F. (author) *Earth's Climate – Past and Future.* New York: W.H. Freeman and Company, pp. 383-404.
Ruddiman, W.F. (2001b) 'Chapter 8: Astronomical control of solar radiation', in: Ruddiman, W.F. (author) *Earth's Climate – Past and Future.* New York: W.H. Freeman and Company, pp. 174-192.
Ruddiman, W.F. (2001c) 'Chapter 3: Climate archives, data and models', in: Ruddiman, W.F. (author) *Earth's Climate – Past and Future.* New York: W.H. Freeman and Company, pp.54-83.
Ruddiman, W.F. (2001d) 'Chapter 7: Back into the icehouse: the last 55 million years', in: Ruddiman, W.F. (author) *Earth's Climate – Past and Future.* New York: W.H. Freeman and Company, pp.147-171.
Ruddiman, W.F. (2001e) 'Chapter 2: Earth's climate system today', in: Ruddiman, W.F. (author) *Earth's Climate – Past and Future.* New York: W.H. Freeman and Company, pp.18-53.
Ruddiman, W.F. (2003) 'Orbital insolation, ice volume, and greenhouse gases', *Quat. Sci. Rev.*, 22, pp.1597-1629.
Ruddiman, W.F. (2004) 'The role of greenhouse gases in orbital-scale climatic changes', *E.O.S.*, 285(1), pp. 6-7.
Rühlemann, C., Müller, P.J., Schneider, R.R. (1999) 'Organic carbon and carbonate as paleoproductivity proxies: Examples from high and low productivity areas of the tropical Atlantic', in: Fischer, G. and Wefer, G. (eds.) *Use of Proxies in Paleoceanography*. Amsterdam-Berlin-Heidelberg- London-New York: Springer, pp. 315-344.
Russell, A., Nelson, B., Erez, J. and Lea, D. (1994) 'Uranium in foraminiferal calcite as a recorder of seawater uranium concentrations', *Geochim. et Cosmochim. Acta*, 58, pp. 671-681.
Rutherford, S. and D'Hondt, S. (2000) 'Early onset and tropical forcing of 100,000-year Pleistocene glacial cycles', *Nature*, 408, pp. 72-75.

Saavedra-Pellitero, M., Baumann, K.-H., Gallagher, S.J., Sagawa, T., Tada, R. (2019) 'Paleoceanographic evolution of the Japan Sea over the last 460 kyr – a coccolithophore perspective', *Mar. Micorpal.*, 152, pp. 101720.
Sagawa, T., Toyoda, K., Oba, T. (2005) 'Sea surface temperature record off central Japan since the Last Glacial Maximum using planktonic foraminiferal Mg/Ca thermometry', *J. Quat. Sci*., 21, pp. 63-73.
Sagawa, T., Ikehara, K., Irino, T., Nakagawa, T., Takahashi, S., Kubota, Y., Matsuzaki, K., Suzuki, Y., Kozaka, Y., Lu, S., Tada, T., Holburn, A., Henderson A., Huang, H.-H. (2015) 'Cruise report of R/V Kairei, KR15-10, precise chronology for the late Pleistocene Japan Sea sediments and its application to paleoceanography off Wakasa Bay', *Japan Agency for Marine-Earth Science and Technology (JAMSTEC)*, 58 pages.
Sagawa, T., Nagahashi, Y., Satoguchi, Y., Holburn, A., Itaki, T., Gallagher, S.J., Saavedra-Pellitero, M., Ikehara, K., Irino, T., Tada, R. (2018) 'Integrated tephrastratigraphy and stable isotope stratigraphy in the Japan Sea and East China Sea using IODP sites U1426, U1427, and U1429, Expedition 346 Asian monsoon', *Prog. Earth Planet. Sci.*, 5(18), pp. DOI 10.1186/s40645-018-0168-7.
Sancetta, C. (1982) 'Distribution of diatom species in surface sediments of the Bering and Okhotsk seas', *Micropaleontology,* 2(8), p. 221-257.
Sato, H. (1994) 'The relationship between late Cenozoic tectonic events and stress field and basin development in northeast Japan', *J. Geophys. Res.*, 99(B11), pp. 22261-22274.
Scheffer, F. and Schachtschabel, P. (1984) *Lehrbuch der Bodenkunde*. Stuttgart: Enke Verlag, 442 pages.
Schefuβ, E., Schouten, S., Janse, J.H.F., Sinnighe Damsté, J.S. (2003) 'African vegetation controlled by tropical sea surface temperatures in the mid-Pleistocene period', *Nature*, 422, pp. 418-421.
Schlanger, S.O. and Douglas, R.G. (1974) 'The pelagic ooze-chalk-limestone transition and its implication for marine stratigraphy', in: Hsü, K.J. and Jenkyns, H.C. (eds.) *Pelagic sediments: On land and under the sea*. International Association of Sedimentology, Special Publication, volume 1. Oxford: Blackwell Scientific Publications, pp. 117–148.
Schonfeld, J. (2012) 'History and development of methods in recent benthic foraminiferal studies', *J. Micropal.,* 31: 53-72.
Schrag, D.P. (1999) 'Effects of diagenesis on the isotopic record of late Paleogene tropical sea surface temperatures', *Chem. Geology*, 161, pp. 215-224.
Schubert, C.J. and Calvert, S.E. (2001) 'Nitrogen and carbon isotopic composition of marine and terrestrial organic matter in Arctic Ocean sediments: Implications for nutrient utilization and organic matter composition', *Deep-Sea Res.,* 1(48): 789-810.
Sexton, P.E., Wilson, P.A., Pearson, P.N. (2006) 'Microstructural and geochemical perspectives on planktic foraminiferal preservation: “glassy” versus “frosty”', *Geochem., Geophys., Geosys.*, 7(12), pp. GC001291.
Sexton, P.E., Wilson, P.A. (2009) 'Preservation of benthic foraminifera and reliability of deep-sea temperature records: Importance of sedimentation rates, lithology, and the need to examine test wall structure', *Paleoceanography*, 24, pp. PA2208.
Shackleton, N.J. and Opdyke, N.D. (1973) 'Oxygen isotope and palaeomagnetic stratigraphy of equatorial Pacific core V28-238: oxygen isotope temperatures and ice volumes on a 10^5 year and 10^6 year scale', *Quat. Res.*, 3, pp. 39-55.
Shackleton, N.J. (1974) 'Attainment of isotopic equilibrium between ocean water and the benthonic foraminifera genus *Uvigerina*: Isotopic changes in the ocean during the last glacial', *Cent. Natl. Rech. Sci. Coloq. Int*., 219, pp. 203-209.

Shackleton, N.J. and Opdyke, N.D. (1976) 'Oxygen-isotope and paleomagnetic stratigraphy of Pacific core V28-239: late Pliocene to latest Pleistocene', *Geological Society of America Memoir,* 145, pp. 449-464.
Shackleton, N.J. (1977) 'Carbon-13 in Uvigerina: tropical rainforest history and the equatorial Pacific carbonate dissolution cycles', in: Andersen, N.R., Malahoff, A. (eds.) *The Fate of Fossil Fuel CO_2 in the Oceans*. New York: Plenum Press, pp. 401-427.
Shackleton, N.J. (2000) 'The 100,000 year ice age cycle identified and found to lag temperature, carbon dioxide and orbital eccentricity', *Science*, 289, pp. 1989-1902.
Smith, B.N. and Epstein, S. (1971) 'Two categories of $^{13}C/^{12}C$ ratios for higher plants', *Plant Physiology*, 47, pp. 380-384.
Son, M., Song, C.W., Kim, M.-C.,Cheon, Y., Cho, H., Sohn, Y.K. (2015) 'Miocene tectonic evolution of the basins and fault systems, SE Korea: dextral, simple shear during the East Sea (Sea of Japan) opening', *J. Geol. Soc.*, 172(5): 664–680.
Sosdian, S. and Rosenthal, Y. (2009) 'Deep-sea temperature and ice volume changes across the Pliocene-Pleistocene climate transitions', *Science*, 325, pp. 306-310.
Sosdian, S., Rosenthal, Y., Toggweiler, J.R. (2018) 'Deep Atlantic carbonate ion and $CaCO_3$ compensation during the ice ages', *Paleoceanogr. Paleoclim*., 33, pp. 546-562.
Stax, R. and Stein, R. (1994) 'Quaternary organic carbon cycles in the Japan Sea (ODP-Site 798) and their paleoceanographic implications', *Palaeogeogr., Palaeoclimatol., Palaeoeco*l., 108, pp. 509-521.
Stein, R., Littke, R., Stack, R. and Welte, D.H. (1989): Quantity, provenance, and maturity of organic matter at ODP-Sites 645, 646, and 647: Implications for reconstruction of paleoenvironments in Baffin Bay and Labrador Sea during Tertiary and Quaternary time. In: Srivastava, S.P., Arthur, M.A., et al. (eds.) *Proceedings of OPD, science results 105*. College Station (Texas): Ocean Drilling Program, p. 185-208.
Stein, R. (1991) 'Reconstruction of depositional environments from sediment data', in Bhattacharij, S., Friedman, G.M., Neugebauer, H.J., Seilacher, A. (eds.) *Lecture Notes in Earth Sciences*, volume 34, pp. 21-28.
Stein, R. and Stax, R. (1992a) 'Short- and long-term variations in flux rates and composition of organic carbon at sites 798 and 799 through late Cenozoic times: Implications for basin evolution, paleoclimate, and paleoceanography in the Sea of Japan', in: Pisciotto, K.A., Ingle, J.C.Jr., von Breymann, M.T., Barron, J. et al. (eds.) *Proceedings of the Ocean Drilling Program, Scientific Results*, *Volume 127/128, part 1*. College Station, Texas: ODP, pp. 457-470.
Stein, R. and Stax, R. (1992b) 'Late Cenozoic changes in flux rates and composition of organic carbon at sites 798 and 799 (Sea of Japan)' in: Pisciotto, K.A., Ingle, J.C.Jr., von Breymann, M.T., Barron, J. et al. (eds.) *Proceedings of the Ocean Drilling Program, Scientific Results*, *Volume 127/128, part 1*. College Station, Texas: ODP, pp. 423-437.
Stern, J.V. and Lisiecki, L.E. (2014) 'Termination 1 timing in radiocarbon-dated regional benthic $\delta^{18}O$ stacks', *Paleoceanography and Paleoclimatology*, 29(12), pp. 1127-1142.
Sun, Y., Clemens, S.C., An, Z., Yu, Z. (2006) 'Astronomical timescale and palaeoclimatic implication of stacked 3.6-Myr monsoon records from the Chinese Loess Plateau', *Quat. Sci. Rev.*, 25, pp. 33–48.

Sun, Y., An, Z., Clemens, S.C., Bloemendal, J., Vandenberghe, J. (2010) 'Seven million years of wind and precipitation variability on the Chinese leoss plateau', *E.P.S.L.*, 297, pp. 525-535.
Sun, Y., Yin, Q., Crucifix, M., Clemens, S.C., Araya-Melo, P., Liu, W., Qiang, X., Liu, Q., Zhao, H., Liang, L., Chen, H., Li, Y., Zhang, L., Dong, G., Li, M., Zhou, W., Berger, A., Zhisheng An, Z. (2019) 'Diverse manifestations of the mid-Pleistocene climate transition', *Nature Comm.*, 10. doi.org/10.1038/s41467-018-08257-9.
Tachikawa, K., Rapuc, W., Dubois-Dauphin, Q., Guihou, A., Skonieczny, C. (2020) 'Reconstruction of ocean circulation based on neodymium isotopic composition', *Oceanography*, early release/in press.
Tada, R., Koizumi, I., Cramp, A., Rahman, A. (1992) 'Correlation of dark and light layers and the origin of their cyclicity in the Quaternary sediments from the Japan Sea', in: Pisciotto, K.A., Ingle, J.C.Jr., von Breymann, M.T., Barron, J., et al. (eds.) *Proceedings of the Integrated Ocean Drilling Program, scientific results, 127/128 (Part 1)*. College Station (Texas): Integrated Ocean Drilling Program, pp. 577–601.
Tada, R. (1994) 'Paleoceanographic evolution of the Japan Sea', *Paleogeogr., Paleoclim., Paleoecol.*, 108, pp. 487-508.
Tada, R., Irino, T., Koizumi, I (1999) 'Land-ocean linkages over orbital and millennial timescales recorded in late Quaternary sediments of the Japan Sea', *Plaeoceanography*, 14(2), pp. 236-247.
Tada, R. (2004) 'Onset and evolution of millennial-scale variability in the Asian Monsoon and its impact on paleoceanography of the Japan Sea', in: Clift, P.D., Kuhnt, W., Wang, P., Hayes, D. (eds.) *Continent-ocean interactions in the east Asian marginal seas*. Washington D.C.: AGU Monograph, Series 149, pp. 283-298.
Tada, R., Murray, R.W., Alvarez Zarikian, C.A., Anderson, W.T., Jr., Bassetti, M.-A., Brace, B.J., Clemens, S.C., da Costa Gurgel, M.H., Dickens, G.R., Dunlea, A.G., Gallagher, S.J., Giosan, L., Henderson, A.C.G., Holbourn, A.E., Ikehara, K., Irino, T., Itaki, T., Karasuda, A., Kinsley, C.W., Kubota, Y., Lee, G.S., Lee, K.E., Lofi, J., Lopes, C.I.C.D., Peterson, L.C., Saavedra-Pellitero, M., Sagawa, T., Singh, R.K., Sugisaki, S., Toucanne, S., Wan, S., Xuan, C., Zheng, H., and Ziegler, M. (2013) *Integrated Ocean Drilling Program Expedition 346 Preliminary Report, Asian Monsoon - Onset and Evolution of Millennial-Scale Variability of Asian Monsoon and its Possible Relation with Himalaya and Tibetan Plateau Uplift*. College Station (Texas): Integrated Ocean Drilling Program, 111pp.
Tada, R., Murray, R.W., Alvarez Zarikian, C.A., Anderson, W.T., Jr., Bassetti, M.-A., Brace, B.J., Clemens, S.C., da Costa Gurgel, M.H., Dickens, G.R., Dunlea, A.G., Gallagher, S.J., Giosan, L., Henderson, A.C.G., Holbourn, A.E., Ikehara, K., Irino, T., Itaki, T., Karasuda, A., Kinsley, C.W., Kubota, Y., Lee, G.S., Lee, K.E., Lofi, J., Lopes, C.I.C.D., Peterson, L.C., Saavedra-Pellitero, M., Sagawa, T., Singh, R.K., Sugisaki, S., Toucanne, S., Wan, S., Xuan, C., Zheng, H., and Ziegler, M. (2015a) 'Expedition summary', in: Tada, R., Murray, R.W., Alvarez Zarikian, C.A., and the Expedition 346 Scientists (eds.) *Proceedings of the Integrated Ocean Drilling Program, volume 346.* College Station, Texas: Integrated Ocean Drilling Program. doi:10.2204/iodp.proc.346.101.2015.
Tada, R., Murray, R.W., Alvarez Zarikian, C.A., Anderson, W.T., Jr., Bassetti, M.-A., Brace, B.J., Clemens, S.C., da Costa Gurgel, M.H., Dickens, G.R., Dunlea, A.G., Gallagher, S.J., Giosan, L., Henderson, A.C.G., Holbourn, A.E., Ikehara, K., Irino, T., Itaki, T., Karasuda, A., Kinsley, C.W., Kubota, Y., Lee, G.S., Lee, K.E., Lofi, J., Lopes, C.I.C.D., Peterson, L.C., Saavedra-Pellitero, M., Sagawa, T., Singh, R.K., Sugisaki, S., Toucanne, S., Wan, S., Xuan, C., Zheng, H., and Ziegler, M. (2015b)

'Site U1427', in Tada, R., Murray, R.W., Alvarez Zarikian, C.A., and the Expedition 346 Scientists (eds.) *Proceedings of the Integrated Ocean Drilling Program, volume 346.* College Station, Texas: Integrated Ocean Drilling Program. doi:10.2204/iodp.proc.346.108.2015.

Tada, R., Murray, R.W., Alvarez Zarikian, C.A., Anderson, W.T., Jr., Bassetti, M.-A., Brace, B.J., Clemens, S.C., da Costa Gurgel, M.H., Dickens, G.R., Dunlea, A.G., Gallagher, S.J., Giosan, L., Henderson, A.C.G., Holbourn, A.E., Ikehara, K., Irino, T., Itaki, T., Karasuda, A., Kinsley, C.W., Kubota, Y., Lee, G.S., Lee, K.E., Lofi, J., Lopes, C.I.C.D., Peterson, L.C., Saavedra-Pellitero, M., Sagawa, T., Singh, R.K., Sugisaki, S., Toucanne, S., Wan, S., Xuan, C., Zheng, H., and Ziegler, M. (2015c) 'Methods', in Tada, R., Murray, R.W., Alvarez Zarikian, C.A., and the Expedition 346 Scientists (eds.) *Proceedings of the Integrated Ocean Drilling Program, volume 346.* College Station, Texas: Integrated Ocean Drilling Program. doi:10.2204/iodp.proc.346.102.2015.

Tada, R., Zheng, H. and Clift, P.D. (2016) 'Evolution and variability of the Asian monsoon and its potential linkage with uplift of the Himalaya and Tibetan Plateau', *Progr. Earth Pl. Sci.*, 3, pp. 4-30.

Tada, R., Irino, T., Ikehara, K., Karasuda,A., Sugisaki, S., Xuan, C., Sagawa, T., Itaki, T., Kubota, Y., Lu, S., Seki, A., Murray, R.W., Alvarez-Zarikian, C., Anderson, W.T., Bassetti, M.-A., Brace, B.J., Clemens, S.C., da Costa Gurgel, M.H., Dickens, G.R., Dunlea, A.G., Gallagher, S.J., Giosan, L., Holbourn, A.E., Kinsley, C.W., Soo Lee, G., Lee, K.E., Lofi, J., Lopes, C.I.C.D., Saavedra-Pellitero, M., Peterson, L.C., Singh, R.K., Toucanne, S., Wan, S., Zheng, H., Ziegler, M. (2018) High-resolution and high-precision correlation of dark and light layers in the Quaternary hemipelagic sediments of the Japan Sea recovered during IODP Expedition 346. *Progress in Earth and Planetary Science* 5(19). https://doi.org/10.1186/s40645-018-0167-8

Tiedemann, R., Sarnthein, M., Shackleton, N.J. (1994) 'Astronomic timescale for the Pliocene Atlantic $\delta^{18}O$ and dust flux records of ODP Site 659', *Paleoceanography*, 9, pp. 619-638.

Tissot, B.P. and Welte, D.H. (1984) *Petroleum Formation and Occurrence.* 2nd Revised and Enlarged Edition. Amsterdam-Berlin-Heidelberg- London-New York-Tokyo: Springer, 699pp.

Tomašových, A., Kidwell, S.M., Alexander, C.R., Kaufman, D.S. (2019) 'Millennial-scale age offsets within fossil assemblages: Result of bioturbation below the taphonomic active zone and out-of-phase production', *Paleoceanogr. Paleoclim.*, 34, pp. 954–977.

Tomczak, M. and Godfrey, J.S. (1994) *Regional Oceanography: An Introduction*. London: Pergamon, 422 pp.

Toyofuku, T., Kitazato, H., Kawahata, H., Tsuchiya, M. and Nohara, M. (2000) 'Evaluation of Mg/Ca thermometry in foraminifera: comparison of experimental results and measurements in nature', *Paleoceanography*, 15(4), pp. 456-464.

Trauth, M.H. (2013) ' TURBO2: A MATLAB simulation to study the effects of bioturbation on paleoceanographic time series', *Comput. Geosci.*, 61, pp. 1-10.

Tsuji, T., Miyata, Y., Okada, M., Mita, I., Nakagawa, H., Sato, Y., Nakamizu, M. (2005) 'High-resolution chronology of the lower Pleistocene Otadai and Umegase Formations of the Kazusa Group, Boso Peninsula, central Japan-Chronostratigraphy of the JNOC TR-3 cores based on oxygen isotope, magnetostratigraphy and calcareous nannofossils', *J. Geol. Soc. Japan*, 111, pp. 1–20 (in Japanese with English abstract).

Tzedakis, P.C., Crucifix, M., Mitsui, T., Wolff, E.W. (2017) 'A simple rule to determine which insolation cycles lead to interglacials', *Nature*, 542, pp. 427-432.

Ujiié, H. and Ichikura, M. (1973) 'Holocene-uppermost Pleistocene planktonic foraminifers of a piston core from off San'in district, Sea of Japan'. *Transac. Proc. Paleontol. Soc. Japan*, 91, pp. 137-150.
Ujiié, H., Tanaka, Y., Ono, T. (1991) 'Late Quarternary paleoceanographic record from the middle Ryukyu Trench slope, northwest Pacific', *Mar. Micropal.*, 18, pp. 115-128.
Ujiié, H. and Ujiié, Y. (1999) ' Late Quaternary course changes of the Kuroshio Current in the Ryukyu Arc region, northwestern Pacific Ocean'*, Mar. Micoropal.*, 37, pp. 23-40.
Ujiié, Y., Ujiié, H., Taira, A., Nakamura, T., Oguri, K. (2003) 'Spatial and temporal variability of surface water in the Kuroshio source region, Pacific Ocean, over the past 21,000 years: evidence from planktonic foraminifera', *Mar. Micropal.*, 49(4), pp. 335-364.
Van Krevelen, D.W. (1984) 'Organic geochemistry – old and new', *Org. Geochem.*, 6, pp. 1-10.
Van Soest, R.W.M., Boury-Esnault, N., Vacelet, J., Dohrmann, M., Erpenbeck, D., De Voogd, N.J., Santodomingo, N., Vanhoorne, B., Kelly, M., Hooper, J.N.A. (2012) 'Global diversity of songes (porifera)', *PLoS One*, 7(4), pp. e35105.
Viaggi, P (2018) 'δ^{18}O and SST signal decomposition and dynamic of the Pliocene-Pleistocene climate system: new insights on orbital nonlinear behaviour vs. long-term trend', *Prog. Earth Pl. Sci.,* 5. doi: 10.1186/s40645-018-0236-z.
Voigt, J., Hathorne, E.C., Frank, M., Holburn, A. (2016) 'Minimal influence of recrystallization on middle Miocene benthic foraminiferal stable isotope stratigraphy in the eastern equatorial Pacific', Paleoceanography, 31, pp. 98-114.
Wagner, T. and Dupond, L.M. (1999) 'Terrestrial organic matter in marine sediments: analytical approaches and eolian-marine records in the central equatorial Atlantic', in: Fischer, G. and Wefer, G. (eds.) *Use of proxies in paleoceanography*. Amsterdam-Berlin-Heidelberg- London-New York: Springer, pp. 547-574.
Wagner, T., Zabel, M., Dupont, L., Hotvoeth, J., Schubert, C.J. (2003) 'Terrigenous signals in sediments of the low-latitude Atlantic – Implications for environmental variations during the late Quaternary, part I: organic carbon', in: Wefer, G., Mulitza, S., Ratmeyer, V. (eds.) *The south Atlantic in the late Quaternary – Reconstruction of material budgets and current systems*. Amsterdam-Berlin-Heidelberg- London-New York: Springer, pp. 295-322.
Wang, Y.J., Cheng, H., Edwards, R.L., An, Z.S., Wu, J.Y., Shen, C.C., Dorale, J.A. (2001) 'A high-resolution absolute-dated late Pleistocene monsoon record from Hulu Cave, China', *Science*, 294, pp. 2345-2348.
Wang, P. (2004) 'Cenozoic deformation and the history of sea-land interactions in Asia', in Clift, P., Wang, P., Kuhnt, W., Hayes, D. (eds.) *Continent-ocean interactions within East Asian marginal seas*. Geophysical Monograph 149. Washington D.C.: American Geophysical Union, pp. 1-22.
Wang, Y., Cheng, H., Edwards, R.L., Kong, X., Shao, X., Chen, S., (2008) 'Millennial- and orbital-scale changes in the East Asian Monsoon over the past 224,000 years', *Nature*, 451, pp. 1090-1093
Waples, D.W. and Sloan, J.R. (1980) 'Carbon and nitrogen digenesis in deep sea sediments', *Geochim. et Cosmochim. Acta*, 44, pp. 1463-1470.
Watanabe, Y.W., Watanabe, S., Tsunogai, S. (1991) 'Tritium in the Japan Sea and the renewal time of the Japan Sea deep water', *Mar. Chem.*, 34, pp. 97-108.
Watanabe, S., Tada, R., Ikehara, K., Fujine, K., Kido, Y. (2007) 'Sediment fabrics, oxygenation history, and circulation modes of Japan Sea during the Late Quaternary', *Palaeogeogr., Palaeoclim., Palaeoecol.*, 247, pp. 50-64.

Wefer, G., Berger, H.W., Bijma, J., Fischer, G. (1999) 'Clues to ocean history: A brief overview of proxies', in: Fischer, G. and Wefer, G. (eds.) *Use of proxies in paleoceanography*. Amsterdam-Berlin-Heidelberg- London-New York: Springer, pp. 1-68.
Willeit, M., Ganopolski, A., Calov, R., Brovkin, V. (2019) 'Mid-Pleistocene transition in glacial cycles explained by declining CO2 and regolith removal', *Sci. Adv*., 5, pp. eaav7337.
Wilson, P.A., and Opdyke, B.N. (1996) 'Equatorial sea-surface temperatures for the Maastrichtian revealed through remarkable preservation of metastable carbonate', *Geology*, 24, pp. 555–558.
Wilson, P.A. and Norris, R.D. (2001) 'Warm tropical ocean surface and global anoxia during the mid-Cretaceous period', *Nature*, 412, pp. 425–429.
Wilson, P.A., Norris, R.D., Cooper, M.J. (2002) 'Testing the Cretaceous greenhouse hypothesis using glassy foraminiferal calcite from the core of the Turonian tropics on Demerara Rise', *Geology*, 30, pp. 607-610.
Yamamoto, K., Iryu, Y., Sato, T., Chiyonobu, S. (2006) 'Responses of coral reefs to increased amplitude of sea-level changes at the mid-Pleistocene climate transition', *Palaeogeogr., Palaeoclim., Palaeoecol.*, 241, pp. 160-175.
Yanagi, T. (2002) 'Water, salt, phosphorus and nitrogen budgets of the Japan Sea', *J. Oceanogr*., 58, pp. 797–804.
Yokota, M., Okada, H., Arita, M., Ikehara, K., Moritani, T. (1990) 'Distribution of heavy minerals in the bottom sediments of the southern Sea of Japan, off the Shimane Peninsula, southwest Japan', *Scientific Reports of the Department of Geology, Kyushu University*, 16, pp. 59-86 (in Japanese with English abstract).
Yokoyama, Y., Lambeck, K., De Deckker, P., Johnston, P., Fifield, K. (2000) 'Timing of the last glacial maximum from observed sea-level minima', *Nature*, 406, pp. 713-716.
Yokoyama, Y., Kido, Y., Tada, R., Minami, I., Finkel, R.C., Matsuzakim H. (2007) 'Japan Sea oxygen isotope stratigraphy and global sea-level changes for the last 50,000 years recorded in sediment cores from the Oki Ridge', *Palaeogeogr., Palaeoclim., Palaeoecol.*, 247, pp. 5-17.
Yoon, S. (1997) Miocene-Pleistocene volcanism and tectonics in southern Korea and their relationship to the opening of the Japan Sea. *Tectonophysics*, 281: 53-70.
Yu, J., Elderfield, H., Greaves, M. and Day, J. (2007) 'Preferential dissolution of benthic foraminiferal calcite during laboratory reductive cleaning', *Geochem., Geophys., Geosys.*, 8(6), p. Q06016.
Zachos, J.C., Pagani, M., Sloan, L., Thomas, E., Billups, K. (2001) 'Trends, rhythms, and aberrations in global climate 65 Ma to present', *Science*, 292, pp. 686-693.
Zachos, J.C., Kroon, D., Blum, P., et al. (2004) 'Explanatory notes', in: Zachos, J.C., Kroon, D., Blum, P., et al. (eds.) *Proceedings of the Ocean Drilling Program, Initial Reports, volume 208* College Station (Texas): Ocean Drilling Program, 63pp.
Zhao, D., Wan, S., Clift, P.D., Tada, R., Huang, J., Yin, X., Liao, R., Shen, X., Shi, X., Li, A. (2018) 'Provenance, sea-level and monsoon climate controls on silicate weathering of Yellow River sediment in the northern Okinawa Trough during late last glaciation', *Palaeogeogr., Palaeoclimatol., Palaeoecol*., 490(15), pp. 227-239.
Zhao, D., Wan, S., Clift, P.D., Tada, R., Huang, J., Yin, X., Liao, R., Shen, X., Shi, X., Li, A. (2019) 'Quaternary sedimentary record in the northern Okinawa Trough indicates the tectonic control on depositional environment change', *Palaeogeogr., Palaeoclimatol., Palaeoecol*., 516(15), pp. 126-138.
Zhou, X., Lyu, X., Liu, C., Liu, Z., Li, Q., Jin, X., Zhang, H., Dadd, K. (2019) ' Depositional mechanisms for upper Miocene sediments in the South China Sea

central basin: Evidence from calcareous nannofossils', *Marine Mircopal*., 151, pp. 101768.

Chapter 9: Appendices

Appendix A

A digital version (Excel file) of samples used in this thesis with their respective depth scale conversions, age estimates, mass accumulation rates and results of geochemical, palaeontological and sedimentological analyses is attached to this thesis.

Appendix B

Possible diagenetic alterations on foraminiferal shells can impact on their geochemical records (chapter 3, section 3.5.9), therefore a combined SEM/EDX investigation was carried out which results are presented here.

Foraminifera shells were isolated from one surface sample (KR 15-10, Site WB10, MC03, 0-1 cm; chapter 3, section 3.3) and eight down-hole samples from geochemical and grain-size extrema that contain sufficient amounts of foraminiferal shells to allow for both isotope and SEM/EDX analyses, and suggested to be of the worst preservation state contained in the samples using low-resolution light microscopic analyses (table I).

Sample	Depth (m CCSF-D)	Shells of …	$CaCO_3$ (wt%)	TOC (wt%)	<63 µm (wt%)
Surface sample	0	*Uvi.*, *Pach.* (d)	*	*	*
B-30-2-16	262.62	*Uvi.*,	6.41	1.0	96.5
B-42-3-83	326.03	*Pach., Bull.*	15.99	1.9	93.44
A-51-2-98	377.32	*Uvi.*,	19.99	1.8	95.4
A-63-4-7	440.03	*Uvi.*,	6.75	1.9	91.7
A-70-1-113	470.83	*Pach.*	6.91	1.9	88.55
A-74-1-36	488.86	*Uvi.*, *Bull.*	*	1.7	97.7
A-79-3-4	514.74	*Bull.*	6.08	1.1	99.45
A-80-3-25	518.24	*Uvi.*,	8.58	1.1	91.4

Table I. Samples used in SEM/EDX diagenesis survey containing *Uvigerina spp.* (*Uvi.*), *G. bulloides* (*Bull.*) and/or *N. pachyderma* (dextral in surface sample, sinistral in down-core samples) and highlighting the geochemical and grain-size (<63µm, wt%) extrema (orange). Asterisked (*) analyses were not executed.

Benthic foraminifera

The visual inspection of benthic foraminifera shells (*Uvigerina spp.*) from the surface sample (figure Ia-c), an example of good preservation, shows well-preserved primary shell features, such as strong costae (figure Ia) and fine pores on surfaces (figure Ib, location indicated by red box in figure Ia), and open pore channels, continuing through from the surface through the shell wall, and onto the inner surfaces (figure Ic). It is likely that, if this sample had undergone diagenetic alteration, these features would be obscured by a secondary calcite layer (abiotic, diagenetic calcite layer) or as a shell infill. During another diagenetic process in foraminifera shells, recrystallisation, the micro-granular shell wall structure would have been replaced by larger, blocky calcite crystals (*c.f.* Sexton et al., 2006; Edgar et al., 2015; Voigt et al., 2016). There are small areas of less densely packed pores on the outer surface of most shells (figure Ib), which may be an artefact of sample preparation, e.g. wet-sieving or attaching to SEM stub (Maryline Jeanne Vautravers, pers. com.,

March 2017). Overall, the SEM/EDX results indicate little diagenetic alteration of *Uvigerina spp*. shells of the surface sample.

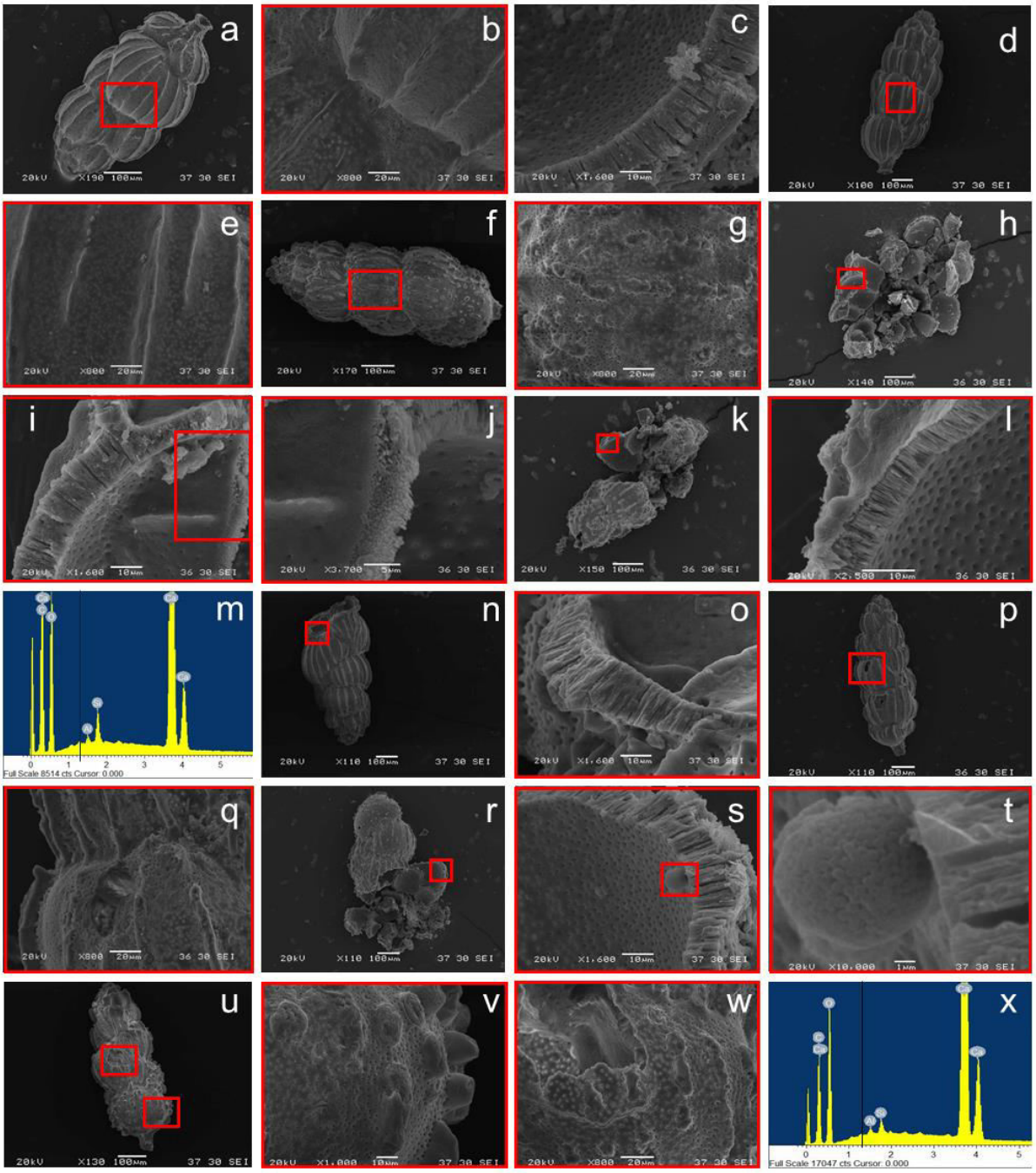

Figure I. SEM images and EDX spectra of the surface sample (fig. Ia-c) and down-core samples (fig. d-x). Sorted by depth and sample name this table shows samples B-30-2-16 (fig. Id-e), A-51-2-98 (fig. If-m) with an EDX spectrum (fig. Im) of a suspected diagenetic layer (see fig. II), A-63-4-7 (fig. In-o), A-74-1-36 (fig. Ip-t) as well as A-80-3-25 (fig. Iu-x) with an EDX spectrum (fig. Ix) of the outer surface seen in fig. Iw. Red boxes indicate the position of higher-resolution images, presented in subsequent photographs. The vertical black line at 1.3 keV in the EDX spectra (fig. Im and Ix) indicates the position a Mg-peak, which would be indicative of diagenetic calcites.

The down-core samples (figures Id-x) show a similar good preservation with *Uvigerina spp*. shells often appearing translucent (or “glassy”) in low-resolution light microscopy, a sign of excellent preservation (*c.f.* Pearson et al., 2001; Pearson and Burges, 2008; Sexton et al., 2006; Edgar et al., 2015). This good preservation is probably owed to the lithofacies (see chapter 3, section 3.2.2). In general, the

preservation of foraminiferal shells is better in clay-rich sediments and in settings with high sedimentation rates (>30 m/Ma, Fox and Wade, 2013), which is both correct for the setting at Site U1427 having sedimentation rates of ~300-900 m/Ma and being dominated by clayey silt (Tada et al., 2015b).

The good preservation is demonstrated by non-obscured pores on the outer surfaces, for example in sample B-30-2-16 (figure Id-e). Sample A-51-2-98 show signs of diagenetic alteration in some shells and places (figure If-m). Outer surfaces of shells from this sample (figure If) show less pronounced costae and, at higher resolution (figure Ig), small areas with reduced pore-density are visible, just like in the surface sample. Figure Ih shows the same shell crushed with the internal wall-structure visible, showing pores continuing through the wall onto the inner surfaces (figures Ii-j). Sometimes shells show larger wall-crystals in cross-sections indicating possible recrystallisation (figures Ik-l). These enlarged crystals are, however, not the typical micron-scale crystals typical from recrystallisation during diagenesis (Sexton et al., 2006; Fox and Wade, 2013; Voigt et al., 2016), which are several micro-metres in size, but here they are smaller and their arrangement still follows the original wall-structure, running parallel to the original pore channels instead of obscuring them, suggesting these crystals have been formed before or during early burial.

Another sign of minor diagenetic alteration may be seen in the outer surface which, in some areas, shows pores being obscured by a thin layer, which could be of secondary diagenetic nature (figure Il). Contradicting this is the good visibility of pores on internal surfaces (no diagenesis within the shell) and the EDX spectrum of this layer, which does not reveal a composition typical for diagenetic calcite (figure Im).

EDX spectra give qualitative element compositions of patches on the shell surfaces, with peak heights and their relation to each other providing information on the elements in their relative (higher/lower) concentrations. In this case, the suspected diagenetic layer consists mainly of Ca and O, as expected for calcite ($CaCO_3$). The prominent C-peak can be ignored, as it originates from contamination of the carbon-coating, used to reduce charging, and from the device's detector lens, which too contains C. The minor amounts of silicon (Si) and aluminium (Al) are another contamination typical for the device (Dr. Isabel Acre Garcia, pers. com. August 2016). Typically, diagenetic calcite layers contain much more Mg than pristine foraminiferal calcite (e.g. Bentov and Erez, 2006; Sexton et al., 2006), which would appear at the position of at 1.3 keV, indicated by a vertical black line in figure Im. The EDX-spectrum of sample A-51-2-98 does however only show Mg in traces and not an Mg-peak, suggesting the layer apparently obscuring some surface ornamentation is unlikely a diagenetic calcite layer.

In summary on sample A-51-2-98, it very interesting to see different optical preservation stages of *Uvigerina spp*. shells within a single sample, although the chemistry does not seem to have changed dramatically; hinting towards, even if a small selection of shells are analysed in this study, the geochemical implications are valid for the entity of shells within the sample.

Sample A-63-4-7 (figures In-o) again shows little signs of diagenesis, as do the shells in sample A-74-1-36 (figures Ip-t). In both samples, pores are visible on the inner and outer surfaces of shells and pore channels continue through the shell walls. Some shells show small, roundish to elongated holes (figure Ip-q), which could be an artefact of sample preparation (M.J. Vautravers, pers. coms., March 2017) or a sign of beginning dissolution (M. Leng, pers. comm., March 2019). Another shell from this

sample contains a pyrite fromboids, which could have contributed to the formation of the holes (figure It). Pyrite fromboids (FeS_2) are commonly formed in environments with organic matter decomposition (see chapter 5, section 5.3.4), such as Site U1427, and when pyrite reacts with oxygen, it dissolves and releases sulfuric acid, which is corrosive to calcite (Flügel, 2004b). Hence, the presence of pyrite fromboids could explain holes in the shells of this sample.

The deepest sample, A-80-3-25, shows little signs of diagenetic alteration (figures Iu-x). Holes occurring in some shells could again be a sign of dissolution or a preparation artefact, as discussed above (figure Iv). Overall, shells show pristine outer surfaces with pores being visible (figure Iw) and the EDX spectrum shows no significant amount of Mg on investigated layers on the outer surfaces (figure Ix).

In summary, the preservation of *Uvigerina spp*. shells at Site U1427 is generally very good, showing little signs of diagenetic alteration or overgrowths in SEM analyses and qualitative geochemical composition (EDX). Even the samples, formerly identified as having a poor preservation from low-resolution light microscopy, did not show greater degrees of alteration. The good preservation implies that the generated paleo-records, i.e. $\delta^{18}O_{Uvigerina\ spp.}$ and $\delta^{13}C_{Uvigerina\ spp.}$, presented in chapters 4 and 6, are reflecting the original paleo-signals and, hence, that excursions described by the $\delta^{18}O$ and $\delta^{13}C$ records are closely linked paleo-environmental changes at Site U1427. These results furthermore give confidence in the suitability of the chosen Mg/Ca cleaning protocol and resulting temperature estimates (chapter 6) as poor preservation and diagenetic overgrowths would have made a different cleaning protocol necessary (see Chapter 3, section 3.5.10).

Planktonic foraminifera

For the survey of possible diagenetic alteration of planktonic foraminifera shells the samples as shown in table I were analysed. One surface sample containing only *N. pachyderma* dextral coiling (not sinistral coiling nor *G. bulloides*), used as an example for good preservation, and four down-core samples containing either *N. pachyderma* (s) or *G. bulloides* or both were analysed (see table I).

The surface sample shows *N. pachyderma* (d) shells with blocky diagenetic-like crystals on the outer surfaces (figures IIa-b) and a thin layer on the inside of the shell (figure IIe). In wall cross-sections pore channels are open (figures 7.5.c-f), suggesting limited recrystallisation. In some shells there are remnants of the original organic membrane of the living organism in the shell wall (*c.f.* Sexton et al., 2006; arrow in figure IIe). It therefore seems like the blocky crystals on the outside may not be a sign of poor preservation of the shells overall.

Down-core *N. pachyderma* (s) and *G. bulloides* shells look similar to the surface sample with blocky crystals on the outside but otherwise well preserved original features, including remnants of the organic membrane (figures IIg-x). A view into the shells and in into their wall supra-structure shows unobscured pores on surfaces, and usually open pore channels continuing through the walls (e.g. figures IIe, i, m, o), a micron-scale wall crystals (figures IIw, m) and only occasionally a thin layer on the shell inside, likely being the remnants of the organic membrane (figure IIx). A range in preservation states can occur in the same sample (figures IIp-t). This co-existence of good and bad preservation has also been found in benthic foraminifera (see above). No EDX analyses were undertaken as no secondary calcite layers were seen under SEM. Overall, the planktonic foraminifera shells suggested limited diagenetic alteration and isotope records should still reflect original environmental signals.

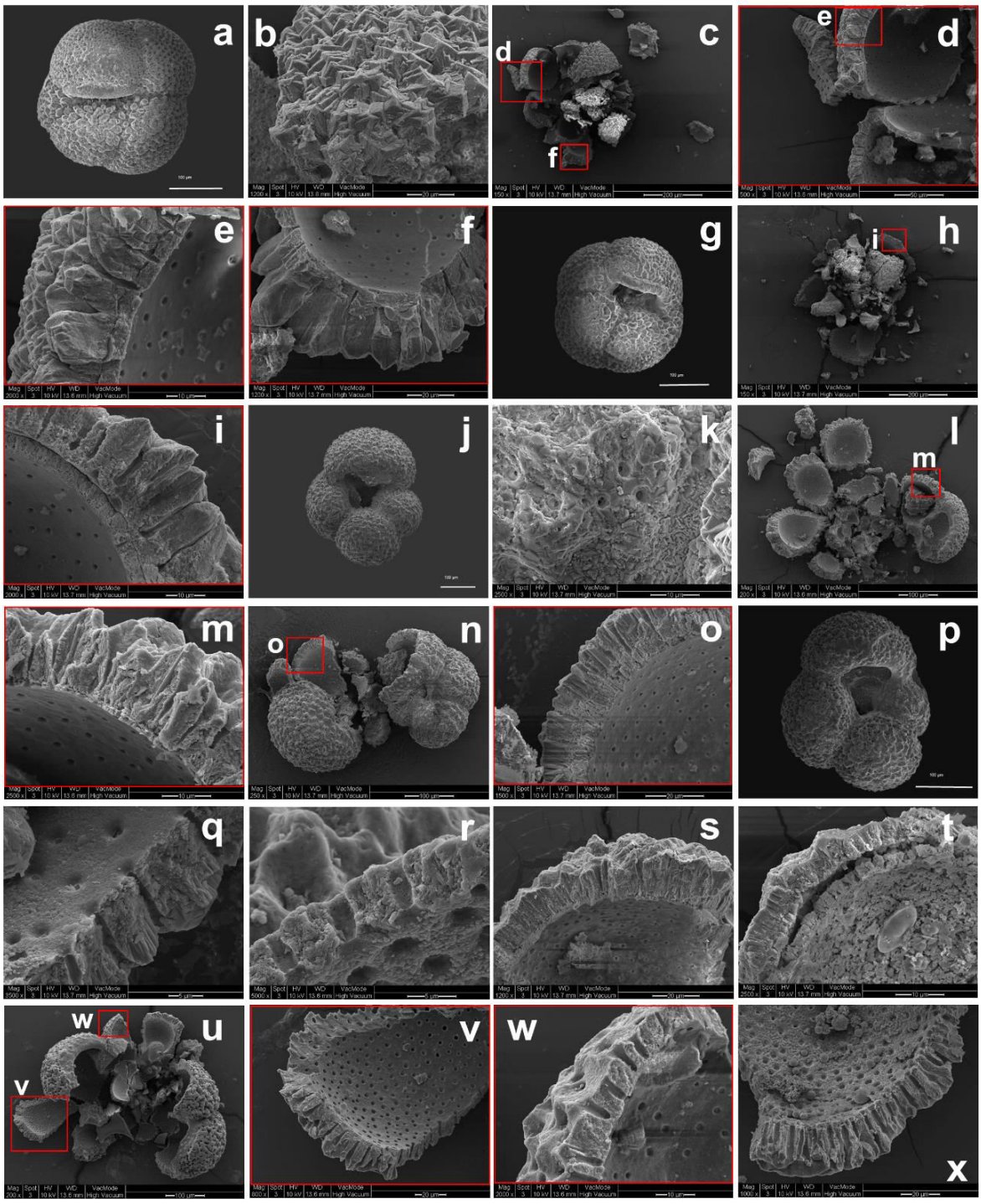

Figure II. SEM images of surface sample, *N. pachyderma* (d) (fig. IIa-f), and down-core *N. pachyderma* (s) and *G. bulloides* shells. Down-core SEM photographs of sample B-42-3-83 showing *N. pachyderma* (s) (fig. IIg-i) and *G. bulloides* (fig. IIj-o), A-74-1-36 showing *G. bulloides* (fig. IIp-r) well preserved and *G. bulloides* in a poorer preservation state with blocky crystals throughout the shell, filled pores and an unusual looking inside layer (fig. IIs-t). The deepest sample, A-79-3-4, shows *G. bulloides* only, well preserved but with pyrite fromboids within its shell chambers (fig. IIu-x).

Appendix C

There are fundamental changes in the climate dynamics across the MPT as described in chapter 2. Timings and possible drivers are still part of the scientific debate and, although the mechanisms are not the focal point of this thesis, the insights gained from the sediments of Site U1427 are summarised here.

Structure of the MPT: gradual versus abrupt changes

The general structure, i.e. gradual or abrupt, is part of the current scientific debate (see chapter 2, section 2.3). Overall, the geochemical records of Site U1427 suggest the MPT is a gradual process from MIS 39 to 25, after which an abrupt increase in the amplitude of changes in the proxy records appears and persists, i.e. during MIS 24-17 (see chapters 4-6) and to the most recently deposited sediments (see e.g. Sagawa et al., 2018).

The early stage of the record, MIS 39-36, is characterised by high amplitude variations in the geochemical records. Between MIS 35 and 25 the difference between glacials and interglacials in the geochemical records become smaller, as a result of enhanced marine productivity during glacials and similar productivity levels during interglacials (see chapter 5). This reduces the amplitude of variability in the geochemical records, while their frequency remains high. At the same time benthic $\delta^{18}O$ is highly variable, likely caused by a strengthening and more variable EASM (see chapters 5 and 6). The combination highly variable $\delta^{18}O$ and reduced expression of glacials and interglacials in the productivity/input records makes the differentiation between glacials and interglacials in the interval MIS 39-25 more challenging (see Chapter 4). With the onset of MIS 24 well-expressed G-IG cycles return, showing higher amplitudes in the geochemical records. Previous studies of Site U1427 have shown that the strong G-IG cyclicity in marine productivity continues to the most recent sediments, i.e. MIS 16-1 (see Sagawa et al., 2018; Gallagher et al., 2018; Black et al., 2018).

A similar behaviour of high amplitude/low frequency, followed by an interval of lower amplitudes, i.e. a lull in the 100 ka frequency, and the re-emergence of high amplitudes has been described from analysis of the LR04-stack (Clark et al., 2006). In detail, LR04 shows the emergence of pronounced and longer G-IG cycles present from 1250ka, followed by a lull in the 100-ka-frequency and lower amplitudes during MIS 29-25, until from ~900 ka (MIS 22) when the 100-ka signal regains power (Clark et al., 2006). A frequency analysis attempted on the geochemical records of Site U1427 showed none of the expected frequencies across MIS 39-17, which may be a statistical artefact due to the shortness of the sediment interval (pers. coms. Erin McClymont, July 2017). However, the absence of distinct frequencies in this interval (~1300-800 ka) has also been identified in power spectra analyses of the LR04-stack (Willeit et al., 2019).

A pronounced shift during the MPT occurs at Site U1427 during MIS 24, when the sudden appearance of the freshwater lens shifts the shallow, southern Japan Sea in the suggested palaeoceanographic mode 1 (see chapter 6). This appears to be preceding a significant sea-level fall described in global sea-level reconstructions from MIS 22 (e.g. Bintanja et al., 2005; Elderfield et al., 2012; Rohling et al., 2014; see chapter 6). The shift to palaeoceanographic mode 1 during glacials persists to MIS 17, as do the higher amplitudes in proxy record variability and the prolonged G-IG cycles (see chapter 4, table 4.3 and/or figure 4.4).

There is an ongoing scientific debate on the exact structure, i.e. abrupt or gradual, and timing of the MPT (chapter 2). No contribution to the onset/end of the MPT debate can be made as the encompassed sediments are from the centre of the MPT from 1256 to 687 ka. However, at Site U1427 the MPT is expressed as a rather gradual process/transition between MIS 39 and 25, with an abrupt shift during MIS 24-22, and the onset of more pronounced and prolonged glacial-interglacial cycles from MIS 21 onwards (MIS 21-17) (see chapter 4, section 4.4.3).

The 900-ka-event

A prominent feature of the MPT is the interval MIS 24-22, when the Japan Sea-typical light glacial $\delta^{18}O$ values emerge and which is characterised by extremely low marine productivity and relatively high terrigenous input (see chapters 4 and 5). Globally, MIS 24-22 is distinct in various proxy records and is considered to be associated with global sea-level and temperature fall and the enhanced storage of atmospheric CO_2 in the oceans (see chapter 2, section 2.3) (e.g. Raymo et al., 1997b; Hoogakker et al., 2006; Elderfield et al., 2012; Rohling et al., 2014; Farmer et al., 2019b). The so-called 900 ka-event (Elderfield et al., 2012), which has been identified in the open ocean (*cit. op.*) as well as in marginal marine seas like the Mediterranean Sea (Rohling et al., 2014), is also pronounced in the Japan Sea (this study).

At Site U1427 the interval is characterised by the sudden appearance of a freshwater imprint on the $\delta^{18}O_{\textit{Uvigerina spp.}}$ record from MIS 24 onwards. Across MIS 24-17 glacials persistently switch into palaeoceanographic mode 1, which is proposed to persist at TSS sill level stands of less than 40-50 m and during which little or no TWC inflow was possible. This implies that sea-levels dropped enough to isolate the Japan Sea during glacial sea-level lowstands of MIS 24-17 (see chapter 6, sections 6.4, 6.5). It is unlikely that local tectonic movements caused the TSS to shoal during MIS 24, as there is no evidence for local tectonic movements (Yoon, 1997; Kitamura and Kawagoe, 2006; Itaki et al., 2016; Zhao et al., 2019). There is however a sea-level drop visible in sea-level reconstructions (figure 6.5d) that is similar to that of MIS 22, which seems to have a great impact on the shallow, southern Japan Sea than on the open ocean.

Previously published sea-level reconstructions show a significant sea-level drop of up to ~120 m below present no earlier than during MIS 22 (Haq et al., 1987; Lisiecki and Raymo, 2005; Bintanja et al., 2005; Sosdian and Rosenthal, 2009; Elderfield et al., 2012; Rohling et al., 2014; Berends et al., 2019) and which is explained by expanding ice sheets (Mudelsee and Schulz, 1997; Sosdian and Rosenthal, 2009; Elderfield et al., 2012). In the Japan Sea, a sea-level reconstruction from shallow water deposits near Site U1427 suggests aerial exposure of the deposition centre during MIS 22 and sea-levels that could have been as low as 15 m during MIS 24, while deposition otherwise took place in 30-100 m water depth across MIS 39-17 (figures 6.5e) (Kitamura and Kawagoe, 2006; Kitamura, 2016). The shoaling during MIS 24 could have been enough to tip the shallow, southern Japan Sea into the suggested restricting/isolating palaeoceanographic mode 1 (chapter 6, section 6.4, 6.5). The mode switch occurring during MIS 24, preceding the more significant sea-level drop of MIS 22, demonstrates the great sensitivity of the sediments of Site U1427 to sea-level fluctuations across the MPT.

Suppressed interglacial MIS 23

The most prominent feature in the geochemical records of Site U1427 is the interval MIS 24-22, with a supressed interglacial MIS 23 in between, that could not be identified based on the combination of the $\delta^{18}O_{Uvigerina\ spp.}$ and b* records. While adjacent interglacials, i.e. MIS 21 and 25, are evident in characteristic excursions in $\delta^{18}O$ and b*, MIS 23 is obscured, which may partly be an issue of temporal resolution of the $\delta^{18}O_{Uvigerina\ spp.}$ record. The absence of higher $\delta^{18}O$ values relative to glacials from MIS 24-17 suggests the freshwater lens that formed during MIS 24 and impacted on $\delta^{18}O$ values persisted during MIS 23. This restriction could either be the result of continued low TSS sill water stands that prevented the unrestricted inflow of the TWC (see chapter 6) or, alternatively, TSS sill stands did allow the TWC to enter but $\delta^{18}O$ values remained low because of a dominance of low-saline/low $\delta^{18}O$ East China Sea Coastal Water over the inflow of Tsushima Current Water, overprinting the global temperature/ice volume signal in $\delta^{18}O$ records of Site U1427.

MIS 23 only emerges as a narrow peak in productivity indicators, i.e. $CaCO_3$ flux, $\delta^{13}C_{org}$, $\delta^{13}C_{Uvigerina\ spp.}$ and as a short-lived interval of higher TOC contents, suggesting nutrient input to prime productivity was possible during MIS 23, although maybe lower than during other interglacials (see chapter 4 and 5). The nutrient input could be linked to via the TSS or input from nearby land, which cannot be excluded in a setting of such close proximity to land as Site U1427 (see figure 3.1).

The weak expression of MIS 23 at Site U1427 fits well to the global expression of this interglacial. Elderfield et al. (2012) call MIS 23 a suppressed interglacial, caused by high ice volume accumulation during MIS 24 and an insolation minima in the southern hemisphere, which contributed to reduced melting during MIS 23. Both of these processes weakened the expression of MIS 23. Global climate culminated in the ice sheet expansion of MIS 22 and the associated 900-ka-event. This maximum ice sheet expansion is thought to mark the onset of the full glaciations that prolonged glacial cycles as a result of longer time needed for melting, and the emergence of the modern 100 ka frequency (Elderfield et al., 2012). Speculatively, the low $\delta^{18}O$ and enhanced marine productivity at Site U1427 during MIS 23 could be caused by continued snow/ice melting in the Japanese isles and within the Japan Sea, which would lead to a continued release of freshwater and nutrients into the otherwise near isolated basin.

Most intriguingly, while at open ocean sites the sea-level fall during MIS 22, i.e. the 900 ka-event, is more significant than that during MIS 24 (see chapter 2, section 2.3) the relatively smaller sea-level drop during MIS 24 has had a greater impact on the sediments at Site U1427, shifting into a new palaeoceanographic mode, which persists during glacials to the present.

Lengthening of G-IG cycles

From 1.2 Ma onwards glacials may have become long and cold enough to allow ice sheet expansion beyond high latitudes/polar regions and high altitudes/mountains, covering north America, the Alps, and in the African mountains, which is characteristic for the 100 ka world, which persists since MIS 22 (Head and Gibbard, 2005). The most extreme/extensive glaciations in the northern hemisphere have been restricted to the last 900ka, i.e. MIS 22-present (Head and Gibbard, 2005). Around MIS 22 the 100 ka signal also becomes statistically significant in

marine $\delta^{18}O$ records (e.g. Imbrie et al., 1992; Clark et al., 2006; Sosdian and Rosenthal, 2009; Kitaba et al., 2011).

The identified whole G-IG cycles, i.e. MIS 38-18, show variations in lengths across the MPT. Although an attempted frequency domain analysis did not show any of the anticipated frequencies, cycles change from long (average 55 ka; MIS 39-36) to short (average ~40 ka; MIS 35-25) and back to prolonged (>50 ka; MIS 21-17) (see chapter 4, table 4.3). This trend of long to shorter and the return and persistence of prolonged G-IG cycles has also been described from other MPT records, including the LR04-stack (Clark et al., 2006; Elderfield et al., 2012). The above G-IG cycle lengths of Site U1427 need to be taken cautiously due to i) the effects of bioturbation on the assumed linear sedimentation rate between age markers in the calculation of cycle lengths and ii) difficulties in identifying MIS between 35 and 27, which made identifying their exact beginning/end very challenging (see chapter 4).

Assuming the change from 41 ka to quasi-100 ka frequency took place during the investigated interval, it was a rather gradual process based on the geochemical records of Site U1427. The most characteristic feature in the proxy records of Site U1427 likely related to more extreme glacials, which are characteristic for the modern 100 ka world, are more pronounced glacial excursions, e.g. in $\delta^{18}O_{Uvigerina\ spp.}$ and/or $\delta^{13}C_{org}$. During MIS 24-22 the two records show very low values and the return to similar values during subsequent glacials, MIS 21-17 (see chapter 6, figures 6.5).

Saw-tooth structure of glacial terminations

A characteristic feature of the modern 100-ka-world is their internal structure, which is asymmetrical and saw-tooth like. Before the MPT transitions from a glacials to interglacials and vice versa were gradual processes with slow ice build-up and decay, in contrast, since the MPT glacial terminations have become more rapid than their onsets leading to a saw-tooth structure in the G-IG cycles (see figure 2.4; Lisiecki and Raymo, 2005). Feedback mechanisms between cryosphere, atmosphere and oceans are thought to control this process, and the existence of the saw-tooth structure has been suggested to imply the switch to a non-linear response to insolation forcing of the climate system (Maslin and Ridgwell, 2005). Proposed mechanisms for the fast collapse of the large ice sheets and rapid glacial terminations include the termination being triggered by a collapse in Southern Ocean stratification with a consequential abrupt increase in CO_2 outgassing from the oceans into the atmosphere (Basak et al., 2018; Gray et al., 2018; Kender et al., 2018). The increased atmospheric greenhouse gas concentrations increase atmospheric temperatures and lead to rising sea-levels. The higher sea-levels speed-up the deglaciation by melting continental ice sheets from the top (though higher atmospheric temperatures) and from beneath by melting marine ice shelfs through undercutting with warm water (Maslin and Ridgwell, 2005).

At Site U1427 the structure of glacial termination is relatively smooth during MIS 39-26, but saw-tooth like terminations appear in the geochemical records from MIS 22/21 onwards. The saw-tooth structure is especially pronounced in b* and $\delta^{13}C_{org}$ (chapter 5), but it is less pronounced in the benthic foraminiferal $\delta^{18}O$ record, which usually shows saw-tooth structure, e.g. LR04-stack. The absence of rapid glacial terminations in $\delta^{18}O_{Uvigerina\ spp.}$ could be caused by an insufficiently low resolution, although this record's resolution is comparable with that of LR04, containing 10-20 samples per cycle. Therefore it is more likely the absence of the saw-tooth structure

is a sign of $\delta^{18}O$ at Site U1427 is being controlled or influenced by processes other than only the global ice sheet waxing and waning. One most likely factor is the EASM (see chapter 2, section 2.4).